Modeling and control of MEMS tweezers for the characterizations of enzymateic reactions on DNA molecules

Nicolas Lafitte

Année : **2012**

THÈSE

présentée à

L'U.F.R. DES SCIENCES ET TECHNIQUES
DE L'UNIVERSITÉ DE FRANCHE-COMTÉ

pour obtenir le

GRADE DE DOCTEUR DE L'UNIVERSITÉ DE FRANCHE-COMTÉ

en **AUTOMATIQUE**
(Ecole Doctorale Sciences Physiques pour l'Ingénieur et Microtechniques)

Modeling and control of MEMS tweezers for the characterizations of enzymatic reactions on DNA molecules

par :

Nicolas LAFITTE

Soutenue le 4 Avril 2012 devant la Commission d'Examen :

Rapporteurs :		
Mme	**Alina VODA**	Maître de Conférences HDR, Université Joseph Fourier, Grenoble 1
M.	**Stéphane RÉGNIER**	Professeur des Universités, Université Pierre et Marie Curie, Paris 6
Examinateurs :		
M.	**Vincent CROQUETTE**	Directeur de Recherche CNRS, ENS, Paris
M.	**Hiroyuki FUJITA**	Professeur, University of Tokyo, Japon
M.	**Bruno LE PIOUFLE**	Professeur des Universités, ENS de Cachan, SATIE
Directeurs de thèse :		
M.	**Dominique COLLARD**	Directeur de Recherche CNRS, LIMMS/CNRS-IIS, Tokyo, Japon
M.	**Yann LE GORREC**	Professeur des Universités, ENSMM, Besançon
M.	**Yassine HADDAB**	Maître de Conférences, ENSMM, Besançon

Acknowledgments

I would like to first thank my advisors Professors Dominique Collard and Hiroyuki Fujita in Tokyo (Japan), and Professors Yann Le Gorrec and Yassine Haddab in Besançon (France). I was fortunate to learn from different cultures and points of view, ... hoping to have learnt the most. Their education and their expertise have been essential in this research.

I would like to thank Professor Alina Voda and Professor Stéphane Régnier , as part of the reading committee for their time. Their comments and inputs were very helpful scientifically but also in terms of confidence for the preparation of the defence. I would like to thank also the members of my oral exam committee, Professors Vincent Croquette and Bruno Le Pioufle. It was a great honour and a privilege for me to have the chance to present my research work to them.

I would like to express all my gratitude to my great colleagues, especially Dr. Hervé Guillou, Dr. Momoko Kumemura and Dr. Laurent Jalabert, who help me a lot during my research. Beside their human skills and their kindness which make everything easier, they have been constantly giving me advices, ideas, knowledge who help me to learn, acquire competences and grow up. This dissertation would have not been possible without them. I want to extend it to student colleagues Rémy Abergel, Vincent Pansu and Rémy Tourvielle with who I shared valuable (research) times.

I would like to thank some people who, during my work, give me attention and help me to move forward ... so in a random order Dr. Jerôme Dejeu, Ing. Patrick Rougeot, Dr. Ioan Alexandru Ivan, Pr. Pierre Lambert, Dr. Cagatay Tahran, Ing. Christophe

Guttin, Dr. Yannick Rondelez, Dr. Satoko Yoshizawa, Dr. Dominique Fourmy and Dr. Christophe Yamahata.

I am also grateful for what I have received from every members of the laboratory of Pr. Fujita and LIMMS laboratory. I appreciate the daily life with them, their friendship and their permanent support. I would like to extend my gratitude to the secretaries in LIMMS, Fujita Lab and Toshiyoshi Lab which make everything possible and the life easier for us.

And finally and the most important, I would like to thank my parents Pierre and Cristina Lafitte and my close friends for their unconditional love and encouragement, which led to my Ph.D. degree. They include, but are not limited to, Aurélie Collado, Séverine Claret, Anne-Sophie Lenoir, Fanny Evenou, Marie Savioz, Christina Grentzelou. They have been great friends, who gave me with abnegation (so hard the task is) the courage to move forward and finish my study.

Contents

1

Introduction

In molecular biology, direct manipulation of single DNA molecules allowed researchers to investigate DNA properties and to go forward in the comprehension of molecular interactions and mechanisms. However, if Watson and Crick have discovered fifty years ago the special structure of the DNA and received the Nobel prize "for their discoveries concerning the molecular structure of nucleic acids and its significance for information transfer in living material" [Watson 1953], it is only over the two past decades that direct visualizations of and measurements on macromolecules lead to important discoveries on DNA machinery.

A variety of remarkable techniques such as fluidic, electric, magnetic and optical traps has been successfully used to position and characterize nano scale objects and molecules. However experiments relying on these techniques involve long and complex preparations needing important skills and drastic conditions. For instance optical and magnetic tweezers are maybe the most impressive techniques enabling to trap one single molecule of DNA among others, and allowing to directly study the properties of the DNA in many different conditions. These achievements have undoubtedly illuminated the nature of interactions between DNA and proteins and the constraints within which the cellular machinery operates.

However such specific and complex techniques are difficult to implement in real time. As a consequence there are not well adapted to reply to the huge demand in systematic analysis and real-time biological and medical applications. An alternative approach consists in using flexible and easy to use tools such as MEMS systems. To achieve these expected features, **the objective of this work was to demonstrate the single DNA molecule manipulation and characterization by micro-machined silicon-based tweezers.**

Accordingly MEMS tweezers have been developed and fabricated in order to enable routine trapping and sensing on biological macromolecules (from 1 to 20 µm length). Previously, in early 90s, Washizu et al. reported the electrostatic manipulation of DNA in microfabricated structures [Washizu 1990]. First actuated tweezers were developed for the demonstration of DNA molecules handling by Hashiguchi et al. [Hashiguchi 2003]; and, in 2008, Yamahata et al. present the current design of the silicon nanotweezers which allow the trapping and the sensing of a bundle of biomolecules [Yamahata 2008a].

The current aim is to enhance the performances of the device improving the sensitivity towards single molecule sensing. It has been proven by Yamahata et al. that the mechanical properties of thousands of attached DNA changes the response of the nanotweezers. However work needs to be done towards more relevant experiments to demonstrate the capabilities of such tool for molecular biology studies.

First experiments on DNA-protein interactions are assumed to show and evaluate the sensitivity of device. Concurrently, the set-up of the nanotweezers will be improved in order to achieve relevant and repeatable analysis. This means the enhancement of the electrical instrumentation, the development of complementary microfluidic for biological solution handling and the possible feedback on the design of the nanotweezers. Finally the implementation of a feedback control strategy will improve the sensing sensitivity of the tweezers toward the performances of existing tools.

In concrete terms, the work took place in two sites. On the one hand, the manufacturing (performed by Dr. Laurent Jalabert) and the development of the bioexperiments are done at the Institute of Industrial Science (University of Tokyo, Japan) in the LIMMS/CNRS-IIS (UMI 2820), and especially in the laboratory of Pr. Hiroyuki Fujita. On the other hand, the works on the design and the first implementation of the control strategy have been achieved at the Automation and MicroMechatronics Systems department of FEMTO-ST institute (Besançon, France).

Structure of the manuscript

After a brief **Chapter** of Introduction, the **Chapter** 2 positions the research in its scientific context. This state of art review the techniques of single-molecule experiments cut into the two primary approaches, that is to say fluorescence and force spectroscopies.

The **Chapter** 3 presents the MEMS tweezers for bioexperiments on DNA molecules. The characterization of the microsystem and the experimental setup is detailed. The **Chapter** ends with the model of the device and the way to perform real-time measurements for bioexperiments on DNA .

The **Chapter** 4 describes the methods to trap and characterize DNA molecules. In particular, **Section** 4.4 demonstrates an attractive method for the real-time characterization of DNA-protein interactions.

The **Chapter** 5 presents the feedback approach implemented to improve the performances of the tweezers. Theory, simulations and experimental results show the validity of the approach.

The last **Chapter** gives the conclusions and draws some perspectives with especially the development of new silicon nanotweezers.

Moreover, this work contents **Appendices** which include some complements about the microfabrication of the MEMS tweezers and the microfluidic device; but also detailed reports on device characterizations and FEM simulations and **the slides of the defence** (which have the advantage to show the work chronologically to the difficulties encountered and the latest achievements). Finally the reader will find the glossary referring to the abbreviations of the manuscript and the bibliography.

2

State of the art: single-molecule analysis techniques

Contents

Summary. Many biological reactions are too complex to be fully understood through the use of conventional ensemble techniques, where the individual behavior can not be distinguished, and only average characteristics across billions of molecules can be measured.

It has been early 90s since advances in instrumentation and techniques have enabled single-molecule experiments. Since then, studies of biological processes at the molecular level have been undergoing in an explosive growth with especially remarkable discoveries on DNA properties.

Therefore this **Chapter** is devoted to the presentation of the different techniques for single-molecule experiment. Two broadly defined categories of methods are detailed in two **Sections**: (1) fluorescence imaging and spectroscopy and (2) force-based manipulation and detection.

2.1 Introduction

Over the last two decades single-molecule experiments have enabled the acquisition of a large amount of information on DNA properties. The ability to isolate or manipulate individual molecules have allowed the direct measurement of physical and chemical properties of DNA molecules.

These properties turn out to be important for the cell machinery understanding as structural modifications in the molecule induce changes in the interaction properties with proteins (and conversely molecular motors change the conformation of the molecules). For instance, topoisomerase enzymes unwind and wind DNA in order to facilitate DNA replication. A helicase protein moves along the unwound DNA, separating the two annealed nucleic acid strands of the double-stranded DNA. Polymerase enzymes reproduce new strands against the single-strand DNA templates. During all the replication process, the physical properties and the biological functions of the DNA change according to the interactions with the proteins allowing or proscribing the sequence of events [Alberts 2002]

In related manner there is a large amount of molecules, proteins and enzymes which are important to investigate precisely and not in a statistical way. Many studies have been carried out on the elementary properties of the DNA and especially on the elastic properties for different constraint range [Bustamante 1994, Cluzel 1996, Leger 1999, Bryant 2003]. Otherwise, DNA-proteins interactions have been studied with structural proteins [Leger 1998, Ali 2001, Skoko 2004], topoisomerases [Neuman 2010], helicases [Dumont 2006], polymerases [Gueroui 2002, Abbondanzieri 2005] (with helicase-polymerase combined dynamic interactions [Hamdan 2007]), restriction enzymes [Seidel 2004], intercalators [Vladescu 2007, Celedon 2010], chromatine [Bancaud 2006], ..., as well as molecular motors with myosin [Ishijima 1991] and ATP [Itoh 2004]. Many works on DNA mapping [Bensimon 1994] or cell polymers [Amblard 1996] have also been reported.

In fact single-molecule approaches use a wide variety of techniques from the visualization to the direct manipulation of molecules. Nevertheless, by single-molecule experiments, it is assumed to investigate the properties of individual molecules that can be distinguished for the purpose of an experiment or analysis. However analysis are not ever done with a *single* molecule. The interest arises from *discrete* molecule experiments, where individual molecules are differentiated from an *ensemble*.

On the one hand, large advances have been achieved enabling single-molecule visualization. Scientists developed powerful manipulation techniques where the DNA is attached to a substrate and observed by fluorescence [van Mameren 2008, Haustein 2004]. For instance, polymerase enzymes were fluorescently labeled to monitor their activity on a single-molecule of DNA previously combed onto a surface [Kim 2007].

On the other hand, new approaches were developed to directly interact with the molecules, e.g. optical tweezers, magnetic tweezers, atomic force cantilevers (known as AFM) and microfibers [Neuman 2008, Moffitt 2008]. The response of single DNA molecules to a stretching or a twisting stress gives direct access to the physical properties of the molecule. Remarkable mechanical properties of DNA were discovered and protein interactions with DNA were measured by the changes in the mechanical properties of the strands [Strick 2000a, Bustamante 2003].

Thereafter, these techniques will be introduced in more details into two **Sections**: (1) fluorescence imaging and spectroscopy and (2) force-based manipulation and detection. Discussions will be devoted to their advantages such as the sensitivity to single molecules and their drawbacks such as the implementation, the fabrication or the sensing method.

2.2 Fluorescence spectroscopy

Old school chemical experimentations in test tubes (or culture tubes or sample tubes) do not allow accurate analysis of the tested chemical or biological reactions (**Figure** 2.1). Evidently, in test tubes, detection of a single fluorescent molecule is hindered by the presence of billions of molecules and further by noise of the setup. Therefore, highly diluted fluorescently labeled sample solutions, devoid of any fluorescent impurities, must be combined with small probe volumes. Techniques for the fluorescence excitation and spatial confinement of samples have been developed to attain the visualization of single molecules.

Fig. 2.1. Two small test tubes held in spring clamps, commonly used to monitored chemical reaction by fluorescence. (Source Wikipedia, article about "test tube", Sept. 2011).

Nowadays, a vast variety of techniques combining microfluidics and fluorescence microscopy features obtained the discrete monitoring of biological macromolecules.

In their paper, [Haustein 2004] detailed technically the features of the microscopy to achieve the sufficient high temporal and spatial resolution: correlation analysis of fluctuation of the fluorescence intensity (Fluorescent Correlation Spectroscopy), Cross-Correlation Spectroscopy using two spectrally separated fluorescent probes, Fluorescence Resonance Energy Transfer between 2 distant fluorophore-labeled molecules, ...

[van Mameren 2008] described the techniques in microfluidics to accomplish molecule separation or isolation and visualization.

2.2.1 Molecular combing

Molecular combing is certainly the easiest way to stretch long and soft DNA molecules. The technique uses a receding air-water interface to stretch the macromolecules (**Figure** 2.2). On the one hand, DNA tends to bind to hydrophobic glass surface. On the other hand, surface tension at meniscus extends the molecules resulting in stretched molecules on the glass surface. The interaction surface/DNA is probably due to hydrophobic affinities of some parts of the double-stranded DNA. The attachment is enough strong as the rehydration of the sample is possible without detachment.

[Bensimon 1994] demonstrates the first proof of the concept. However the forces generated by the air-water interface, about 0.5 nN, cause structural changes in the

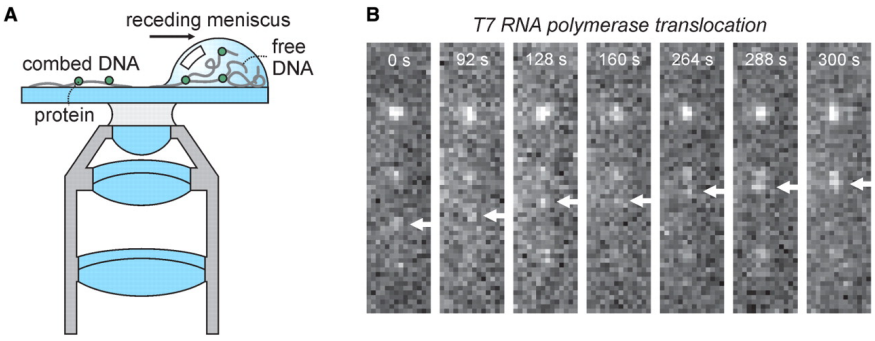

Fig. 2.2. Attachment of single DNA molecules on a glass surface. (A) DNA is stretched and immobilized using hydrophobic glass substrate and a receding air-water interface. After rehydratation of the sample the DNA stays firmly attached to the glass slide [van Mameren 2008]. (B) Real-time visualization of the motion of a RNA polymerase along combed DNA strands. The directional movement of the RNA polymerase along a DNA molecule is observed using the incorporation of fluorescent into RNA strand (Scale bar = 2.5 µm) [Kim 2007].

DNA molecules affecting the DNA-protein interactions. Therefore, specific solutions were brought by engineering the liquid properties and lowering the surface tension [Gueroui 2002] or using a flow to control the stretch. A second aspect to consider is the number of attachments of the molecules on the surface. For some subsequent analysis reasons, the glass is coated with polymers such as PDMS or PMMA to only attach the DNA in a few places.

DNA visualization is achieved with fluorescent dyes, but most of them are intercalating dyes such as YOYO-1 modifying the structure of the DNA. Alternatively, only ends of DNA can be labelled (e.g. with biotin) or the interacting molecules is labeled (like RNA strands in **Figure** 2.2).

This molecular combing has found powerful application in mapping and analyzing complete genomes by hybridization[1]. Diverse applications of the technique are presented in [Lebofsky 2003].

2.2.2 Surface-thetered DNA extended in flow

An evolution of the previous combing technique is to specifically attach the end of the DNA to the surface and stretch the DNA controlling a liquid flow in a microfluidic channel (**Figure** 2.3). The molecule is especially prepared on one end adding a biotin molecule (i.e. by hybridizing one of its single-stranded overhangs to a short complementary strand modified with biotins). Then the molecules attach to the surface coated with biotin-binding protein (e.g. streptavidin) and are uncoiled from their natural compact conformation applying appropriate flow-induced forces.

[1] Hybridization uses a complementary DNA or RNA strand which is labeled to localize a specific DNA or RNA sequence.

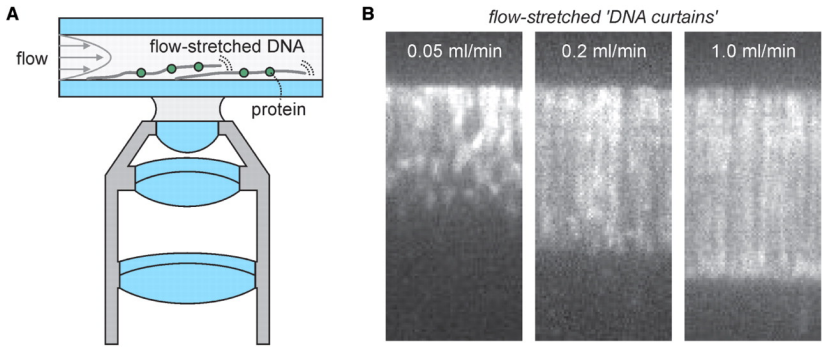

Fig. 2.3. Stretching of surface-attached DNA using continuous flow. (A) Schematic of the assay. DNA is attached to the glass surface from one end. To overcome the entropic forces that keep the DNA compact a continuous flow is applied, extending the DNA. Visualization of DNA or associated proteins can be realized using fluorescence microscopy [van Mameren 2008]. (B) Application of this assay to YOYO-labeled λ-DNA, demonstrating how DNA stretching and extension depends on the flow rates [Granéli 2006].

Some improvements of the techniques are brought attaching a bead at the other end of the molecule. The drag force on the bead significantly exceeds the drag on the DNA, making the force homogeneous along the extension of it. This technique takes advantages of the progress made in microfluidics and the development of flow chambers with velocity profile theories and enhancement. This flow-stretching approach has been applied to study fluorescently labeled proteins diffusing along DNA [Granéli 2006]. An evolution was brought using a magnetic bead in order to couple hydrodynamic forces with magnetic forces controlling the bead[2] [Smith 1992].

2.2.3 DNA fixed to an optically bead extended in flow

To overcome problems related to the glass surface-molecule interactions, the molecule is finally attached to an optically trapped bead away from the surface and stretched by the other end controlling a liquid flow in a flow channel (**Figure** 2.4). The attachment chemistry to the bead could be the same previously described. The sphere is optically trapped in the focus of an intense near-infrared laser beam[3].

Many studies were led implementing this technique with the aim of following the function of helicase enzymes acting as motors on DNA. For example in **Figure** 2.4, RecA[4] is fluorescently labelled to follow their activity on a trapped DNA molecule. The reparation of the DNA requires the formation of a RecA nucleoprotein filament which were monitored in the experiment of [Galletto 2006]. The technique helped the characterization of the rates of nucleation and growth, and the involvement of ATP hydrolysis.

[2] Magnetic trap are introduced later in the **Section** 2.3.2 describing Magnetic Tweezers.
[3] The physics enabling the trapping of the bead is explained later in **Section** 2.3.1 or in [Neuman 2004], describing Optical Tweezers principle.
[4] RecA are a DNA repair protein for *Escherichia coli* DNA (λ-DNA). The homologous protein in *Homo sapiens* is called RAD51.

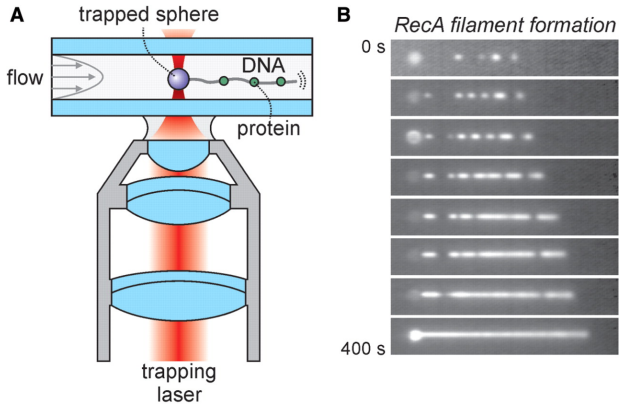

Fig. 2.4. Stretching of DNA held with one side in an optical trap using continuous flow. (A) Schematic of the assay. DNA is attached to a bead from one end, the bead is held in an optical trap. To overcome the entropic forces that keep the DNA compact a continuous flow is applied extending the DNA. DNA or associated proteins can be visualized using fluorescence microscopy [van Mameren 2008]. (B) Application of this assay to the formation of RecA filaments. λ-DNA is incubated with fluorescent RecA and filament formation is monitored by fluorescence. The length of the DNA increases with the RecA binding [Galletto 2006].

2.2.4 DNA thetered between two optically trapped beads

The idea of this new evolution is to clear out the drawbacks related to the use of flow. Here the molecule is stretched in between two optically trapped beads (**Figure** 2.5). Consequently the force is homogenous distributed along the molecule. Furthermore, the fact that the technique does not require continuous flow enables more pertinent experiments on DNA-protein interactions (i.e. without imposing a preferential direction by the flow).

Moreover optical trapping permits more accurate measurement of the forces applied to the DNA than the flow-induced forces which are complicated to implement and control. The force and the extension of the DNA is controlled through the distance between the two traps[5].

The implementation of this technique enables the simultaneous quantitative sensing of the force applied to the molecule and the direct visualization of enzymes binding or moving on the DNA using fluorescence. [Arai 1999] use optical trapping in microfluidics to analyze the mechanical properties of filamentous structures (DNA and actin[6]). They were able to control the shape of the filaments and experiment the critical bending or the knot diameter that filaments are able to take in the cell. For instance, actin filaments break at the knot when the knot diameter falls below 0.4 μm with an unusual low force around 1 pN.

[5] The physics enabling the trapping of the bead is explained later in **Section** 2.3.1 or in [Neuman 2004], describing Optical Tweezers principle.

[6] Actin is a monomer forming actin polymers which are involved in the cytoskeleton, i.e. the "skeleton" of the cells. Consequently they participate to the contraction, the motility and the division of the cells.

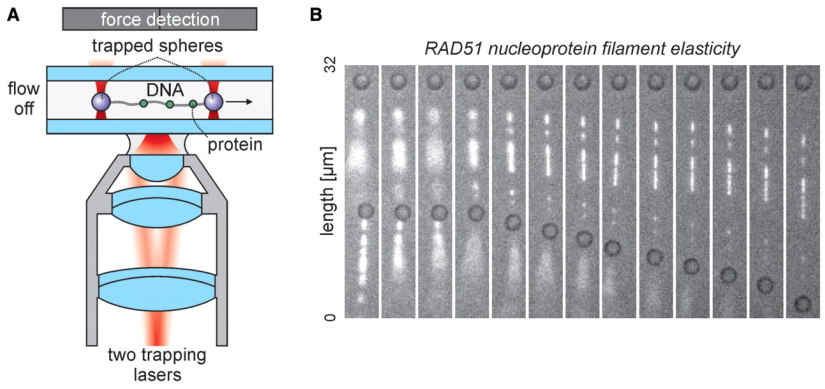

Fig. 2.5. Enhanced control using two force-measuring optical traps. (A) Schematic of the dual-trap assay. After suspending a single DNA molecule in between two trapped beads, the DNA can be manipulated without the application of force. In addition, optical tweezers can be employed to quantitatively detect the forces exerted on the DNA. The fluorescence from DNA-labeled dyes or fluorescently labeled DNA-binding proteins is detected using a CCD camera [van Mameren 2008]. (B) The assay setup employed by [van Mameren 2006] in the study of the elasticity of RAD51 nucleoprotein filaments formed on double-stranded DNA. One DNA molecule is suspended in between two optically trapped beads (dark circles). (A second molecule is attached from the lower bead and freely diffusing once buffer flow is switched off.) Tension is applied to the DNA by increasing the distance between the traps. The differentiated extension of the fluorescent, RAD51-coated segments and the dark, uncoated segments can be directly seen. The increasing suppression of thermally excited diffusion of the DNA is readily observed.

2.2.5 Discussion

In this **Part**, we present the tools that has been developed for the direct visualization of macromolecules. Much efforts have been performed to enable high resolution in time and in space. However the limitations arise from the fluorescence microscopy features.

The two common experimental setups for measuring fluorescence at the single-molecule level are confocal microscopy and total internal reflection fluorescence (TIRF) microscopy (**Figure** 2.6). In confocal microscopy, a laser is focused through the objective lens of a microscope, exciting only a small volume. The emission can be split into multiple channels for acquisition. To image many molecules, a piezo stage is typically used to scan the slide. The benefit of confocal microscopy is that a time resolution on the order of micro-seconds can be achieved. In the TIRF microscopy, an excitation light is brought to the sample creating an evanescent wave that excites only those molecules within a few hundred nanometers of the quartz surface. The fluorescence emission is then sent through the objective and is recorded on a CCD camera. The benefit of TIRF over confocal microscopy is that a larger area of the slide can be imaged. The drawback of this method is that the camera limits the time resolution to few milliseconds. Several other optical configurations, which are less reported in the literature, also permit single fluorescent molecule detection (cf. especially HILO [Tokunaga 2008] and NSOM [Edidin 2001]).

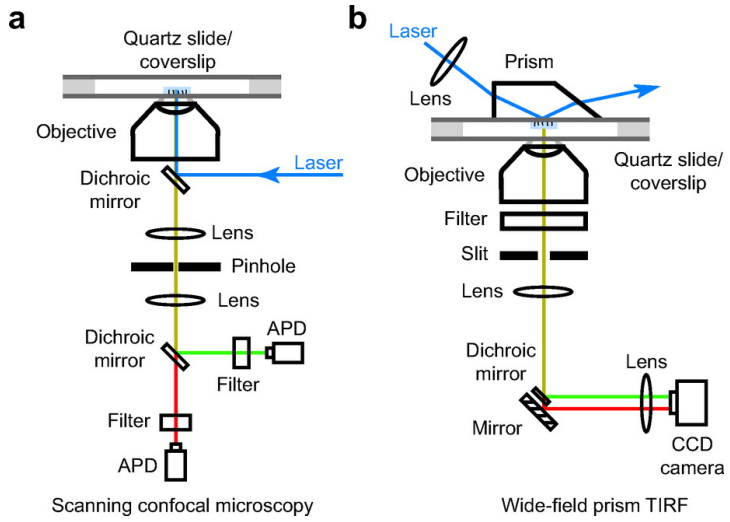

Fig. 2.6. Conventional experimental setups used for single-molecule fluorescence. (a) A typical confocal microscope with both the excitation light and emission going through the objective lens. (APD = avalanche photodiode). (b) A prism-type TIRF microscope where the excitation light is reflected through a prism on top of the slide and the emission goes through the objective. Image from [Cornish 2007].

To obtain a good signal-to-noise ratio (SNR) of the single-molecule signal, the approach needs to deal with a combination of conditions as a small focal volume, large absorption cross-section, high photo-stability, operation below saturation of the molecular absorption and a high fluorescence quantum yield of fluorescence. For fluorescence issues, one has to rigorously exclude fluorescent impurities (i.e. fluorescence background), minimize the volume probed and select adequate fluorophores (which pose severe limitations owing to photobleaching and blinking). Fluorescent background and volume probed are solved by enhancing the experiment setup, i.e. the microscopy and the microfluidic features.

The most important limitations of these techniques arises from the labeling of the DNA molecules or proteins. For instance, most of DNA fluorescent dyes are intercalating agents, i.e. they come in between the two strands or chains of the DNA forming its helical shape. These dyes have substantial effects on the extension and the mechanical properties of the DNA (depending on the labeling density) and might in this way influence the interaction of proteins with the DNA. Solutions are reported in the literature to minimize effects on the "normal" properties of the molecules, and new kinds of emitters such as semiconductor nanocrystals, silver nanoclusters, and new derivatives of fluorescent proteins appear [Bruchez Jr 1998, Giepmans 2006, Vosch 2007]. However results are altered by the presence of these extra samples, e.g. changing the rates of protein attachment.

A second limitation of these techniques is the unusual extension of the molecules. In cell, DNA molecules are in random coil in a three-dimensional configuration enabling jump processes of proteins sliding along the DNA. This feature is suppressed by the single-dimensional extension of the molecules making a difference between processes inside the

cell and in such experiments. However, all the techniques nowadays developed uncoil DNA and characterize the force interactions between DNA and proteins in this way.

2.3 Force spectroscopy

Simultaneously to optical spectroscopy development, nanotechnology engineering has enabled the emergence of powerful tools enabling the direct manipulation of single molecules. These techniques have in common to direct interact with the molecules in between specific probes. The measurement of probe displacements or forces permits the sensing of mechanical properties of the molecules or interactions between proteins and single molecules.

An exhaustive enumeration of single-molecule manipulation tools would be a heterogenous list of techniques or knowledges dealing with basic physical principles (as electric or magnetic field gradients), microfabrication features (e.g. with micro-size beam manufacturing), or smart ideas (as flow-induced stretching or membrane probes). Nevertheless the most commonly known and used are quite obviously Optical Tweezers (OT), Magnetic Tweezers (MT) and Atomic Force Microscopy (AFM). However interesting experiments were also achieved with micro-needle [Cluzel 1996], or biomembrane force probe [Evans 1995]. Let us give some details on such tools.

2.3.1 Optical tweezers

Since its principle demonstration [Ashkin 1986], optical traps have been widely applied to a variety of biological systems as DNA molecules [Arai 1999, van Mameren 2006], kinesin motors [Block 1990, Svoboda 1993], virus [Mammen 1996] or cells [Block 1989].

In a typical experiment, biological polymers, membranes, cells, microtubules are attached in between two optically trapped beads or a trapped bead and a glass surface (**Figure** 2.7). Then the rheological properties of these objects are probed through the motion of the trapped bead. The force is deduced from the measurement of the relative motion of the bead with respect to the trap center and force. Nano-meter displacements and pico-newton forces can be detected. Thus this technique is particularly appropriate for studying forces and displacement at the molecular level.

Although the full theory of the optical trap is quite complex, it is well demonstrated in the first report of the principle [Ashkin 1986] and in this detailed paper [Rohrbach 2002]. Practical features are described in this long review [Neuman 2004].

The measurement are proceeded in the following manner. An optical trap is formed by tightly focusing a laser beam with an objective lens of high numerical aperture. Dielectric particles in the vicinity of the focus experience a three-dimensional restoring force directed toward the focus. Typically for small displacements (< 150 nm) of the polarized particle from the equilibrium position, the force gradient is linearly proportional to the displacement, and the optical trap is well approximated as a linear spring. The spring constant, or stiffness, depends on the steepness of the optical gradient (how tightly the laser is focused), the laser power and the polarizability of the particle.

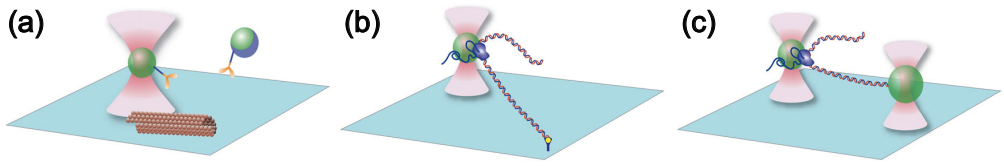

Fig. 2.7. Schematics of optical tweezers-based assays. (a) A bead (in green) is trapped by the focus of an infrared laser (in red). Interaction force between kinesin molecules (in yellow) coated on the bead and microtubule (brown tube) attached to the surface are determined from the displacement of the bead [Block 1990, Svoboda 1993]. (b) In a tethered assay, a DNA molecule is tethered in between a clamped glass surface and a trapped bead directly or through an enzyme (RNA polymerase in purple). As the DNA is transcribed, the bead is pulled along the DNA by the polymerase. By moving the stage to compensate for this motion, thereby keeping the bead at the same position in the optical trap, long transcriptional records can be obtained at a constant force [Neuman 2003]. (c) In the dumbbell assay, DNA is attached to a second bead, which is held in a second optical trap. The force on the bead can be kept constant by moving one of the traps [Abbondanzieri 2005]. Schematics have been taken from [Neuman 2008]

Therefore measurements require previous calibration of the position and the force. Usually the spring constant is identified from the characterization of Brownian motion or moving the probe through a known distance. Accordingly the force measurement is deduced from the Hooke's law ($F = -kx$). [Neuman 2004] detailed the method for calibration and measurements in his review paper.

The limitations arise from the use of a laser to form the optical trap. A possible heating of the solution and the generation of local convection currents may influence the measurements of enzymatic activity for example. Furthermore, laser in the near-infrared wavelengths is usually used to minimize photodamage of the specimens without eliminating all the risks.

With this technique, the range of applied forces is $0.1 - 100$ pN. The low limit is set by the lowest stiffness needed to ensure trap stability, while the upper limit is set by the maximum power. The range of displacement is usually limited to the linear range of the trap, i.e. ~ 150 nm. For larger displacements, the experimental setup is enhanced incorporating actuation and control of the stage. Experimental result resolutions are reported under the nanometer and millisecond levels.

2.3.2 Magnetic tweezers

The concept of magnetic tweezers (MT) is similar to that of optical tweezers. Single molecule can be manipulated by attaching it to an electromagnet with a paramagnetic core material and operating in a high magnetic field gradient (**Figure** 2.8).

One of the distinctive feature of the MT is that it can be used to extend and rotate molecules. These characteristics are ideally suited to the study of DNA enzymes such DNA topoisomerases which unwind ds-DNA [Strick 2000b] or rotary motors such as F_0F_1ATPase [Itoh 2004].

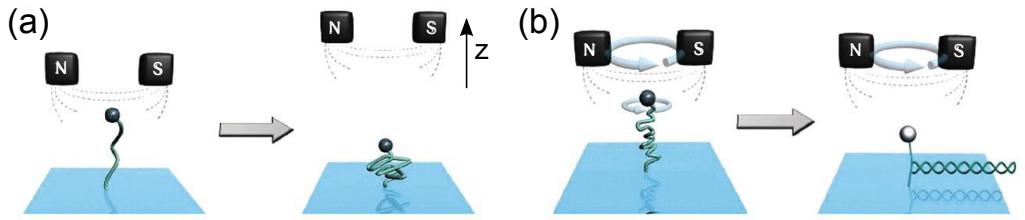

Fig. 2.8. Schematic sketch of the magnetic tweezers technique. (a) The setup consists of a DNA molecule attached to a magnetic bead and to a glass surface for instance. A pair of magnets above the bead produces a magnetic field gradient (dashed lines) along the axial direction, which results in a force on the bead directed upward toward the magnets. The magnets can be lowered (raised) to increase (decrease) the stretching force acting on the DNA. (North and south pole magnets are respectively labeled N and S.) (b) Thanks to the magnetic properties of the bead, torque forces can also be applied to the sample. Starting from a relaxed configuration, the DNA molecule becomes more and more tangled as the magnets rotate, and eventually loops of helices (plectonemes) are formed. Sketches have taken from [Salerno 2010].

The measurement are proceeded in the following manner. The MT are placed above the sample holder of an inverted microscope, and biological polymers (typically DNA) are attached in between a controllable magnetic bead and a glass surface. Forces are proportional to the gradient of the square of the magnetic field. However forces can be important and roughly constant in between the magnets, resulting in a very low effective stiffness (reported 10^{-6} pN/nm). Experiments are usually performed at a constant force (at force clamp). The sample is illuminated through the gap in the magnets, and interference fringes between unscattered and scattered light produce a well-defined pattern which permit the measurement of the height position of the bead. Lateral motions of the particle is measured by centroid tracking.

The MT are capable to exert forces in excess of 1 nN (with electromagnets) or 200 pN (with small permanent magnets). As aforementioned, one of the distinctive feature of the MT is that torque experiments can be applied to molecules. Estimates of the applied torque for a 1 µm magnetic bead are in excess of 10^3 pN.nm, which is nevertheless much larger than molecular torques. MT are the unique tools to enable torque experiments on single molecules. However, the large applied torque limits the use of this feature and moreover the direct measurement of the rotation required special labeling of the molecule [Lipfert 2010].

Finally, as for optical tweezers, sensitivity is limited by the video-based detection, which prevent the direct measurement of very fast or very small displacements. This technique also allows full 3D manipulation, but this requires cumbersome feedback system in addition to the sophisticated setup.

2.3.3 Atomic Force Microscopy

AFM is very versatile tool widely used for imaging, measuring, and manipulating matter at the nanoscale. [Binnig 1986] discovered the principle in 1986 after the development of Scanning Tunneling Microscope (STM).

Basically AFM consists of a cantilever with a sharp tip at its end that is usually used to scan surfaces for topography at sub-nanometer resolution (thousand times better than the optical diffraction limit). When the tip is brought into proximity of a sample surface, forces between the tip and the surface lead to a deflection of the cantilever according to the stiffness of the cantilever. Depending on the studies, the forces that are measured with an AFM include mechanical contact force, van der Waals forces, capillary forces, chemical bonding, electrostatic forces, magnetic forces and Casimir forces for instance.

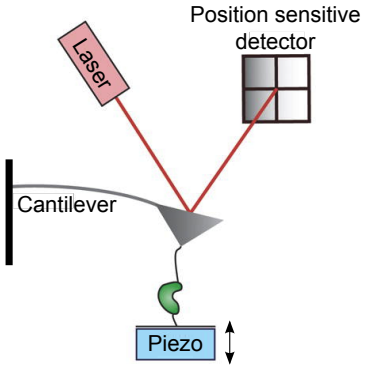

Fig. 2.9. Atomic force microscopy sketch, which consists of a cantilever with a sharp tip (in gray) held above a piezoelectric scanning stage (in light blue). A cantilever exerts tension on a molecule of interest attached to the tip. Deflection of the cantilever is measured from the displacement of a laser (red beam) reflected off on a position-sensitive detector, and force is modulated by adjusting the position of the sample piezoelectrically. Sketch has been taken from [Greenleaf 2007].

The AFM also allows measurements of inter and intra-molecular interaction forces at the piconewton-level. In order to measure the mechanical properties of the sample molecule, the ends of the biological molecule need to be prepared to specifically attach respectively the AFM probe and the surface (**Figure** 2.9). Non specific binding is also possible, but results in uncertainties in the attachment and subsequent data measurement interpretation. Therefore many methods of attachment were developed using antibodies, streptavidin-biotin bonds, avidin-biotin bonds but anyhow the contribution of the attachment must be considered in the elastic response of the system.

Single-molecule extension is commonly obtained by the z-displacement of the piezo-actuated stage, and forces are generally calculated from the bending of the cantilever with a known spring constant. Molecules of interest are described as springs that generate a restoring force when they are mechanically stretched. Therefore the extension is the distance between the anchoring points, i.e. between the cantilever tip and the glass surface.

AFM-based force spectroscopy has emerged as a very popular tool to study pico to nanonewton-level forces such as the rupture of molecular bonds (covalent bonds or enzyme-DNA interactions) [Weber 1989, Engel 1991, Bustamante 1995, Shao 1995,

Ueda 1999, Krasnoslobodtsev 2007]. Commercial AFM are available from several suppliers but usually customized experimental setups are built where the cantilever is changed and functionalized with respect to the target analysis. The accuracy of the measurements is determined by the quality of the piezoelectric stage and the implementation of closed-loop position feedback control.

The main limitation of AFM stems from the large size of the probe, which imposes high stiffness (~ 1 N/m) and important losses in liquid environment (resonance quality factor flattening to 1 in liquid). Besides the forces associated with many biological processes are difficult to study with AFM. On the other hand, surface functionalization and bio-liquid preparation are required to avoid nonspecific molecule binding, undesirable interactions with the surface and subsequent artifact in data measurement. It can be difficult to distinguish interactions of the tip with the molecule of interest from nonspecific interactions or inappropriate contacts with the molecule of interest.

2.3.4 Conclusion

Force spectroscopy methods evidently opened the way for new types of experiments in molecular biology. Direct measurement of forces at the molecular level has enabled to detect, quantify and understand forces governing the interactions between the molecules in the cell. Nevertheless these techniques still show some particularities and limitations which are summarized in **Table** 2.1.

Indeed one specificity of these methods is the need to attach the ends of the molecule to a probe (which can be a bead or a tip). Ideally the bonds should not affect the mechanical and the biological properties of the molecule, binding the ends of the molecule and supporting infinite load. However the required chemistry to attach the probes is not easy and attachments are usually approximated ranging from nonspecific adsorption and tight covalent bonds. Special care is required during the preparation and during the experiment to avoid unexpected bindings (e.g. nonspecific binding with the surface or the probe) and artifacts in data.

	Optical tweezers	Magnetic tweezers	AFM
Displacement resolution (nm)	$0.1 - 2$	$2 - 10$	$0.5 - 1$
Temporal resolution (s)	10^{-4}	10^{-2}	10^{-3}
Stiffness (N/m)	$10^{-6} - 10^{-3}$	$10^{-9} - 10^{-6}$	$0.1 - 100$
Force range (pN)	$0.1 - 100$	$0.001 - 200$	$10 - 1000$
Displacement range (nm)	$0.1 - 10^5$	$0.1 - 10^4$	$0.1 - 10^4$
Probe size (µm)	$0.1 - 10$	$0.1 - 10$	$100 - 250$
Features	3D manipulation High resolutions	Rotation Constant-force assays	High-force assays "Simple" setup
Limitations	Photodamage Heating Complex setup	Complex setup	High stiffness Large minimal force

Table 2.1. Comparison of single-molecule force spectroscopy techniques [Neuman 2008].

Besides the measurement in these methods relies in the precision and the accuracy of the determination of the probe. The quality of the results depends on the environment and the related noises such as mechanical vibrations or acoustic and electromagnetic interferences.

In micromechanical systems fundamental resolution is typically limited by thermal motion which is related to the effective stiffness of the system. Spatial resolution is determined by the thermal noise of the probe which is given through the deflection:

$$\delta x = \sqrt{\frac{k_B T}{\alpha}}$$

where δx is the position magnitude induced by the noise, $k_B T$ is the thermal energy and α which can be the intrinsic stiffness of the probe (in the case of OT or AFM) or the stiffness of the molecule (in the case of MT). Fundamental resolution arises dealing with a trade-off between time resolution, i.e. the filtering constant which is lower than the motion roll-off frequency, and the experimental conditions, i.e. the stiffness of the system and, to a lesser extent, the hydrodynamic drag on the probe [Gittes 1998].

The resulting resolution (in micromechanical systems) are therefore improved by increasing the stiffness, reducing the bandwidth or decreasing the drag losses. Temporal resolution is inversely proportional to the bandwidth. Maximal resolution in terms of position, force and time is fairly achieved by minimizing hydrodynamic drag on the probe motion. This implies to consider probe dimensions and viscosity of the biological liquid.

2.4 Conclusions

The technical advances in single-molecule tools over the past two decades have been bringing a large amount of informations in fields as diverse as structural biology, enzymology, nanotechnology and systems biology. For recent reviews, one can read the following articles [Bustamante 2003, Haustein 2004, van Mameren 2008, Neuman 2008, Moffitt 2008, Walter 2008]. Nevertheless some limitations of single-molecule tools still remain and are needed to be addressed.

Concisely, single-molecule approaches:

1. provide a way to "just look at the thing" seeing single-molecule behavior and moving out of statistical analysis;
2. enable the direct quantitative measurement of mechanical properties of single biomolecules and their assemblies, including the forces generated by biological motors (10^{-2} to 10^4 pN);
3. ease the quantitative measurement of the kinetics (microseconds to minutes) or statistics of complex biological processes;
4. work at the low numbers observed for nucleic acids, proteins, enzymes as in a living cell (typically 1 to 1000);
5. reveal rare or transient species along a reaction pathway, which are averaged out in statistical measurements;

6. and allow the miniaturization and multiplexing of biological assays such as DNA sequencing.

Several directions of improvement are led for the future of single-molecule microscopy. The combination of tools to measure mechanical forces while monitoring in real-time by fluorescence where the force is exerted is a first enhancement achieved for better understanding of molecular structural biology [Ishijima 1998, Moffitt 2008].

Besides performing the similar experiments *in vivo* where individual proteins and enzymes function in their natural environment will be an unparalleled advance. Questions on how cells generate and respond to forces at the molecular level will be addressed. Few and preliminary achievements have been performed with magnetic probes [Sacconi 2005, de Vries 2005].

Another route to increased information content must to be increasing parallelism and throughput in force spectroscopy measurements [Chiou 2005]. Parallel assays have to be developed enabling access to a large number of observables at a time, allowing multiplexing or understanding of complex biological processes.

Silicon nanotweezers for DNA molecules manipulation

The review of techniques of single-molecule manipulation makes appear that a large range of tools exist with different specifications. [Walter 2008] provide "guidelines for choosing the right approach from the available single-molecule toolkit" depending the target analysis (see **Figure** 2.10).

An axe of development for molecular spectroscopy is the simplification, the automatization and the parallelization of the measurements. This implies to develop simple tool for (1) easing the biological experiments and (2) enabling multiple experiments. For example, on the one hand, simple molecule trapping without labeling requirement is a significant enhancement for systematic analysis. On the other hand, multiplying experiments may use molecular tool easy to provide (e.g. fabrication and cost concerns) and to implement (e.g. with appropriate integration of actuation and sensing).

For that specific purpose, nanotweezers based on silicon technology are designed and fabricated. Silicon nanotweezers and experiments with nanotweezers are introduced from the next **Chapter**.

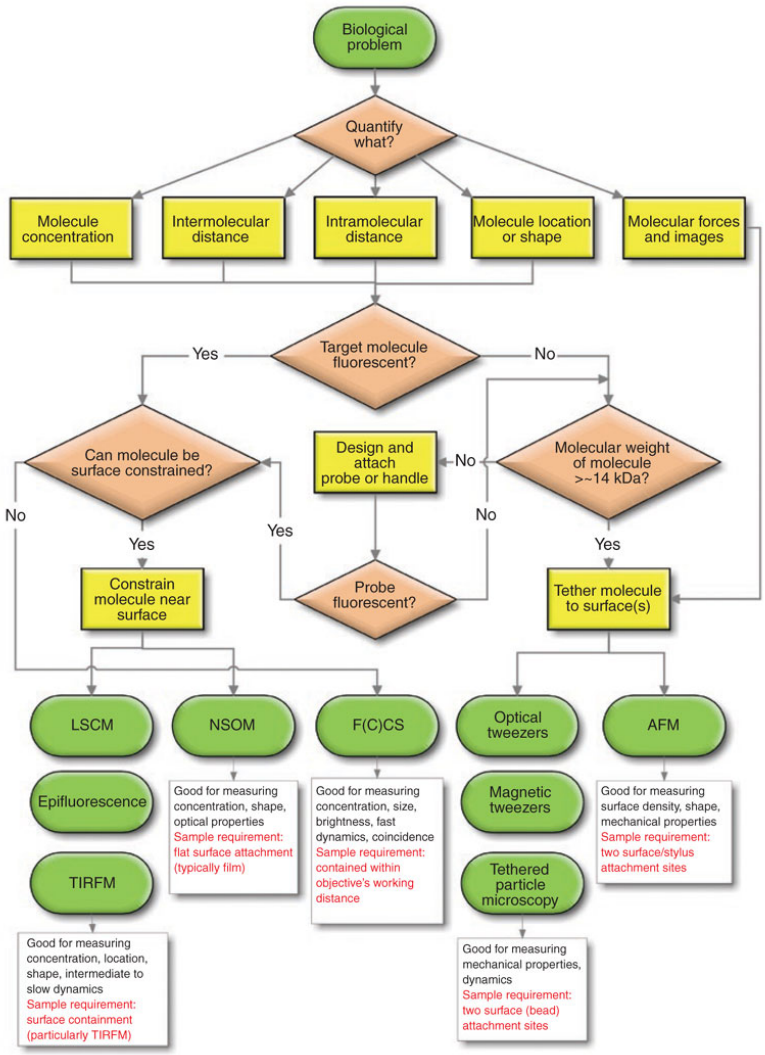

Fig. 2.10. Flowchart to select a suitable single-molecule technique to study a given biological problem. Image from [Walter 2008].

3

Silicon nanotweezers for bioexperiments on DNA

Contents

Summary. The project of this work, i.e. the development of "Silicon nanotweezers for bioexperiments on DNA", proposes a new approach for molecular biosensing with low cost batch-fabricated silicon nanotweezers. By directly handling molecules in biological solution with mechanical sensing, this research aims to replace traditional test tube assays or microfluidic approaches with deterministic interrogation of the molecules. Accordingly, with an appropriate integration of MEMS features, we demonstrate a simple and systematic way of analysis which can not be achieved by AFM, magnetic or optical tweezers.

Hereafter, the first part is devoted to a short introduction to MEMS technology. The next part is dedicated to the design, the fabrication and experimental setup of the device. Then, are presented the several characterizations performed for the validation and the modeling of the tweezers. Finally, the **Chapter** concludes with the parametric model of the device including the links with the external environment (through the sensitivity of the parameters to the temperature for instance or the study of the tweezers' behavior when inserted in liquid medium).

3.1 Introduction to MEMS technology

Microelectromechanical systems **(MEMS)** are originally small integrated devices or systems that combine electrical and mechanical components. Characteristic dimensions range from the sub micrometer level (100 nm) to the millimeter level (100 µm), and merge at the nano-scale into nanoelectromechanical systems **(NEMS)**. In fact MEMS extend the fabrication techniques developed for the integrated circuit (IC) industry to add mechanical elements such as beams, gears, springs and membranes to devices.

The development of the MEMS technology benefited of the fast-growing IC industry and subsequent progress on materials and techniques for micromanufacturing such as microsystems have nowadays spread numerous fields ranging from fundamental nanosciences to applications in biology or biochemistry with the manipulation of molecules and the emergence of Lab-On-Chip systems. A broad range of devices, architectures and operations have been investigated for studies dedicated to the micro and the nano scales. Besides passive mechanisms and sensors, several active devices such as turbines [Mehregany 1988], linear and rotative motors [Fan 1989, Sarajlic 2010], resonators [Tang 1989], switches [Cai 2003], grippers (see further) and fingers [Lu 2003] have been successfully accomplished at the microscale. Suitable actuation is achieved taking advantages of the specificities of the microworld. Beyond the decrease of the weight in L^3 (length cubed), the downscaling benefits to some actuations based on physic principles such as electrostatic forces which are inappropriate at the macroscale.

Among the family of new devices, microgrippers focused much interest. A first motivation rose from the ability to handle micro-size objects for their positioning or assembling. Forces and dimensions of the microgrippers are usually the more appropriate for the safe manipulation of micro-objects. The second reason comes from the reduced size of the grippers itself that allows to perform these manipulations in tiny areas.

Accurate manipulation of micro-sized objects is an important concern needed to be solved and improved. In terms of applications, a large segment is open with the manipulation and the assembly of objects always smaller, which requires more precision and force control (besides accuracy and speed of operations). In early works, studies investigates several types of actuation and integration for manipulation. Every actuation suitable at the micro-scale work were studied: electrostatic [Volland 2002, Molhave 2004], magnetic [Kim 2005], thermal [Molhave 2005, Chronis 2005], piezoelectric [Arai 1998] and SMA [Kohl 2000, Roch 2003]. Additionally, several devices aiming improved force/displacement control characteristics has been demonstrated with different designs and mechanisms. Some mechanical solutions for the amplification of the displacement [Millet 2004] or for linear displacement through mechanical feedback [Yamahata 2008a] were successfully adopted from the macro-scale to the micro-scale.

The trend followed by the new family of grippers is to develop monolithical or all-integrated microgrippers. Electrostatic comb-drive and differential capacitive sensor seem to be the techniques the more used and the more suitable for batch-fabrication, low consumption with good performances. [Beyeler 2007] developed generic microgrippers for diverse micro-object manipulations as biological cells. These grippers shows 100 µm actuation range with 100 nN resolution (or 4 nm resolution with flexure springs of 25 N/m), and a force sensor sensitivity of 1 mV/µN.

For the specific manipulation of biological molecules, solutions were provided by emerging nanotechnologies as described in **Chapter** 2. Aforementioned techniques require special treatment and labelization of the tool or the molecules for an appropriate attachment and manipulation. The particularity of such manipulations is to handle very small objects with uncommon shapes in comparison to solid shapes of the grippers. DNA molecules are only 2 nm wide and extremely soft matter when they are longer than 50 nm [Bouchiat 1999].

Silicon nanotweezers have been developed in the laboratory of Professor Fujita (IIS, University of Tokyo) with specific features for the trapping of filamentary molecules such as DNA. Taking advantages of the MEMS technology, these tweezers integrate actuator and sensor on a single chip, and are fabricated through standard clean-room processes. Hereafter, the device is detailed.

3.2 Design and fabrication of silicon nanotweezers

The current design and the fabrication of the tweezers have been developed previously to this work [Yamahata 2008a]. However, in this **Section**, the design and the features are summarized for modeling purposes and characterization.

3.2.1 Design

Figure 3.1 shows a three-dimensional illustration of the device. It consists of two sharp tips that act as electrodes for both DNA trapping by dielectrophoresis (cf. **Section** 4.1) and conductivity measurement of DNA molecules [Yamahata 2008b]. One tip is fixed and the other one is moved with an electrostatic actuator. The motion (x-direction) of the electrode can be measured using two capacitances with gaps that vary in proportion to the electrode displacement. As described above, the device consists of three parts:

- Two sharp tips,
- A series of comb-drive actuators,
- A differential capacitive sensor.

The tweezers layout and the different features are detailed in **Appendix** B (with **Figures** B.1 and B.2).

3.2.1.1 An electrostatic actuation

The actuation is provided by electrostatic forces in an interdigitated comb architecture, one of the most widely used forces in the design of submicrometer-size systems [Tang 1989, Legtenberg 1996, Clark 1999, Zhou 2003, Dai 2007]. The total displacement is rather shorter than what is possible in a parallel plate architecture, but the force is exclusively dependent on the actuation voltage (and not on the electrode position), which provides for simpler control of the actuation.

The design of a comb drive actuator requires the study of the electrostatic forces generated between the two electrodes. The electrostatic field between the two electrodes is commonly described as a simple parallel plan model (i.e. electric fields confined to the cross-sections of the individual comb fingers). Force corrections are studied

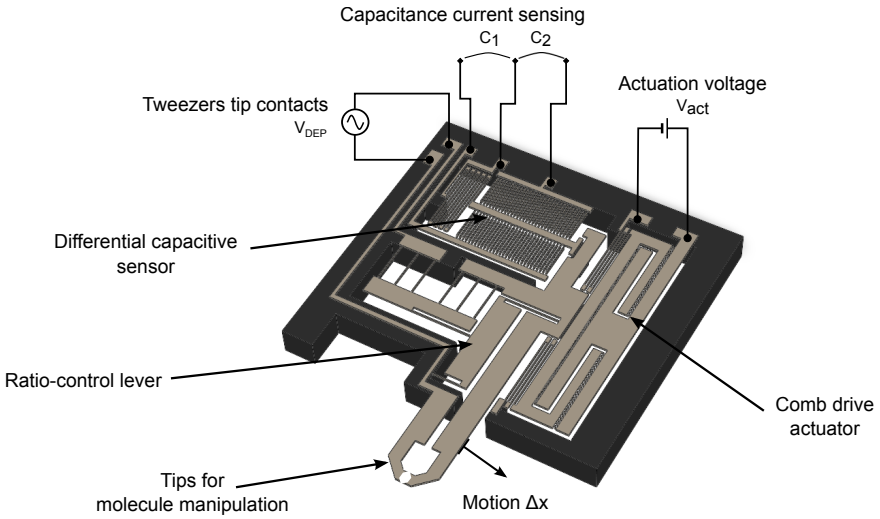

Fig. 3.1. 3D schematic view of the silicon nanotweezers. The mobile electrode is electrostatically actuated (V_{act} is the actuation voltage) and its displacement, Δx, results in a change in the capacitances C_1 and C_2. Dielectrophoresis force is generated applying a sinusoidal voltage V_{DEP} between the tip electrodes. External dimensions: 4 mm × 5 mm.

in [Johnson 1995] taking into account unengaged regions interactions. Here, a simple model is considered to evaluate the force magnitude order. The identification of the model parameters through experimental data will adjust the values.

The local forces are obtained by applying the principle of virtual work. According to the energy preservation E_C, this invested mechanical work W_{es} will increase the electrical energy stored within the capacitance with $dW_{es} = F_x dl$. The electrostatic force F_x acting on the mobile electrode of the capacitance C compound by the comb fingers is:

$$F_x = \frac{\partial W_{es}}{\partial x} = \frac{\partial E_C}{\partial x} = \frac{1}{2}\frac{\partial CV^2}{\partial x} = \frac{1}{2}V^2\frac{\partial C}{\partial x} = \frac{1}{2}V^2\frac{\partial}{\partial x}\left(\epsilon_0 \frac{N\,(l+\Delta x)\,t}{g}\right) \tag{3.1}$$

$$= \epsilon_0 \frac{Nt}{2g}V^2 = \alpha_{CD} \times V^2 \tag{3.2}$$

$$F_x = 8.85.10^{-12} \times \frac{440 \times 30.10^{-6}}{2 \times 2.10^{-6}} \times V^2 = 29.2.10^{-9} \times V^2 \tag{3.3}$$

with N the number of fingers, l and t the length and the thickness of the fingers, g the gap between the opposite fingers, ϵ_0 the vacuum permitivity and V the potential difference between the electrodes, i.e. the actuation voltage.

Finally the electrostatic force **Equation** in comb actuators is **Equation** 3.2. The force is not linearly dependent on the actuation voltage V but square dependent. However, this force acting in the x-direction or along the length l of the fingers is independent of $(l + \Delta x)$, that is to say that the force is constant with the displacement.

3.2.1.2 A capacitive sensor

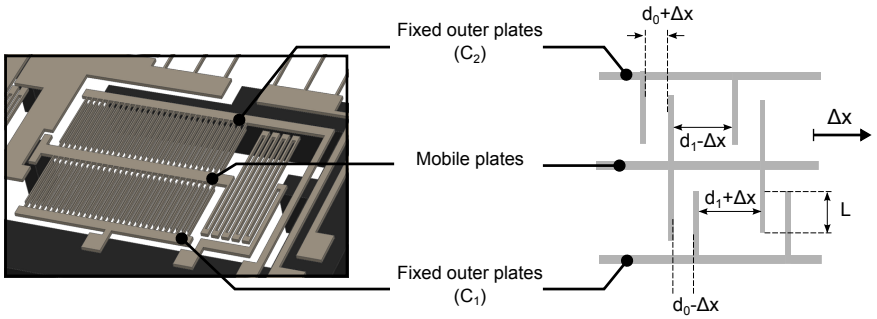

Fig. 3.2. Focus on the differential capacitive sensor. The right schematic illustrates displacement sensing through C_1 and C_2 capacitance variations. [Yamahata 2008a]

The tip displacement is measured by a differential capacitance sensor which is suitable for bulk micromachining and compact integration [Sun 2005]. The sensor is designed in a tri-plate configuration with transverse combs. A central electrode is mechanically connected to the mobile tip and moves in between two fixed electrodes creating two differential capacitances C_1 and C_2 whose difference, ΔC, is related to the displacement, Δx (**Figure** 3.2).

$$\Delta C = C_1 - C_2 \tag{3.4}$$

$$\Delta C = \varepsilon_0 N_b L t \left[\left(\frac{1}{d_0 - \Delta x} + \frac{1}{d_1 + \Delta x} \right) - \left(\frac{1}{d_0 + \Delta x} + \frac{1}{d_1 - \Delta x} \right) \right] \tag{3.5}$$

ε_0 is the vacuum permittivity, N_b the number of capacitance electrodes in opposition, t the device thickness, L the electrode length and, d_0 and d_1 the initial distances between repeating combs. For small displacements as $\Delta x \ll d_0 < d_1$, a first order approximation of the **Equation** 3.5 gives a linear relationship between ΔC and Δx (**Equation** 3.6).

$$\Delta C = \varepsilon_0 N_b L t \left[\left(\frac{1}{d_0} \frac{1}{1 - \frac{\Delta x}{d_0}} + \frac{1}{d_1} \frac{1}{1 + \frac{\Delta x}{d_1}} \right) - \left(\frac{1}{d_0} \frac{1}{1 + \frac{\Delta x}{d_0}} + \frac{1}{d_1} \frac{1}{1 - \frac{\Delta x}{d_1}} \right) \right]$$

$$\Delta C \simeq \varepsilon_0 N_b L t \left[\frac{1}{d_0} \left(1 + \frac{\Delta x}{d_0} + o\left(\frac{\Delta x}{d_0} \right) \right) + \frac{1}{d_1} \left(1 - \frac{\Delta x}{d_1} + o\left(\frac{\Delta x}{d_0} \right) \right) \right.$$
$$\left. - \left(\frac{1}{d_0} \left(1 - \frac{\Delta x}{d_0} + o\left(\frac{\Delta x}{d_0} \right) \right) + \frac{1}{d_1} \left(1 + \frac{\Delta x}{d_0} + o\left(\frac{\Delta x}{d_0} \right) \right) \right) \right]$$

The equation finally becomes:

$$\Delta C \simeq 2\varepsilon_0 N_b L t \left(\frac{1}{d_0^2} - \frac{1}{d_1^2}\right) \Delta x = \alpha_{CS} \times \Delta x \tag{3.6}$$

$$\simeq 2 \times 8.84.10^{-12} \times 30 \times 450.10^{-6} \times 30.10^{-6} \times \left(\frac{1}{(5.10^{-6})^2} - \frac{1}{(20.10^{-6})^2}\right)$$

$$\simeq 269.10^{-9} \times \Delta x \tag{3.7}$$

Theoretically C_1 and C_2 are equal such as the differential sensing is 0 when there is no actuation. Besides according to the **Equation** 3.6 the relation between the motion and the differential capacitance is linear. The capacitances are measured through the measurements of the currents flowing through C_1 and C_2 (see **Section** 3.3).

Nevertheless because of micro-fabrication concerns, the sensor is not perfectly balanced and the sensitivity of the sensor is approximatively twice less than the theoretical value. This part will be explained later and concerns every feature of the device as the following mechanical suspensions.

3.2.1.3 Mechanical suspensions

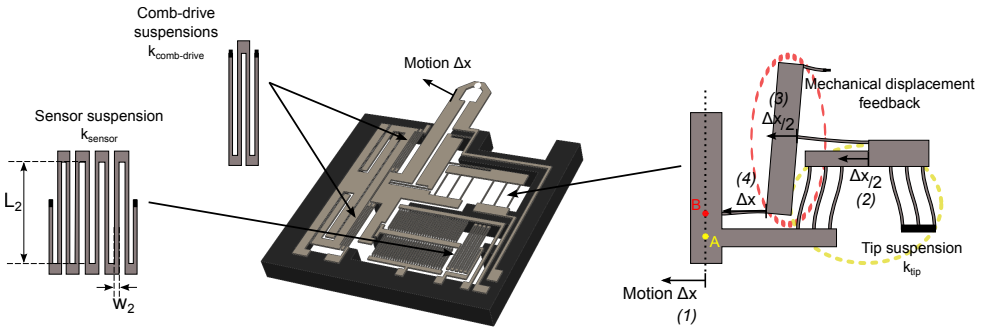

Fig. 3.3. Overview of the mechanical suspensions supporting the linear displacement of the tweezers tip. In the right, the tip suspension integrates a mechanical feedback (or ratio-control lever) imposing a linear displacement in the x-direction. A point displacement imposes the same displacement in point B avoiding any rotation of the tip (follow (1) → (2) → (3) → (4)).

The mobile part of the system is suspended by flexible beams. Commonly used in microsystem design, folded beam springs are designed to lengthen effective beam lengths, decrease their mechanical stiffness and enhance displacement ranges. In the current design, three sets of suspensions are used to, both, support the mobile parts of the system (the comb-drive actuator, the mobile tip and the capacitive sensor) and to provide electrical connections for actuation and sensing (**Figure** 3.3).

A very compliant system is ideally suitable to sense the effects of mechanical properties of biological molecules on the tweezers response. Indeed the equivalent rigidity of biological macromolecules are very low, i.e. about 30 µN/m for λ-phage DNA[1]

[1] λ-DNA molecules are about 16.5 µm-length and contains about 48.500 nucleobase base pairs (48.5 kbp).

[Bustamante 2003], which are used in the bioexperiments developed in the next **Chapter**. On the other hand, a minimum stiffness force is required (1) to survive the fabrication processes, (2) in order to support the system weight and (3) to prevent attractive and sticking surface forces in the comb-drive actuator and the capacitive sensor.

The total stiffness is derived from $k = k_{\text{comb-drive}} + k_{\text{sensor}} + k_{\text{tip}}$ where $k_{\text{comb-drive}}$, k_{sensor} and k_{tip} are defined as:

$$\begin{aligned} k_{\text{comb-drive}} &= 2 \times \frac{1}{4} \frac{E \times t_1 \times {w_1}^3}{{L_1}^3} \\ k_{\text{sensor}} &= \frac{1}{8} \frac{E \times t_2 \times {w_2}^3}{{L_2}^3} \\ k_{\text{tip}} &= \frac{3}{2} \frac{E \times t_3 \times {w_3}^3}{{L_3}^3} \end{aligned} \tag{3.8}$$

with E the material Young's modulus (165 GPa [Dolbow 1996]) and L_i, w_i, t_i the respective length, width and thickness of the suspension beams. Dimensions and values of the tweezers springs are reported in **Table** 3.1.

However, some dimensions of the tweezers' mask are very sensitive to micro-fabrication steps as etching process. After our etching process, dimensions are regularly 1 to 2 µm reduced, such as small dimensions as suspension widths largely change.

Springs i	Dimensions $L_i \times w_i \times t_i$ (µm)	Stiffness (N/m)
1	$1000 \times 15 \times 30$	8.4
2	$1000 \times 15 \times 30$	2.1
3	$600 \times 15 \times 30$	116.0
Total		126.5

Table 3.1. Theoretical characteristics of the tweezers springs.

The movable tip of the tweezers is a free-free beam supported by the aforementioned suspensions. Ideally if the actuation is exclusively linear in the x-direction, the tip should move without any rotation and moment. However electrostatic comb actuators show lateral instability, such that a small unbalanced position (in the orthogonal y-direction) will be amplified by the actuation force (until lateral sticking of the combs).

Adapting a solution found in a macrosize device for a high precision linear scan mechanism [Spanoudakis 2003], two points of the movable arm are constrained to move of the same distance Δx. Following the indice numbers in **Figure** 3.3, point A makes move the intermediate parallelogram of the suspension of half of the distance ($\Delta x/2$). This parallelogram 1 is connected to the middle of a second parallelogram (through a small flexible beam). Because the upper end of the parallelogram 2 is connected to the mechanical ground and the middle moves of $\Delta x/2$, the below end moves of twice the distance $\Delta x/2$ (i.e. Δx). At last, this below part of the parallelogram 2 controls a second

point of the movable arm (called point B) imposing the identical displacement Δx. Thus the design is dedicated to avoid rotational discrepancy and lateral shift deviations.

3.2.2 Microfabrication

The fabrication of the MEMS nanotweezers is based on Reactive Ion Etching (RIE), local oxidation and anisotropic etching of silicon. The starting material for our prototype was a SOI substrate having the following characteristics: (100)−oriented, 30 µm-thick silicon active layer / 2 µm-thick buried oxide (SiO_2) insulator / 400 µm-thick silicon handling substrate.

Here, two aspects of the microfabrication are developed to help the understanding of the device features. For more details, a process flow is described in **Appendix** A.

3.2.2.1 Electrical isolation

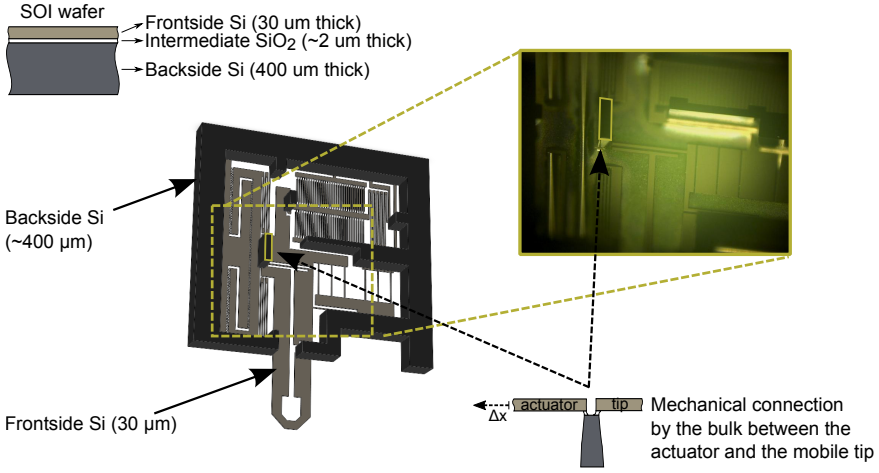

Fig. 3.4. Backside view of the tweezers chip. The mechanical links by the bulk layer of the SOI substrate are delighted with closed-up microscope image of the link between the comb-drive actuator (on the left) and the mobile tip (on the right). In the bottom right, a side view of the link is drawn.

One of the key features of the silicon tweezers is to integrate actuator and sensor in the same chip. Both parts work with electrical characteristics which require an electrical isolation between the different parts. For this purpose, a Silicon-On-Insultor (SOI) is used. The bulk silicon used as a support is isolated from the frontside silicon thanks to the intermediate SiO_2 layer. The different connection lines and pads are drawn on this frontside layer without any direct connection between actuation, sensing and tip contact lines (as shown in light gray color in **Figure** 3.1).

Moreover electrical connections to the movable parts are achieved through the aforementioned mechanical suspensions. However to isolate the mobile actuator, the mobile tip and the mobile central sensor electrodes, which are mechanically connected, two

mechanical links are provided by localized paths by the bulk Si layer and electrically isolated by the intermediate SiO_2 layer. **Figure** 3.4 shows the mechanical link between the actuation and the mobile tip enabled by the backside layer.

In **Appendix**, **Figure** B.1 (**Page** 111) delights the critical consequence of defective backside silicon etching. The bulk machining requires high aspect ratio etching through the 400 µm thickness of the layer to avoid possible disconnections between the frontside and the bulk silicon layers.

3.2.2.2 Tip shaping

The second key feature of the device is the shaping of the tip as a molecule prehensor. Details about the DNA molecule manipulation are given in **Chapter** 4. However, tip design is an important issue for DNA trapping. Sharp tips are required for the generation of a high electric field (1 MV/m at 1 MHz) in between the tips – inducing the attraction of dielectric particles as DNA. DNA strands elongate along the electric field lines resulting in their precise trapping in between the ends of the tweezers tips (**Figure** 3.5 (a)).

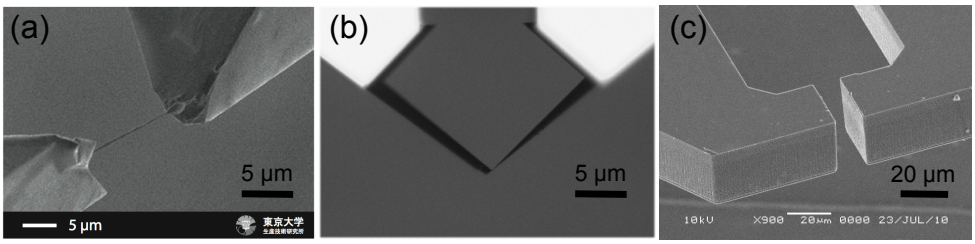

Fig. 3.5. Pictures of the micromachined tweezers tips. (a) SEM image of DNA bundle trapped in between sharp tips. (b) Microscope image of very sharp tips for molecule handling and trapping of small molecules (with length inferior to 1 µm). (c) SEM image of tips designed for cell characterizations.

This structure can be obtained by a process combination of anisotropic wet etching of silicon (KOH or TMAH etching) and local oxidation of silicon techniques as sketched in **Figure** 3.6 and reported in [Hashiguchi 2003]. At last, a thin aluminum film is evaporated on the front side. Indeed, aluminum acts as a very good anchoring material for DNA molecules (cf. **Section** 4.1 for DNA trapping concerns).

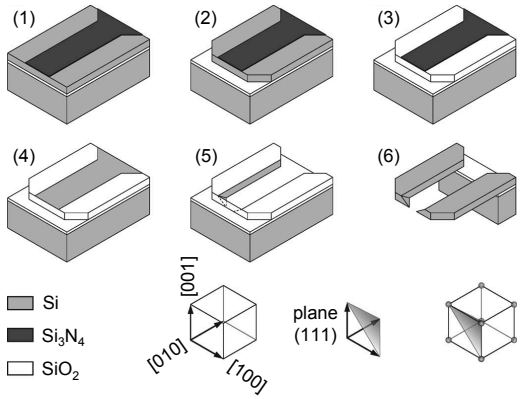

Fig. 3.6. Fabrication process of the sharp silicon nanotweezers using Silicon-On-Insulator technology. The crystallographic orientation is indicated with Miller indices. [Yamahata 2008a]

The different important parameters for the tweezers design are gathered in **Table** 3.2.

Tweezers part	Parameters	Value
Actuator	Electrostatic force	29.2×10^{-9} N/V^2
Sensor	Capacitive sensing	269×10^{-9} F/m
Mechanical tweezers	Stiffness	126.5 N/m

Table 3.2. Elementary design parameters of silicon nanotweezers.

These first parameters may allow to start static characterizations of the device, but for dynamic characterizations, the mass of the mobile part is required. The losses of the system will be identified after dynamic measurements of the tweezers' motion. Meanwhile mass of the tweezers can also be evaluated. From the mask of the device, the surface on the frontside silicon layer is 3.07 mm^2 and the surface of the 2 links by the backside silicon layer is 0.09 mm^2. Assuming that the contribution of the intermediate 2 µm-thick SiO_2 layer (which is mostly etched) is neglectable, the mass is:

$$M = \rho_{\mathrm{Si}} \times (S_1 \times t_1 + S_2 \times t_2) \tag{3.9}$$

$$= 2330 \times \left(3.07.10^{-9} \times 30.10^{-6} + 0.09.10^{-9} \times 400.10^{-6}\right)$$

$$= 215.10^{-9} + 84.10^{-9} = 299 \text{ µg} \tag{3.10}$$

where ρ_{Si} is the density of bulk silicon, S and t the respective surface and thickness of the frontside and backside silicon.

However an important uncertainty arises from the etching of the backside layer. As illustrated in **Figure** B.1 (**Page** 111), the etching of the 400 µm-thick silicon is not perfectly straight and leads sometimes to disconnections between the frontside and the

backside. The mass of the backside layer is probably lighter but remains complicated to evaluated precisely.

Actually these particularities of the silicon nanotweezers cause many difficulties during the fabrication. On the one hand, the tip gap has to suit to the trapping of molecules. Typically for λ-DNA molecules, the anisotropic etching is foreseen to result in sharp tips with gap of 10 to 12 µm. Larger gap makes the trapping of these molecules impossible. Shorter gap makes the molecules not completely extended in between the tips. On the other hand, we have seen that the etching of the 400 µm-thick silicon backside results sometimes in disconnections between the frontside and the backside. This occurs when the DRIE etching is not perfectly perpendicular leading to an overetching (this is our case) or an underetching at the base of the patterns.

Moreover the comb drive structure of the actuator with small gaps causes also difficulties during the frontside silicon patterning step. Because there are such kind of small gaps to etch, other parts of the tweezers (such as the mechanical suspensions) are regularly overetched. On small aperture, the etching rate is smaller than on large aperture, because it is more difficult to extract the products of reaction especially when the aspect ratio (depth/diameter or width) is high. Practically, the high density of comb drive separated by a gap (aperture) of 2 µm needs more time to be completed compared to wide areas. The overetching is regularly measured as ~ 1 µm, that is a reduction of 2 µm per rectangular beams.

These concerns during the microfabrication of the devices are supposedly the reasons why some of them are not usable after fabrication and why among the good tweezers there are so important discrepancies of characteristics (e.g. resonance frequency) in between them.

3.3 Characterizations of the tweezers

After clean-room fabrication, tweezers' chips are mounted and bonded on a Printed Circuit Board (PCB), enabling electrical connection with measurement instruments (**Figure** 3.7). In **Appendix** C, the experimental setup in its environment (i.e. in "bio-room") with all the required equipments and instruments is illustrated.

The actuation of the tip is quite straightforward. A voltage is required to generate a force. However, a high current is possible when a contact occurs and may cause the destruction of the device. The sensing of the motion is more complicated and is explained hereafter.

The sensing of the motion is operated through the measurement of the differential capacitance ΔC (**Equation** 3.6). Hereafter, we developed two instrumentation chains that can be used for static and dynamic measurements. In both configurations, the strategy is to create alternative currents through the capacitances C_1 and C_2. The key point is to measure very small currents around picoampere-level.

On the one hand, in static mode, the electrodes of the capacitances C_1 and C_2 are immobile. An alternative voltage is applied on C_0 (1 V_{rms} at 10 kHz) generating the required currents, which amplitudes I_1 and I_2 depend on C_1 and C_2 electrode gaps. On

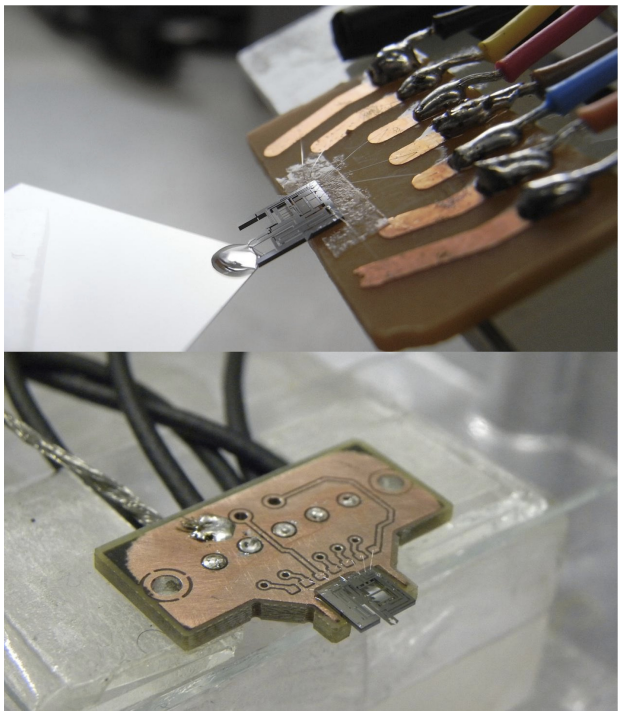

Fig. 3.7. MEMS tweezers chip mounted and bonded on its PCB board. Upper picture shows the previous PCB design while below is illustrated the new PCB currently used.

the other hand, in dynamic mode, the central electrode (C_0) moves with the tweezers tip such as a constant voltage (3 V) can be applied on C_0 and creates dynamic currents i_1 and i_2 related to the motion.

The resulting currents flowing through the capacitances C_1 and C_2 are converted into voltages V_1 and V_2, respectively, by two low-noise current-to-voltage (A/V) preamplifiers from Signal Recovery (model 5182, http://www.signalrecovery.com). The low input impedance of the preamplifier (virtual ground) ensures an accurate current conversion. Finally a lock-in amplifier from NF (model LI 5640, http://www.nfcorp.co.jp) allows accurate measurement performing the magnitude-phase detection of the differential inputs ($V_1 - V_2$) at the reference frequency. The reference frequency is the frequency of the central plate excitation signal in static mode or the motion frequency (related to the actuation signal frequency) in harmonic mode.

Figure 3.8 shows a sketch of the measurement principle in static mode while **Figure** 3.12 shows the principle in harmonic mode. In a full dynamic mode (e.g. in step response characterization), the dynamic response of the device is directly available at the outputs of the A/V pre-amplifiers.

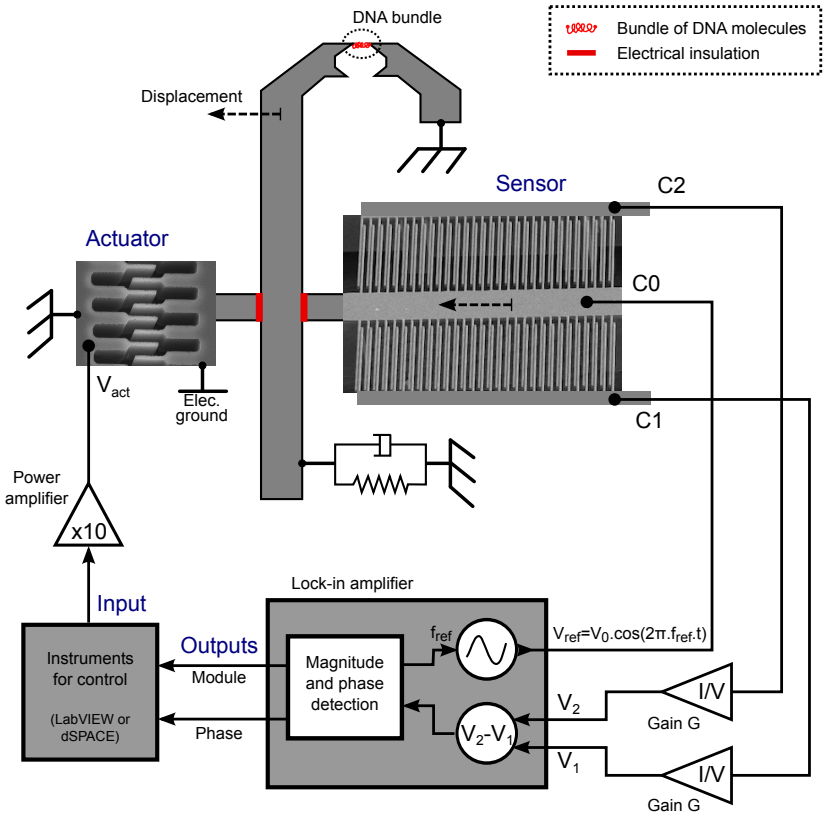

Fig. 3.8. Electromechanical scheme of the tweezers and electrical connections for actuation and displacement sensing in static mode configuration. The actuator and the sensor are illustrated by SEM images. Straight red lines represent electrical insulation between parts.

Differential measurements should allow full range measurements eliminating common mode (i.e. measurement of the capacitances at zero-displacement), and enable a significant noise/perturbation rejection.

However C_1 and C_2 characteristics are not perfectly balanced to allow complete perturbation rejection by differentiation. An example will be afforded by the direct actuation-to-sensor coupling concern. Coupling of large alternating signals as actuation (up to 3 V peak-to-peak with small sensing signals can not be avoided without special care. Despite the relatively low frequency of the mechanical actuation (< 3 kHz), size of microsystems and distance between the lines favor coupling between signals.

Finally the asymmetry of the sensor layout and the coupling between the lines (bonding wires and PCB's lines) makes C_1 signal more sensitive to actuation signal than C_2 signal (cf. **Figures** 3.11).

3.3.1 Static characterizations of the tweezers

Using the aforementioned configurations and controlled by a PC equipped with LabVIEW programs and GPIB interface, MEMS tweezers are characterized in real-time in static and dynamic mode.

For static actuation, the differential capacitance change, ΔC, is measured by the acquisition chain schematized in **Figure** 3.8. A sinusoidal input signal V_{ref} supplied by the internal reference of the lock-in amplifier is applied to the central plate of the capacitive sensor (port C_0). The amplitude of the detected voltage V_{out}, is related to ΔC by the acquisition chain gain:

$$V_{\text{out}} = G.2\pi.f_{\text{ref}}.V_{\text{ref}}.\Delta C \tag{3.11}$$

where G is the preamplifier gain, V_{ref} and f_{ref} are respectively the amplitude and the frequency of the signal applied on C_0. All the voltages are expressed in RMS value.

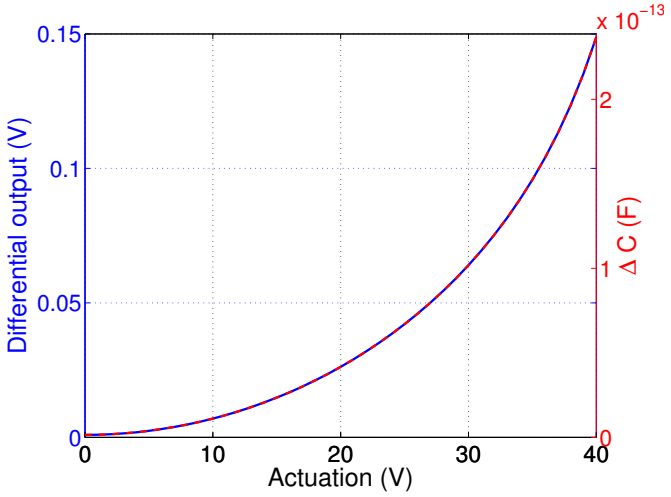

Fig. 3.9. Static characterization of the output of the device capacitive sensor (Tweezers RV20). The function is primarily quadratic due to the actuator function (cf. **Equation** 3.12). The right and left axis correspondence is $V_{\text{out}} = G \times V_{\text{ref}} \times 2\pi f \Delta C = 10^7 \times 1 \times 2\pi \times 10.10^3 \times \Delta C$.

Figure 3.9 shows the output signal of the sensor for actuations from 0 to 40 V. The conversion output signal to equivalent displacement has been fitted with optical measurement (**Figure** 3.10). The proportional sensing gain α_{CS} (from **Equation** 3.6) is identified and then compared to the theory.

Aforementioned optical measurements have been performed with interferometer from SIOS Meßtechnik GmbH, and have allowed direct characterization of the tip displacement and of the actuator characteristic. Dashed line shows the theoretical displacement (i.e. **Equation** 3.12) with identified values for the control implementation in **Chapter** 5, i.e.:

$$\Delta x = \frac{\alpha_{CD} \times V^2}{k_{\text{tw}}} \approx \frac{30.5.10^{-9}}{43.5} \times V^2 \approx 0.7.10^{-9} \times V^2 \tag{3.12}$$

The square law model of the actuator is well identified and fits the tip displacement for actuation from 0 to 40 V. However, for large displacements (> 0.5 µm), the approximation of the sensor function is not valid anymore. More details on the single sensitivities of C_1 and C_2 are given further and their non-linearities are justified.

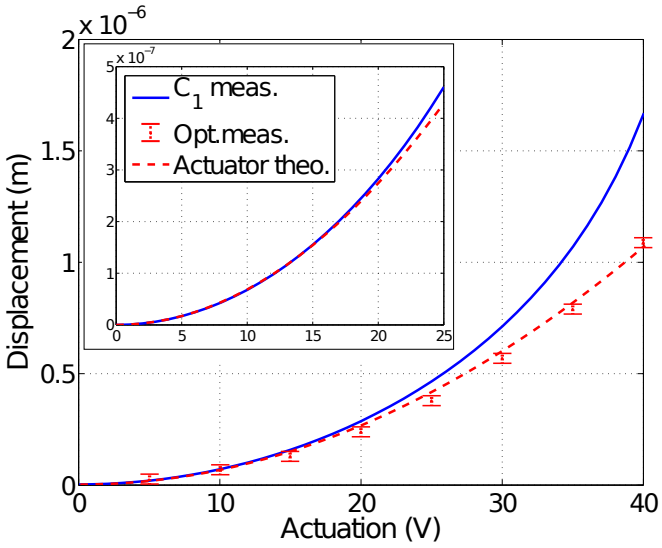

Fig. 3.10. Static characterization of the displacement with the capacitive sensor of the device (Tweezers RV20). Corresponding displacement is extracted from the sensor model, the actuator model and validated by measurements performed with interferometer. Insert focuses on the 0-to-25 V actuation range where the square modeling with identified parameters seems to fit with the experimental data. In dashed line, the theoretical displacement due to the actuation force is plotted (**Equation** 3.12).

Finally, from the experimental results, the sensor is 1.9 times less sensitive from the theoretical value expected with respect to device's mask dimensions. Theoretical value for α_{CS} (269×10^{-9} F/m) is identified to 140×10^{-9} F/m (**Equation** 3.7). Difference of d_0 dimension explains partly the loss of sensitivity.

The dimensions d_0, d_1 and t are very sensitive to fabrication processes, due to their small values (respectively 5, 20 and 30 µm). d_0 et d_1 have been especially observed under optical microscopy and evaluated around 6.7 and 21.2 µm (± 0.5 µm depending on the device). Indeed sensor sensitivity equation (**Equation** 3.6) is highly dependent on d_0. With an overetching of 1.7 µm as previously mentioned, the sensor gain is reduced by a factor 1.9.

Characteristic	Parameters	Theoretical values	Experimental values	Method
Actuator gain	α_{CD} (N/V^2)	29.2×10^{-9}	30.5×10^{-9}	Optical measurement
Sensor gain	α_{CS} (F/m)	269×10^{-9}	140×10^{-9}	Sensor static measurement
Mechanical stiffness	k_{tw} (N/m)	126.5	43.5	Force sensor

Table 3.3. Identified parameters of silicon nanotweezers after static characterization (Tweezers RV20).

Linearities and approximations of the sensor functions

As aforementioned, for small displacements as $\Delta x \ll d_0 < d_1$, a first order approximation leads to a linear relationship for the differential measurement $C_1 - C_2$ (i.e. ΔC) function of Δx. The function for C_1 and C_2 are:

$$C_{1/2} = \varepsilon_0 N_b L t \left(\frac{1}{d_0 \mp \Delta x} + \frac{1}{d_1 \pm \Delta x} \right) \tag{3.13}$$

$$C_{1/2} \simeq \varepsilon_0 N_b L t \left[\frac{1}{d_0} \left(1 \pm \frac{\Delta x}{d_0} + o\left(\frac{\Delta x}{d_0} \right) \right) + \frac{1}{d_1} \left(1 \mp \frac{\Delta x}{d_1} + o\left(\frac{\Delta x}{d_0} \right) \right) \right] \tag{3.14}$$

where ε_0 is the vacuum permittivity, N_b the number of capacitance electrodes in opposition, t the device thickness, L the electrode length and, d_0 and d_1 the initial distances between repeating combs.

From the experimental data, we observe that, for large displacements (larger than 500 nm corresponding to actuation voltage superior to 25 V), the C_1 and C_2 may not be considered as linear. The quadratic behavior is mostly due to the square law of the comb-drive actuator, but after 25 V-actuation the functions of C_1 and C_2 do not follow the same tendency. C_1 becomes more sensitive since Δx is not neglectable compared to d_0 (5 µm). C_2 is becoming less sensitive.

According to **Equations** 3.13 and 3.14, **Figure** 3.11 demonstrates the effect of the non-linear function of capacitive sensor and the effect of approximations on large displacements. The **Figure** shows the experimental data and the theoretical functions (with and without approximations) plotted with real dimensions of the sensor (especially $d_0 = 6.7$ µm and $d_1 = 21.2$ µm).

However, despite the correction of the dimensions and the use of the sensor function without approximations, the difference between the experimental data and the theoretical curves are due to the modeling error on the actuator square law model.

These characterizations show the complexity to develop an accurate model for a large range of displacements. A good modeling was demonstrated for actuation from 0 to 20 V, but for larger displacements or modeling at different operating ranges, the model parameters need to be identified again. We pointed also the difficulty to identify parameters. In concrete terms, output depends as well on sensor and actuator parameters. Diverse methods of characterizations (cf. **Appendix** D and F) had to be developed to

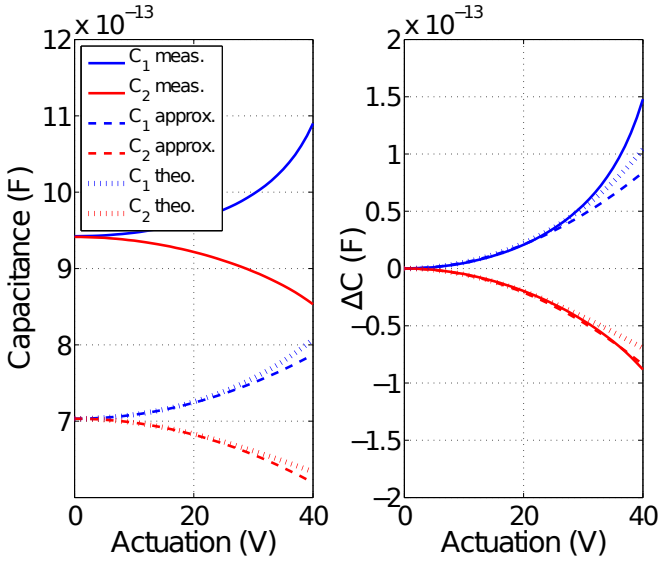

Fig. 3.11. Characterization and identification of the capacitances C_1 and C_2 of the capacitive sensor (Tweezers RV20) (2). The left graph shows the C_1 and C_2 capacitance evolutions with respect to the actuation. Curves are compared with theoretical curves with approximation (dashed lines) (**Equation** 3.13) and without approximation (dotted lines) (**Equation** 3.14) from the actuator model and the sensor model with parameters calculated from the evaluated dimensions ($d_0 = 6.7$ µm and $d_1 = 21.2$ µm). The right graph shows only the variations ΔC_1 and ΔC_2.

discriminate as much as possible the different parameters and understand unconsidered phenomena.

3.3.2 Dynamic characterizations of the tweezers

In dynamic mode, the central electrode C_0 of the sensor moves with the tweezers tip such as a constant voltage V_0 can be applied on C_0 and creates dynamic currents i_1 and i_2 related to the motion dynamics. The sensing of the capacitive currents is related to the motion through:

$$\begin{aligned} i_1 - i_2 &= \frac{dQ_1}{dt} - \frac{dQ_2}{dt} = \frac{d\left(C_1 V_0\right)}{dt} - \frac{d\left(C_2 V_0\right)}{dt} \\ &= V_0 \times \frac{d\Delta C\left(t\right)}{dt} \\ &= V_0 \times \alpha_{CS} \frac{d\Delta x\left(t\right)}{dt} \end{aligned} \tag{3.15}$$

where Q_1 and Q_2 are the charges of the capacitances C_1 and C_2 respectively, $\Delta x(t)$ the displacement of the tip, and $\frac{d\Delta x(t)}{dt}$ its velocity. Consequently, in the limits of the sensor approximations, the output is related to the velocity of the motion of the tip.

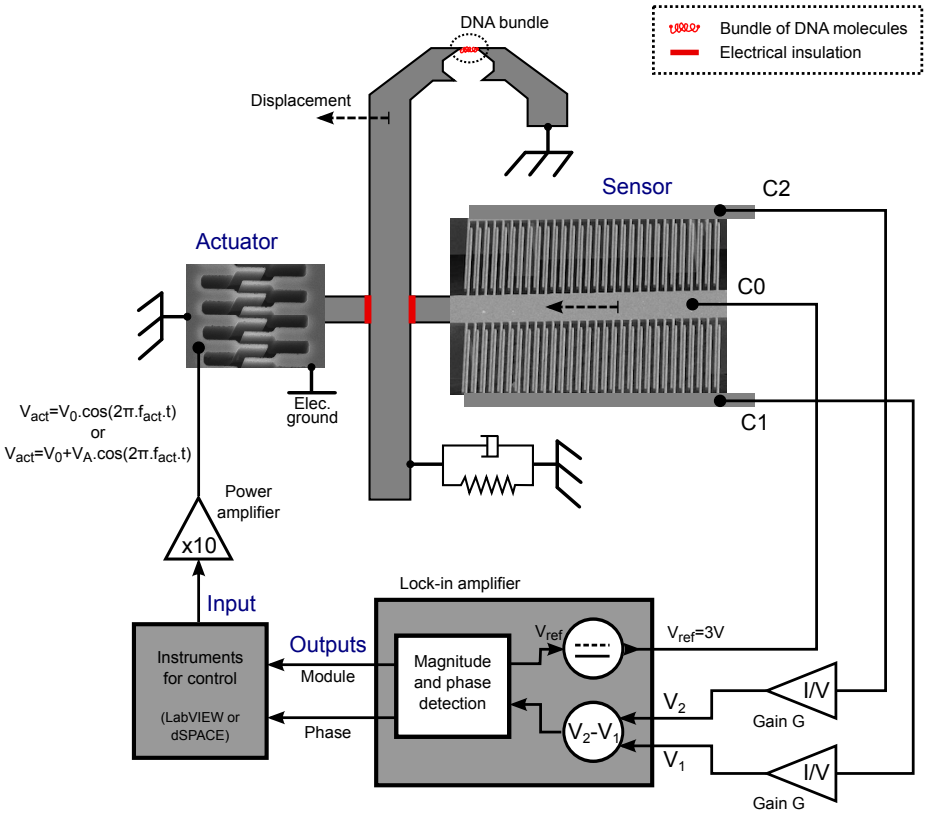

Fig. 3.12. Electromechanical scheme of the tweezers and electrical connections for actuation and displacement sensing in harmonic mode configuration. The actuator and the sensor are illustrated by SEM images. Straight red lines represent electrical insulation between parts.

Harmonic response analysis

The harmonic analysis of the tweezers is performed with the measurement configuration of **Figure** 3.12. The actuation signal, V_{act}, is directly provided by the internal oscillator of the lock-in amplifier or by a signal generator (Agilent 33220A) synchronized with the lock-in amplifier. A DC voltage, $V_{C0} = 3$ V, is supplied on the central plate of the capacitive sensor. The amplitude and phase of the tweezers oscillations are measured using the second harmonic mode detection (i.e. at the frequency $2f$) since the generated force has a quadratic dependence with the actuation voltage:

$$F_x = \alpha_{CD} \times V_{\text{act}}^2 \tag{3.16}$$

$$= \alpha_{CD} \times \left(V\sqrt{2}sin\left(2\pi ft\right)\right)^2$$

$$= \alpha_{CD} \times V^2 \times \left(1 - cos\left(2\pi(2f)t\right)\right) \tag{3.17}$$

A constant force is generated related to $\alpha_{CD} \times V^2$, but is not sensed since it does not generate AC currents. The harmonic force at $2f$ is sensed and the sensor output is

function of $\alpha_{CD} \times V^2$ as well. This technique eliminates the coupling capacitive current at the fundamental mode between the actuator and the sensor electrodes, thus enabling better characterization of the mechanical motion.

Figure 3.13 shows the frequency response of the device and outlines the mechanical resonance at 2100 Hz. This main resonance is fitted with a 2^{nd}-order differential equation, stemmed from a damped mass-spring system:

$$M\ddot{x} + \nu\dot{x} + k_{\text{tw}}x = F_x = \alpha_{CD}V_{\text{act}}^2 \tag{3.18}$$

where M is the mass of the mobile part, k_{tw} the mechanical stiffness, ν the viscous losses related parameter, $F_x(= \alpha_{CD}V_{\text{act}}^2)$ the electrostatic force, f_{r} the resonance frequency and Q the quality factor of the resonance. k_{tw} and F_x parameters are reported in **Table** 3.3, but M and ν need to be identified. Firstly the identification is approximatively performed by reverse calculation of the resonance frequency and quality factor equations (**Equations** 3.19 and 3.20), then the frequency response curve is accurately fitted with least mean square algorithm.

$$f_{\text{r}} = \frac{1}{2\pi}\sqrt{\frac{k_{\text{tw}}}{M} - \frac{1}{2}\frac{\nu^2}{M^2}} \tag{3.19}$$

$$Q = \frac{\sqrt{k_{\text{tw}}M}}{\nu} \tag{3.20}$$

Equation 3.18 is recasted into transfer function to allow magnitude/phase plot of the velocity ($\dot{x}$) with measurement data:

$$T(\jmath\omega) = \frac{1}{k_{\text{tw}}} \frac{(jw)}{\frac{M}{k_{\text{tw}}}(\jmath\omega)^2 + \frac{\nu}{k_{\text{tw}}}(\jmath\omega) + 1} \tag{3.21}$$

Finally the amplitude and the phase measurements are related to following equations:

$$\text{Amplitude} = G \times V_{C_0} \times \alpha_{CS} \times \text{abs}\left(T(\jmath\omega)\right) \times \alpha_{CD} \times V^2 \tag{3.22}$$

$$\text{Phase} = \text{angle}\left(T(\jmath\omega)\right) \tag{3.23}$$

where as aforementioned, G is the amplification gain of the A/V preamplifiers. They are supposed to be used in their bandwidth such as the gain is stable in the experimented frequency range and there is no phase shift. **Figure** 3.14 (log-log plot) demonstrates the good accuracy of the identified model with the tweezers' behavior. The values for tweezers RV20 are summed up in **Table** 3.4.

Figure 3.15 shows the corresponding displacement for a 3 V_{pp} actuation at different frequencies. In fact, two modes appear clearly at 4000 Hz and 4700 Hz. According to the phase function, the motion do not seem to be in the direction of the sensing. The phase is not clearly rotating as at 2100 Hz. However according to the amplitude function showing antiresonance/resonance curve shape, the corresponding motion seems to combine x-direction with probably z-direction (out of chip plane direction), opposing

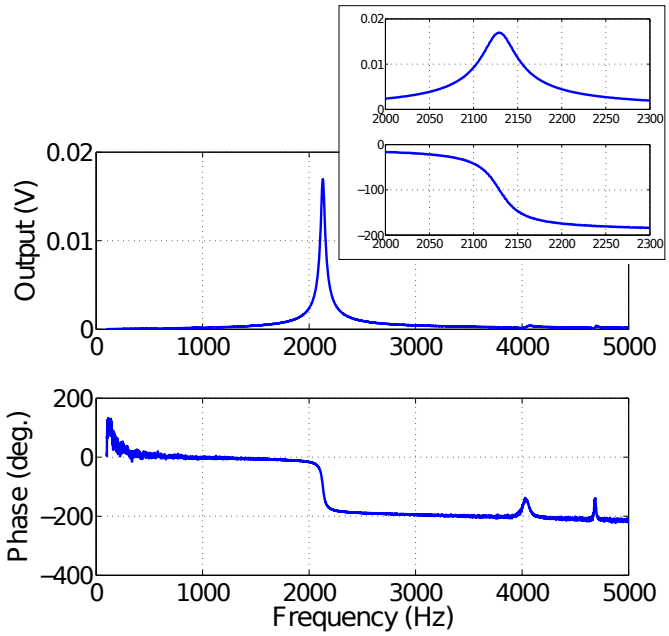

Fig. 3.13. Harmonic analysis of the silicon nanotweezers (Tweezers RV20). Displacement is actuated with 1 V_{RMS} signal at several frequencies (from 100 to 5000 Hz with 1 Hz step). Measurements are performed through the integrated differential sensor. V_{output} corresponds proportionally to the velocity of the motion of the tip. The insert shows a close view of the main mechanical resonance of the system.

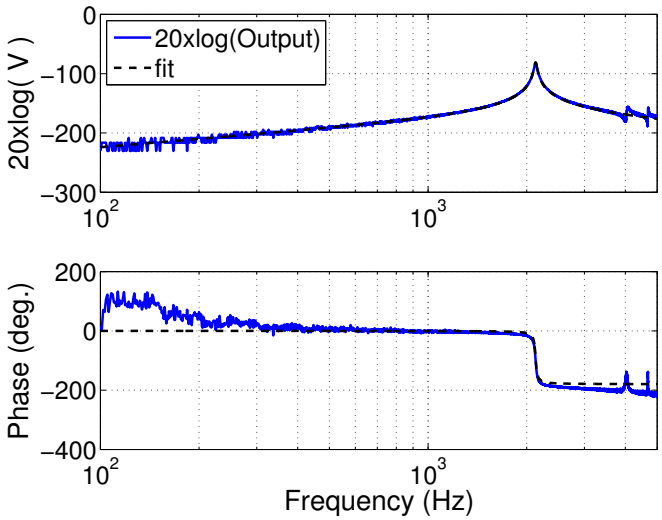

Fig. 3.14. Harmonic analysis of the silicon nanotweezers (Tweezers RV20). Plot on log-log scale of the **Figure** 3.13. Measurement data are fitted with the transfer function of a 2nd-order system (**Equations** 3.22 and 3.23).

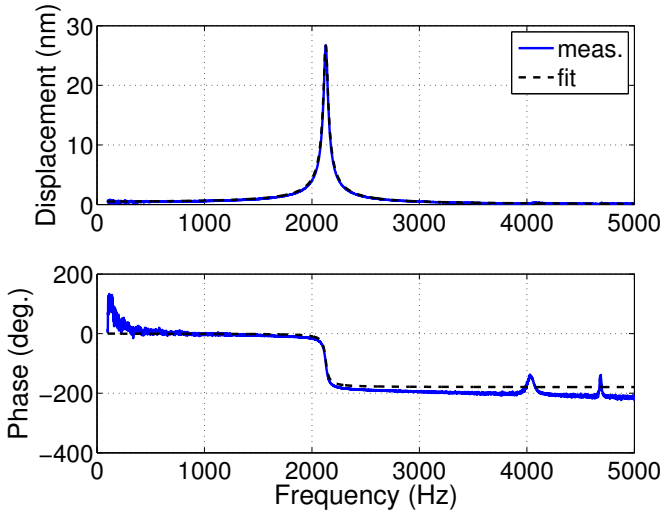

Fig. 3.15. Harmonic analysis of the silicon nanotweezers (Tweezers RV20). Corresponding displacement of the **Figure** 3.13. Measurement data are fitted with the transfer function of a 2^{nd}-order system (**Equations** 3.22 and 3.23).

the motion to the previously mode shifted motion and enhancing the x-displacement after the resonance and the subsequent phase rotation. This hypothesis is asserted by fast-motion video-based measurements in **Appendix** D.

Characteristic	Parameters	Theoretical values	Experimental values	Method
Actuator gain	α_{CD} (N/V^2)	29.2×10^{-9}	30.5×10^{-9}	Optical measurement
Sensor gain	α_{CS} (F/m)	269×10^{-9}	140×10^{-9}	Sensor static measurement
Stiffness	k_{tw} (N/m)	126.5	43.5	Force sensor
Viscosity	ν (N.s/m)	*N.A.*	60×10^{-6}	Dynamic measurements
Mass	M (kg)	299×10^{-9}	250×10^{-9}	Dynamic measurements
Resonant frequency	f_{r} (Hz)	3274	2099	Calculation
Quality factor	Q		55	Calculation

Table 3.4. Table of the identified parameters of the tweezers RV20.

Step response analysis

With the same setup of the harmonic analysis, i.e. measuring the derivative of the displacement Δx by applying a constant voltage on the central electrode C_0, the device is characterized with step responses. However, the time acquisition of the output signal is performed through a dSPACE prototyping box with A/D converter board (DS 2004).

Figure 3.16 shows the damped-oscillating response of the tweezers to step actuation. Actuation is set around an operating point (16.8 V) corresponding to a displacement of 180 nm. Small displacement steps of 20 nm are commanded applying step from 16 to 17.6 V and conversely. These experiments have been performed in **Chapter** 5 in order to show open-loop system response.

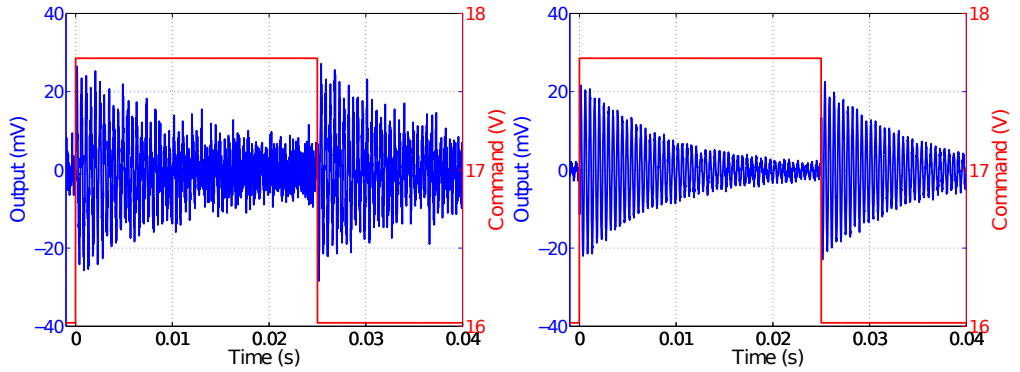

Fig. 3.16. Step response of the silicon nanotweezers (Tweezers RV20). The left graph shows measurement performed with 10^8 gain A/V preamplifiers, while right graph data are performed with 10^8 Low Noise gain A/V preamplifiers.

Figure 3.17 shows close-up view of the step responses and comparison between the experimental data and the model. Zoom on the curves enables to see the difference of noise level between the two amplification modes. However it does not allow to visualize the drawbacks of the 10^8 LN gain bandwidth in comparison with the 10^8 gain bandwidth. As it is discussed with the feedback implementation, the reduced bandwidth of the Low Noise mode bring phase shift to the output signal (around $-12°$ at 2 kHz).

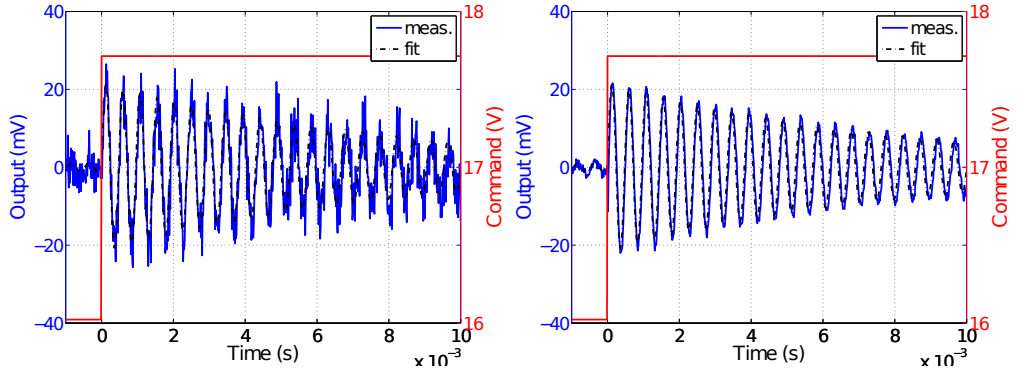

Fig. 3.17. Step response of the silicon nanotweezers (Tweezers RV20). The left graph shows measurement performed with 10^8 gain A/V preamplifiers, while right graph data are performed with 10^8 Low Noise gain A/V preamplifiers. Measurement data are fitted with the transfer function of a simple 2^{nd}-order system (**Equation** 3.18).

This set of characterizations enables the modeling of the silicon nanotweezers with respect to the theoretical laws used for the design. The system's parameters have been identified:

- from static experiments for the actuator gain α_{CD} and the sensor gain α_{CS},
- from experiments with force sensor for the mechanical stiffness k,
- and from identification of dynamic responses (frequency or step responses) for the mass M and the losses due to the viscosity ν.

In conclusion, it appears that for small displacements (< 30 nm), a 2^{nd}-order model can accurately predict tweezers' behavior. However a fine study of the step response characteristics (**Figure** 3.16) shows different oscillation frequencies for positive (170 to 190 nm) and negative (190 to 170 nm) steps. In positive step, the response oscillates at 2094.6 Hz when in negative step, it oscillates at 2100.4 Hz. Focusing on the mechanical stiffness k_{tw}, it corresponds to a variation of 60 mN/m (assuming the model is relevant and the other parameters stable). With the will of sensing the mechanical rigidity of single molecule of DNA (i.e. 30 µN/m, cf. **Chapter** 4), this point may be a source of inaccuracy for the sensing. For relevant bio-molecule sensing, experiments are intended to be performed in frequency mode (with a sinusoidal actuation) around an operating point.

Moreover, we pointed, in **Figure** 3.14, the presence of other dynamics than the main resonance, especially at higher frequencies. These modes are not considered with the simple model but may be a problem at the time of the control design and implementation.

3.3.3 Optical characterizations

Optical characterizations have been performed thanks to a MEMS Analyzer instrument from Polytec (and by interferometry with an interferometer from SIOS Meßtechnik GmbH). Direct access to the motion of the tip turns out essential to (1) check displacement of the tip, (2) characterize the parameters of the model (especially of the actuator and the sensor independently) and (3) reveal non expected behaviors.

On the one hand, fast dynamic motion in-plane and out-of-plane were characterized through stroboscopic video microscopy but with low spatial resolution (100 nm) (see **Appendix** D). On the other hand, interferometry measurement allowed in x-displacement characterization with very high resolution until 0.1 nm.

Characterization of different modes

Figures 3.18 and 3.19 show time and frequency responses of the device. Experiments have been performed with tweezers JST33 which does not present the same characteristics than tweezers RV20. Both devices are not originally from the same wafer and same fabrication. For instance, its resonance frequency is around 2460 Hz (when $f_{\text{RV20}} = 2100$ Hz). However their designs are identical and their behavior are similar.

Due to the measurement resolution of the MEMS analyzer based on microscopy imaging resolution, the experiment was performed with high voltage step (0 to 30 V) or sinusoidal (10 V_{pp}) in order to operate with large displacements (> 0.1 µm). Time step characterization shows the low damped step response of tweezers with natural frequency

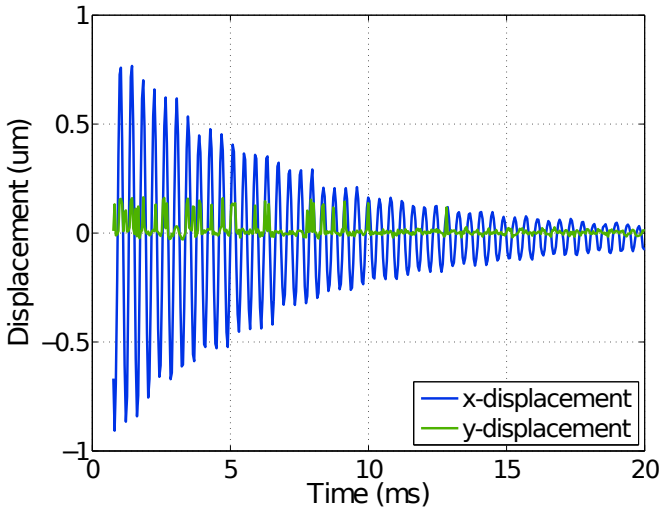

Fig. 3.18. 30 to 0 V negative step response characterization of the MEMS tweezers with MEMS Analyzer (Polytec). (Tweezers JST33).

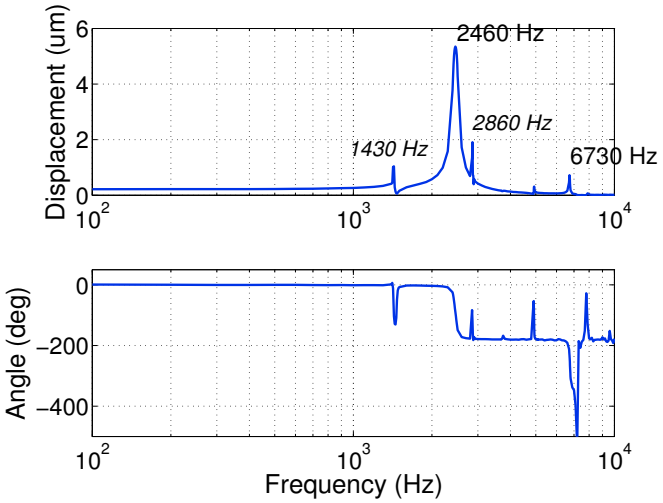

Fig. 3.19. Motion dynamics characterizations with stroboscopic video microscopy (MEMS Analyzer, Polytec). 10 V_{pp} AC excitation. (Tweezers JST33).

around 2460 Hz. In the transverse direction, with the low resolution of the instrument, we are not able to detect relevant transverse motion.

Frequency experiments enabled to characterize harmonic behavior of the tweezers with a 10 Hz step. **Figure** 3.19 outlines 4 or 5 modes in the experimented frequency range from 100 Hz to 10 kHz. Despite the theoretical unidirectional actuation in x-direction, MEMS analyzer videos demonstrate out-of-plane and transverve motion resonances. Indeed, the **Figure** makes appear a predominant mode at 2460 Hz, however a second resonance is shown in x-direction at 6730 Hz. The phase curve is accordingly

shifting from $-180°$ to $-360°$. Other resonances, especially at 1430 Hz, demonstrate a chaotic phase measurement. Focusing on the video images available in **Appendix**, it appears that for an actuation at 1430 Hz, the tip moves vertically, i.e. alternatively blurring the image (**Figure** D.6 in **Appendix** D).

This significant out-of-plane mode is, at this point, unjustified and complicated to explain. The actuation is a priori not operated in the z-direction. However, initially the mobile part is pushed down by its own mass. The actuation force lift up the movable part and actuate it in the z-direction. This assumption is checked by characterizing the stiffness actuating the movable part in the z-direction. Theoretically, the equivalent stiffness in the z-direction is evaluated modifying **Equations** 3.8 (**Page** 25), inverting the inertial moments I_x by I_z.

$$I_x = \frac{tw^3}{12} \tag{3.24}$$

$$I_z = \frac{wt^3}{12} \tag{3.25}$$

Table 3.1 reporting equivalent stiffness in x-direction becomes **Table** 3.5.

Springs i	Dimensions $L_i \times w_i \times t_i$ (µm)	Stiffness (N/m)
1	$1000 \times 15 \times 30$	33.4
2	$1000 \times 15 \times 30$	8.4
3	$600 \times 12 \times 30$	371.3
Total		413.1

Table 3.5. Theoretical characteristics of the tweezers springs in z-direction (out-of-plane direction).

Theoretically, the equivalent stiffness in the z-direction is very high (413.1 N/m) compared to the x-direction stiffness (126.5 N/m) leading to a higher frequency dynamic. However the characterization of this stiffness with a force sensor tool (FT-S540, FEMTO-TOOLS) shows an effective stiffness of 22.8 N/m (cf. **Appendix** F). Finally assuming the mass of the movable part ($M = 250 \times 10^{-9}$ kg), the resonance frequency, related to a simple mass-spring system must be effectively around 1500 Hz.

However the reasoning is not so easy since the mechanical structure of the tweezers is complex. The complex spatial distribution of the mass, constraints and forces leads to several motion modes possible combining translations and rotations along the different axis. In the following **Section**, finite element simulations were conducted to understand these unpredictable dynamics. **Figure** 3.22 (**Page** 47) demonstrates the existence of two dynamics (with an important out-of-plane motion component) before the expected one.

In conclusion, the device demonstrates several dynamics in the bandwidth from 0 to 10 kHz. The predominant mode around 2 or 2.5 kHz (depending on the device) is well

characterized and easily identified. The other modes seem to be less important in terms of motion amplitude since they are not easily characterized through the integrated sensor. However despite their low amplitudes, the drawback arise from their proximity with the main resonance.

Characterization of large-displacement behavior

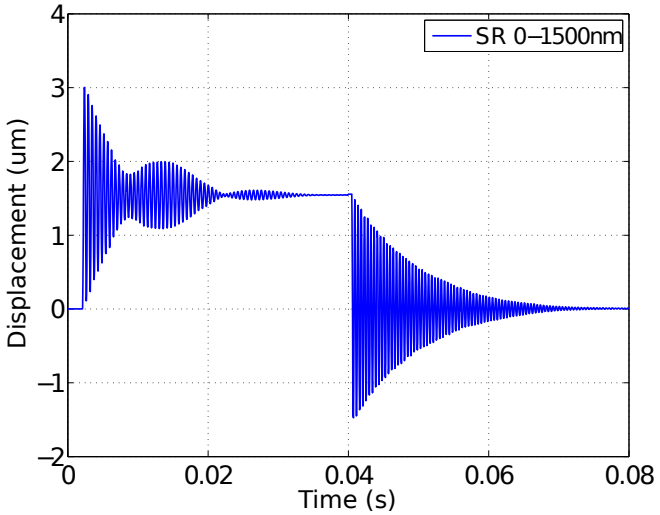

Fig. 3.20. Device characterizations in large displacement. Motion measurement by interferometry for step from 0 to 1.5 µm. (Tweezers RV20).

During the characterization of the tweezers, it appeared very different behaviors according to the conditions and especially the considered operating point. **Figure** 3.20 shows the step responses for large displacements around the initial point (0 µm) and 1.5 µm. The measurements have been performed by interferometry, discriminating the role of the sensor in the response. From 1.5 to 0 µm displacement step, the response show common damped oscillations with an exponential decay. However the step to 1.5 µm exhibits more complex response with a modulation of the damped oscillations. Apparently, around this point, the system shows complex dynamic combining at least two frequencies.

Frequency characterization with large offsets demonstrates the presence of important resonances with close frequencies when the tip is moved from the initial point (**Figure** 3.21). Measurements have been performed, through the output of the integrated sensor, with a small AC signal (200 mV) combined with different offsets from 10 to 40 V. Typically, 40 V-offset experiment corresponds to frequency responses around 1.2 µm-displacement offset (cf. **Figure** 3.9).

With the increase of the actuation offset, the typical resonance frequency of the system decreases. For large offsets (> 30 V_{DC}), the decrease is superior to 10%. This decrease may be explained by a decrease of the equivalent stiffness of the suspensions under large bending, but can also be explained considering the growth of interactions

between unengaged regions in the comb electrodes of the actuator. If their interactions are considered as parallel plate actuators, an equivalent negative stiffness can be obtained (i.e. a force function of Δx) also explaining the decrease of the resonance frequency.

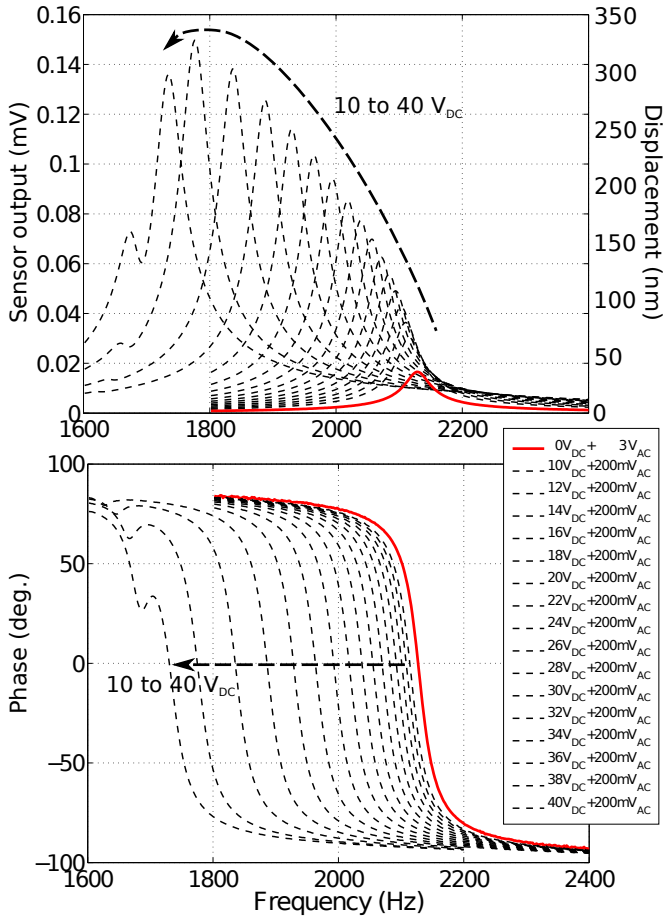

Fig. 3.21. Device characterizations at different operating points. In red and plain line is plotted as reference the frequency response of the system to typical actuation without offset (such as **Figure** 3.13). (Tweezers RV20).

Here are shown two characteristics of the device behavior which have not been taken into account during the first characterization. Furthermore, complementary finite element simulations have been conducted in the following **Section** providing more explanations about the unpredicted dynamics. In the next **Section**, the sensitivities of the different dynamics are also simulated to justify and move toward the more accurate model for biological molecule sensing.

3.3.4 Finite-element simulations

Previous characterizations have revealed several possible dynamics for the mechanical motion and this concern starts to be limitative at the time to implement the feedback control. This simulations have been performed lastly to understand the dynamics of the mechanical structure and to re-design the tweezers with a better understanding of the structure.

Simulations with COMSOL Multiphysics are performed in order to characterize phenomena which are neglected by the theory adopted for the modeling. However, here we also attempt to demonstrate:

- the pertinence to drive the intended mode rather than the other modes;
- the sensitivity of the intended mode for the characterization of the mechanical parameters of molecules.

Either static or dynamic simulations have been conducted. The detailed of the simulation conditions and of the studies are further explained in **Appendix** E.

Preliminary static simulations confirm the stiffness of the system in the actuated direction. With the mask's dimensions, a value of 136.43 N/m is found (instead of 126.45 N/m). The difference with the theoretical value is due to the effect of the parallelogram used as a mechanical feedback in the calculation of the stiffness (cf. **Paragraph** 3.2.1). When simulations are conducted without the parallelogram, the equivalent stiffness becomes 122.50 N/m.

Finally these first simulation results are in agreement with the simple model obtained from the small bending of the suspension beams. Furthermore, parametric simulations on the suspension dimensions show the effect of the overetching of the suspensions dimensions on the mechanical stiffness.

Eigenfrequency studies

Eigenfrequencies of the structure are studied to evaluate the modes of the structures. The simple modeling of the device based on the consideration of a single mass and stiffness just allow to predict one dynamic of the device.

Figure 3.22 shows the first four modes of the structure. Results demonstrate that the two first dynamics are not the expected one and show out-of-plane (i.e. out of xy-plane) motions. Therefore the third eigenfrequency is the frequency of the mode in which the device is intended to work. The fourth eigenfrequency is another mode with out-of-plane motion.

Knowing the resonance frequency and the stiffness in the x-direction, we are able to identify the inertia of the device with the following equation (derived from the **Equation** of the resonance frequency of a second order mechanical system):

$$M = \frac{k_x}{(2\pi.f)^2} = \frac{136.43}{(2\pi \times 3338.78)^2} \simeq 310 \times 10^{-9} \text{ kg} \tag{3.26}$$

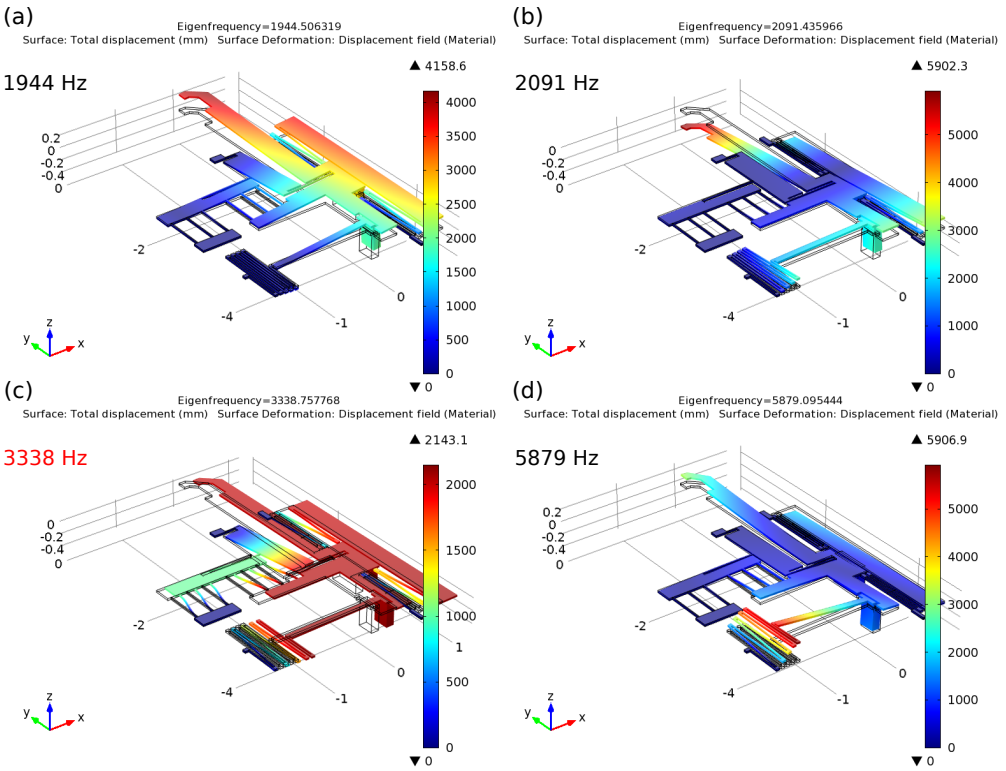

Fig. 3.22. Eigenfrequency simulations of the mechanical structure of the nanotweezers. The first 4 modes of the structure are shown.

However the expected frequency (3338 Hz) differs considerably from the experimentally characterized one around 2500 Hz.

Table 3.6 summarizes the eigenfrequencies of the device for several dimensions of the suspensions. Suspensions widths and thicknesses are important parameters for explaining the wide variation of the device characteristics. Width w and thickness t are at the cubic power for the calculation of the mechanical stiffness of a bending beam. Furthermore their sizes are small enough to be very dependent to fabrication processes.

By optical characterizations, width can vary from 10 to 14 µm and silicon thickness from 27 to 30 µm. The thickness of the silicon is a more stable dimension than the widths of the beams. However first tweezers were fabricated with {**27**/2/400 µm}-layer SOI wafer, when new tweezers are fabricated with {**30**/2/400 µm}-layer SOI wafer.

Simulations of the dynamic sensitivities

The simulations conditions are explained in **Appendix** E, and **Figure** E.6 (**Page** 127) shows the boundary conditions set in order to simulate the mechanical contribution of molecules trapped in between the tips. **Figure** 3.23 shows the evolution of the frequency of the first four modes of the tweezers. Results prove that the third mode (moving in the x-direction) is the more sensitive for the characterization of mechanical stiffness at the end of the tip.

Dimensions	1st eigenfreq.	2nd eigenfreq.	**3rd eigenfreq.**	4th eigenfreq.
$t = 30$ µm (new SOI wafer)				
$w = 15$ µm	1944	2091	**3338**	5879
$w = 13$ µm	1778	1948	**2680**	5879
$w = 10$ µm	1525	1701	**1849**	4180
$t = 27$ µm (previous SOI wafer)				
$w = 13$ µm	1596	1754	**2634**	5144
$w = 12$ µm	1606	1763	**2422**	5154

Table 3.6. Eigenfrequencies of the mechanical structure of the nanotweezers according to the suspension width w and the silicon thickness t.

Studies have been extended to equivalent stiffness in the y- and z-directions, and likewise to added mass. **Table** 3.7 summarizes a sample of results to compare the sensitivity of all the modes depending on the conditions. The frequency shifts for 1 N/m (which represents about 30 thousands of λ-DNA molecules) in y- and z-directions and for 1×10^{-9} kg (which represents about 20 billions of λ-DNA molecules) are not significant in comparison with the shift of the frequency of the third mode for stiffness in the x-direction.

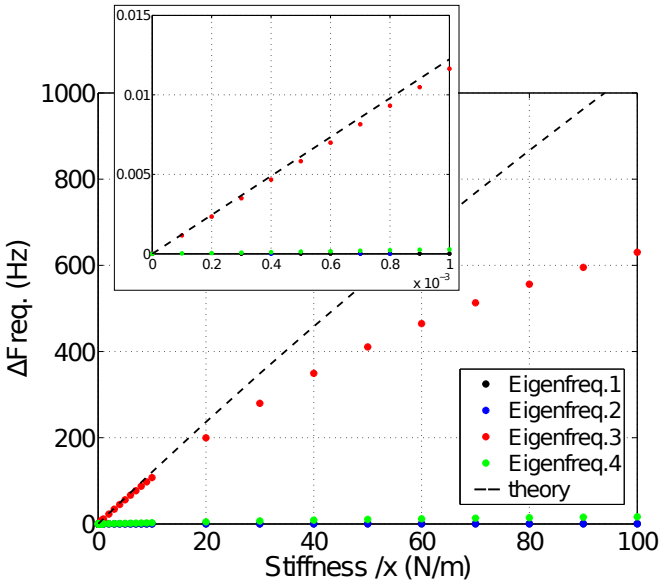

Fig. 3.23. Eigenfrequency simulations of the mechanical structure of the nanotweezers according to DNA molecule mechanical parameters. DNA molecules are simulated with a stiffness k_x along the x-direction. Dots for eigenfrequencies 1, 2 and 4 are closed to 0. Theoretical curve for eigenfrequency 3 is calculated from **Equation** 3.27.

Furthermore the sensitivity of the intended mode is compared to the theoretical curve based on an equivalent mass-spring-damper system and using **Equation** 3.27.

$$\Delta f = \frac{1}{2\pi}\sqrt{\frac{k + k_{\mathrm{DNA}}}{M}} - \frac{1}{2\pi}\sqrt{\frac{k}{M}} \tag{3.27}$$

where $k = 136.43$ N/m and $M = 310 \times 10^{-9}$ kg (which are values extracted from COMSOL static and dynamic simulations). For small extra stiffness $k_{\mathrm{DNA}} < 1$ mN/m, this simple model is in agreement with the FEM simulations. After $k_{\mathrm{DNA}} > 1$ mN/m, the mode is less sensitive than the model predicts.

Mechanical parameters	1st eigenfreq.	2nd eigenfreq.	**3rd eigenfreq.**	4th eigenfreq.
k_{DNA}				
$k_x = 1$ N/m	< 0.1 Hz	< 0.1 Hz	11.5 Hz	0.3 Hz
$k_y = 1$ N/m	0.6 mHz	8.1 mHz	5.6 mHz	< 0.1 mHz
$k_z = 1$ N/m	17.6 Hz	207.3 Hz	0.2 Hz	39.1 Hz
M_{DNA}				
$M = 1 \times 10^{-9}$ kg	-8.6 Hz	-31.6 Hz	-5.2 Hz	-51.9 Hz

Table 3.7. Eigenfrequency simulations of the mechanical structure of the nanotweezers according to DNA molecule mechanical stiffness k_{DNA} and mass M_{DNA}.

In the next **Part**, the nanotweezers will be considered as a second order mechanical system for measurement and sensing of bio-physical properties of DNA molecules, for overall dynamic analysis and for the control design. Nevertheless one has to keep in mind the potential drawbacks of the use of such simplified model during the integration phase (such as are neglected dynamics).

3.4 Real-time measurement

The design of nanotweezers is devoted to the sensing of the mechanical properties of the biological molecules. Hereafter, the principle of measurement is detailed.

3.4.1 Model of the device

In previous **Sections**, we developed an accurate dynamic model of the device which allows measurement of the mechanical properties of a trapped object by monitoring the changes in the frequency response. Basically, the tweezers are characterized as a mechanical mass-spring system integrating transducers for actuation and sensing. **Table** 3.8 sums up the features of the model of the silicon nanotweezers. Performing dynamic measurements, we expected to detect changes in the resonance frequency and amplitude of the overall system which are in fact consequences of the changes in mechanical parameters of the trapped object.

Figure 3.24 depicts the equivalent dynamic model of the nanotweezers and the equivalent stiffness and losses when molecules are extended between the movable and the fixed tips.

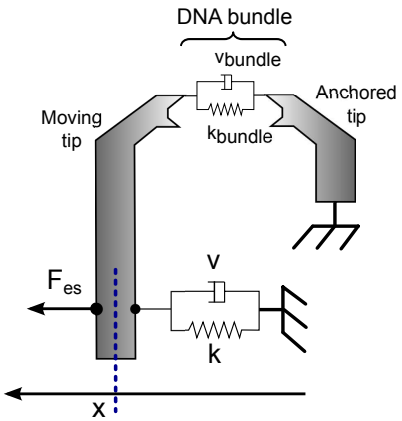

Fig. 3.24. Equivalent dynamic model of the silicon nanotweezers. DNA molecules are represented by a purely viscous damper and purely elastic spring connected in parallel (Kelvin-Voigt model).

Features	Parameters	Theoretical values	RV20 tw. values
Actuation			
	$F_x = \alpha_{CD}.V^2$	$29.2 \times 10^{-9}.V^2$	$30.5 \times 10^{-9}.V^2$
Mechanical system			
	Mass M (kg)	299×10^{-9}	250×10^{-9}
	Stiffness k_{tw} (N/m)	126.5	43.5
	Viscosity ν (N.s/m)	$N.A.$	60×10^{-6}
Sensing			
	$\Delta C = \alpha_{CS}.\Delta x$	$269 \times 10^{-9}.\Delta x$	$140 \times 10^{-9}.\Delta x$
	$\Delta I = \frac{d}{dt}(V_0.\Delta x)$		
	$\Delta V = G.\Delta I$	10^7 or $10^8.\Delta I$	

Table 3.8. Table of model parameters for silicon nanotweezers.

3.4.2 Measurement principle

3.4.2.1 Dynamic measurement in real-time

One part of the objectives is to achieve real-time monitoring of biological processes with high time resolution. We previously showed the dynamic characterization of the nanotweezers by the frequency sweep characterization of the resonance amplitude peak and

phase shift. The sweep of frequencies followed with the identification of the resonance characteristics allowed 10 second-time resolution measurement which was enough to characterize DNA-enzymes interactions with small concentrations of enzymes and high number of DNA molecules [Kumemura 2010].

Nevertheless, in order to perform fast characterization of the resonance, we implemented Phase-Locked Loop (PLL) algorithm based on the injective phase function of a 2^{nd} order model. The PLL produces a signal of the form $A \times sin(\omega t)$ and monitors the system response adjusting the drive frequency, $\omega = 2\pi f$, to maintain a phase difference of $-90°$ for displacement or $0°$ for velocity measurement compared to the drive signal, i.e. at the system resonance. The lock-in amplifier allows the accurate measurement of the magnitude-phase of the electrical output signal at the reference frequency, and enables the algorithm implementation with software for prototyping and development such as LabVIEW or dSPACE.

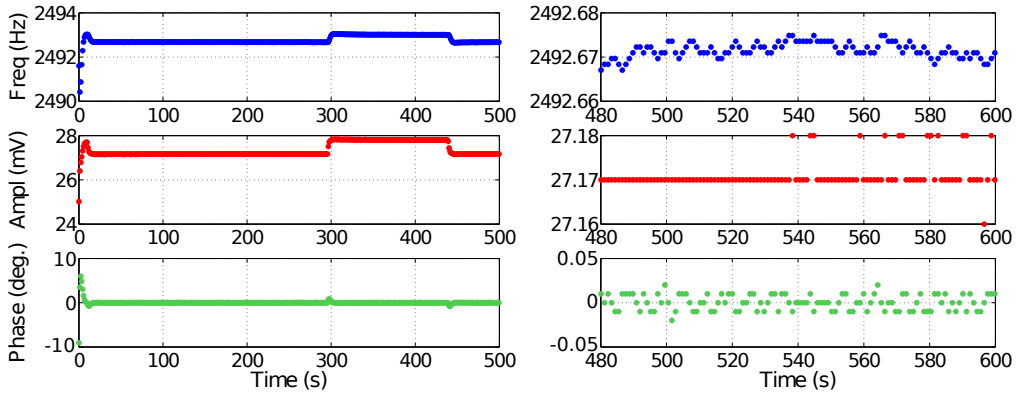

Fig. 3.25. Monitoring of the resonance frequency of the nanotweezers by Phase-Lock Loop (PLL). The left graph demonstrates the good convergence of the algorithm at the beginning for finding the resonance frequency of the system and when the system parameters are perturbed switching on and off the light (at $t = 300$ s and $t = 450$ s). The right graph demonstrates the resolution of the measurements of the resonance frequency and amplitude. (Tweezers RV12).

Figure 3.25 shows the real-time monitoring of the resonance by PLL algorithm. At the beginning of the experiment, the system tends to stimulate the tweezers at its resonance frequency, i.e. at 2492.6 Hz for the tweezers RV12. During the period from 300 to 450 s, the device is perturbed by heating it with the focused light of the microscope. The resonance frequency and its amplitude increase due to this perturbation. The effect of the light on the mechanical structure have not been characterized. Switching off the light, the resonance frequency recovers its previous value. The PLL algorithm works correctly with sub-second time resolution and with time establishment inferior to 2 s for sudden parameter changes.

Figure 3.25 demonstrates also the resolution of the system detection. With the current setup, the minima detectable shifts are 1 mHz for the frequency (i.e. the resolution of the signal generator) and 10 µV for the output voltage (i.e. the resolution of the lock-in

instrument). However, with the close-up view on two minutes of experiments from 480 to 600 s, we can observe that the resonance frequency varies from 2492.667 to 2492.675 Hz, that is to say ±8 mHz. Environment conditions are not completely controlled, so we considered this variation as the uncertainty on the system parameters.

By derivation of **Equation** 3.19 with respect to k_{tw}, the sensitivity of the sensing on the stiffness parameter is deduced:

$$\frac{\partial f_{\mathrm{r}}}{\partial k_{\mathrm{tw}}} = \frac{1}{2\pi} \frac{1}{2M\sqrt{\frac{k_{\mathrm{tw}}}{M} - \frac{1}{2}\frac{\nu^2}{M^2}}} \simeq 20 \text{ Hz.}\,(\mathrm{N/m})^{-1} \tag{3.28}$$

i.e. the precision on the stiffness parameter is (in air):

$$\Delta k_{\mathrm{tw}} = \frac{\Delta f}{\frac{\partial f_{\mathrm{r}}}{\partial k_{\mathrm{tw}}}} = \frac{0.008}{20} \simeq 0.4 \text{ mN/m} \tag{3.29}$$

The accuracy on the stiffness measurement is ±0.4 mN/m, that is to say 14 molecules of λ-DNA (if the accuracy is the same in biological solutions).

3.4.3 Effect of unmodeled parameters

With the developed method for real-time measurement, we showed the possibility to monitor system's parameter variations. Hereafter, we study the effect on the dynamic characteristic of the tweezers of the environmental conditions as room temperature and experimental conditions such as immersion in liquid.

3.4.3.1 Effect of the temperature

Figure 3.26 shows the variations of the frequency response of the system to temperature variations. The experiment has been performed during night time in "bio-room" with air-conditioner control set at 25 °C. The system is characterized in real-time with PLL program, while temperature is measured close to the device with a thermo-resistance. Others environmental conditions as pressure and humidity have not been measured.

The experiment demonstrates a direct relation between the dynamic parameters of the system (the resonance frequency f_r and amplitude A_r) and the temperature. Accordingly:

$$\frac{\Delta f_{\mathrm{r}}}{\Delta T} \approx -0.36 \text{ Hz.}^{\circ}\mathrm{C}^{-1} \tag{3.30}$$

$$\frac{\Delta A_{\mathrm{r}}}{\Delta T} \approx -0.32 \text{ mV.}^{\circ}\mathrm{C}^{-1} \tag{3.31}$$

3.4.3.2 Effect of the medium

By frequency sweep method, the resonance of the system has been characterized for different insertion of the tweezers' tips in liquid. On the one hand, **Figure** 3.27 shows the effect of the insertion depth on the resonance of the system. The resonance frequency and the Q factor decreases when the tips are deep in a liquid medium. The trend of the

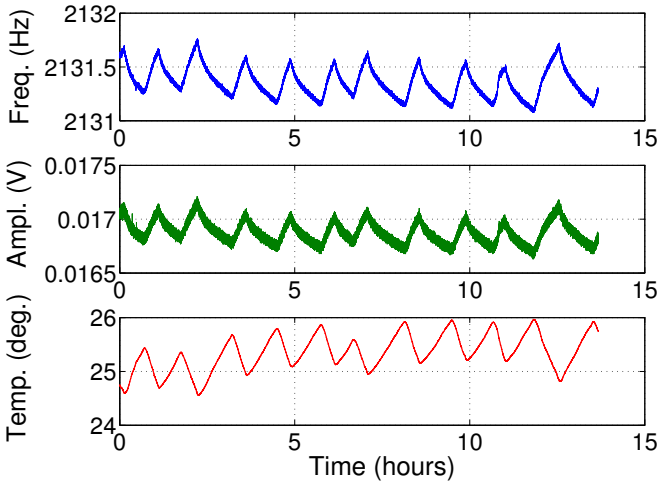

Fig. 3.26. Tweezers parameter dependence with environment temperature. The system is characterized in real-time with PLL program, while temperature is measured close to the device with a thermo-resistance. (Tweezers RV14).

Q factor is easily understandable considering more important losses in liquid than in air due to drag forces. For the frequency trend, the inertia of the motion is increased with the insertion in liquid.

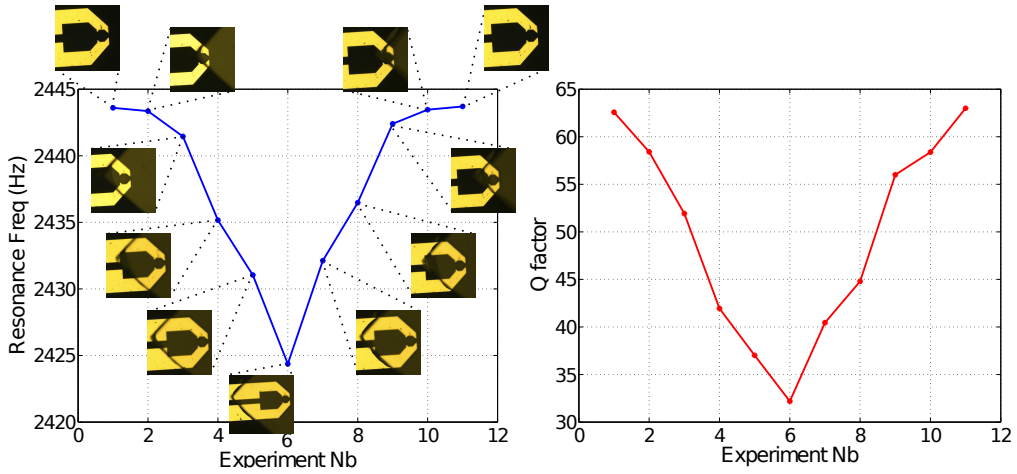

Fig. 3.27. Tweezers parameter dependence with insertion in dionized water. (Tweezers JST29).

On the other hand, **Figure** 3.28 shows experimental results with different configurations of immersion. Experiments 1 and 4 show same resonance characteristics (such as experiments 1 and 11 of **Figure** 3.27). In experiment 4, the fixed tip is partly immersed when the movable tip is in air. It confirms that the dynamic response of the system is only dependent on the movable tip. Experiment 3 of **Figure** 3.28 exhibits same characteris-

tics than experiments 3 and 9 of **Figure** 3.27 when both tips are immersed. Experiment 2 demonstrates a resonance dominated by a "thightening" of the device. In this case, only the movable part is immersed in the liquid. The losses have increased due to the drag forces in the liquid, but the frequency increased.

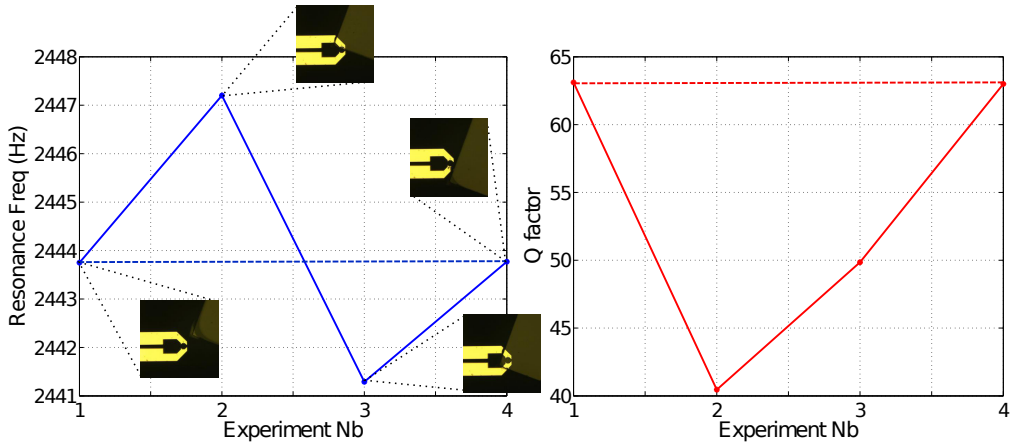

Fig. 3.28. Tweezers parameter dependence with insertion in dionized water (2). (Tweezers JST29).

3.4.3.3 Set-up characterizations

From [Yamahata 2008a], the resolution of the measurement have been enhanced thanks to an improvement of the experimental setup. For instance, **Figure** 3.7 illustrates the improvement of the PCB support to avoid coupling between the actuation and the sensing. Moreover such improvement is mandatory for the implementation of control feedback.

Figure 3.29 demonstrates the importance of the system isolation from external electric fields present in a room equipped with various appliances and instruments. Experiments previously performed in a Faraday cage has been moved inside a minimal metallic box were all the connection have been changed with grounded coaxial wires (**Figures** C.1 and C.2). The **Figure** 3.29 illustrates the frequency spectrum of the sensor outputs in normal and isolated conditions. In normal conditions, the time output signal shows perturbed amplitude with several environmental signals. In grounded box conditions, the frequency actuation f and $2f$ are well identifiable. Peaks at 50 and 100 Hz are still visible but with low amplitude.

Figure 3.29 demonstrates the importance of isolating the sensing signals from the actuation signal. The tweezers are stimulated with sinusoidal signal at its resonance frequency applying an AC voltage at $f = f_r/2$ with null offset. **Equation** 3.17 demonstrates that the actuator generates forces at $2f$. Regardless the **Figure** 3.29 shows signal at the frequency f coming from the actuation and not from the motion sensing. The PCB support has been enhanced with 3 layers of ground with especially ground planed

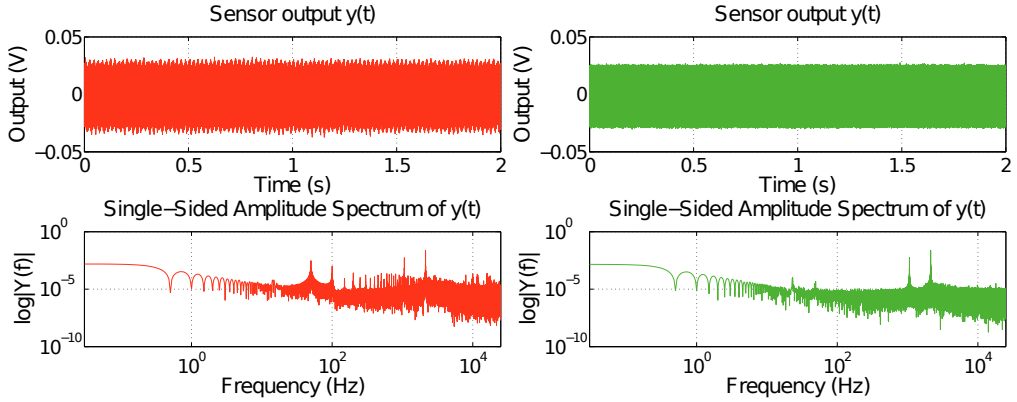

Fig. 3.29. Frequency characterizations of the noise of the tweezers sensor output, in regular room conditions (left) and in a grounded box (right). Tweezers are stimulated with sinusoidal signal at its resonance frequency. Uppers graphs shows sensor outputs while below are represented frequency analysis of the output signals. (Tweezers RV12).

below and above the silicon chip (**Figure** C.2). In improved conditions, the time output signal shows a diminution of the frequency modulation between f and $2f$.

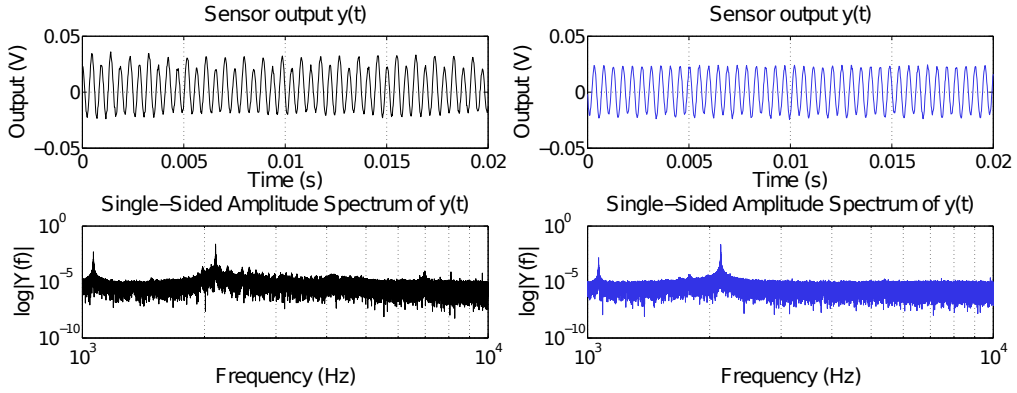

Fig. 3.30. Frequency characterizations of the noise of the tweezers sensor output, in Faraday cage (left) and in a grounded box with special 3-layer PCB (right). Tweezers are stimulated with sinusoidal signal at its resonance frequency. Uppers graphs shows sensor outputs while below are represented frequency analysis of the output signals. (Tweezers RV12).

3.5 Conclusion

This last **Part** of the chapter introduced to the features for sensing with silicon nanotweezers. Based on a mechanical damped mass-spring model, measurements are performed monitoring changes in the dynamic response of the system. That way mechanical stiffness and losses of an object trapped in between the tweezers' tips are expected to

be characterized. The current setup allows to detect changes in the resonance frequency of 8 mHz, leading to a resolution on the stiffness parameter of 0.4 mN/m. This value is equal to the equivalent mechanical stiffness of about 14 molecules of λ-DNA. The sensing of bio-mechanical interactions on λ-DNA with the tweezers will be presented in the next **Chapter**.

For the biological experiments, the tweezers needs to be inserted in biological solutions containing DNA molecules or enzymes. We showed the effect of the insertion of the tips in liquid on the system response. In order to keep the measurement resolution characterized in air and avoid the losses in liquid medium, the sharp tips will be immersed at the minimum required. Furthermore, we demonstrated that the dynamic response of the system is sensitive to experimental conditions as temperature and immersion in liquid for instance. The stability of the meniscus between the tip, the biological liquid and the air will be an important feature to manage in order to sense biological reactions.

Finally, **Figures** 3.29 and 3.30 illustrated the importance of the experimental setup conditions. The silicon system is driven through actuation and sensing using electrical features. We demonstrated an important coupling between the actuation and the sensing mainly due to the miniaturization of the system. As firstly implemented, the measurement have been performed at different frequency than the actuation frequency using the square law of the actuator. However, with the goal to implement a control strategy, the setup have been improved to work around one operating point with linear conditions. Indeed, the control design is based on linear models that involves the linearization of the system and the actuator (**Equation** 3.33). The motion frequency will be the same than the actuation frequency. For that purpose, a special care have been dedicated to the insulation and the extraction of the sensing current.

$$
\begin{aligned}
F_x &= \alpha_{CD} \times V_{\text{act}}^2 && (3.32)\\
&= \alpha_{CD} \times \left(V_0 + V_{\text{ac}} sin\left(2\pi f t\right)\right)^2 \\
&= \alpha_{CD} \times \left(V_0^2 + 2V_0 V_{\text{ac}} sin\left(2\pi f t\right) + V_{\text{ac}}^2 sin^2\left(2\pi f t\right)\right) \\
&= \alpha_{CD} \times \left(\left(V_0^2 + \frac{V_{\text{ac}}^2}{2}\right) + 2V_0 V_{\text{ac}} sin\left(2\pi f t\right) - \frac{V_{\text{ac}}^2}{2} cos\left(2\pi 2 f t\right)\right) \\
&\simeq \alpha_{CD} \times \left(\left(V_0^2 + \frac{V_{\text{ac}}^2}{2}\right) + 2V_0 V_{\text{ac}} sin\left(2\pi f t\right)\right) \text{ if } V_0 \gg V_{\text{ac}} && (3.33)
\end{aligned}
$$

4

Bioexperiments on DNA with silicon nanotweezers

Contents

Summary. Bioexperiments with silicon nanotweezers have been performed on DNA molecules following routine methods as intended. Firstly, thanks to the electrical contacts to the tips, DNA molecules are easily trapped by dielectrophoresis. Biocharacterizations can start in solution, in air or in vaccuum with static and dynamic mechanical stimuli. Using the integrated sensor, changes in the responses of the tip displacement can be observed enabling the characterization of the mechanical properties of the DNA bundle.

A second step was achieved by the real-time sensing of bioreactions on DNA. The frequency response of the system is continuously monitored during the time of the reaction. Experiments were performed with the digestion of DNA bundles with *Hin*dIII restriction enzymes, and with binding interactions between DNA and Ethidium Bromide molecules. The last experiments demonstrate the direct application of the device achieving the sensing of structural modifications in the DNA molecule induced by biological or chemical interactions with proteins.

4.1 Trapping of DNA molecules

The first step for the characterization of DNA molecules is to trap molecules in between the tweezers' tips. Indeed, DNA molecules are routinely trapped in aqueous solution using dielectrophoresis forces. [Washizu 1990] demonstrates the electrostatic orientation and dielectrophoresis (DEP) of DNA under a high-intensity field produced in microfabricated electrode system.

4.1.1 Principle of the dielectrophoresis

DNA is a photoelectrolyte in that it has many ionizable phosphate groups along its length. In solution, the macromolecule becomes all along charged surrounded by a cloud of ions. The ions are electrostatically bonded to the molecule but are easy to move along, i.e. a DNA molecule is highly polarizable along its length.

Therefore the orientation of DNA is the same as that of nonspherical particles resulting from the interaction between the external field and the induced dipole. [Washizu 1990] reports a study of the orientation of λ-phage DNA molecules[1] with frequency dependence from 40 kHz to 2 MHz. The paper concludes that the optimal frequency for the orientation is experimentally 1 MHz. At this frequency, voltage up to 150 V_{pp} is applied to microfabricated electrodes with gap of $60 - 150$ µm, yielding a field strength of higher than 10^6 V/m.

Typically this method have been adopted for the precise positioning of DNA molecules [Washizu 1995], or a single DNA molecule [Kumemura 2007] (**Figure** 4.1).

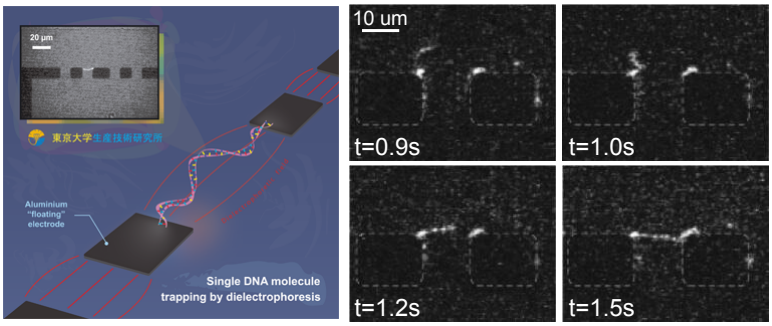

Fig. 4.1. Isolation and trapping of long single DNA molecules using high electric field between integrated electrodes in a microfluidic environment. The video frames detail the process of DNA trapping [Kumemura 2007].

4.1.2 Application to the nanotweezers

The design of the tweezers have been done in such a way to integrate conductive electrodes for DNA trapping by DEP (cf. **Chapter** 3). Therefore the trapping of a bundle of molecules is achieved by applying an AC electric field on tip electrodes.

[1] λ-phage DNA (commonly called λ-DNA) is the DNA molecule of the bacteriophage λ. λ-DNA molecules contains about 48.502 nucleobase base pairs (48.5 kbp)

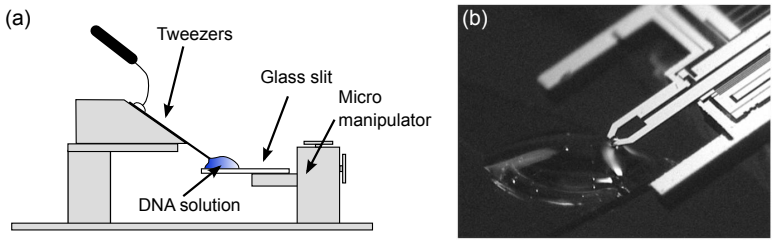

Fig. 4.2. Experimental setup of the DNA trapping. (a) Schematic of the setup. Tweezers are brought at the surface of a DNA solution droplet. (b) Photography of the tweezers tips at the surface of DNA solution droplet for DNA molecule trapping.

For all the biomechanical experiments described in this chapter, we used a solution of double-stranded λ-DNA obtained from Takara bio Inc (http://www.takara-bio.com). λ-DNA is the DNA molecule of the bacteriophage λ. It is about 16.5 µm-long and contains about 48.502 nucleobase base pairs (i.e. 48.5 kbp).

The initial solution is originally highly concentrated in DNA molecules (0.34 µg/µL). The solution is diluted 2 to 10 times with deionized water (Milli-Q water). The more the solution is concentrated, the easier the trapping is. However, in pratical terms, the trapping of DNA is driven by several features. On the one hand, the number of trapped DNA or the size of the DNA bundle which is related to the duration of the DEP and the number of molecules in solution. On the other hand, DNA molecules tend to attach to all the surfaces such glass slides, microfluidic channel walls and tweezers' tips, so that the use of a low concentrated solution is more appropriate. Finally the best conditions were to use 10 times diluted DNA solution and performing DEP during 10 minutes.

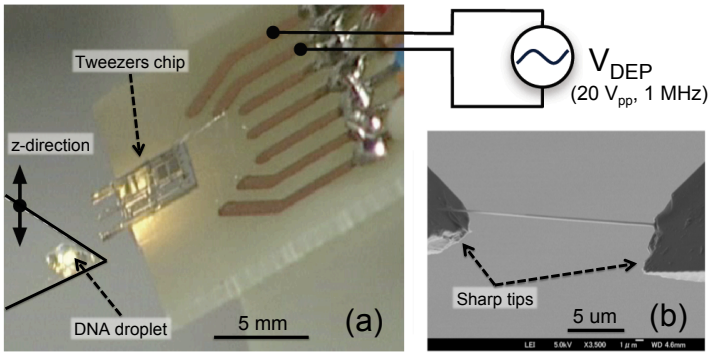

Fig. 4.3. Trapping of DNA molecules with silicon nanotweezers by dielectrophoresis. (a) An AC voltage (V_{DEP}) is applied between the 2 tips of the tweezers, in order to create a non uniform electric field in between. A cover glass on which the DNA solution droplet is deposited are moved in z-directions. (b) SEM image of trapped molecule bundle.

After dilution, a small droplet of the DNA solution is put on a glass slide. The nanotweezers are mounted on an optical microscope (Keyence VHX-500 Digital Micro-

scope) and are brought in contact with the surface of the droplet with a 3D precision micromanipulator (**Figure** 4.2).

Then, the high AC electric field, i.e. $V_{\mathrm{DEP}} = 20\ \mathrm{V_{pp}}$ at 1 MHz for a gap of 10 µm (10^6 V/m), is applied for 10 minutes (**Figure** 4.3 (a)). The DNA molecules elongate along the electric field lines, and move toward the regions where the field is stronger, i.e. precisely at the end of the sharp tips. The tips are sharpened with an anisotropic process for generating high electric field gradients and coated with aluminum to provide a substrate for strong grafting of the DNA phosphatedeoxyribose backbone to the oxidized aluminum (**Figure** 4.3 (b)).

After the experiments, the bundle can be broken and removed by blowing air and rinsing the tips with water. Also, the DEP experiment could be repeated as long as the aluminum coating remained on the silicon tips.

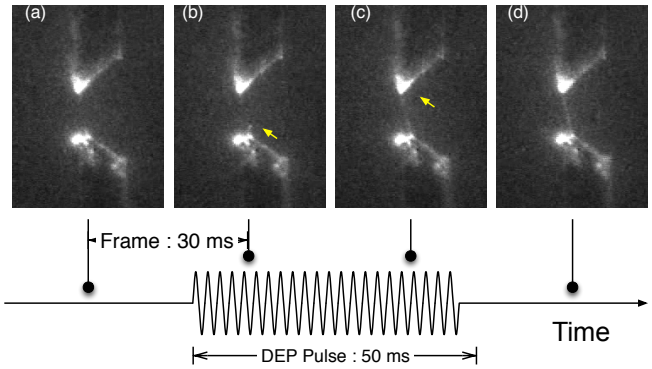

Fig. 4.4. Successive video frames captured during the trapping of a single DNA molecule with the tweezers using pulsed DEP. The arrow shows single DNA molecule elongating and finally bridging the tips [Kumemura 2011].

4.1.3 Discussion

DNA molecules are routinely trapped in between nanotweezers' tips using dielectrophoresis forces. Moreover using pulsed DEP (i.e. periodically very short duration excitation), silicon tweezers can be used to trap a single DNA molecule [Kumemura 2011]. However this method needs to deal with two principal limitations caused by the high voltage DEP signal:

1. Avoid the electrolysis of the water creating oxygen and hydrogen gas bubbles;
2. And prevent excessive heat and subsequent convection flow, under the high electric field.

Furthermore, questions about the formation of a bundle of DNA molecules need to be addressed. **Figure** 4.4 demonstrates the elongation of a single DNA molecule under electric field constraint. However in the case of a bundle of hundreds or thousands of molecules, the arrangement of the bundle needs to be studied. Are all the molecules stretched parallel, forming an equivalent stiffness which is the sum of the single molecule rigidities? This issue has not been answered during this work.

Thereafter, in order to move toward systematic bioexperiments, the trapping of DNA molecules should be integrated in an automatizable sequence of operations. During the experiment process, the handling of the biological solutions, the insertion of the tweezers tips through the liquid meniscus, and the control of the experiment conditions are the key issues to deal with. To work in optimal conditions, a new method have been developed with the design of a complementary microfluidic chip with the versatile polydimethylsiloxane (PDMS) material.

The development of a PDMS microfluidic chip is explained in **Section** 4.2. Then, biocharacterizations of molecules and reactions on DNA with tweezers are explained in **Section** 4.3 and 4.4.

4.2 Microfluidics for bioexperiments with nanotweezers

As the characterization of biological phenomena with MEMS tweezers is based on the tracking of parameters, obtaining reliable biological environment is essential for relevant and high-sensitive experiments. Experiments have firstly been performed in solution droplet (e.g. **Figure** 4.2). Despite the small size of the droplet, it represents an important volume of liquid (> 10 µL) and of molecules (which can be very expensive for some proteins as DNA drugs). Further, a small droplet of liquid (< 1 µL) is prone to quick evaporation disabling experiments with reaction time higher than a minute (which is already very fast for a biological reaction). Consequently, a complementary microfluidic device has been designed and fabricated in order to:

- Provide solutions in time: for instance DNA solution, then deionized water for washing, and a solution of proteins;
- Control of solution volumes and concentrations
  - mainly liquid evaporation concern;
- And control of the meniscus during the immersion of the tips.

4.2.1 Design of the microfluidic device

A first design of a microfluidic device in PDMS have been performed with passive microchannels and an open microchamber allowing the insertion of the tweezers' tips. However microfluidic flow control systems such as syringe, peristaltic or piston pumps are poorly adapted to the manipulation of fluid volumes in the sub-microliter range, leading in long settling times, inopportune pulses and a lack of reproducibility.

Therefore, the microfluidic device is based on the integration of an open chamber and the integration of pneumatic valves nearby the reaction chamber for fast commands of the inlets and the outlet (**Figure** 4.5).

We fabricated our valves using crossed-channel architecture [Unger 2000, Melin 2007]. The device is made of PDMS sealed layers and a glass substrate. A thin layer is produced to implement the small controllable flow channels, when a thick layer is produced for the control channels and the implementation of the open reaction chamber. The two layers are fabricated by replica molding from two masters and sealed together. The valve membranes are formed where the control and the flow channels intersect orthogonally.

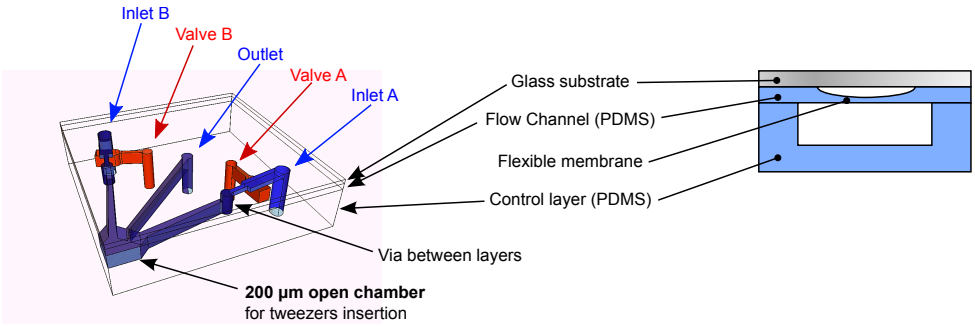

Fig. 4.5. (Left) 3-D schematic of the open microfluidic device: Flow channels and the open reaction chamber (in blue) and control channels (in red). (Right) Cross-section view of the device: A two-layer polydimethylsiloxane (PDMS) push-up microfluidic valve. An elastomeric membrane is formed where the flow channel is positioned orthogonal to the control channel directly above. Fluid flow is out of the page. Inspired from [Melin 2007].

The control layer is bonded underneath the flow layer forming push-up valves, and the flow layer is sealed with a glass slide as top layer for optical convenience.

Flow channel wafer is patterned with AZ-4903 photoresist. The resist is reflowed by thermal heating to form rounded-shape. The shape of the flow channel is consequential for proper actuation and hermetic closing of the valve. The 10 µm-thin elastomeric membrane is created above the patterns by adjusting the PDMS spin coating speed. Control channel wafer is patterned with SU-8 photoresist. Lastly a 200 µm-thick chamber is implemented to insert the 30 µm thickness of tweezer probes.

4.2.2 Working principle

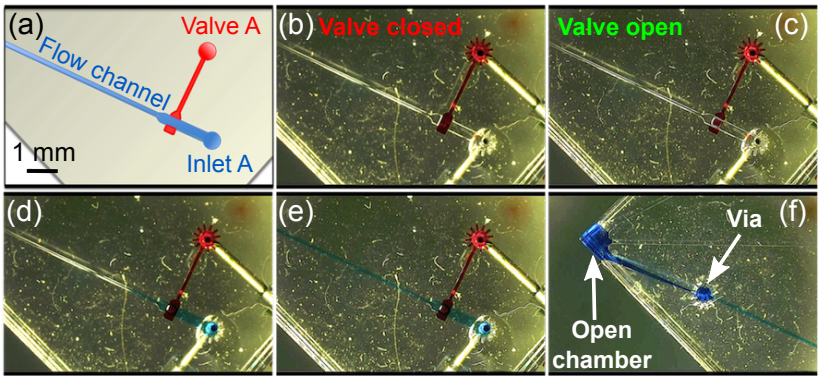

Fig. 4.6. Video sequences of the controlled filling of the reaction cavity. (a) Red channel is the membrane-valve control while blue channel is the biological solution channel. (b) Red control channel is under pressure (100 kPa) closing the valve. (c) Control pressure is released; the valve is open. (d) The pressure released; blue "biological" solution flow crossed the valve. (e) The blue "biological" solution is reaching the reaction cavity. (f) The blue "biological" solution is properly filling the open reaction cavity.

At the cross-section, channels are 600 µm-wide, making the active area 600 µm by 600 µm and determining the valve actuation pressure (100 kPa). **Figure** 4.6 is a sequence of video images showing the microfluidic in action. The red-colored liquid controls the blue-colored liquid. When pressure is applied to the lower channel, the membrane deflects upward and closes the upper channel stopping the flow. When the pressure is released, the blue liquid flows in the direction of the open chamber. Via was implemented to allow liquid transition between the flow channels and the open chamber (**Figure** 4.6 (f)).

Finally, combined with a convenient solution pressure (< 10 kPa), the response time of the device is fast enough (< 10 ms) to precisely fill the reaction chamber making it suitable for the control of the biological solutions. Furthermore, the valve stops tightly and hermetically the channel such as the open chamber does not overflow after closing the valve.

4.2.3 Discussion

Trapping of DNA have been performed once in the designed microfluidic. **Section** 4.3.2 presents results of real-time sensing of the trapping of DNA molecules. It clears the way for monitoring the formation of the DNA bundle. It enables especially the control of the bundle required for the following bioexperiments on DNA.

However, as aforementioned, the problem of the evaporation of small amount of liquid is complicated to tackle. Trying to compensate the evaporation rate with proper filling of the chamber is too complicated to achieve, and leads to stochastic movement of the meniscus. The microfluidic will be updated in order to deal with this concern. Two solutions have been considered:

1. Integrate a reservoir with a larger opening to the air such as the interface meniscus will preferably recede at that opening. At the tweezers' interface the meniscus will not move at the micro-scale. The evaporation in the reservoir can be compensated with proper filling.
2. Close the microfluidic with a special packaging of the tweezers' chip.

The first solution has been experimented showing first promising results. During one hour, meniscus at the tweezers' interface did not move while at the larger interface the meniscus receded. However the design needs to fulfill the specification of using a minimum amount of solution. The second solution was not tested but is in action. Its complexity makes it long to implement and experiment.

At last, another concern is to deal with the propensity of the DNA molecules and proteins to attach on surfaces. For this purpose, we coated the microfluidic walls with MPC polymers (2-methacryloyloxyethyl phosphorylcholine, also known as Lipidure®), flowing MPC solution inside the device before experiments. All the surfaces are occupied by MPC polymers preventing afterwards attachment of DNA or proteins.

4.3 Characterization of DNA molecules

In **Chapter** 3, **Section** 3.4, we described the method to characterize the mechanical parameters of the system. Basically the resonance of the system is measured, and changes

are perceived when conditions are changing. **Figure** 4.7 shows the equivalent model of the system when DNA molecules are trapped in between the tweezers' tips. One tip of the tweezers is actuated conducting to the mechanical stretching (< 30 nm) of the DNA molecules. The equivalent elastic stiffness and viscous damping of the molecule bundle (i.e. Kelvin-Voigt model) change as well as the resonance of the system.

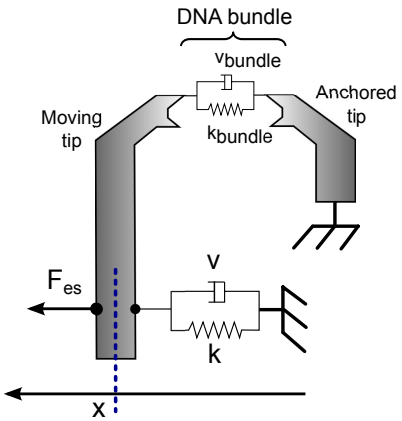

Fig. 4.7. Equivalent dynamic model of the silicon nanotweezers. DNA molecules are represented by a purely viscous damper and purely elastic spring connected in parallel (Kelvin-Voigt model).

4.3.1 Characterizations of DNA bundle

Figure 4.8 demonstrates the changes of the resonance response because of the DNA bundle characteristics. In black, the bare tweezers resonates at 2565 Hz (Tweezers A2). Respectively after two different trappings by DEP, the resonance frequency of the systems increased to 2765 Hz and 3340 Hz. In accordance the quality factor is about 65 for the bare tweezers and respectively 56 and 17 for both measurements with DNA. The two experiments were conducted with the same tweezers; the first bundle was removed before the second trapping.

The first bundle is smaller than the second one, i.e. it contains less molecules of DNA. The trapping were performed with two different DEP durations. For the thicker bundle, the DEP voltage was applied during 20 min, twice the regular duration used for the thin bundle (10 min). The number of molecules in the bundles are not known since the experiments are performed in air. The rigidity of molecules are much higher in air than in solutions.

From [Bustamante 2003] (and the force-extension plot of the paper), we can deduce the stiffness of a single λ-DNA molecule (i.e. 48.5 kbp) to approximatively 30×10^{-6} N/m in solution. Accordingly, the number of molecules in the bundle is presumed and monitored after trapping or during experiments performing measurement in solution.

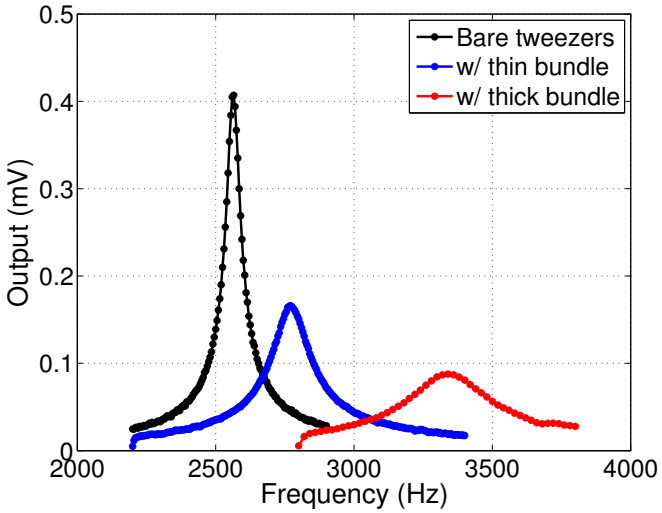

Fig. 4.8. Characterizations of DNA molecule bundle through frequency response of the silicon nanotweezers, in air at atmospheric pressure. Frequency response is measured with the lock-in amplifier. A clear increase of the resonant frequency, together with a decrease of the Q factor, could be observed after DNA trappings [Yamahata 2008a]. (Tweezers A2 with I/V preamplifier gain set at 10^7).

4.3.2 Characterizations of the trapping of DNA molecules

Despite previous measurements, the interest of the method arises from the characterizations of DNA in biological conditions. Hereafter we demonstrated the real-time monitoring of the trapping of DNA molecules.

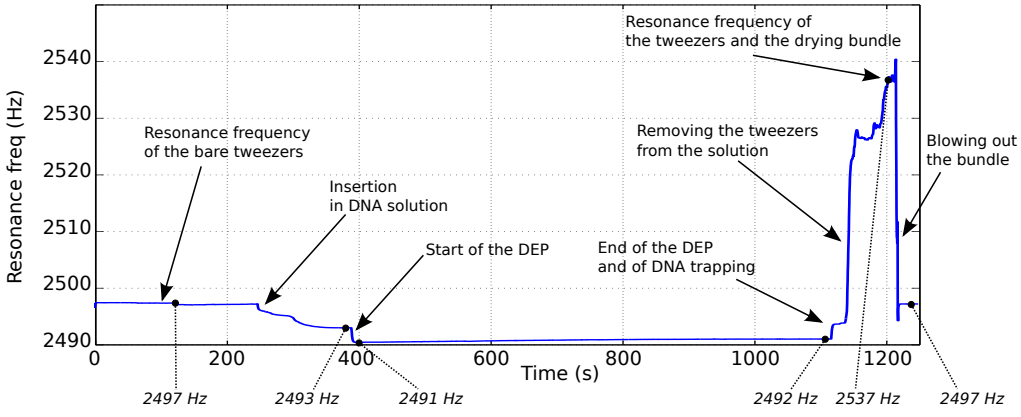

Fig. 4.9. Real-time monitoring of the DNA trapping experiment. The resonance frequency of the tweezers is monitored during all the trapping experiment. The different steps of the experiment are sensed and spotted. (Tweezers JST26).

Trapping experiment

Figure 4.9 shows the monitoring of the resonance frequency of the system during the 21 minutes of the trapping experiment. At the start, the resonance frequency of the device (Tweezers JST26) is approximatively 2497.4 Hz in the air. After insertion of the tip in DNA solution, it decreased to about 2493 Hz (effect already described in **Section** 3.4.3.2). Then, at $t = 400$ s, after application of the DEP voltage (10 V_{pp} at 1 MHz), the resonance frequency decreased again to 2491 Hz. This effect is repeatable and subsequently expected, but its origin is not understood.

After 10 minutes of trapping, the DEP voltage is stopped and the tips are removed from the solution. The resonance frequency of the system increased because of the presence of a bundle of DNA and continues to increase with the probable drying of the bundle. A microscope visualization confirms that a DNA bundle has been trapped in between the two tips.

Finally after blowing out the bundle, the tweezers recover the initial resonance characteristic at 2497.4 Hz.

Characterization of the trapping

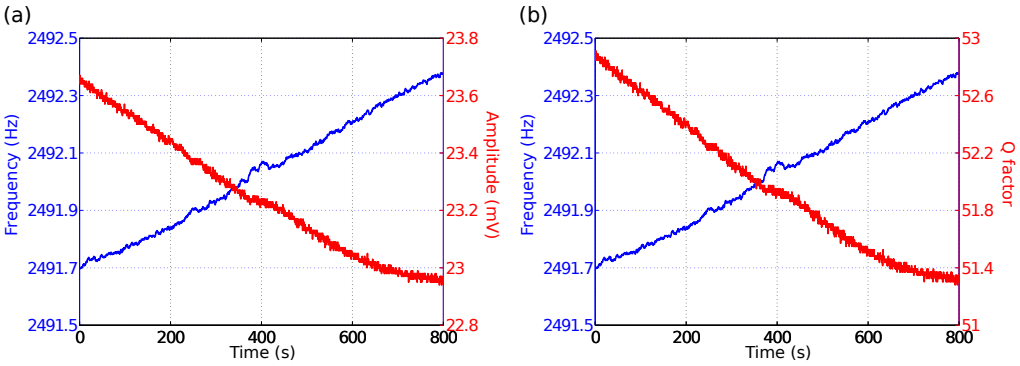

Fig. 4.10. Real-time monitoring of the trapping of DNA molecules. (a) Tweezers + λ-DNA bundle resonance frequency and amplitude are plotted as a function of DEP time. (b) The resonance frequency is plotted with the equivalent quality factor. (Tweezers JST26).

Figure 4.10 focus on the resonance characteristics (frequency and amplitude) during the DEP time. As trapping proceeds and as intended, the resonance frequency increases due to the addition of the rigidity of the DNA bundle k_{bundle}. At the same time, Q tends to decrease as the viscous losses due to the bundle increase.

4.3.3 Discussion

From the evolution of the resonance response and the model of the bare tweezers (for which parameters have been identified and are reported in **Table** 4.1), the characteristics of the bundle are monitored in real-time during the trapping. Therefore, the time evolutions of the bundle rigidity and viscosity can be deduced from the resonance through the **Equations** 4.1 and 4.2:

$$f_r = \frac{1}{2\pi}\sqrt{\frac{(k_{tw}+k_{bundle})}{M} - \frac{1}{2}\frac{(\nu+\nu_{bundle})^2}{M^2}} \simeq \frac{1}{2\pi}\sqrt{\frac{k_{tw}+k_{bundle}}{M}} \tag{4.1}$$

$$Q = \frac{\sqrt{(k_{tw}+k_{bundle})M}}{\nu+\nu_{bundle}} \simeq \frac{\sqrt{k_{tw}M}}{\nu+\nu_{bundle}} \tag{4.2}$$

where k_{bundle} is the equivalent stiffness of the bundle and ν_{bundle} the equivalent viscosity due to losses. **Equation** 4.1 can be approximated since on the one hand $\frac{k}{M}$ term is 10^5 times higher than $\frac{\nu^2}{M^2}$ term, and on the other hand $\frac{\partial f_r}{\partial k} \times \Delta k$ sensitivity is 10^6 times more important than $\frac{\partial f_r}{\partial \nu} \times \Delta \nu$ (for same relative variations of k_{tw} and ν from their initial values, see **Table** 4.1). **Equation** 4.2 is approximated through experience, for instance data from **Figures** 4.10 and 4.11). After processing of the data, the variation of the parameter ν_{bundle} is more consequent than the stiffness parameter k_{bundle}.

Figure 4.11 shows the increase of the stiffness and of the viscous losses in the bundle during trapping. However, after $t = 400$ s, both curves do not follow anymore the same evolution, though the experimental conditions were adequate with especially a stable meniscus around the tweezers' tips during the 10 minute of DEP.

This raises the question of the bundle formation. At the beginning, it is probable that DNA molecules elongate completely in between the tips adding their single mechanical characteristics. Afterwards, with the formation of the bundle, molecules may come to attach the bundle without bridging entirely the opposite tips. In this case, the model is more complex than the simple addition of characteristics.

Characteristics	Parameters	Experimental values
Stiffness	k_{tw} (N/m)	46.8
Viscosity	ν (N.s/m)	56.2×10^{-6}
Mass	M (kg)	190×10^{-9}
Resonant frequency	f_r (Hz)	2497
Quality factor	Q	53

Table 4.1. Table of the identified parameters of the tweezers JST26.

In this experiment, precise frequency measurements allow the sensing of 10×10^{-3} Hz shifts. Knowing the single molecule rigidity (30×10^{-6} N/m), **Figure** 4.12 shows the number of trapped molecules, deduced from the stiffness evolution. Focusing on the first 300 seconds, the trapping rate is then about 0.9 molecule/second.

In conclusion, these achievements demonstrate the possibility:

- To control the trapping of DNA molecules for coming bioexperiments on DNA;
- To characterize the formation of DNA bundle by dielectrophoresis.

This last point needs to be improved for the coming bioexperiments on the bundle. Indeed, besides the monitoring of the bundle features, a good modeling of the molecule arrangement is a fundamental concern to answer how bioreactions can occur.

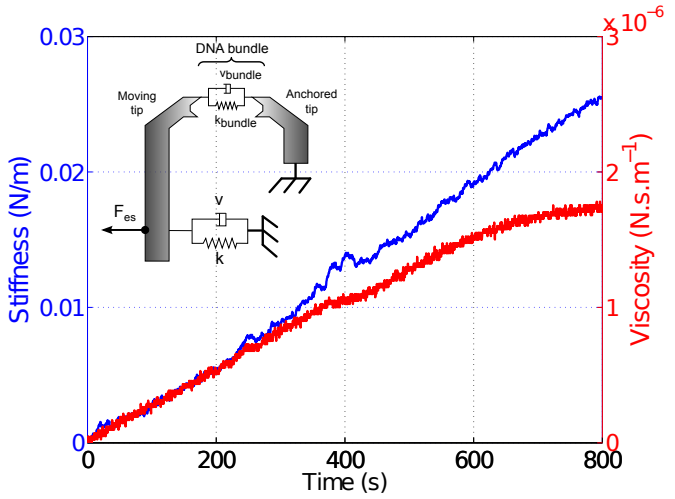

Fig. 4.11. Bundle rheological model evolution during trapping. Stiffness and viscosity are deduced from the model of the bare tweezers and **Equations** 4.1 and 4.2.

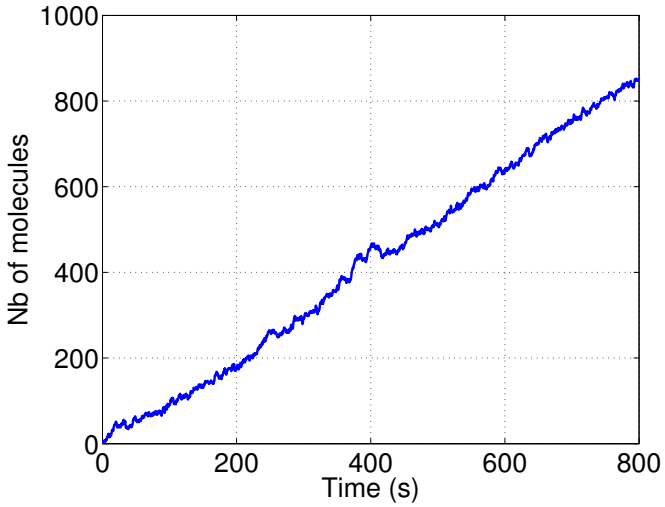

Fig. 4.12. Evolution of trapped λ-DNA molecules during DEP time. Number of trapped molecules is deduced from bundle rheological model and the single molecule rigidity 30×10^{-6} N/m.

4.4 Characterizations of bioreactions on DNA

After the trapping of DNA molecules, here is described the method for the kinetic characterization of bioreactions on DNA with silicon tweezers. Two experiments have been performed with two types of molecules and two types of interactions with DNA. Firstly are reported experiments with *Hin*dIII restriction enzymes which have the ability to cut DNA at specific recognition nucleotide sequences. Secondly experiments with Ethidium Bromide molecules are described. Ethidium Bromide is an intercalating agent commonly used as a fluorescent tag to detect nuclear acids in molecular biology.

4.4.1 With restriction enzymes (*Hin*dIII)

*Hin*dIII is a type II site-specific deoxyribonuclease restriction enzyme that cleaves the double stranded DNA (dsDNA) at a specific nucleotide sequence (i.e. AAGCTT for *Hin*dIII). These enzymes play an important role in bacteria protection against viruses : they destroy viral DNA by cutting it in specific sites, preventing insertion and transcription in bacterial DNA. They are widely used by biologists and biochemists for several applications [Pingoud 2001, Roberts 2005].

In this new development, we immersed a trapped DNA bundle in a solution containing *Hin*dIII. The goal is to characterize the kinetic of the interactions between the restriction enzymes and the DNA molecules. We presume to sense in real-time the digestion of the bundle by monitoring the decrease of the mechanical parameters of the bundle.

4.4.1.1 Materials and methods

*Hin*dIII was purchased from New England BioLabs Inc (`http://www.neb.com`). *Hin*dIII was dissolved with appropriate buffer solution, and diluted with deionized water. The *Hin*dIII restriction enzyme cuts (digests) λ-DNA in 7 restriction sites per molecule.

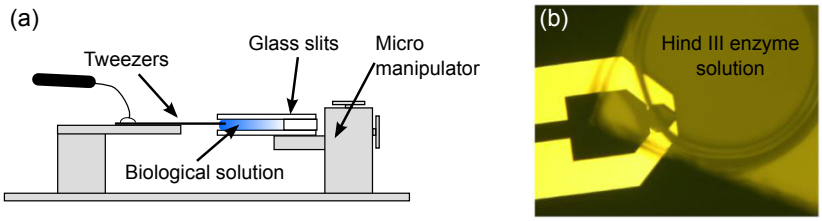

Fig. 4.13. Experimental setup of the bioreaction experiment with *Hin*dIII enzymes. (a) Schematic of the setup (side view). Tweezers are immersed inside a slit made of glass slits and containing the enzyme solution. (b) Microscopy photography of the tweezers tips inside the experimental slit and inside the enzyme solution.

In the first step, DNA bundle is trapped by dielectrophoresis as previously described. The tweezers tips are brought to the surface of the DNA solution (droplet) on a cover slip and an AC voltage is applied between the tips (1 MHz, 20 V_{PP}) during 10 minutes (**Figures** 4.2 and 4.3).

Next, *Hin*dIII solution is pipetted in a reaction cell made from a pair of cover slips with a 300 µm gap. The probes of MEMS tweezers with trapped DNA bundle are introduced into the reaction cell from the open side with a micromanipulator (**Figure** 4.13).

The bundle digestion was measured in the real-time through frequency response of the tweezers + DNA system. Frequency response of the system is continuously recorded by frequency span with 20 s-time resolution. The resonance frequency and the quality factor are extracted by identification with a damped resonator model. (The PLL algorithm was not used for this experiment.)

4.4.1.2 Results

Figure 4.14 shows the frequency response of MEMS tweezers at the beginning and at the end of the DNA digestion. As digestion proceeds, f_r decreases due to the reduction of the stiffness of the attached bundle. Simultaneously, Q is increasing as the viscous losses in the bundle are reduced with the decreasing bundle cross section. Extraction using the damp resonator model allowed good precision measurement with 0.06 Hz and 0.15 resolutions for respectively the resonance frequency and the Q factor.

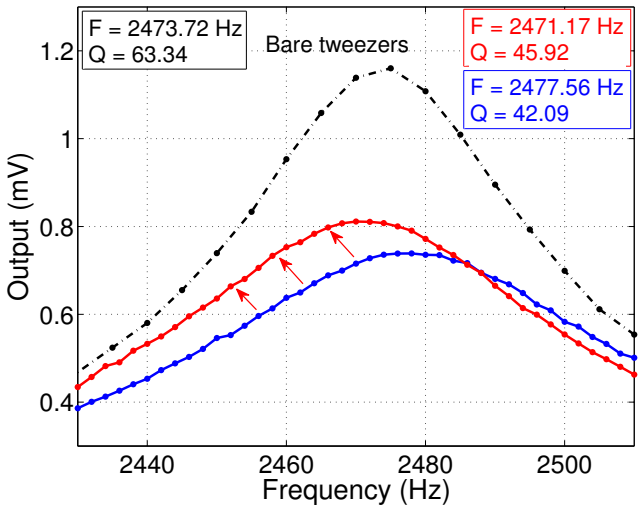

Fig. 4.14. Tweezers frequency response in solution, before and after *Hin*dIII experiment. (Blue) with bundle; (red) without bundle at the end of the experiment. (Black) bare tweezers for comparison (without bundle and in air). (Tweezers JST26).

Figure 4.15 shows the resonance frequency and Q variation for the complete biomolecular reaction continuously monitored for 1 hour. The curves are compared with control experiments (without enzyme and without DNA) for sake of validation. In addition, the complete digestion was confirmed by visual observation. i.e. at the end of the experiment, no DNA molecule bridged the tips.

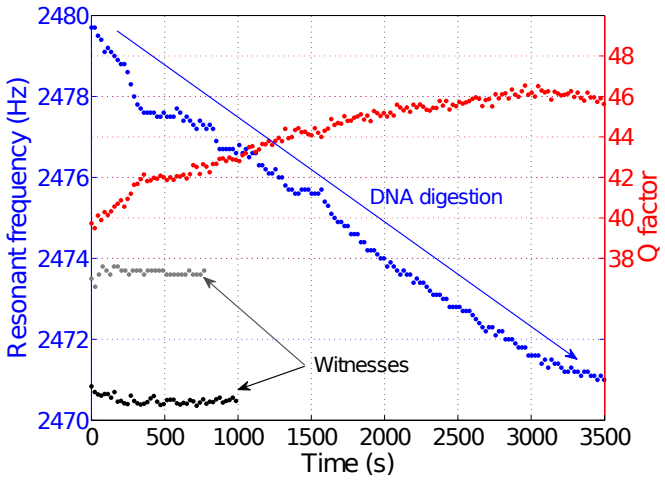

Fig. 4.15. Tweezers + DNA bundle resonance frequency and quality factor vs. digestion time in *Hin*dIII solution. Responses in solutions without *Hin*dIII enzymes are also plotted for control. In gray, tweezers + DNA in buffer. In black, bare tweezers in buffer. (Tweezers JST26).

4.4.1.3 Discussion

The Kevin-Voigt viscoelastic model for the bundle was used and shows that both stiffness and viscosity components decrease as the digestion progresses (**Figure** H.9). Finally the effect of concentration of *Hin*dIII on the digestion dynamics was also examined.

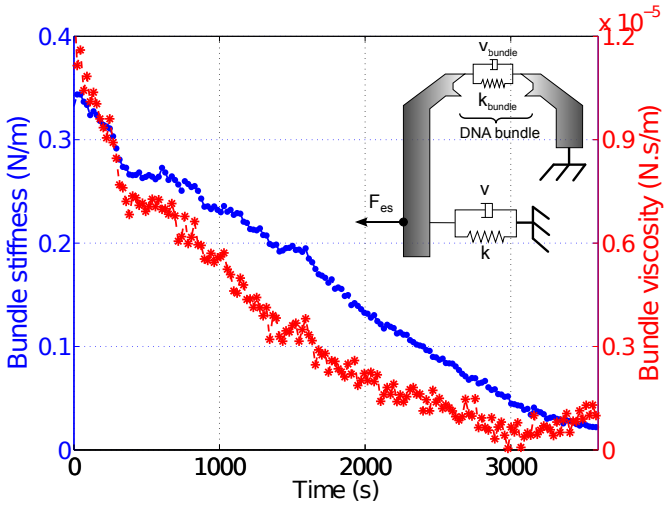

Fig. 4.16. Bundle rheological model, stiffness and viscosity evolution during digestion.

Figure 4.17 shows the time variation of the calculated number of DNA in the bundle for three different concentrations. The number of molecules is extrapolated from the

extracted bundle stiffness divided by the single λ-DNA rigidity (30×10^{-6} N/m). The number of molecules, normalized by the initial one, shows an exponential decay with time. The identified time constant is inversely proportional to the enzyme concentration (especially for thin bundles and high concentration).

This behavior follows the Langmuir binding kinetic model [Bunimovich 2006] when the number of unoccupied binding sites is proportional to the remaining DNA. This is reasonable as the binding sites do not remain occupied by the enzyme, DNA is digested and new sites are always exposed.

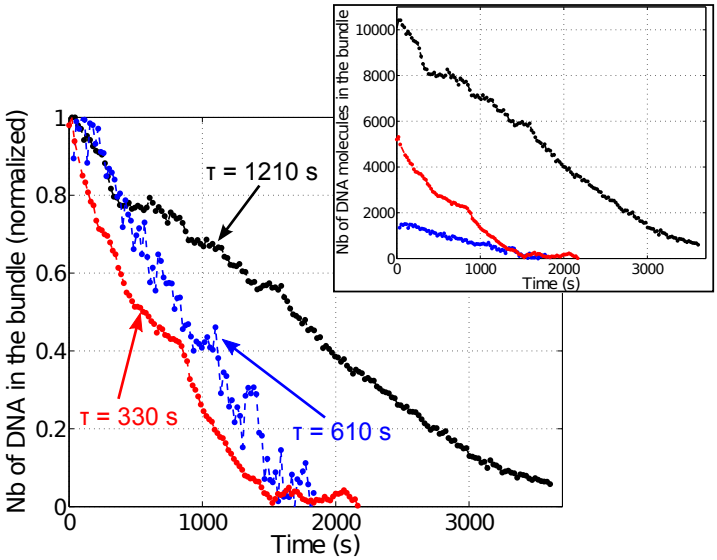

Fig. 4.17. Effect of *Hin*dIII concentration on DNA bundle digestion. Evolution of the normalized number of molecule with time for 3 different *Hin*dIII dilution. Insert: Unnormalized values for the 3 different experiments.

4.4.2 With intercalating agents (Ethidium Bromide)

Hereafter, experiments with Ethidium Bromide molecules are described. Ethidium Bromide (EtBr) is an intercalating agents commonly used as a fluorescent tag to detect nuclear acids in molecular biology. Such type of intercalation reactions can interfere with biochemical processes involving protein-DNA contacts such as recombination, replication and gene expression and can induce mutagen cells. Several studies have been carried out to determine molecule binding properties [Vladescu 2007] as well as to develop DNA drugs to prevent mutagen cell proliferation [Hurley 2002].

Because it inserts itself between the strands of dsDNA and deforms its structure, we presume that the interactions would change the mechanical characteristics of the DNA bundle.

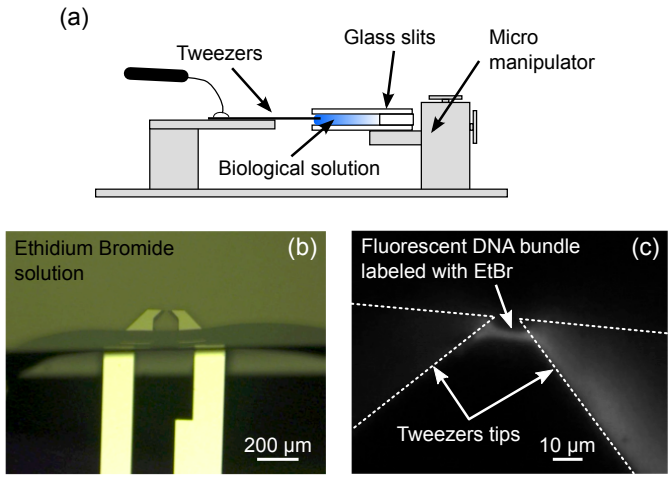

Fig. 4.18. Experimental setup of the bioreaction experiment with Ethidium Bromide proteins. (a) Schematic of the setup (side view). Tweezers are immersed inside a slit made of glass slits and containing the protein solution. (b) Microscopy photography of the immersed tweezers into Ethidium Bromide solution (top view). (c) DNA bundle examined by fluorescence microscopy.

4.4.2.1 Materials and methods

Ethidium bromide (EtBr) is purchased from GE Healthcare Biosciences (http://www.gelifesciences.com). The solution was simply diluted with deionized water and used in this experiment at two different concentrations (2.5 and 250 µM).

Likewise for *Hin*dIII experiments, DNA molecules are firstly trapped. The tweezers tips are brought to the surface of the DNA solution (droplet) on a cover slip and an AC voltage is applied between the tips (1 MHz, 20 V_{PP}) during 10 minutes (**Figures** 4.2 and 4.3). Afterwards EtBr solution is pipetted in a slit made from a pair of glass slips with a 300 µm gap. The probes of MEMS tweezers with trapped DNA bundle are introduced into the reaction cell from the open side with micromanipulator (**Figure** 4.18).

The resonance characteristics (the frequency and the amplitude) of the system are continuously recorded using PLL algorithm with 0.6 s-time resolution.

4.4.2.2 Results

From the immersion start and as the binding of molecules proceeds in the DNA bundle, the resonance frequency increases (**Figure** 4.19), and the Q factor decreases. Besides witness curves are plotted showing no reaction in absence of active molecules.

Blue, red and green curves have been recorded with the same trapped bundle (**Figure** 4.19). For the witnesses, the bundle were immersed in DI water with the same previously described experimental procedure. At the end of the EtBr experiment, the fluorescence of the bundle is checked in order to confirm the effective binding of EtBr on DNA molecules (**Figure** 4.18(c)). Precise measurements allowed the precise sensing of 10×10^{-3} Hz frequency shifts.

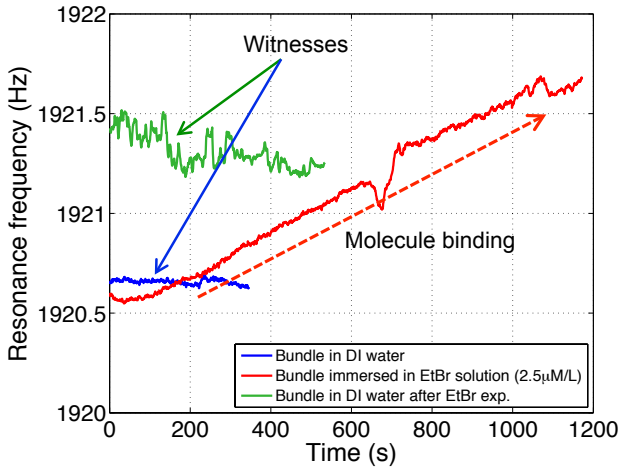

Fig. 4.19. Tweezers + bundle resonance frequency vs. time in Ethidium Bromide solution (2.5 μM concentration) in red. (In blue) the resonance frequency of the tweezers + bundle in DI water before the EtBr experiment; (in green) after the EtBr experiment (witnesses). (Tweezers RV12).

4.4.2.3 Discussion

In previous works, especially reported in [Vladescu 2007], the effect of EtBr was studied on the effective extension of DNA due to the intercalations of molecules. Though the deformation at different ligand concentrations was proven through measurements of the needed forces to extend denatured DNA, the reaction kinetic was not demonstrated. Our approach enables the time characterizations of bioreactions. However the method differs since several single molecules are trapped in between the probes.

To prove the real sensing of the molecule bindings as well as previously reported DNA digestion, we experimented with two different EtBr concentrations (2.5 μM and 250 μM). The corresponding Kevin-Voigt viscoelastic models for the bundle was identified and both stiffness and viscosity components show a similar increase (**Figure** 4.20).

Conversely, the stiffness and losses increase with the intercalation of molecules inside the bundle. Both curves show a similar temporal evolution of the bundle properties with the binding of molecules. However, close-up view on the kinetics shows a rising time independent to the ligand concentration (**Figure** 4.21).

This raises the question of the effect of molecule intercalation on the mechanical properties of the bundle. In [Rocha 2007], the authors demonstrate that for low drug concentrations, drug intercalation in the DNA molecule increases the rigidity of the complex. This is consistent with the prediction that molecule intercalation stabilizes the DNA double helix. They have performed melting experiments with various EtBr concentrations, from 0 to 2.5 μM. For high drug concentrations, they showed that

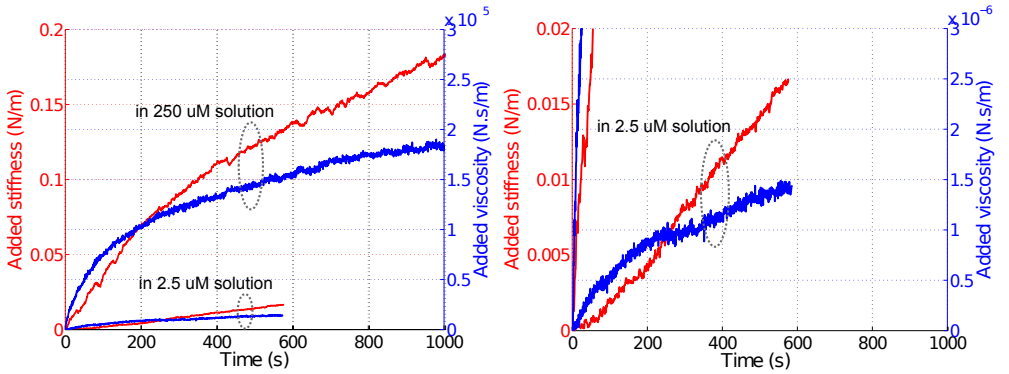

Fig. 4.20. Evolutions of the bundle stiffness (in red) and viscosity (in blue) during molecule binding on the DNA. Experiments were performed with 2 different concentrations (2.5 µM and 250 µM EtBr concentrations).

the persistence length[2] of the complexes decays abruptly and remains constant in the concentration range studied.

In our experiment, we probably experimented at very high concentrations. However, more data under a variety of solution conditions are needed to examine and better quantify this effect. Besides, better understanding of the bundle architecture is required to understand the diffusion of the intercalators in the bundle.

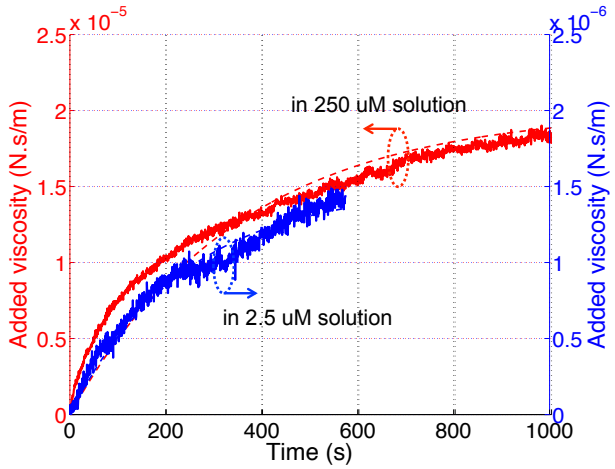

Fig. 4.21. Kinetic characterization of the 2 reactions. Results on viscosity evolution show similar time constant, independently to ligand concentration.

[2] The persistence length is a basic mechanical property quantifying the stiffness of a polymer. See [Bouchiat 1999] for "Estimating the Persistence Length of a Worm-Like Chain Molecule from Force-Extension Measurements."

4.5 MEMS tweezers, a biomolecular tool for routine analysis

In this **Chapter**, the features of silicon nanotweezers for bioexperiments on DNA have been demonstrated through:

1. Routine trapping of DNA molecules;
2. Control of the trapping;
3. And real-time monitoring of bioreactions on DNA bundle.

Results with two different molecules with two different interaction modes with DNA demonstrate the possibilities for systematic characterization of reactions on DNA. We would like to move further with the EtBr molecule experiment, so that such way of characterizations can, for example, ease fast development of drugs, as DNA drugs regularly use same mechanics to impede mutagen cell proliferation.

Furthermore, a complementary microfluidic device has been designed and fabricated for pertinent experiments at the molecular level.

However, the resolution of the reported experiments (DNA trapping control, DNA digestion with *Hin*dIII or DNA binding with Ethidium Bromide) does not allow to sense reaction at the single molecule level.

Several issues need to be answered to enhance the analysis with MEMS tweezers:

1. The understanding of the bundle formation;
2. The subsequent model of DNA bundle and of the reactions on such bundle of molecules;
3. The improvement of the resolution of the measurements, in order to compete with optical tweezers and magnetic tweezers.

5

Feedback approach

Contents

Summary. In this **Chapter**, we present an improvement of the parameter sensitivity of silicon nanotweezers used in biomolecule sensing with the help of closed-loop control technique.

In **Chapter** 3, the direct manipulation of molecules with sensor-integrated MEMS tools was introduced for systematic and real-time biological analysis at the molecular level. However, bio-experiments with nanotweezers showed a maximal resolution of about tenth of λ-DNA molecules (cf. **Chapter** 4), which is still under the sensitivity of magnetic or optical tweezers. Accordingly, based on the implementation of a real-time feedback control, we show that it is possible to increase the sensitivity of the controlled nanotweezers for biological parameter detection of DNA molecules.

5.1 Introduction to control technology for microsystems

The first example of MEMS device involved in a closed-loop system is MEMS accelerometers which have been used to sense and decide when to fire the car airbags. Besides, with the development of MEMS technologies and with the aim of developing applications and subsequent markets, control strategies are now thought and adopted towards micromachines, as macro-scale machines intended.

The main interest of control in nanotechnologies seems to arise from nano-positioning concerns [Devasia 2007]. Nano-positioning involves displacement with high resolution and accuracy, manipulation of object, and component assembly. It requires the fulfillment of specifications such as accuracy and high speed operations. They are mostly similar to those that are usually asked to address in macro-system concerns. Many works have been done for nanopositioning [Croft 1999, Schitter 2001, Stemmer 2005, Rifai 2007, Leang 2007] and on precise and fast scanning with AFM [Salapaka 2002, Fleming 2003, Salapaka 2005]. A first attempt to apply it at consumer level can be found in HDD applications [Hosaka 2001].

[Humphris 2000] reports interesting achievement in the sensitivity enhancement of an Atomic Force Microscope. AFM usually shows resolution of the order of fractions of a nanometer for surface topography, taking advantage of high frequency vibration modes ($>$ 100 kHz) and very high resonance quality factor (over 10^4) in high-vaccuum conditions [Dubourg 2003]. However, the complete immersion of the AFM cantilever in liquid environment leads to a drastic decrease of the resonance quality factor under 10, and of the measurement resolution. Thereby, the authors have demonstrated the effective implementation of a **positive feedback**[1] system able to increase the quality factor by 2 orders of magnitude (over 300) in a liquid environment.

[Soen 2007] developed a control strategy of a closed-loop micromachined accelerometer for an enhancement of the sensor sensitivity over the open loop driven system. Acceleration sensing with microsystems is commonly based on the sensing of a mass displacement thank to a capacitive sensor. These accelerometers deal with the sensing sensitivity and the maximum displacement before signal distortion which are both related to mechanical stiffness and the capacitance gaps but in an opposite way. This work provides a solution through the design of a closed-loop system using electrostatic feedback actuation for maintaining the mass position at 0. Thus the acceleration sensing is given by the control signal. The same group developed a robust digital control for tunneling current measurement system [Ahmad 2012].

Our original idea was to *change* the parameters of our system to make it more appropriate for the sensing of the mechanical characteristics of DNA molecules. As reported in **Chapter** 2, optical and magnetic tweezers show performances that allow the sensing of events on a single DNA molecule. Accordingly most of the studies on single molecules use AFM, optical or magnetic tweezers.

The idea of using a feedback approach to emulate a stiffness modification arises from the mechanical characteristics of the device. As aforementioned in **Chapter** 3, a minimum mechanical rigidity force is required to survive the fabrication processes, in order to support the system weight and to prevent attractive and sticking surface forces in the comb-drive actuator and the capacitive sensor. The stiffness of the silicon nanotweezers (i.e. 50 N/m) is about 10^6 higher than the equivalent stiffness of the optical and magnetic tweezers (see **Table** 2.1, **Page** 15) and of the λ-DNA molecules (i.e. 30 mN/m). This requires a drastic resolution of the measurements for the sensing of the number of molecules in the bundle for example.

[1] Positive feedback in biology: Lactation involves positive feedback in that the more the baby suckles, the more milk is produced, via a surge in prolactin secretion.

5.2 Improvement of the parametric sensitivity by a feedback approach

The design of the nanotweezers has consisted in the integration of all the features for a complete system. Actuation, sensing and tips for the prehension of biomolecules have been designed on a single millimetric die of silicon, leading to a complex mechanical structure (**Figure** 3.3, **Page** 24). A detailed model of the device is quite complicated to obtain considering the complexity of the suspension system, the nonlinearities and the distributed aspect of the involved phenomena.

Consequently, in what follows we are going to use a simplified model (linear) to implement our control strategy. This simplified model is derived to capture the main dynamic properties of the nanotweezers.

5.2.1 Dynamic modeling

As a first approximation, by neglecting the spatially distributed nature of the tip, the system can be represented by an equivalent mass-spring-damper system shown in Figure 5.1 where k represents the sum of stiffness of the suspensions according to **Equation** 3.8 (**Page** 25).

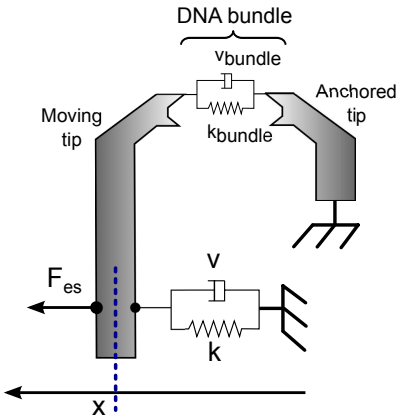

Fig. 5.1. Equivalent dynamic model of the silicon nanotweezers. DNA molecules are represented by a pure viscous damper and pure elastic spring connected in parallel (Kelvin-Voigt model). (2)

From Newton's second law we can write:

$$M\frac{d^2x}{dt^2} + (\nu + \nu_{bundle}(t))\frac{dx}{dt} + (k + k_{\text{bundle}}(t))\,x = F_{es} \tag{5.1}$$

where M is the mass of the movable part of the device, ν is the equivalent viscosity of the system, k is the stiffness of the suspensions and F_{es} is the electrostatic force applied

to the tip through the comb-drive actuator ($\propto V^2$) according to **Equation** 3.2 (**Page** 22). This is a second order system of resonant frequency f_r and quality factor Q defined by:

$$f_\mathrm{r} = \frac{1}{2\pi}\sqrt{\frac{k + k_\mathrm{bundle}\,(t)}{M} - \frac{1}{2}\frac{(\nu + \nu_{bundle}\,(t))^2}{M^2}} \tag{5.2}$$

$$Q = \frac{\sqrt{(k + k_\mathrm{bundle}\,(t)) \times M}}{\nu + \nu_{bundle}\,(t)} \tag{5.3}$$

Equation 5.1 is recasted under equivalent controllable canonical state space representation (A, B, C) where $A \in \mathbb{R}^2, B \in \mathbb{R}^{(2,1)}, C \in \mathbb{R}^{(1,2)}$ and X is the state vector (displacement & velocity) $X = \begin{pmatrix} x \\ \dot{x} \end{pmatrix}$.

$$\dot{X} = \underbrace{\begin{bmatrix} 0 & 1 \\ -\dfrac{(k + k_\mathrm{bundle}\,(t))}{M} & -\dfrac{(\nu + \nu_{bundle})}{M} \end{bmatrix}}_{A} X + \underbrace{\begin{bmatrix} 0 \\ \dfrac{1}{M} \end{bmatrix}}_{B} F_{es} \tag{5.4}$$

And

$$y = \underbrace{\begin{bmatrix} 1 & 0 \end{bmatrix}}_{C} X \tag{5.5}$$

when the displacement is measured with the interferometer, or

$$y = \underbrace{\begin{bmatrix} 0 & 1 \end{bmatrix}}_{C} X \tag{5.6}$$

when the velocity is measured with the integrated capacitive sensor.

Identification

For the design and the development of the feedback controller, the model of the device is identified at an operating point. The parameters of the system are identified through 40 nm step responses around 260 nm offset. The identification is achieved through standard recursive approach by using least square method. Identified model parameters are summarized in **Table** 5.1.

Mechanical parameters	
M (kg)	280×10^{-9}
k (N/m)	47.8
ν (N.s/m)	48×10^{-6}
Comb-drive actuator	
α_es $\left(\mathrm{N/V^2}\right)$	30.5×10^{-9}

Table 5.1. Numerical values of the identified model parameters.

The identified parameters are quite different from the ones computed from theoretical dimensions. Indeed differences have been pointed out between the theoretical and the "real" geometrical dimensions of the device after fabrication, leading to important parameter uncertainties. Tiny structures as mechanical suspensions are more delicate to overetching, changing significantly related parameters as device stiffness.

5.2.2 Feedback approach

5.2.2.1 Parameter sensitivity

As previously discussed, the aim is to improve the sensitivity of the device to the mechanical rigidity of DNA molecules. The resolution of the measurements is of particular importance to performing relevant biosensing with silicon nanotweezers. In **Chapter** 4, we demonstrated an appropriate sensing of the DNA mechanical properties through the monitoring of the resonance characteristics with a minimum detectable frequency shifts of 10 mHz. Our original idea is to change the resonance parameters of our system in order to enhance the frequency shifts when the bundle changes.

Therefore, the minimum change in DNA molecules numbers that can be sensed is related to the sensitivity of the tweezers, that is to say $\partial f_\mathrm{r}/\partial k$ (coming from **Equation** 5.2):

$$\frac{\partial f_\mathrm{r}}{\partial k} = \frac{1}{2\pi} \frac{1}{2M\sqrt{\dfrac{k}{M} - \dfrac{1}{2}\dfrac{\nu^2}{M^2}}} = \frac{1}{8\pi^2 M f_\mathrm{r}} \tag{5.7}$$

It appears that for a given stiffness variation (associated with a given DNA bundle stiffness variation) the variation of f_r is even more pronounced when f_r is small. Accordingly the control strategy will be to reduce the resonant frequency of the closed-loop system. This is the opposite strategy used for mass detection. Usually for measurement with micro-cantilever, the higher modes of vibration are chosen in order to increase mass sensitivity [Dohn 2005, Ghatkesar 2007].

Consequently, sensitivity to stiffness variation can be enhanced by designing a low resonant frequency sensor. However, since it remains problematic to design and fabricate new MEMS device with very low stiffness ($\ll 1$ N/m), we propose to emulate such a compliant system using a closed-loop control strategy.

5.2.2.2 Control strategy

Hereafter, we propose a control strategy using state feedback eigenstructure assignment. The closed-loop resonance frequency is assigned through a complete pole placement. The main drawback of such a control strategy is that it requires to implement an observer to reconstruct the system state vector.

Figure 5.2 illustrates the control strategy as it will be simulated and experimentally implemented. Furthermore in our configuration the observer has to preserve the closed-loop parametric sensitivity and must not amplify too much the measurement noises.

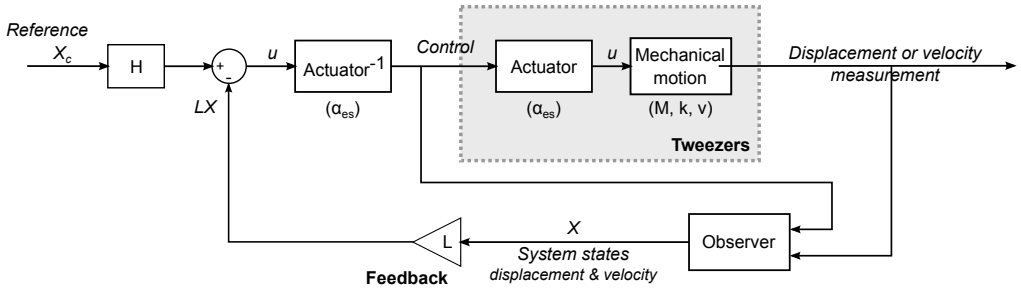

Fig. 5.2. Feedback control scheme. For the implementation of the state feedback L, a state observer is required in order to provide an estimate of the system state. The sensor provides only one measurement at a time, the displacement or the velocity. Moreover, as the actuator of the device obey to a non-linear square equation, the reciprocal function transfer (Actuator^{-1}) is implemented to linearize the control.

5.2.2.3 Eigenstructure assignment using state feedback

Let us now consider the system under its controllable canonical state space representation (A, B, C) given by **Equations** 5.4 and 5.5. The state feedback $L = [l_1\, l_2] \in \mathbb{R}^{(1,2)}$ and the feedforward $H \in \mathbb{R}$ are designed to assign the desired closed-loop poles and to ensure unitary static gain. They are implemented such that $u = Hx_c - LX$. One can write the closed-loop system as:

$$\dot{X} = \underbrace{\begin{bmatrix} 0 & 1 \\ -\dfrac{k+l_1}{M} & -\dfrac{\nu+l_2}{M} \end{bmatrix}}_{A} X + \underbrace{\begin{bmatrix} 0 \\ \dfrac{1}{M} \end{bmatrix}}_{B} F_{es} \tag{5.8}$$

$$M\frac{d^2x}{dt^2} + (\nu + l_2)\frac{dx}{dt} + (k + l_1)\,x = F_{es} \tag{5.9}$$

From **Equation** 5.9, the closed-loop resonant frequency can be written:

$$f_{\text{r-cl}} = \frac{1}{2\pi}\sqrt{\frac{(k+l_1)}{M} - \frac{1}{2}\frac{(\nu+l_2)^2}{M^2}} \tag{5.10}$$

We can note that the closed-loop resonant frequency can be completely assigned by an appropriate choice of l_1 and l_2. In the following the state feedback gain L is computed in order to assign the closed-loop poles such that the system resonates at a lower frequency than the natural frequency of the tweezers. The open loop poles of the tweezers are equal to $z_{1,2} = -85.7 \pm 13.1 \times 10^3 i$. The closed-loop poles are assigned such that the resonant frequency is divided by a given factor β (see first column of Table 5.2) depending on the desired enhancement and in such a way that the damping is kept unchanged.

Table 5.2 sums up the values of the state feedback gain and of the poles of the resulting closed-loop system according to the new resonant frequency. It is noteworthy that the feedback gain L tends to lower the stiffness and the loss parameter of the overall

system. Originally, the modeled stiffness of the tweezers is 47.8 N/m and the modeled viscosity is 48×10^{-6} Ns/m.

Freq.	L	Poles
f_r	$(0, 0)$	$-85.7 \pm 13.1 \times 10^3 i$
$f_r/1.2$	$(-14.6, -8.0 \times 10^{-6})$	$-71.4 \pm 11.0 \times 10^3 i$
$f_r/2.0$	$(-35.9, -24.0 \times 10^{-6})$	$-42.9 \pm 6.7 \times 10^3 i$
$f_r/3.2$	$(-43.1, -33.0 \times 10^{-6})$	$-26.8 \pm 4.3 \times 10^3 i$
$f_r/5.0$	$(-45.9, -38.4 \times 10^{-6})$	$-17.1 \pm 2.9 \times 10^3 i$
$f_r/10$	$(-47.3, -45.0 \times 10^{-6})$	$-8.6 \pm 1.3 \times 10^3 i$

Table 5.2. Pole placement of the closed-loop system according to the resonant frequency placement.

Let us recall that the sensitivity of the resonant frequency to the stiffness is given by:

$$\frac{\partial f_{r\text{-cl}}}{\partial k} = \frac{1}{2\pi} \frac{1}{2M\sqrt{\dfrac{(k+l_1)}{M} - \dfrac{1}{2}\dfrac{(\nu+l_2)^2}{M^2}}} \tag{5.11}$$

$$= \frac{1}{8\pi^2 M f_{r\text{-cl}}} = \frac{1}{8\pi^2 M\,(\beta f_r)} \tag{5.12}$$

When the closed-loop resonant frequency is set to be 10 times lower than the tweezers natural resonant frequency (i.e. $\beta = 10$), the sensitivity to stiffness variation (due to DNA structural modifications for example) is 10 times improved (**Equations** 5.11 and 5.12). Consequently the sensitivity is approximatively 200 Hz.m/N (to be compared with **Equation** 5.7). This ratio has been calculated with precision by the numerical resolution of the matrix A eigenvalues (**Equations** 5.4 and 5.8) of the open loop system and the closed-loop system for different variation of the parameter k.

Figure 5.3 shows the root locus of the open loop and the closed-loop driven tweezers due to variations of the parameter k. **Figure** 5.3 (a) demonstrates that poles moves along the imaginary axis impacting the resonant frequency value f_r (or ω_r in the **Figure**). It is visually noteworthy that the amplitude of the pole motion is larger in the case of the closed-loop systems.

In **Figure** 5.3 (b), the variations of the resonant frequency for the different systems are plotted. Close to 0 (i.e. for very small stiffness variations), the sensitivity of the closed-loop system (related to the slope $\Delta f_r/\Delta k$) is β times greater than the sensitivity of the open loop driven system, where β is the division factor of the system resonance frequency that is imposed via the closed-loop eigenstructure assignment. Therefore the more sensitive system is the system which has been set with the lowest resonant frequency ($\beta = 5$).

Observer design

The observer is looked for under a Luenberger form. Usually the main objective of the observer is to use the model of the system and the available output measurements to

estimate the system state as fast as possible without altering the assigned closed-loop dynamics or amplifying the measurement noises.

Here, in an unusual way, the system is slowed down.The observer should not change the sensitivity insured by the initial state feedback loop. Indeed in our application the separation principle is not anymore satisfied when the parameter (the DNA rigidity) is varying, and the closed-loop sensitivity can consequently be modified.

For the aforementioned reasons, the poles of the observer have to be chosen fast enough, not too high frequency and in such a way that the closed-loop parameters sensitivity is not degraded. The optimal location of the observer poles can be computed by using nonlinear programming. However, in a first instance it has been chosen by trial and error by using the following guidelines:

- the observer is designed to be faster than the original device – with poles at least 2 times faster than the tweezers poles;
- the observer poles are not chosen too fast in order to avoid excessive noise amplification;
- the final location of the observer poles is chosen in order to preserve the sensitivity of the system to stiffness variations.

A discussion about the location of the observer poles is given in **Section** 5.2.3.

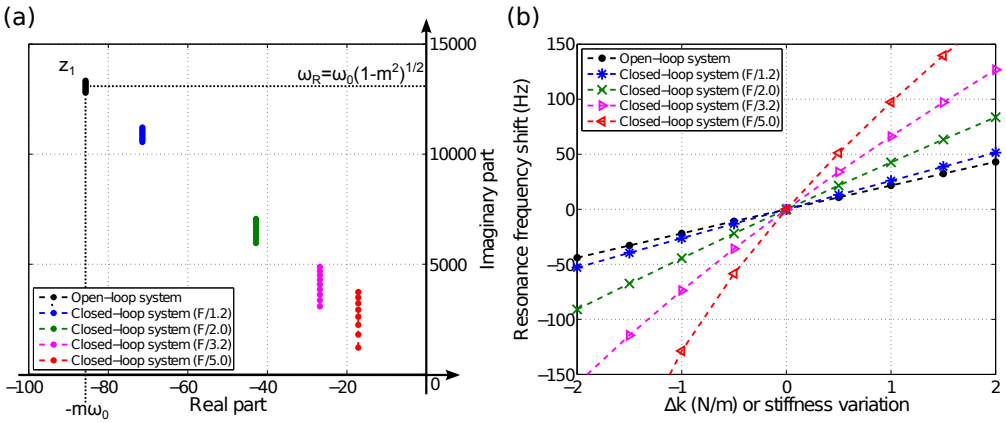

Fig. 5.3. (a) Root locus of the tweezers driven in open loop and in closed-loop. One complex conjugate pole z_1 of the 2nd order equivalent tweezers model is plotted in the s-plan. Equivalent system performances, resonance frequency ω_r and damping m, are shown. Poles of the systems move with the variation of the parameter k. Δk varies from -2 to 2 N/m by 0.5 N/m step. (b) Subsequent evolution of the resonant frequency shift f_r of the open loop system (OLS) and of the different closed-loop systems (CLSs) vs. variations of k. In black, the evolution of the resonant frequency of the OLS. In blue, the evolution of the resonant frequency of the CLS resonating at a frequency 1.2 times lower than the device resonating frequency ($\beta = 1.2$). In green, with the CLS resonating at a frequency 2 times lower ($\beta = 2$). In pink, with the CLS resonating at a frequency 3.2 times lower ($\beta = 3.2$). And in red, with the CLS resonating at a frequency 5 times lower ($\beta = 5$).

5.2.3 Simulation results

Simulation analysis validates the enhancement of the performances on the one hand, and help toward the delicate design of the observer on the other hand. Simulations with observer draw attention to observer dynamic.

From the identified parameters, the feedback scheme (**Figure** 5.2) have been implemented and tested under Matlab/Simulink. **Figure** 5.4 demonstrates a significant increase of the resonance frequency shift between the open loop driven system and the closed-loop system, set as the resonance frequency is 5 times lower ($\beta = 5$). As theoretically expected, the sensitivity of the resonance frequency is 5 times better, compared to open loop driven tweezers, for little variation of k.

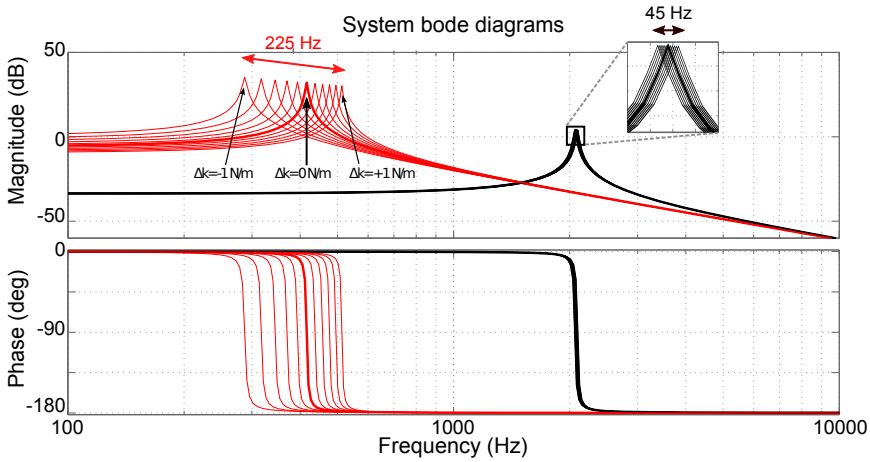

Fig. 5.4. Simulation results. In black line, the tweezer transfer function. In red line, the implemented ($\beta = 5$) closed-loop system transfer function. Both systems undergo a variation of k the system stiffness. Δk varies from -1 to 1 N/m by 0.2 N/m step.

The observer dynamics are chosen via root locus and trial and error. Moreover, the observer design depends on the output matrix C, i.e. in our case if either the displacement or the velocity of the motion is measured. Both features are studied since in the experimental **Section** both configurations are used. Firstly, the case of the displacement measured with the reconstruction of the velocity is simulated.

Velocity state reconstruction

Simulations are conducted with different placements of the observer poles. **Table** 5.3 reports the poles of the observers for which simulation results are presented.

Figure 5.5 shows the root locus of the open loop and the closed-loop driven tweezers with observer (because of variations of the parameter k). In **Figure** 5.5 (b), the motion of the poles of the closed-loop systems implemented with an observer is modified such as (1) the motion along the imaginary part is reduced and (2) the poles move then along the real axis.

Open loop system (Tweezers)	$z, \bar{z} = -85.7 \pm 13.1 \times 10^3 i$
Closed loop system ($\beta = 5$)	$z, \bar{z} = -17.1 \pm 2.6 \times 10^3 i$
Observer 1 ("fast")	$z, \bar{z} = -171.4 \pm 26.1 \times 10^3 i$
Observer 2 ("slow")	$z, \bar{z} = -102.9 \pm 15.7 \times 10^3 i$
Observer 3 ("inadequate")	$z, \bar{z} = -171.4 \pm 13.1 \times 10^3 i$

Table 5.3. Pole placement of the state observer of velocity for state feedback implementation.

The sensitivity of the closed-loop systems implemented with or without an observer are shown in **Figure** 5.6. Closed-loop systems implemented with an observer show a sensitivity in between the open loop driven system and the ideal closed-loop system (without observer). An observer with a 4.2 kHz bandwidth, defined as "fast" observer, allows an increase of the resonance frequency shift but with a small decrease of the range, i.e. with a small loss in the parameter sensitivity. A "slow" dynamic observer (with only 2.5 kHz bandwidth) changes the root locus of the closed-loop system and is about to cancel out the enhancement of the method. Another observer, "observer 3" in **Table** 5.3, cancel out to 0 the resonance frequency shift due to stiffness variations (not plotted in **Figure** 5.6).

In **Figure** 5.7, is plotted the location of the poles of (1) the device, (2) the closed-loop system with $\beta = 5$, and (3) the different observers (see **Table** 5.3). An "inadequate" zone is drawn where the poles of the observer should not be place. If poles are placed in this zone, the resonant frequency sensitivity of such closed-loop systems is then lower than the open loop system.

Displacement state reconstruction

In the case of the measurement of the velocity, the placement of the observer's poles in order to reconstruct the displacement state is different. The root locus of the closed-loop systems are different and the strategy of the pole placement is actually opposite to previously reported (refer to **Figure** 5.7).

Table 5.4 reports the poles of the observers for which simulation results are presented. Observer's poles close to the real axis, i.e. with an imaginary part close to 0, are the more appropriate to reconstruct the displacement state and to preserve the sensitivity of the system to k variations.

Open loop system (Tweezers)	$z, \bar{z} = -85.7 \pm 13.1 \times 10^3 i$
Closed loop system ($\beta = 5$)	$z, \bar{z} = -17.1 \pm 2.6 \times 10^3 i$
Observer 1 ("inadequate")	$z, \bar{z} = -171.4 \pm 26.1 \times 10^3 i$
Observer 2 ("fast")	$z, \bar{z} = -171.4 \pm 2.6 \times 10^3 i$
Observer 3 ("slow")	$z, \bar{z} = -17.1 \pm 2.6 \times 10^3 i$

Table 5.4. Pole placement of the state observer of displacement for state feedback implementation.

In **Figure** 5.8 is plotted the location of the poles of (1) the device, (2) the closed-loop system with $\beta = 5$, and (3) the different state observers for displacement state

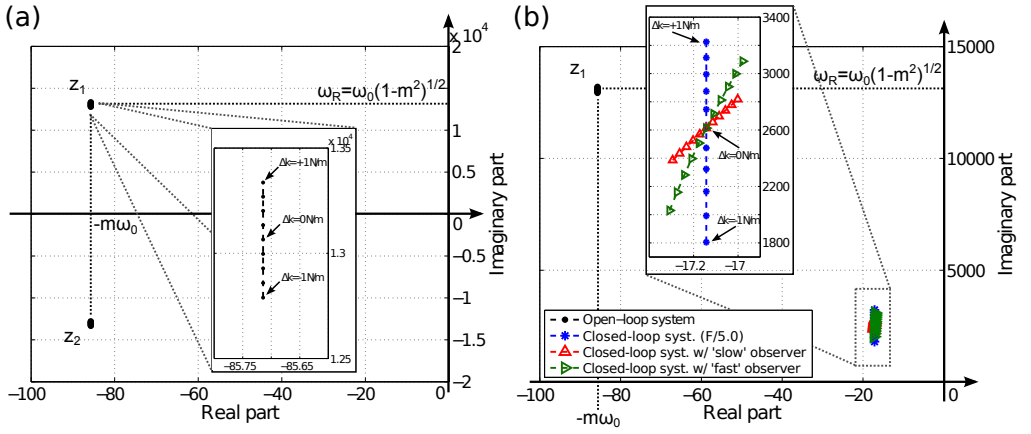

Fig. 5.5. (a) Root locus of the tweezers driven in open loop. Complex conjugate poles z_1 and z_2 of the 2$^{\text{nd}}$ order equivalent tweezers model are plotted in the s-plan. Equivalent system performances, resonance frequency ω_r and damping m, are shown. Close-up are made on z_1 to show pole dependency on k the system stiffness. Δk varies from -2 to 2 N/m by 0.2 N/m step. (b) Root locus of the closed-loop systems ($\beta = 5$) with different state observers of the velocity. Complex conjugate poles are plotted in the positive imaginary half s-plan. In blue dots are plotted the ideal pole path of the closed-loop system due to the k variations (without observer). For different observers designs, poles dependencies (and equivalent performances resonance frequency ω_r and damping m) on k the tweezers stiffness are shown. Δk varies from -1 to 1 N/m by 0.2 N/m step.

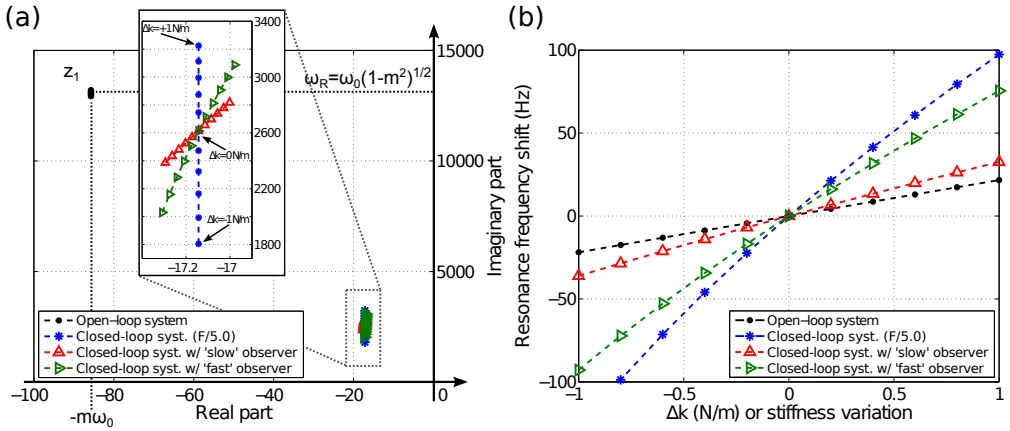

Fig. 5.6. (a) Root locus of the tweezers driven in open loop and in closed-loop. Complex conjugate poles of open loop system and closed-loop systems ($\beta = 5$) implemented with different observers are plotted in the positive imaginary half s-plan. Poles of the systems move with the variation of the parameter k. Δk varies from -1 to 1 N/m by 0.2 N/m step. (b) Subsequent evolution of the resonant frequency shift of the open loop system and of the different closed-loop systems vs. variations of k. Closed-loop systems implemented with an observer show a sensitivity in between the open loop driven system and the ideal closed-loop system (without observer).

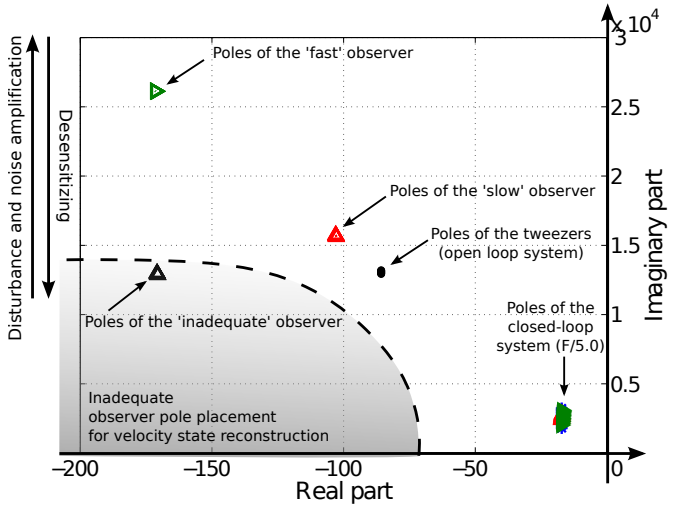

Fig. 5.7. Complex conjugate poles of the open loop system, the closed-loop systems ($\beta = 5$) and of the different observers of velocity (reported in **Table** 5.3) are plotted in the positive imaginary half s-plan. An "inadequate" zone is drawn which represents a pole placement for the observer inadequate for sensing resonant frequency shift due to k variations.

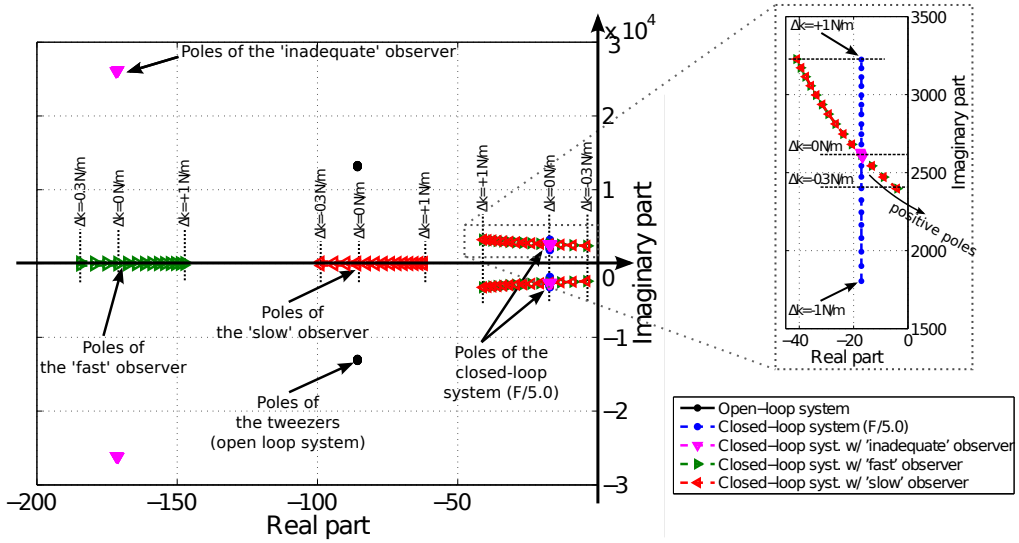

Fig. 5.8. Complex conjugate poles of the open loop system, the closed-loop systems ($\beta = 5$) and of the different observers of displacement (reported in **Table** 5.4) are plotted in the positive imaginary half s-plan. In the right side, the close-up view of the pole of the closed-loop system demonstrates the real part of the poles becomes very sensitive to this variation, inducing to positive poles.

reconstruction. As previously observed, the implementation of the state observer results in a change of the root locus of the system to k variations.

With an appropriate placement of the poles of the displacement observer, the sensitivity of the resonant frequency to stiffness variations can be preserved (**Figure** 5.9). However the close-up view of the pole of the closed-loop system in **Figure** 5.8 demonstrates that the real part of the poles becomes very sensitive to this variation, inducing to positive poles. The range of variations is still enough for our applications, but this difference (i.e. -0.3 N/m) can also be the consequence of an inaccurate modeling of the parameters for instance.

Between the "fast" and the "slow " observers, the root locus of the closed-loop system and the subsequent parameter sensitivity are not changed. However for k variation superior to $+1$ N/m, the poles of the observer and the closed-loop system tend to come closer such as the response of the system is governed by both dynamics and the sensitivity is then modified.

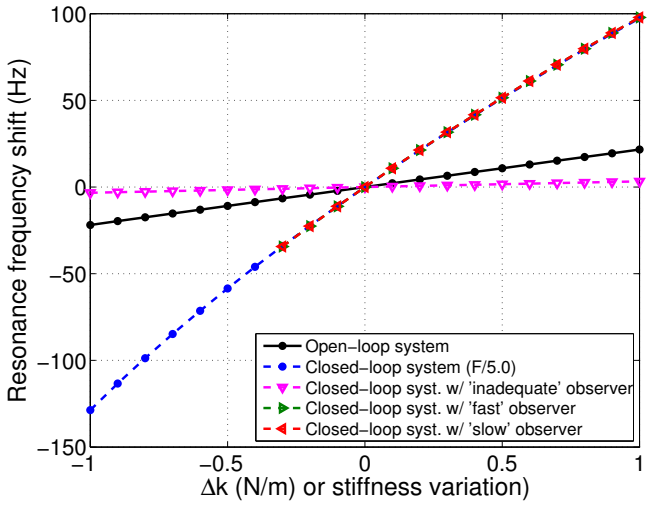

Fig. 5.9. Evolution of the resonant frequency shift of the open loop system and of the different closed-loop systems vs. variations of k. Closed-loop systems implemented with an observer (of the displacement state) show a sensitivity close to the ideal closed-loop system (without observer). A "inadequate" placement of the observer reduces the sensitivity under the one of the open loop driven device.

5.3 Experimental application for extra-stiffness characterization

The experimental validation of the approach is led in two steps. i.e. (1) measuring the displacement of the tip motion by an interferometer, and (2) using the integrated sensor which measures the velocity of the motion. Because the set-up of the tweezers required an improvement in terms of electrical noise and coupling rejection, it was firstly not possible to use the integrated sensor. In practical terms, it was complicated to implement

an adequate observer without considering the high level of noise and of the capacitive coupling from the actuator to the sensor (which is not considered in the model).

5.3.1 Feedback implementation with displacement measurement by interferometry

In this **Part**, the sensor is not taken in account and the measurement is performed with an interferometer from SIOS Meßtechnik GmbH company (http://www.sios.de). The feedback controller and the observer are implemented in a dSPACE's prototyping board (http://www.dspace.de).

The main source of noise is expected to be the noise coming from the interferometry measurement. The resolution of the interferometer is reported to be sub-nanometric, but the difficulty arises from the good focus of the laser spot on the tweezers' tip. The noise amplitude reached is about 1 to 10 nm depending on the preparation of the set-up.

Thereafter, the signals applied to the actuator are step signals in order to characterize the system's dynamics.

5.3.1.1 Experimental set-up

In order to validate the proposed approach from the parameter sensitivity point of view, a dedicated cantilever chip emulates the external stiffness. The chip is mounted on a micromanipulator and a video monitoring allows the contact cantilever/tweezers tip (**Figure** 5.10).

The control strategy is validated for different ratios of reduction of the resonance frequency. The experimental procedure consists in approaching delicately the cantilever beam in contact with the mobile tweezers tip. Then, all time step responses are recorded for several implemented closed-loop systems. At last, the contact is removed and once more all the step responses are recorded without extra rigidity. This method is supposed to guarantee unchanged conditions and same extra stiffness value between the different experiments in order to compare the different performances.

5.3.1.2 Results and interpretation

In **Figure** 5.11 are given the experimental results of the proposed method for the reduction ratios β = 1.1, 1.3, 2, 2.2 and 2.5. For each case, a step reference from 240 to 260 nm is applied to the system and the oscillation frequencies are measured and compared. **Figure** 5.11 (a) shows as reference the step response of the open loop driven system. **Figures** 5.11 (b-c-d-e-f) shows the step responses of the five different implemented closed-loop systems.

Above each displacement graph is indicated the control signal in volt. A special care is taken to avoid any dangerous actuation for the device integrity. Basically, the actuation is empirically limited to 50 V. A 0 to 50 V step actuation should not cause any displacement larger than the gap in between the actuator electrodes, thus avoiding any contact and any critical current flowing through the lines. **Figures** 5.11 (b-c-d) control curves show the feedback effect on the control, in comparison with the basic step control of **Figure** 5.11 (a).

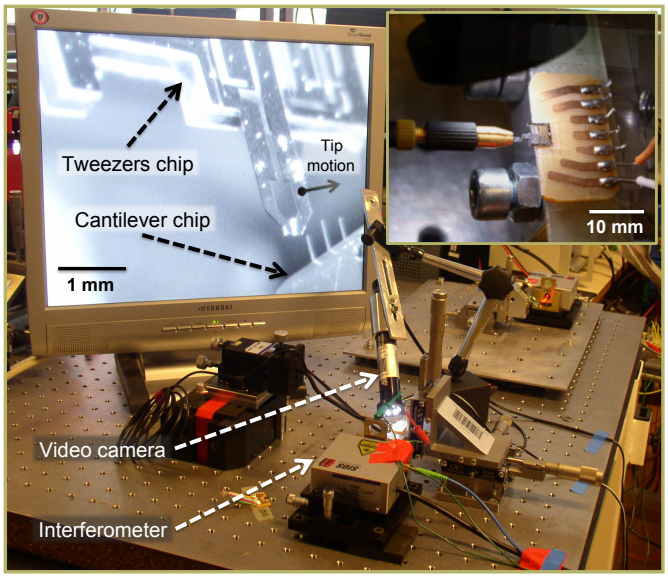

Fig. 5.10. Experimental set-up: the tweezers are illuminated and recorded by a camera, and the tip position is measured by an interferometer from SIOS Meßtechnik GmbH company. In the screen, a cantilever chip is in approach to the tweezers tips. And in the top-right insert, it is a close-up view on the tweezers and on the chip of cantilevers. (At AS2M/FEMTO-ST, Besançon, France).

With the experimental setup described above, the same step responses with an extra stiffness applied to the system have been visualized. The red signals of **Figures** 5.11 show the time responses of each system with an added rigidity. Descending the plots from the open loop driven system to the slowest closed-loop system, it is clear that the signals (blue vs. red) become easier to differentiate.

The oscillation frequencies are estimated with a Fast-Fourier Transform (FFT) algorithm that runs under Matlab environment. Unfortunately, the resulting data are more qualitative than quantitative since the time responses are not long enough (in time) to allow good resolution in the frequency spectrum. For 0.3 s response time length (with a time sampling of 80 kHz), the frequency resolution of the FFT is 19.5 Hz. Then the peak of the oscillation frequency is fitted to permit better difference measurement between spectra.

Table 5.5 summarizes the frequency results of the experiment with the cantilever of 0.3 N/m. The open loop system presents an oscillation frequency shift of +9.3 Hz. The 1st closed-loop system ($\beta = 1.1$), **Figure** 5.11 (b), indicates a shift of +12.1 Hz. **Figure** 5.11 (c) ($\beta = 1.3$) shows a frequency shift of 17.8 Hz and **Figure** 5.11 (d) ($\beta = 2$) a shift of 16.7 Hz. A clear increase of the shift is demonstrated here for a same extra rigidity added to the system. This shift is also depending on the closed-loop systems.

Discussion

Actually results show better performances than expected. The resonance frequency shifts due to a pre-determined added rigidity are larger (+9.3 Hz in open loop) than the sim-

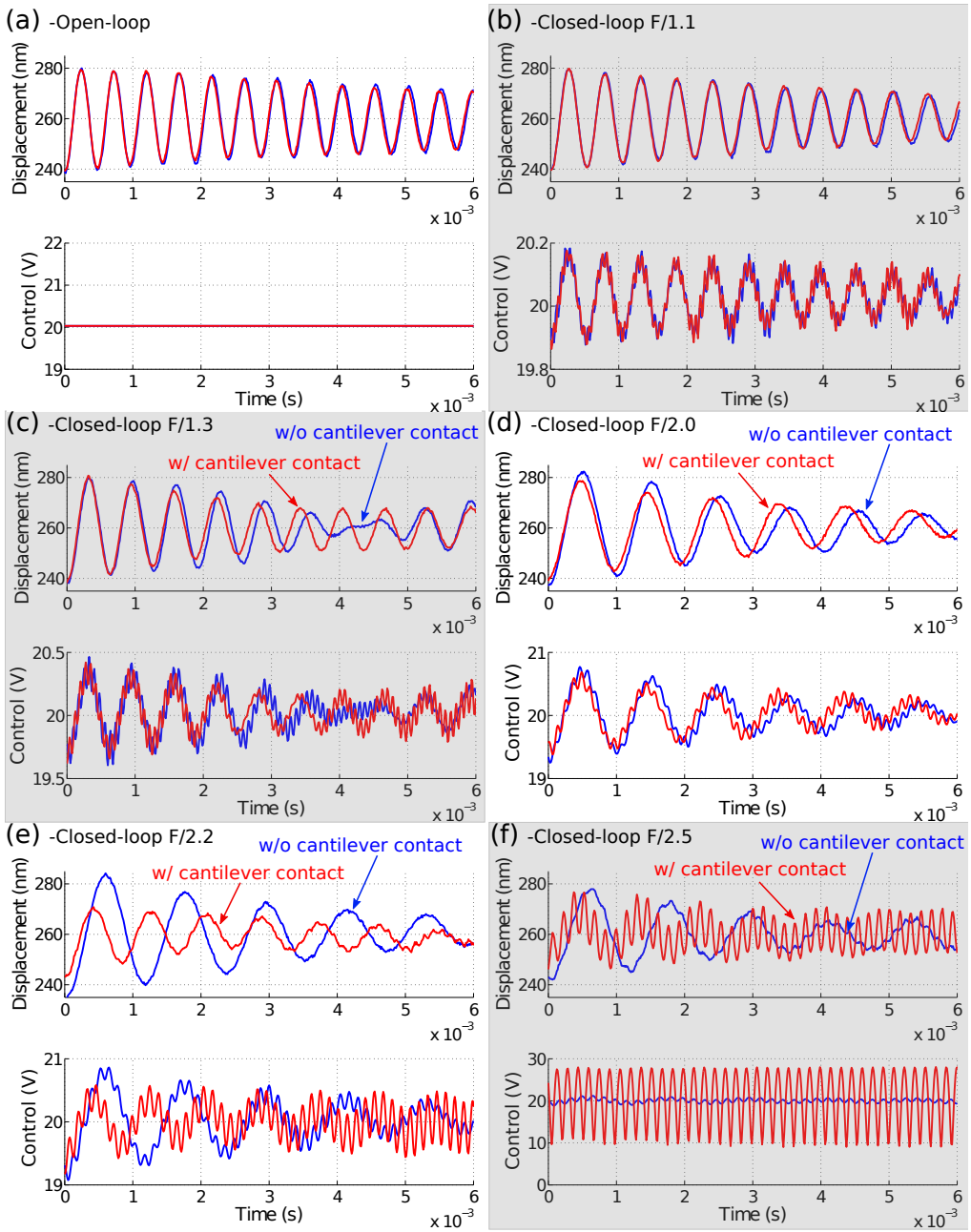

Fig. 5.11. Time step responses of different implemented closed-loop systems for a 240 to 260 nm step reference. In blue lines, the responses without extra added stiffness to the tweezers. In red lines, the responses with cantilever contact on the tweezers tip (cantilever bending stiffness = 0.3 N/m). (a) Open loop driven tweezers. (b) Closed loop system implemented with $f_r/1.1$. (c) Closed loop system with $f_r/1.3$. (d) Closed loop system with $f_r/2.0$. (e) Closed loop system with $f_r/2.2$. (f) Closed loop system with $f_r/2.5$.

System	Resonance freq. (Hz)	Freq. shift (Hz)
Open-loop	2082.3	+9.3
Closed-loop ($\beta = 1.1$)	1886.4	+12.1
Closed-loop ($\beta = 1.2$)	1715.1	+17.8
Closed-loop ($\beta = 1.3$)	1587.8	+16.7
Closed-loop ($\beta = 2.0$)	997.9	+38.8
Closed-loop ($\beta = 2.2$)	847.3	+358.1
Closed-loop ($\beta = 2.5$)	853.4	+349.7

Table 5.5. FFT results of the step response experiment for different closed-loop systems. Related to **Figure** 5.11.

ulated shifts (6.5 Hz in open loop). One possible interpretation is that the mechanical contact between the cantilever beam and the tweezers tip is a punctual and a non-clamped coupling – i.e. that only the bending stiffness of the clamped-free beam is considered.

Furthermore, **Table** 5.5 presents shift results even better than the theory intends, i.e. directly proportional to the ratio factor β. If we focus on **Figure** 5.11 (c), we can observe a modulation of the oscillation with another frequency.

Figure 5.12 shows one of the problems encountered for a complete and accurate implementation of our method. The MEMS tweezers have been considered as a simple second order model neglecting other possible modes. According to **Figure** 5.12 (a) (or **Figure** 5.11 (a)), other modes (or frequencies) are not visualizable and characterizable. Nevertheless, **Figure** 5.12 (c and d) shows the apparition of undesirable modes around 1400 Hz and 1500 Hz. A first consequence is the possible instability of the system when the poles are assigned between 1100 and 1600 Hz. A second consequence is that approaching this limit the sensitivity trend to be unpredictable.

These considerations are the improvement directions addressed for a better understanding and precision of the results. Basically, a complexification of the model and the placement of more than two poles has to be considered. Furthermore a different placement of the poles (acting on the damping parameter of the system) may cause different dynamics and different sensitivities to parameter variations and to unmodeled modes.

Finally experiments have been conducted with three different cantilevers with different stiffness (0.3, 0.35 and 0.65 N/m). **Figure** 5.13 shows the results for the different rigidities. The results demonstrate an enhancement of the frequency shift for the three set of experiments and a logical tendency according to the characterized stiffness. Green rounds (0.65 N/m experiments) show higher shift than the red star dots (0.35 N/m experiments) which show higher shift than the blue dots (0.3 N/m experiments).

The first experimental points show a relevant tendency. From the open loop driven system to the closed-loop system implemented as $f_r/1.3$, the frequency shifts demonstrate a linear enhancement. However the enhancement is even higher than the expected one. After that, the following experiments still show a higher shift, but unfortunately the measured values do not agree with the simulations and do not follow a logical trend.

First it becomes complicated to get a stable and repeatable response from those specific closed-loop systems to slower systems. As previously shown, the responses show the excitation of different dynamics of the device. The modulation of the oscillation

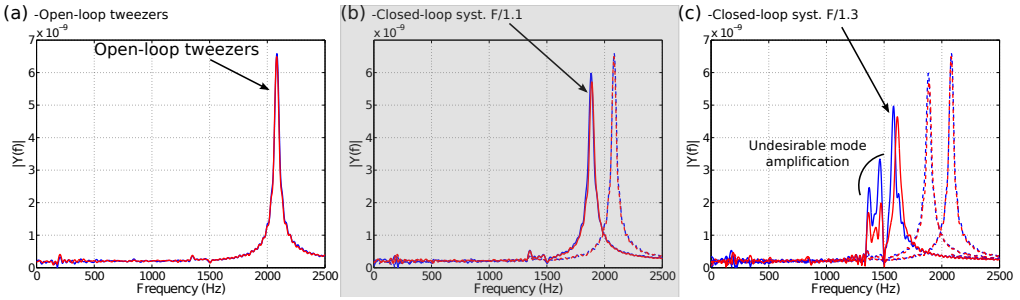

Fig. 5.12. FFTs of the step responses of different closed-loop system for resonance frequency shift measurement. (a) Open loop driven tweezers. (b) Closed loop system implemented with $f_r/1.1$. (c) Closed loop system with $f_r/1.3$. Resonance frequency shifts are caused adding the stiffness of a cantilever (0.3 N/m) (in red lines) (see **Figure** 5.10). In blue lines, the system response FFTs without cantilever contact.

frequencies makes the FFT algorithm more inefficient to determine the good frequency of the closed-loop system resonance. Consequently, (1) the response of such systems is perturbed by unmodeled dynamics and (2) the method of the frequency measurement is not appropriate to determine precisely the frequency performances.

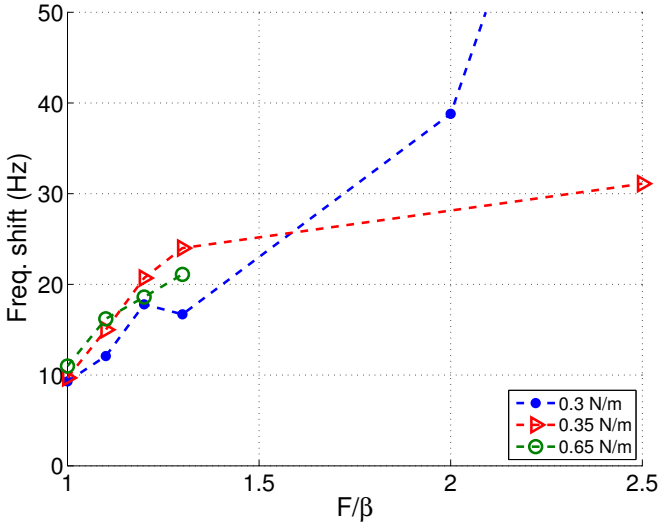

Fig. 5.13. Synthesis of the sensitivity results of implemented feedback method. In abscissa, are informed the division factor (β) applied to the original resonance frequency for the implemented closed-loop system resonance frequency. The resonance frequency shifts are the resonance frequency differences due to the contact of the cantilever of 0.35 N/m (blue dots), 0.35 N/m (red dots) and 0.65 N/m (green dots).

5.3.2 Feedback implementation with velocity measurement using the integrated capacitive sensor

In this **Part**, the motion of the device is measured through the capacitive sensor integrated to the device. As aforementioned, in a given configuration, the sensor allows velocity measurement of the tip motion (see **Pages** 35-36 in **Chapter** 3). The feedback controller and the observer are implemented in a dSPACE's prototyping board.

5.3.2.1 Experimental set-up

The experimental set-up is similar to the previous one, but the cantilever is now mounted on a robotized 3D-micromanipulator (**Figure** 5.14). Linear positioners and controllers from SmarAct GmbH (http://www.smaract.de), using stick-slip principle with piezoelectric actuators, allow nanometric and repeatable positioning of devices. That way, cantilevers are approached to the tweezers' tip in order to reproduce previous experiments. And that way, in a second **Part**, a microfluidic device will be used to immerse the tips and move towards biological applications.

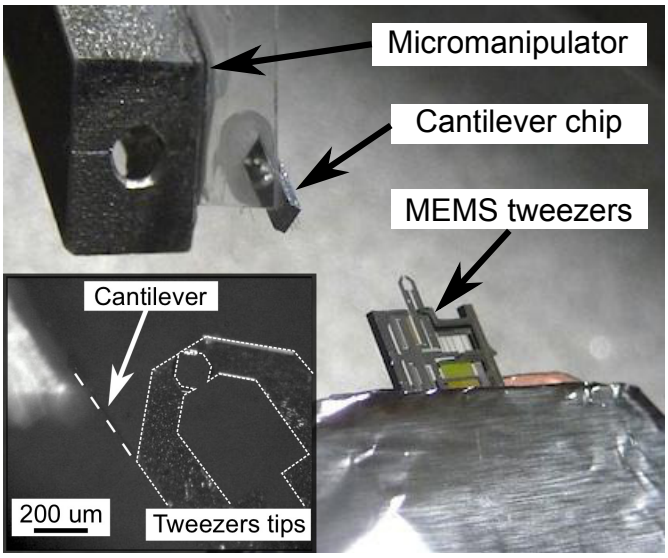

Fig. 5.14. Experimental set-up: the tweezes are fixed while the cantilever is mounted on a robotized manipulator from SmarAct GmbH. The cantilever can be approached toward the tweezers' tip with nanometric accuracy. The tweezers are viewed under Keyence VHX-500 Digital Microscope (http://www.keyence.com/), and the bottom-left insert is the microscopy view of the tweezers and the approaching cantilever. (At IIS/U. of Tokyo, Japan).

The sensing through the integrated capacitive sensor has required many improvements of the chip "packaging". Beforehand, the device was used taking advantages of the square law of the actuator and then performing frequency measurements at the second harmonic of the actuation signal with a lock-in amplifier. The coupling was rejected discarding the

actuation frequency. However, in order to implement the control strategy based on linear theory, works have been done to enable direct sensing of the time signals.

On the one hand, the PCB (for Printed Circuit Board) of the chip has been modified to isolate the sensing lines from the actuation line. The PCB has been updated by a 3-layers PCB with grounded plans minimizing the capacitive coupling between lines. On the MEMS chip, the silicon bulk is connected to the ground. In the next version of the tweezers, a ground plan will be integrated to the frontside silicon to improve the coupling.

On the other hand, the good sensing of the motion is determined by the measurement of small sensor currents (∼pA). The resulting currents are converted into voltages by two low-noise current-to-voltage (A/V) preamplifiers, implying high gain ($> 10^8$ for conversion into mV) compatible with the bandwidth of the tweezers dynamics. In **Appendix** H, **Figure** H.2 (**Page** 140) is shown the bandwidth limit of preamplifiers for 10^8 and 10^8 Low Noise gains. The effect of the phase shift due to the preamplifiers (or other dead-time in the loop due to ADC or DAC for instance) is studied by using (or not) Padé approximation.

5.3.2.2 Results and interpretation

Studies with sinusoidal input signals were performed here for frequency study and PLL experiments.

Frequency study

Figure 5.15 shows the frequency responses of the closed-loop systems with reduction ratios $\beta = 1.1$, 1.2, 1.3, 1.5, 1.7 and 2.0. Frequency plots illustrate that the reduction of the resonance frequency of the system is achieved, but approaching frequencies close to the dynamics at 1400 Hz and 1600 Hz, these frequency responses become unreliable (see especially **Figure** 5.15 (c-d)). This confirms the interference of unmodeled modes around 1400 Hz. However here we conduct experiments with sinusoidal actuation in order to avoid harmonics in the excitation signal.

Furthermore, from this set of experiments one can note that the amplitude of the output of the closed-loop systems are not in adequacy to the theory. Amplitudes of the resonance are much lower than expected, leading to a low quality factor of the resonance. This specificity can be explained by the presence of a delay in the loop. The delay can be the consequence of the limited bandwidth of the preamplifiers or the computation of the feedback by a prototyping board. It can be taken into account with a Padé approximation of the 2^{nd} order.

Figures 5.16 and 5.17 show the frequency responses of closed-loop systems expanded with a second order Padé approximants. State matrix of the device model and of the observer become $\mathbb{R}^{(4,4)}$. Four poles have then to be assigned. The state feedback L becomes $\mathbb{R}^{(1,4)}$. The amplitude of the resonance tends to be in adequacy to the theory. When a delay of 8 µs is considered, the amplitude of the closed-loop system resonance is higher. The approximation of a delay of 16 µs is the limit before unstable closed-loop systems, and the limit giving the best performances in term of the resonance amplitude.

This is the way the delay in the loop was characterized. It approximatively corresponds to the phase shift of the preamplifiers, i.e. $-12°$ at 2 kHz which corresponds to a delay of:

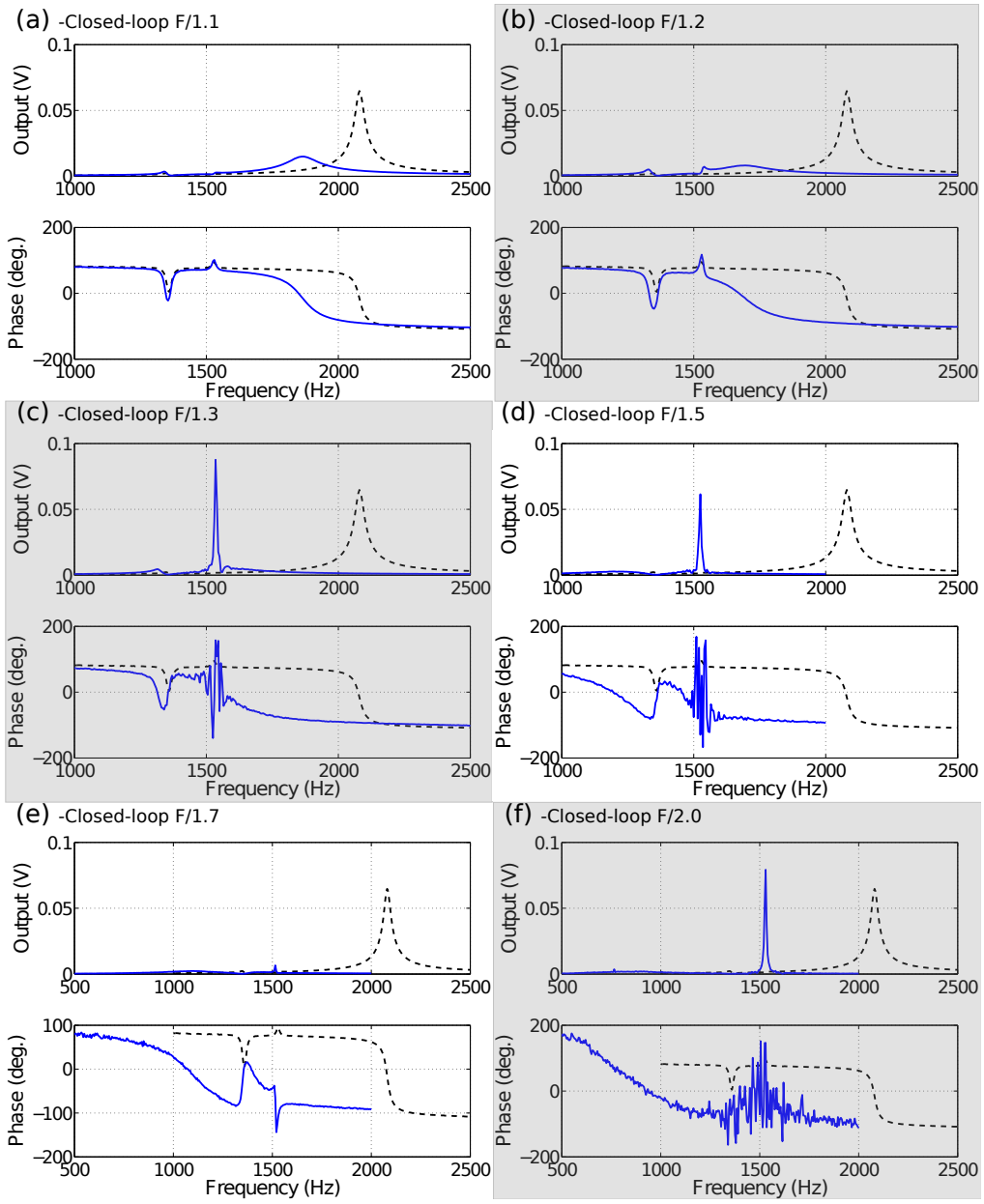

Fig. 5.15. Frequency responses of different implemented closed-loop systems for an actuation of 0.2 V_{PP} with an offset of 20 V. In black dotted lines, is plotted the response of the open loop driven tweezers. In blue lines, the responses of different closed-loop systems. (a) Closed loop system implemented with $f_r/1.1$. (b) Closed loop system implemented with $f_r/1.2$. (c) Closed loop system with $f_r/1.3$. (d) Closed loop system with $f_r/1.5$. (e) Closed loop system with $f_r/1.7$. (f) Closed loop system with $f_r/2.0$.

$$t_{\text{delay}} = \frac{-12^\circ}{360^\circ}\frac{1}{2000} = -16.7\ \mu\text{s}$$

Accordingly the expansion of the model implies to reduce the sampling of the computation from 70 kHz to 50 kHz, with possible consequences on the closed-loop performances.

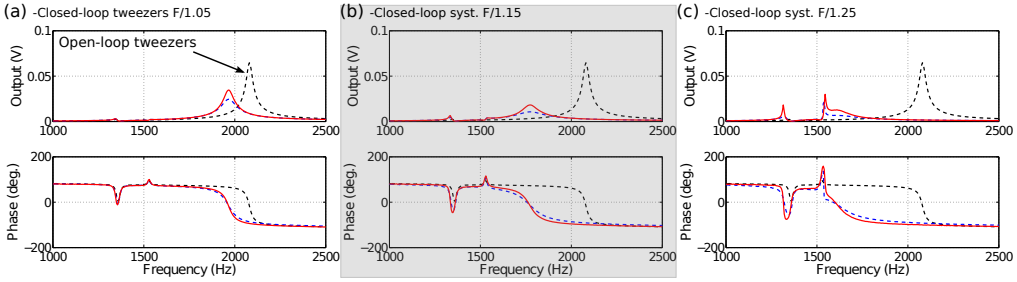

Fig. 5.16. Frequency responses of different implemented closed-loop systems with a Padé approximation for a delay of 8 µs (for an actuation of 0.2 V_{PP} with an offset of 20 V). In black dotted lines, is plotted the response of the open loop driven tweezers. In blue dotted lines, the responses of different closed-loop systems. In red lines, the responses of different closed-loop systems with 2^{nd} order Padé model. (a) Closed loop system implemented with $f_r/1.05$. (b) Closed loop system implemented with $f_r/1.15$. (c) Closed loop system with $f_r/1.25$.

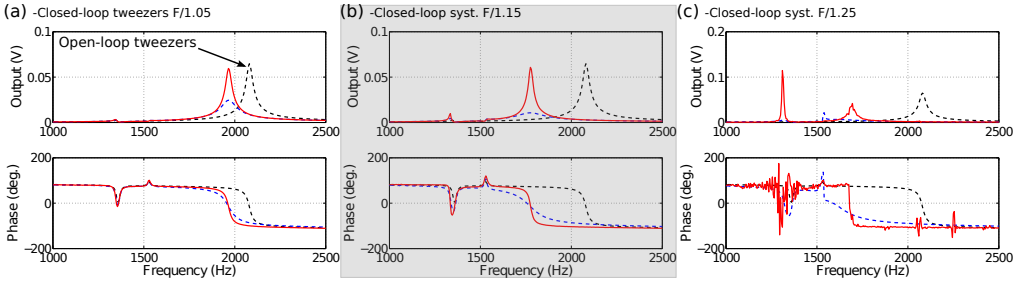

Fig. 5.17. Frequency responses of different implemented closed-loop systems with a Padé approximation for a delay of 16 µs (for an actuation of 0.2 V_{PP} with an offset of 20 V). In black dotted lines, is plotted the response of the open loop driven tweezers. In blue dotted lines, the responses of different closed-loop systems. In red lines, the responses of different closed-loop systems with 2^{nd} order Padé model. (a) Closed loop system implemented with $f_r/1.05$. (b) Closed loop system implemented with $f_r/1.15$. (c) Closed loop system with $f_r/1.25$.

PLL experiments with closed-loop system with $\beta = 1.1$

PLL experiments are performed with the immersion of the tweezers' tips into a microfluidic chamber (**Figure** 5.19). It is expected that the slight immersion of the tweezers change the resonance properties of the system because of the added mass and the viscosity of the liquid (deionized water).

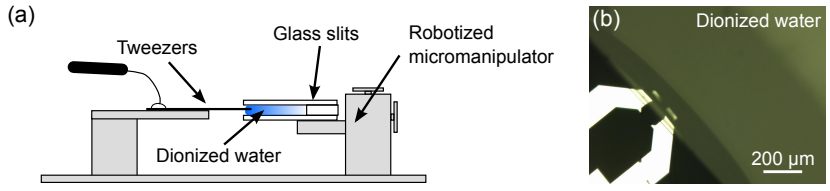

Fig. 5.18. Experimental setup for immersion of tweezers' tips into microfluidic slit containing deionized water. (a) schematic side view of the setup. (b) top view of the immersion of the tips.

First as the actuation is not the usual actuation used for previous bioexperiments (i.e. 3 V_{PP} sinusoidal signal) but 0.2 V_{PP} sinusoidal signal with an offset of 20 V, the performances for both actuation in open loop are shown. As demonstrated, the resonant frequency and the amplitude are different. It comes from the fact that the model depends on the operating point. The amplitude of the displacement is larger in the "linearized" configuration with an offset of 20 V, but 0.2 V_{PP} is the minimum AC voltage applicable. The frequency shift is of -0.6 Hz when the tweezers' tips are immersed in a slit of deionized water (**Figure** 5.18).

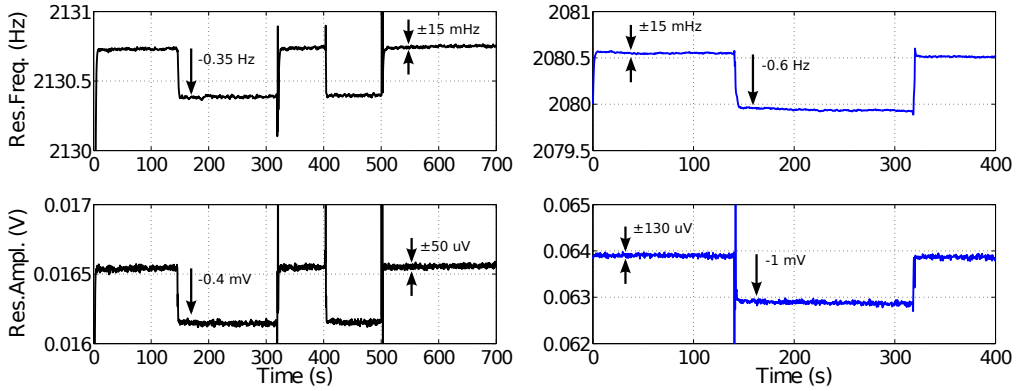

Fig. 5.19. PLL performances of the tweezers driven in open loop. During the experiment, the tweezers' tips are immersed in a slit containing deionized water. (a) the actuation is a 3 V_{PP} sinusoidal signal. (b) the actuation is a 0.2 V_{PP} sinusoidal signal with an offset of 20 V.

Figure 5.20 shows the PLL experiments conducted in open loop and in closed-loop with immersion of the tips in water. The interaction of the device with the medium when the tips are immersed have not been precisely characterized, but from experiments we note that the resonance frequency and the quality factor decrease because of added mass and the viscosity of the liquid. However, after simulations with added mass ΔM (instead of added stiffness Δk), we also expect more shift of the resonance frequency. In open loop, the shift of the resonance frequency is of -0.6 Hz and the amplitude at resonance decreases of -1 mV. In closed-loop, the frequency shift is of -1.6 Hz and the amplitude at resonance decreases of -70 µV. The conditions of the experiments permit comparable and repeatable immersion of the tips thanks to the robotized positioning of

the microfluidic slit. Furthermore, the meniscus between air, the tips and the liquid was stable. The results are stable in air and in liquid allowing good resonance measurements. Therefore we demonstrates anew the enhancement of the sensitivity of the resonance frequency. Nevertheless, without Padé model, the amplitude of the resonance and its sensitivity are very low.

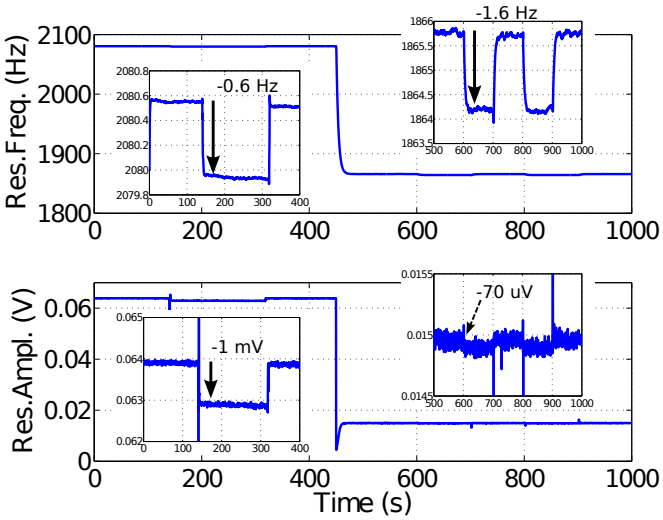

Fig. 5.20. PLL performances of the tweezers driven in open loop and in closed-loop with $\beta = 1.1$. At the beginning of the experiment the tweezers are driven in open loop, then at $t = 450$ s the loop is "closed". During the experiment, the tweezers' tips are immersed several times in a slit containing deionized water. The actuation is a 0.2 V_{PP} sinusoidal signal with an offset of 20 V.

Figure 5.21 shows similar PLL experiments conducted in open loop and in closed-loop with Padé approximation of the loop delay. As characterized in previous frequency study of the closed-loop, a loop delay of 16 µs was modeled with Padé model of the 2^{nd} order. When "closing" the loop (at $t = 450$ s), the amplitude of the resonance is preserved (~ 57 mV) (compare amplitudes of the resonance of **Figures** 5.20 and 5.21).

In open loop, the shift of the resonance frequency is of -0.6 Hz and the amplitude at resonance decreases of -1.5 mV. In closed-loop, the frequency shift is of -1.45 Hz and the amplitude at resonance decreases of -1.1 mV.

5.4 Conclusion

The present study investigates the efficiency of closed-loop approach for the enhancement of the performances of silicon nanotweezers for the detection and the characterization of biological molecules. An improvement of the sensitivity to parameter variations was demonstrated using closed-loop control. Overstepping the limits of the microfabrication and microengineering, a more compliant system with an equivalent stiffness closer to the detected DNA molecule stiffness was emulated.

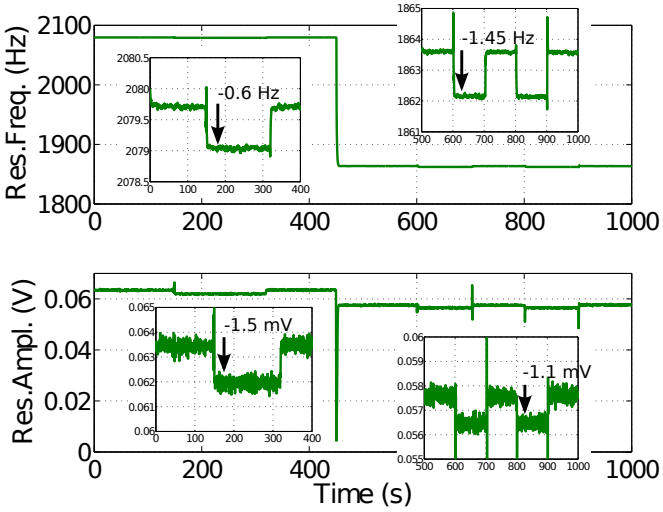

Fig. 5.21. PLL performances of the tweezers driven in open loop and in closed-loop with $\beta = 1.1$ with Padé approximation of a delay of 16 µs. At the beginning of the experiment the tweezers are driven in open loop, then at $t = 450$ s the loop is "closed". During the experiment, the tweezers' tips are immersed several times in a slit containing deionized water. The actuation is a 0.2 V_{PP} sinusoidal signal with an offset of 20 V.

Silicon nanotweezers are an innovative tool to easily trap and stimulate molecules. The integrated sensor allows the implementation of a feedback in order to design a closed-loop controlled system. Simulation results show a significant increase of the resonant frequency shift in response to an increase of the system stiffness, in comparison with a simple open loop method. Considering the electronic read-out capabilities and the current detection method (using a Phase-Locked Loop), this improvement will lead to a decrease of the minimum detectable stiffness.

In open loop method and basically due to the measurement noise, the resolution for frequency shifts is 10 mHz corresponding to a minimum detectable stiffness of 20 mN/m, i.e. approximatively 30 molecules of λ-DNA. With the same frequency shift detection and the presented feedback-control method, under of tenth of molecules of λ-DNA can be sensed. Approaching the sensitivity of one DNA molecule will lead to relevant biological experiments on single molecule with MEMS device as with optical tweezers or AFM.

6

Conclusions and perspectives

The main objective of this Ph.D. work was to associate modeling and dynamic analysis with a real time feedback strategy to allow the precise manipulation of DNA molecules with silicon based nanotweezers, going toward the detection of single molecule variations. Another important part of this work was to characterize the influence of the environment on the tweezers behavior and to provide an appropriate packaging to allow such molecular manipulation.

The work started with the development of biological experiments on λ-DNA molecules. Experiments were successfully conducted with restriction enzymes [Kumemura 2010] and binding molecules [Lafitte 2011]. As previously explained, complementary microfluidic device has been designed and fabricated in order to allow an appropriate immersion of the tweezers' tip and the supply of the biological solutions. Inside this microfluidic reservoir, the real-time monitoring of the trapping of DNA molecules was achieved [Lafitte 2010]. These achievements pave the way for systematic bio-experiments on DNA with these silicon nanotweezers.

However, as the publications report, the resolution of these experiments can not compete with the resolution obtained with tools commonly used for single-molecule experiments (i.e. AFM, magnetic and optical tweezers). After an improvement of the experimental set-up and of the measurement method, the sensing with resolution of tens of λ-DNA molecules is achieved. Nevertheless, the goal of this work is to attain the single molecule resolution. An enhancement of the sensitivity of the tweezers has been thought by the implementation of a control strategy.

The implementation of a state feedback was successfully achieved with an improvement of the sensitivity to mechanical stiffness variation. This opens the way for going further and attaining effectively the single-molecule with batch-fabricated silicon nanotweezers. However this step revealed the existence of other mechanical dynamics and their importance in the modeling concern.

On the one hand, the improvement achieved is more important than the theory intends. On the other hand, it is not possible to implement the feedback in all the conditions. Indeed, the presence of the other dynamics hinder the design of closed-loop system with resonance close to these undesirable frequencies.

Even though the implementation of the state feedback was achieved, its design and implementation need to be improved. It is thought that the fact to neglect the others dynamics affect the experimental performances of the closed-loop systems. A complexification of the model may impose the modeling of the undesirable dynamics or of the spatial complexity of the structure. This task may be difficult since the characterizations of these dynamics and their understanding were not well mastered. That is the reason why new tweezers are now developed with new specifications with respect to modeling and feedback implementation.

Perspectives

We could observe during this work the following difficulties:

- designing complex mechanical structure for a targeted application;
- predicting the real characteristics of a such microfabricated structure;
- determining an accurate model of a such complex structure.

As aforementioned, the main obstacle arose from the difficulty in global understanding of the different dynamics of the device. The nanotweezers have been initially developed in order to work at the resonance frequency of the motion in the actuated direction. The spatial distribution of the mass and the forces due to the integration of the actuation and the sensor leads to the rise of other dynamics.

New design of tweezers

One axis of development is to re-design the device taking in account the specifications coming from the feedback implementation. We have demonstrated that we desired to lower the resonance frequency of the device in order to emulate a compliant system suitable for low-stiffness parameter characterization. One the one hand, the device requires a minimum stiffness force (1) to survive the fabrication processes, (2) in order to support the system weight and (3) to prevent attractive and sticking surface forces in the comb-drive actuator and the capacitive sensor. On the other hand, we design a new mechanical structure in order to reject the other dynamics toward higher frequencies.

Figure 6.1 shows the dynamics of the new structure. The dynamic of interest is now the first and the principal dynamic for the low frequency bandwidth (i.e. up to 3 kHz). This advance leads to a simple and a more accurate modeling of the device. Characteristics comparison between the previous and the new tweezers are reported in **Table** 6.1. First experiments of these new nanotweezers demonstrate characterizations in adequacy to the simulations, and first feedback implementation shows no specific limitation in a bandwidth such as previously.

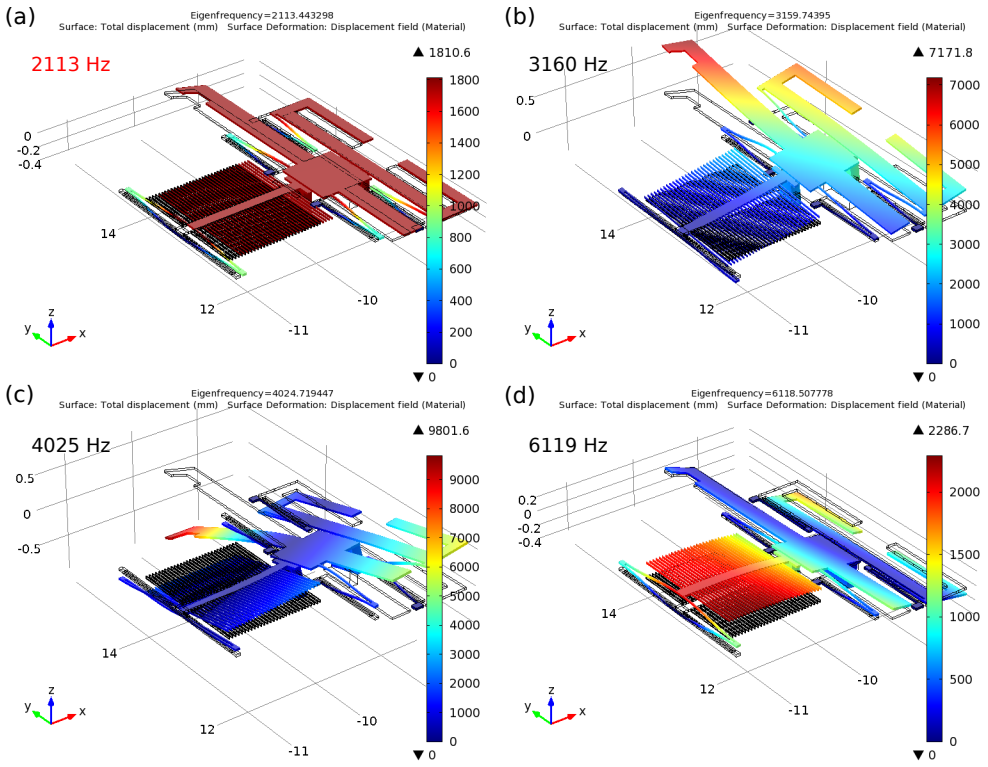

Fig. 6.1. Eigenfrequency simulations of the mechanical structure of newly improved nanotweezers. The first 4 modes of the structure are shown. To be compared with **Figure** 3.22.

Characteristic	Parameters	Values for the new tweezers	Values for the old tweezers
Actuator gain	α_{CD} (N/V^2)	29.2×10^{-9}	29.2×10^{-9}
Sensor gain	α_{CS} (F/m)	360×10^{-9}	269×10^{-9}
Stiffness	k_{tw} (N/m)	58.0	126.5
Viscous losses	ν (N.s/m)	*N.A.*	60×10^{-6}
Mass	M (kg)	329×10^{-9}	299×10^{-9}
Resonant frequency	f_{r} (Hz)	2113	3274
Quality factor	Q	*N.A.*	55

Table 6.1. Theoretical model parameters of new silicon nanotweezers.

Another axis of improvement is the development of microfluidics for relevant bio-experiments. A microfluidic device has been developed with especially pneumatic-actuated valves for the control of the stability of the solutions. However the handling of pneumatic pressure makes the experimental set-up bulky and complicated.

The next microfluidic device which is under progress using PZT-technology may integrate simpler valves which will be actuated by piezoelectric effect using simple voltage (typically 10 to 100 V).

Toward new biological experiments

As aforementioned, biological experiments were conducted and reported with *Ethidium Bromide* which is an intercalating agent commonly used as a fluorescent tag to detect nuclear acids in molecular biology. *Ethidium Bromide* is also well-known to be mutagen. Such type of intercalation reactions interferes with biochemical processes involving protein-DNA contacts such as recombination, replication and gene expression and can induce mutagen cells. Important studies have been carried out to determine molecule binding properties [Vladescu 2007] as well as to develop DNA drugs to prevent mutagen cell proliferation [Hurley 2002].

Paradoxically, active molecules for anti-cancer treatment use reciprocal behavior than mutagen agents. The interest of the biochemist is aroused by the finding that these drugs are, more often than not, inhibitors of nucleic acid synthesis (**Figure** 6.2). Indeed, most of them actually interact physically with DNA so as to distort its structure and function [Waring 1981]. Nowadays development of specific drugs with specific interactions are needed to be designed and tested for less damageable treatment.

Therefore experiments are planned with well-known DNA drugs such as *Netropsin*, *Cisplatin* or *Actinomycin D*.

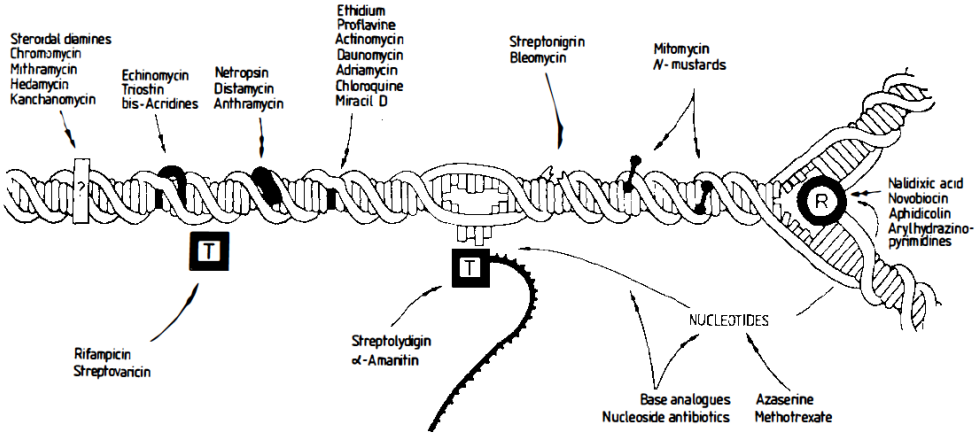

Fig. 6.2. Sites for inhibition of nucleic acid synthesis by antibiotics and drugs. R represents the replicating enzyme complex, T the transcribing enzyme (RNA polymerase). Actions of inhibitors are represented by double-headed arrows and are purely diagrammatic. Image from [Waring 1981].

The primitive objective was to demonstrate the single DNA molecule manipulation and characterization by micro-machined silicon-based tweezers. Finally this work enabled (1) to succeed the complete understanding of the nanotweezers, (2) to perform the real-time monitoring of biological interactions on DNA (in droplets), (3) to develop a microfluidic device inside where the monitoring of the molecules has been achieved, and (4) the implementation of a control strategy which enable to enhance the sensitivity of the system. However, in order to reach the single molecule sensing, new design of the tweezers has also been finished. The single molecule sensing is reachable if the system can accurately constraint to resonate at a frequency 10 times lower than the device one.

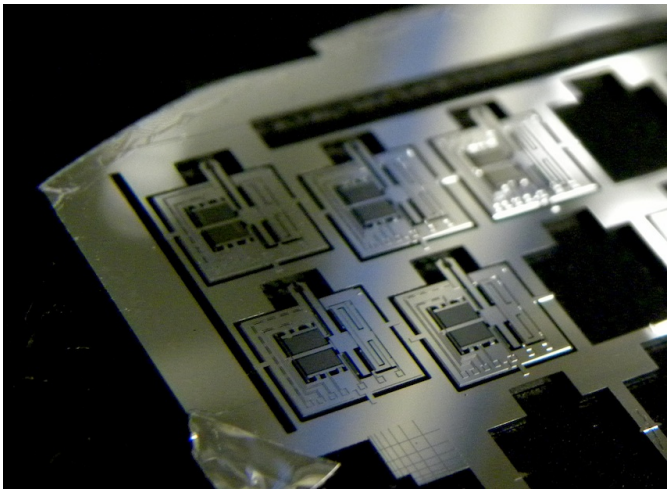

Fig. 6.3. Photography of the newly fabricated tweezers.

A

Simplified process for MEMS tweezers

Process name	DNA tweezers G3 (3^{rd} generation)
Date	January 2009
Author	Dr. Laurent Jalabert (LIMMS Engineer)
Short description	10 µm-gap tweezers for λ-DNA molecule manipulation
Process type	SOI micromachining
Substrate	SOI wafer: 30 µm/2 µm/400 µm, standard resistivity
Masks	2.5″ masks with 2 mm minimum feature
Keywords	SOI, RIE, DRIE, SPM, BHF, TMAH, vapor HF

Summary. This appendix outlines the process necessary for micro manufacturing of the MEMS tweezers. More details can be asked to Dr. Laurent Jalabert (jalabert@iis.u-tokyo.ac.jp).

A.1 Frontside etching

The tweezers are made from SOI wafers with a top Si layer of 30 microns thick ($< 100 >$ oriented), and a BOX of 2 microns as a DRIE stop layer. The wafer is patterned with a 45° angle (in the $< 110 >$ direction).

After cleaning the wafer by a conventional SPM (H_2SO_4:H_2O_2) at 100°C for 20 minutes, and a native oxide removal by BHF (20 seconds), a thin nitride layer SiN is deposited by LPCVD (NH_3:SiH_4) at 800°C for 30 minutes to get $\sim$ 30 nm thin film.

The nitride thin film is patterned by photolithography and dry etching to prevent the Si oxidation (see next steps), similarly to LOCOS process.

The comb drives and capacitive sensor are made on the top side 30 µm-thick SOI layer using a 100 nm-thick Al protection mask for DRIE process.

The wafer is oxidized at 1100°C for 90 minutes in order to protect all the silicon structures with a thick SiO_2 layer ($\sim$ 350 nm) during the tip engineering (that uses wet etching). The SiN layer(30 nm-thick) patterned on the tip area is much less oxidized.

A.2 Tip shaping

To fabricate the sharp tip, the 30 nm-thick SiN is etched by RIE with keeping enough SiO_2 ($\sim$ 300 nm) on the silicon structures. Then the wafer is cleaned by SPM followed by a slight BHF (5 seconds). The wafer is dipped into a TMAH solution, at 70°C for about 1 hour in order to get a sharp tip formation on the $< 100 >$ planes from the previous SiN patterned area. The gap can be adjusted by controlling the over-etching time. Typically, depending on both the initial SiN pattern dimensions and the SOI top silicon thickness, the gap becomes around $\sim$ 10 µm.

A.3 Backside etching

Then the protection SiO_2 layer (300 nm-thick) is etched in BHF, cleaned by SPM again and the native oxide is removed with BHF again. The comb drive, capacitive sensor and the sharp tips are then protected by a SiO_2 thin film (80 nm-thick) during a dry oxidation at 1050°C for 30 minutes. Note that this thin protection layer should not be too thick as it will enlarge also the gap between the silicon structures (comb drives, sensor and tips).

A 150 nm-thick Al is evaporated on top of the wafer, followed by a S1818 spin coated photoresist to protect all the structures during the back side engineering.

The back side is etched by DRIE using a 150 nm-thick Al layer. Then the S1818 and the Al layers (both sides) are removed by acetone and Al etchant respectively. At this step, it remains the BOX oxide (2 µm-thick) that connect all the comb drives and capacitive sensor beams together. Therefore, a final SPM cleaning is possible since it will not damage the thick SiO_2 layer.

A.4 Structure release and aluminum evaporation

Finally, all the SiO_2 layers (BOX and protection layers) are removed by vapor HF and dried in air. This etching induces an under-etching of the SiO_2 BOX layer on the electrical pads. A thin Al layer (50 nm-thick) is evaporated on top of the tweezers for DEP trapping. Due to the BOX under-etching, the thin Al layer does not induce short circuits between the electrical pads.

B

Layout and features of the silicon nanotweezers

Summary. This appendix details the layout and features of the silicon nanotweezers. The important dimensions of the different parts are notified (actuator, sensor, suspensions and tips). The comb-drive dimensions are related to the actuation force (cf. **Equation** 3.2, **Page** 22), the capacitive sensor to the sensing gain (cf. **Equation** 3.6, **Page** 24). Suspensions and mechanical feedback are detailed in **Figure** 3.3. Microfabrication of the tips are explained in **Figure** 3.6.

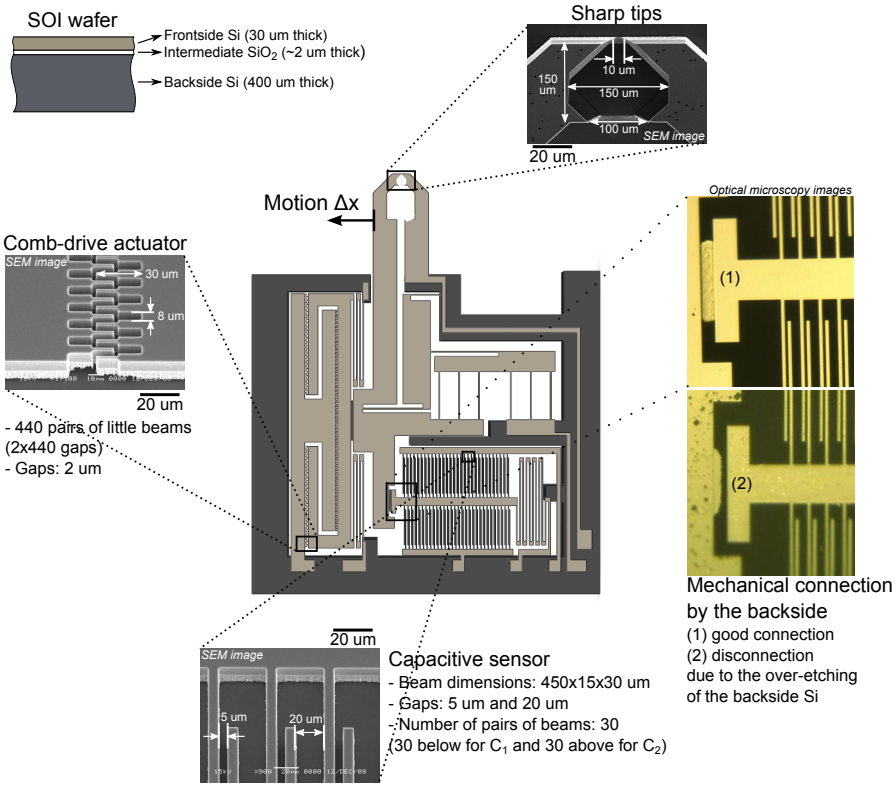

Fig. B.1. General layout and features of the silicon nanotweezers (1).

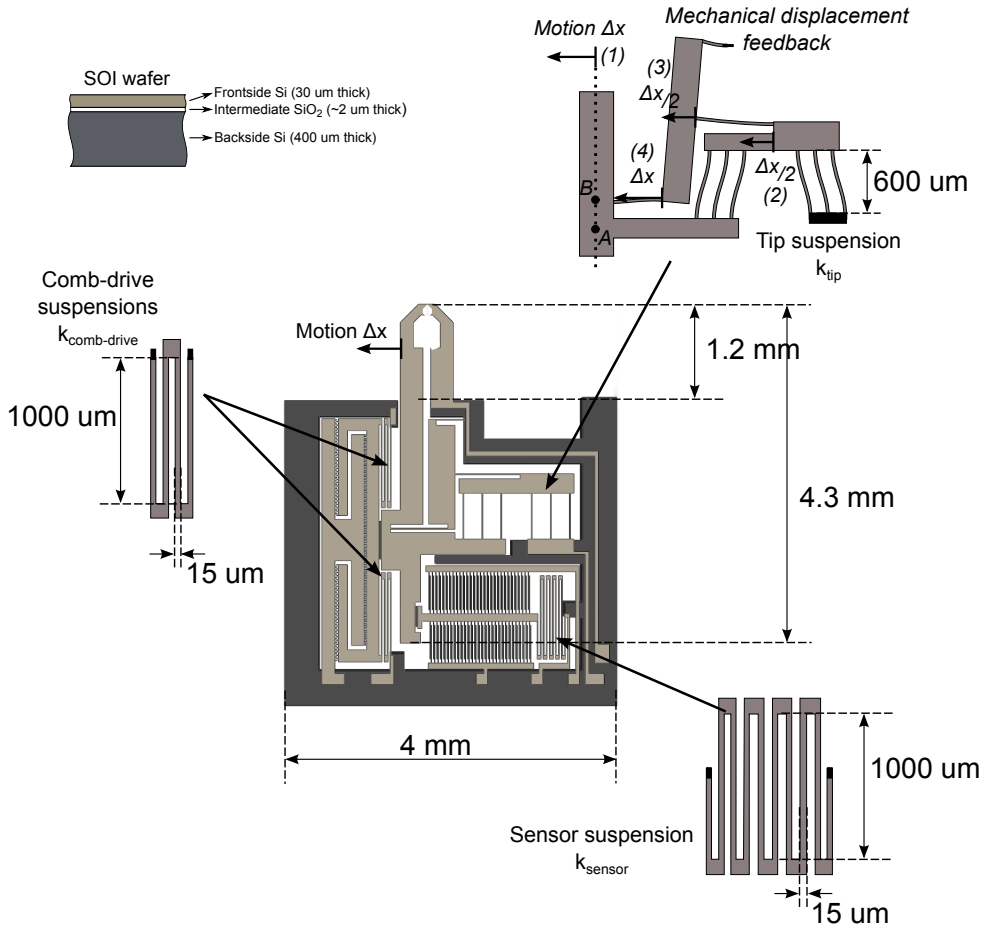

Fig. B.2. General layout and features of the silicon nanotweezers (2). External dimensions: 4 mm × 5 mm.

C

Experimental setup of the silicon nanotweezers

Summary. This appendix shows the experimental conditions of the experiments with silicon nanotweezers. The setup is set in the bio-room of Pr. Fujita (IIS, U. of Tokyo).

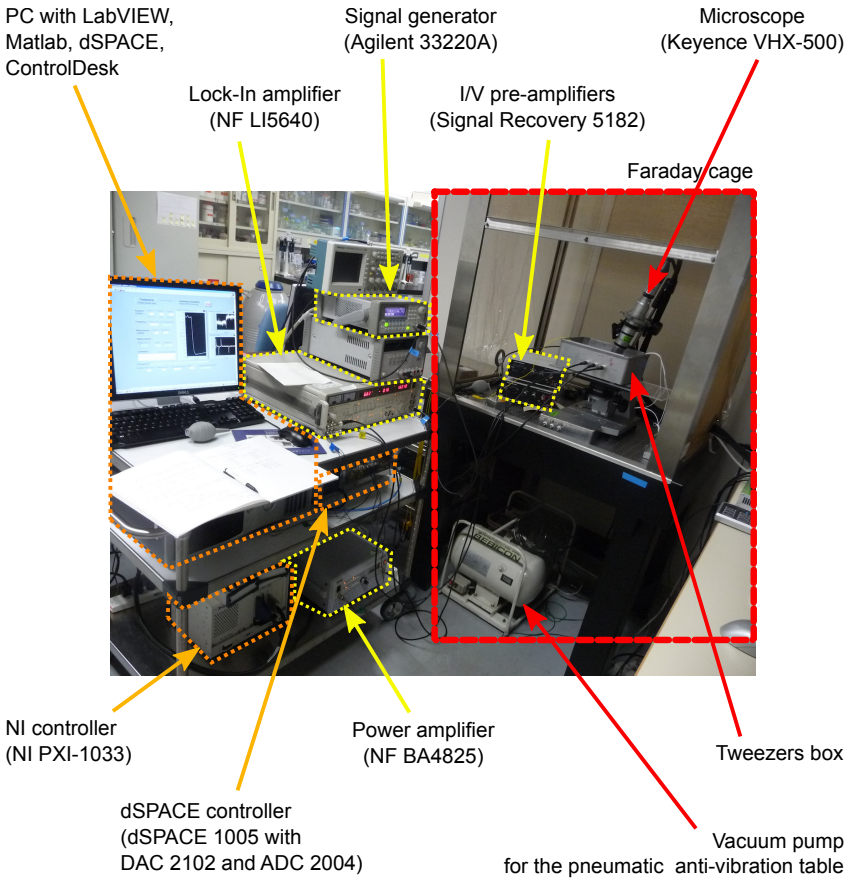

Fig. C.1. Tweezers experimental setup in bio-room.

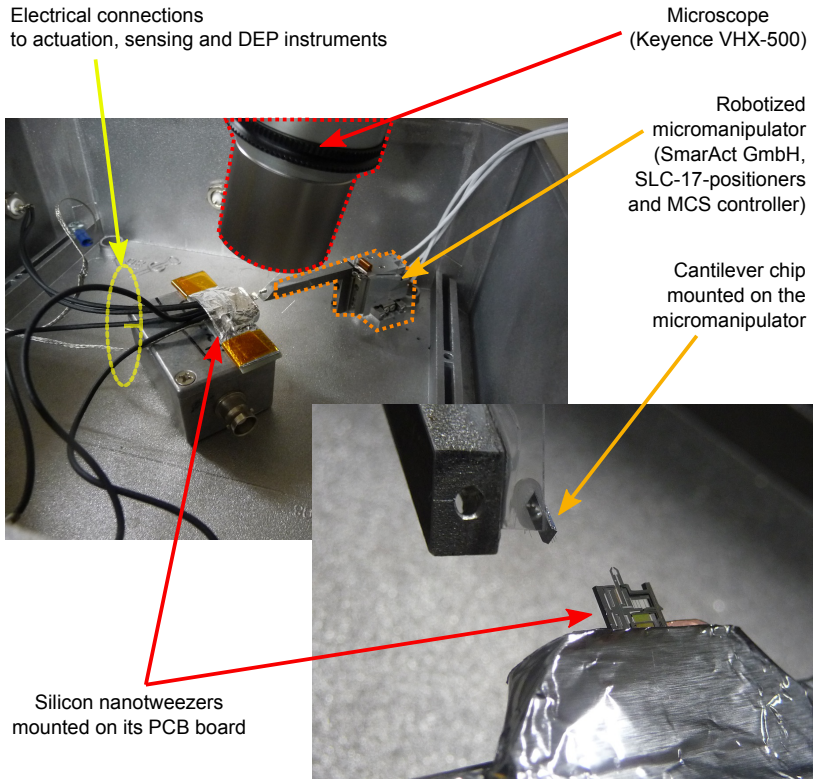

Fig. C.2. Tweezers box of **Figure** C.1.

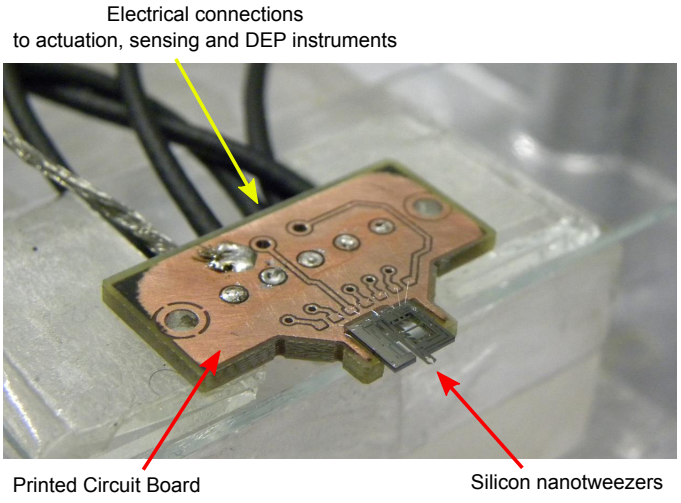

Fig. C.3. MEMS tweezers chip mounted and bonded on a new PCB board.

D

Tweezers characterizations with MEMS Analyzer

Summary. This appendix is here to explain the methodology of tweezers characterizations with MEMS Analyzer of Polytec.

D.1 MEMS Analyzer description

The Micro System Analyzer allows individual or combined in-plane measurements, out-of-plane measurements or topography measurements. It uses light for non-contact measurement of three-dimensional shape and motion in microstructures:

- Laser-Doppler vibrometry for fast out-of-plane dynamics;
- Stroboscopic video microscopy for in-plane motion;
- And white light interferometry for high resolution topography.

For MEMS tweezers motion characterizations, laser Doppler vibrometry for out-of-plane dynamics and stroboscopic video microscopy for in-plane motion will be employed, as explained presently.

Fig. D.1. Micro System Analyzer (MSA-500) from Polytec (www.polytec.com)

D.2 Tweezers characterizations

To precisely measure fast in-plane motion, a stroboscopic technique is applied. Using stroboscopic illumination and digital imaging, motions of fast moving objects can be sharply frozen in time to capture the exact position of the object. Short light pulses synchronized with the periodic motion capture the position at precise phase angles. By shifting the timing of these pulses by phase angle increments, the motion of a moving object can be sampled and reconstructed. **Figures** D.2 and D.4 show the shape tracking (inside the yellow frame) for motion characterizations. Image processing allows to plot shape displacements along x-axis and y-axis (**Figure** D.2).

Stroboscopic technique allows motion measurement with frequencies up to 1 MHz and optimized microscope optics provide nanometer resolution.

D.2.1 Step response characterizations

Dynamics of the MEMS tweezers have been characterized performing through positive and negative step responses. **Figure** D.3 shows the data acquired optically thanks to the MEMS analyzer. It appears that there is no displacement along the y-axis. Several glitches (of 100 nm) are due to the image processing (green line). The displacement is characterized along the y-axis, which is the actuation force direction.

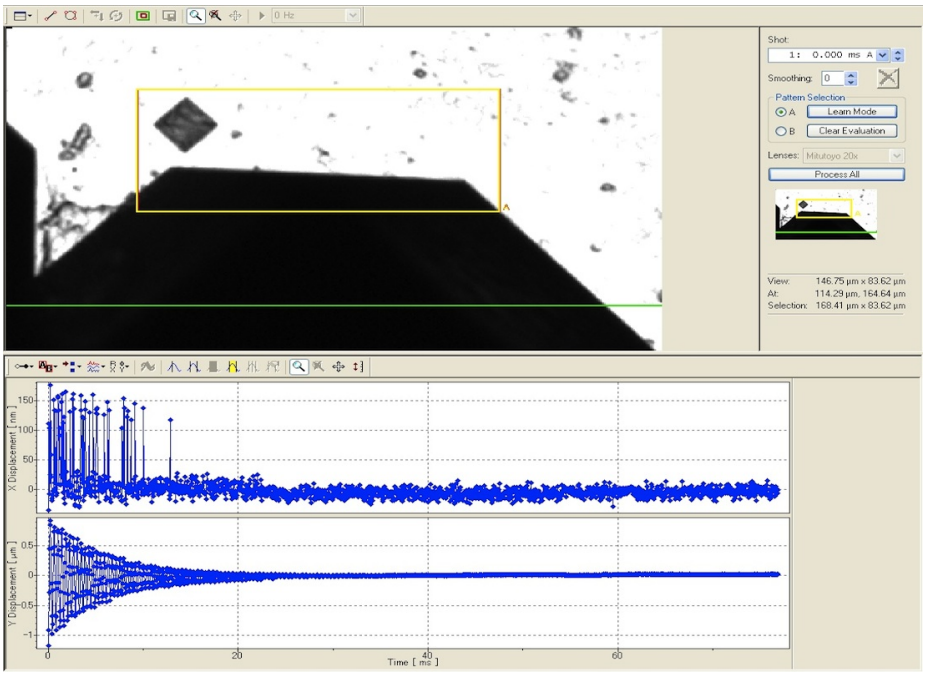

Fig. D.2. Tweezers time step characterization with MEMS Analyzer (Polytec). 30 to 0 V negative step response of the tweezers. Screenshot of Polytec software. (Tweezers JST33).

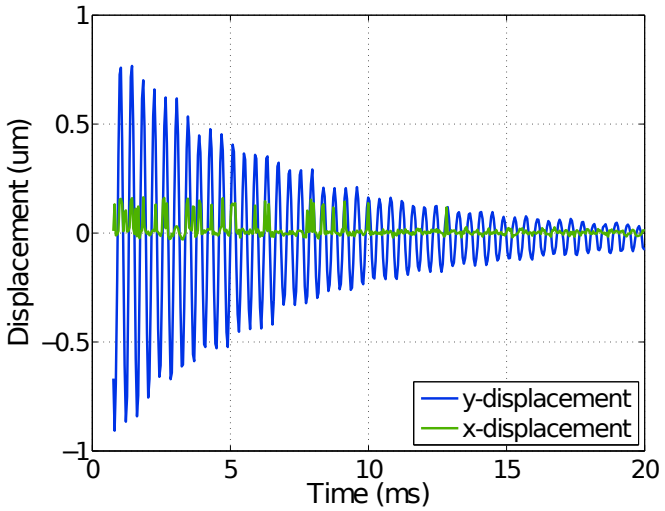

Fig. D.3. 30 to 0 V negative step response characterization of the MEMS tweezers with MEMS Analyzer (Polytec). (Tweezers JST33).

D.2.2 Frequency response characterizations

The characterizations with step responses do not allow easy observation of unexpected dynamics. Others dynamics (if be) are hidden by the important oscillations of the principal mode. A frequency characterizations is performed to observe dynamics into a predefined bandwidth (**Figure** D.4).

Figure D.5 shows semilog plot of the characterizations with MEMS analyzer tool. The main resonance frequency is observed at 2460 Hz, corresponding to the oscillation frequency observed during step excitations. Another in-plane motion resonance is observed around 6370 Hz. In-plane motion modes can be clearly characterized thanks to smooth phase shift of 180°. Before 2460 Hz, the phase shift of the response is 0 ° with the actuation signal. After 2460 Hz. the response is 180° delay shift. After 6370 Hz, the response signal is once again 180° shifted. This in-plane resonance is confirmed by the video recorded by the MEMS analyzer.

In addition, several glitches can be observed on displacement and the phase plots. These glitches are due to the image processing which is not able to track well the shape for these points. Indeed, at these frequencies, the tweezers tip moves out-of-plane causing defocusing and blurring of the images.

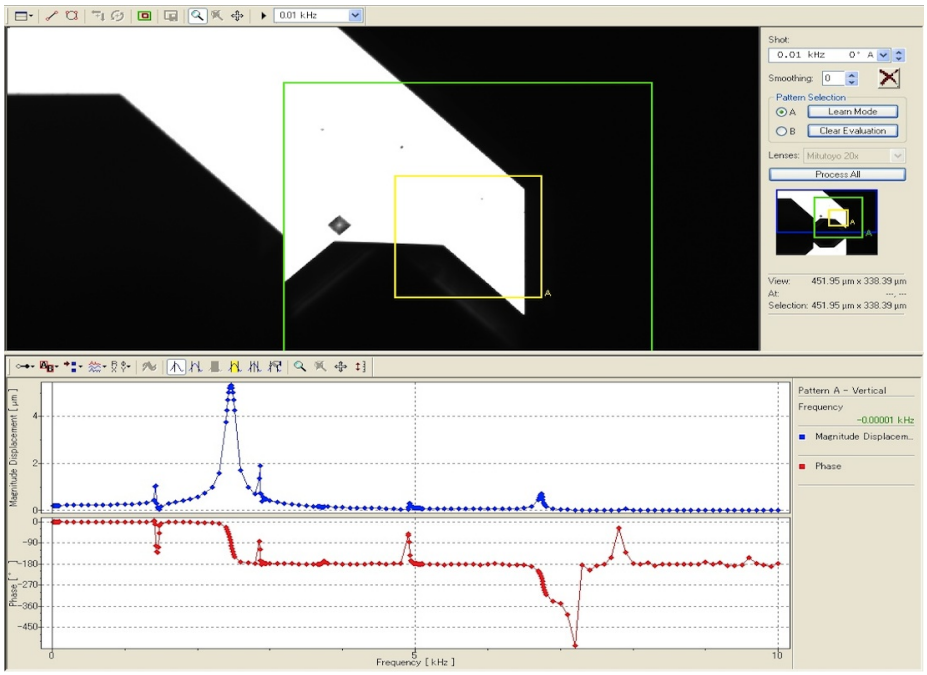

Fig. D.4. Tweezers frequency characterizations with MEMS Analyzer (Polytec). Screenshot of Polytec software. (Tweezers JST33).

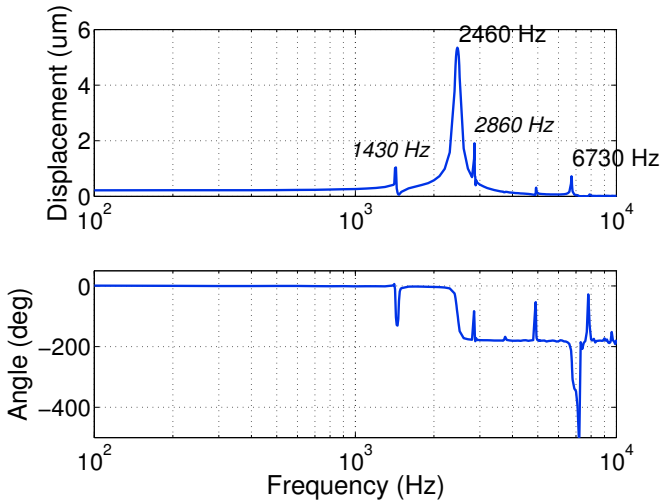

Fig. D.5. Motion dynamics characterizations with stroboscopic video microscopy (MEMS Analyzer, Polytec). 10 V_{pp} AC excitation. (Tweezers JST33).

D.3 Out-of-plane motion characterizations

Previous frequency characterizations revealed different unexpected dynamics:

1. In-plane dynamics (e.g. at 2460 Hz and 6730 Hz) which is in the analyzed plane (xy-plane);
2. And other dynamics which are not well analyzed by the image processing (e.g. at 1430 Hz).

Figure D.6 shows the motion videos of the 3 main observed dynamics. The images of the 1430 Hz shows an out-of-plane motion leading to a periodic focusing and de-focusing of the tip. This explains the erratic image processing provided by the shape tracking and image processing. The images of the 2460 Hz demonstrate the larger displacement amplitude along the direction y-axis (i.e. the actuation direction). It justifies to be the principal resonance of the tweezers. The images of the 6730 Hz reveals another resonance in the plane combining motion mainly in the x-axis with a little motion in the y-axis.

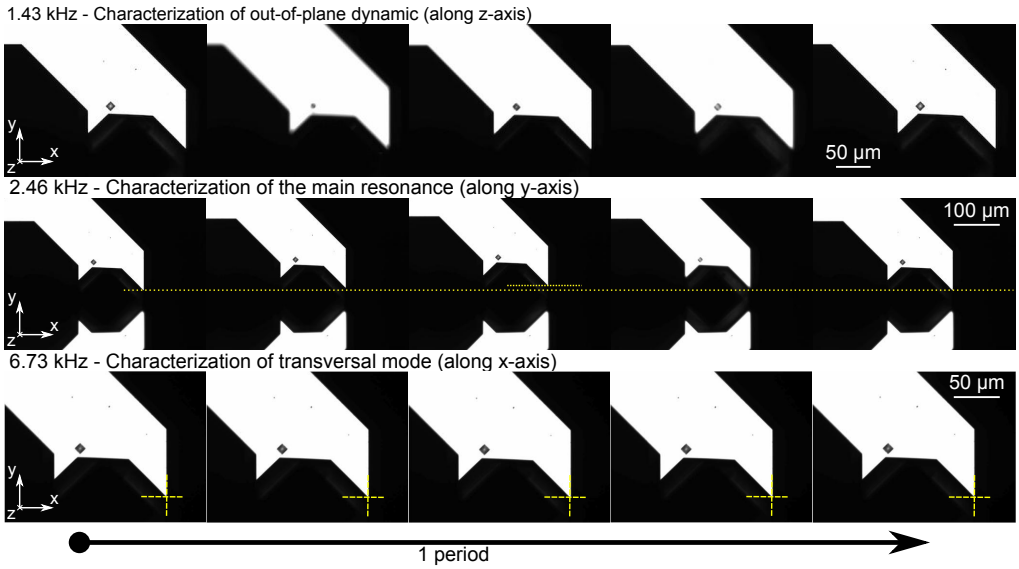

Fig. D.6. Stroboscopy video images of the tweezers dynamics (MEMS Analyzer, Polytec). Frequency characterization with 10 V_{pp} sinus excitation. (Tweezers JST33).

Figure D.7 shows analysis of the 1430 Hz-dynamic by laser Doppler technique. With this technique, we were able to confirm the dynamics which have a motion component along the z-direction.

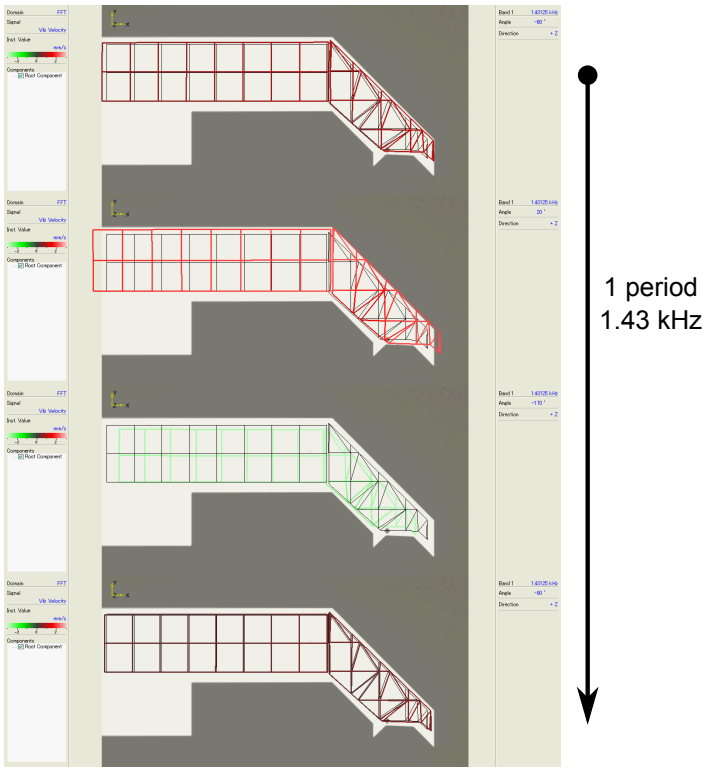

Fig. D.7. Out-of-plane motion characterization of the tweezers by laser Doppler (MEMS Analyzer, Polytec). The tip structure is meshed by the user such all the corners of the mesh are one after one analyzed with the laser. 10 V_{pp} sinus excitation. (Tweezers JST33).

E

Finite element simulations with COMSOL Multiphysics

Summary. This appendix shows COMSOL simulations of the mechanical structure of the nanotweezers. The study helps to understand the dynamics due to the spatial distribution of the mass and the suspensions which have been neglected so far for the device modeling.

E.1 Finite element modeling of the device

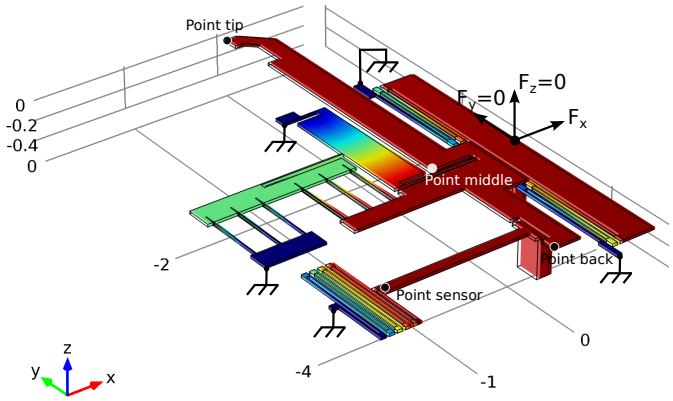

Fig. E.1. Layout of the device in COMSOL Multiphysics. All the boundaries are free except for (1) the 5 faces which are fixed constraint with the underneath bulk silicon and (2) the rightmost face which is actuated by a force F_x along x-axis. Dimensions are in millimeters.

All the movable parts of the nanotweezers were exported to COMSOL Multiphysics from the layouts of the microfabrication masks (**Figure** E.1).

The geometries etched in the frontside silicon are extruded with a thickness of 30 µm. In the bulk silicon are etched the mechanical connection between the three different parts actuator to tip and tip to sensor (cf. **Paragraph** 3.2.2 and **Figure** 3.4). The two

blocks are extruded with a thickness of 400 µm. The thin SiO_2 layer of 2 µm is neglected and is not considered in the following simulations, because we suppose it does not play a mechanical role as long as it holds the front face with the back face. Accordingly, the material is the same for every parts, that is to say silicon with the following parameters for structural simulations:

Young's modulus	$E = 165$ GPa
Poisson's ratio	$\nu = 0.3$
Mass density	$\rho = 2330$ kg/m^3

Table E.1. Silicon parameters for structural simulations [Dolbow 1996].

All the boundaries are *Free* except for:

- the 5 faces which are *Fixed constraint* with the underneath bulk silicon;
- and the rightmost face which is actuated with a *Boundary load* F_x according x-axis.

E.2 Finite element simulations

Finite element method (FEM) are performed in order to characterize phenomena which are neglected by the theory adopted for the modeling. Either static or dynamic simulations have been conducted.

E.2.1 Static simulations

Static simulations allow to define the stiffness of the system and evaluate the assumption that the tweezers' tip is moving along the x-axis. **Figure** E.2 shows the linear displacement of 3 distinct point of the tip in function of the force intensity. The displacement at the level of the tip is 0.5 nm (on 7.5 nm) more important than at the opposite side of the tip (*Pt back*).

Table E.2 gives the displacements of the different evaluated points. Displacements along y- and z- are de facto not significant in comparison to x-displacements. However as aforementioned, x-displacements are not homogenous leading to a small rotation ($< 0.01°$) of the tip according to the z-axis.

For the equivalent stiffness in the x-direction, we evaluated the displacement of the *middle* of the tip where the comb-drive is applied.

$$k_x = \frac{1.10^{-6}}{7.33.10^{-9}} \simeq 136.43 \text{ N/m} \tag{E.1}$$

The difference with the theoretical value (126.45 N/m) is due to the effect of the parallelogram used as a mechanical feedback in the calculation of the stiffness (cf. **Paragraph** 3.2.1). When simulations are conducted without the parallelogram, the equivalent stiffness becomes 122.50 N/m. Finally these first simulation results are in agreement with the simple model obtained from the small bending of the suspension beams.

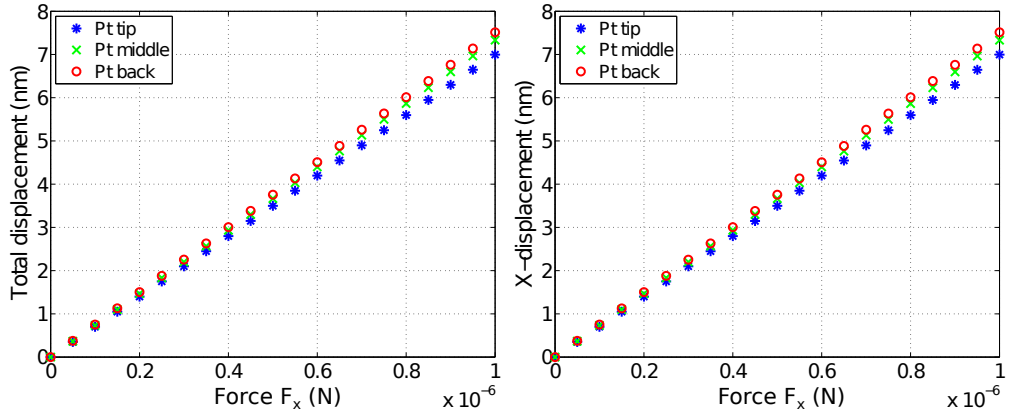

Fig. E.2. Stationary simulations applying force on the comb drive geometry. Pt tip, Pt middle and Pt back correspond to points informed in **Figure** E.1.

Such kind of simulations may be helpful to predict structural deformations of such complex devices. Regarding mechanical stiffness concern, the tweezers are designed such as to show small stiffness for the characterization of small biomolecules and minimum mass for fast and sensitive system.

Point	Total disp. (nm)	x-displ. (nm)	y-displ. (nm)	z-displ. (nm)
Tip	7.51	7.51	0.15	< 0.02
Middle	7.33	7.33	0.15	< 0.02
Back	7.00	7.00	0.14	< 0.02

Table E.2. Static displacements for $F_x = 1$ µN.

E.2.2 Eigenfrequency studies

Next eigenfrequencies of the structure were studied to evaluate the modes of the structures. The simple modeling of the device based on the consideration of a single mass and stiffness just allow to predict one dynamic of the device.

Figure E.3 shows the first four modes of the structure. Results demonstrate that the two first dynamics are not the expected one and show out-of-plane (i.e. out of xy-plane) motions. Therefore the third eigenfrequency is the frequency of the mode in which the device is intended to work. The fourth eigenfrequency is another mode with out-of-plane motion.

Knowing the desired resonance frequency and the stiffness in the x-direction, we are able to identify the inertia of the device with the following equation (derived from the **Equation** of the resonance frequency of a second order mechanical system):

$$M = \frac{k_x}{(2\pi.f)^2} = \frac{136.43}{(2\pi \times 3338.78)^2} \simeq 310 \times 10^{-9} \text{ kg} \tag{E.2}$$

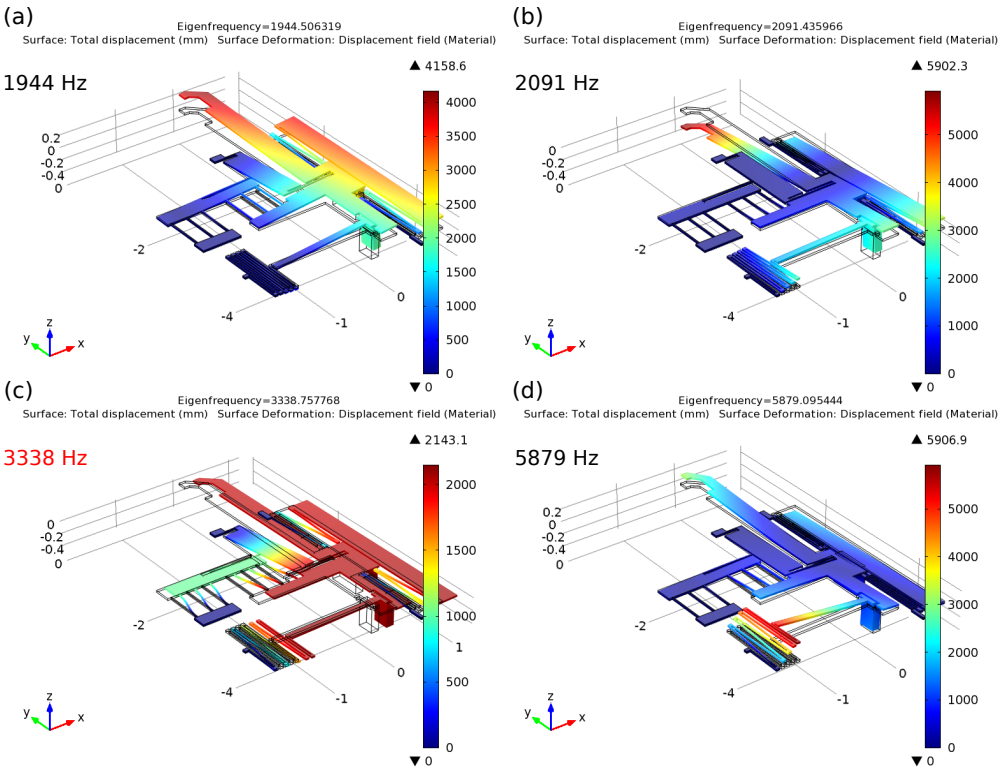

Fig. E.3. Eigenfrequency simulations of the mechanical structure of the nanotweezers. The first 4 modes of the structure are shown.

However the expected frequency (3338 Hz) differs considerably from the experimentally characterized one around 2500 Hz.

Table E.3 summarizes the eigenfrequencies of the device for several dimensions of the suspensions. Suspensions widths and thicknesses are important parameters for explaining the wide variation of the device characteristics. Width w and thickness t are at the cubic power for the calculation of the mechanical stiffness of a bending beam. Furthermore their sizes are small enough to be very dependent to fabrication processes.

By optical characterizations, width can vary from 10 to 14 µm and silicon thickness from 27 to 30 µm. The thickness of the silicon is a more stable dimension than the widths of the beams. However first tweezers were fabricated with {**27**/2/400 µm}-layer SOI wafer, when new tweezers are fabricated with {**30**/2/400 µm}-layer SOI wafer.

E.2.3 Frequency domain simulations

Although previous studies has enabled to characterize unintended dynamics, the tweezers' tip is supposed to be actuated only in the x-direction such as the other modes are not stimulated. The effect of the device's mass can induce forces in the z-direction.

The study has been conducted with the dimensions $t = 27$ µm and $w = 12$ µm which allow to compare the frequency dynamics with the bode diagram experimentally obtained with the MEMS analyzer (**Figure** D.4).

Dimensions	1st eigenfreq.	2nd eigenfreq.	**3rd eigenfreq.**	4th eigenfreq.
$t = 30$ µm (new SOI wafer)				
$w = 15$ µm	1944	2091	**3338**	5879
$w = 13$ µm	1778	1948	**2680**	5879
$w = 10$ µm	1525	1701	**1849**	4180
$t = 27$ µm (previous SOI wafer)				
$w = 13$ µm	1596	1754	**2634**	5144
$w = 12$ µm	1606	1763	**2422**	5154

Table E.3. Eigenfrequencies of the mechanical structure of the nanotweezers according to the suspension width w and the silicon thickness t.

Frequency simulations have been performed applying a force of 1 nN in the x-direction homogeneously distributed on the rightmost face of the device (which correspond to the face electrostatically actuated). **Figures** E.4 and E.5 demonstrates the motion dynamics of the device in function of the frequency. These results in nanometers are qualitative and not quantitive since the simulations were performed with a default damping factor.

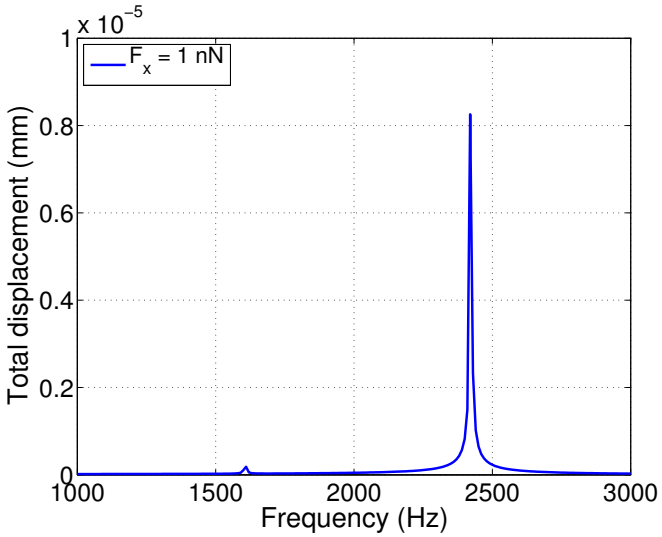

Fig. E.4. Frequency domain simulations of the mechanical structure of the nanotweezers (1). The force F_x is applied in the x-direction such as the comb-drive actuator theoretically works (cf. **Figure** E.1).

Figure E.4 evidences that the intended resonance is mainly stimulated when a force is applied according the x-direction. However it is possible to notice that the first mode at 1596 Hz is also stimulated. The second mode does not appear. **Figure** E.5 confirms the presence of the two modes. The frequency diagrams about the x- and z-displacements

confirm that at 1596 Hz the tip essentially resonates in the z-direction (and not in the x-direction).

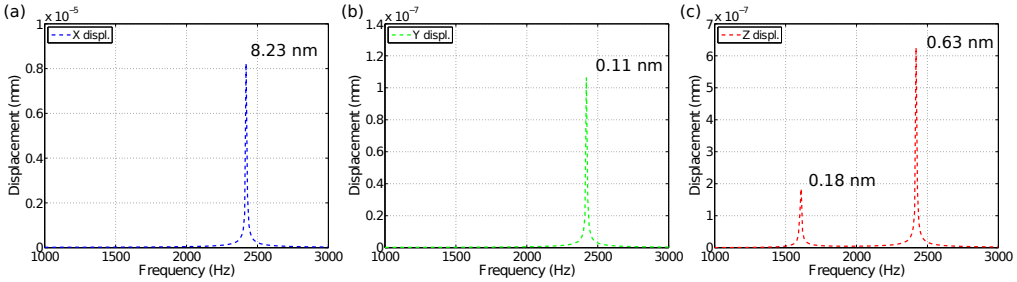

Fig. E.5. Frequency domain simulations of the mechanical structure of the nanotweezers (2). The total displacement is broken in displacements along x-, y- and z-axis, respectively graphs (a), (b) and (c).

E.3 Simulations of the dynamic sensitivities

Previous simulations reveal several possible dynamics for the mechanical structure. Here we attempt using finite element method to demonstrate:

- the pertinence to drive the intended mode rather than the other modes;
- the sensitivity of the intended mode for the characterization of the mechanical parameters of molecules.

The DNA molecules are simulated changing the boundary conditions in place where the molecules are trapped. The studies are conducted assigning *Spring Foundation* and *Added mass* at the end of the tip (**Figure** E.6). A single λ-phage DNA molecule[1], which are the molecules of interest in the bioexperiments performed with the tweezers, has a rigidity of about 30×10^{-6} N/m and a mass of about 50×10^{-21} kg.

Figure E.7 shows the evolution the frequency of the first four modes of the tweezers. Results prove that the third mode (moving in the x-direction) is the more sensitive for the characterization of mechanical stiffness at the end of the tip.

Studies have been extended to equivalent stiffness in the y- and z-directions, and likewise to added mass. **Table** E.4 summarizes a sample of results to compare the sensitivity of all the modes depending on the conditions. The frequency shifts for 1 N/m (which represents about 30 thousands of λ-DNA molecules) in y- and z-directions and for 1×10^{-9} kg (which represents about 20 billions of λ-DNA molecules) are not significant in comparison with the shift of the frequency of the third mode for stiffness in the x-direction.

Furthermore the sensitivity of the intended mode is compared to the theoretical curve based on an equivalent mass-spring-damper system and using **Equation** E.3. For little

[1] λ-DNA molecules are about 16.5 µm-length and contains about 48.500 nucleobase base pairs (48.5 kbp).

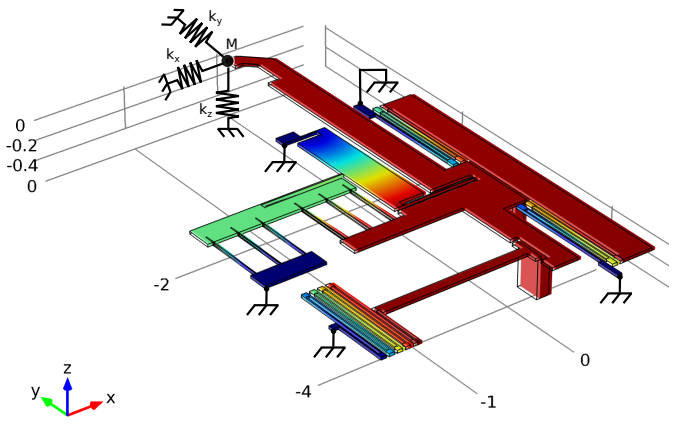

Fig. E.6. Layout of the device in COMSOL Multiphysics. The mechanical effect of the DNA bundle is imitated by a punctual boundary condition at the end of the tip. The equivalent stiffness is represented with a spring with components according the 3 axis (k_x, k_y and k_z), and the mass is represented with an added mass (M). Dimensions are in millimeters.

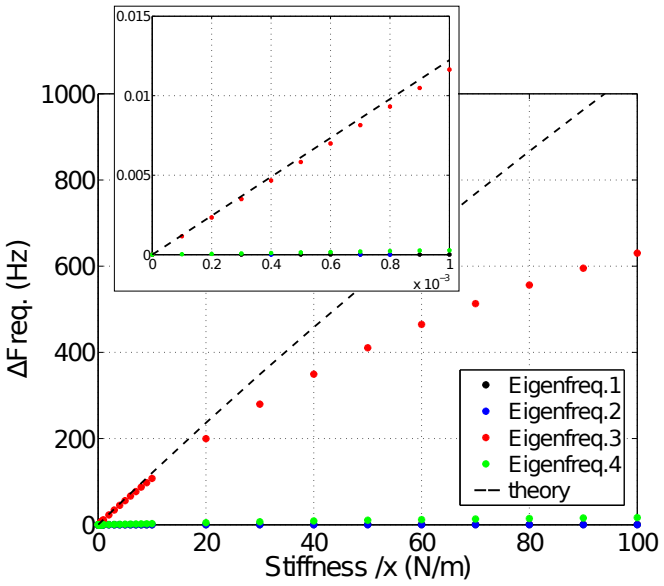

Fig. E.7. Eigenfrequency simulations of the mechanical structure of the nanotweezers according to DNA molecule mechanical parameters. DNA molecules are simulated with a stiffness k_x along the x-direction. Theoretical curve is calculated from **Equation** E.3.

extra stiffness ($k_{\mathrm{DNA}} < 1$ mN/m), the simple model is in agreement with the FEM simulations. Afterwards, the mode is less sensitive than the model predicts.

$$\Delta f = \frac{1}{2\pi}\sqrt{\frac{k + k_{\mathrm{DNA}}}{M}} - \frac{1}{2\pi}\sqrt{\frac{k}{M}} \tag{E.3}$$

where $k = 136.43$ N/m and $M = 310 \times 10^{-9}$ kg.

Mechanical parameters	1st eigenfreq.	2nd eigenfreq.	**3rd eigenfreq.**	4th eigenfreq.
k_{DNA}				
$k_x = 1$ N/m	< 0.1 Hz	< 0.1 Hz	11.5 Hz	0.3 Hz
$k_y = 1$ N/m	0.6 mHz	8.1 mHz	5.6 mHz	< 0.1 mHz
$k_z = 1$ N/m	17.6 Hz	207.3 Hz	0.2 Hz	39.1 Hz
M_{DNA}				
$M = 1 \times 10^{-9}$ kg	-8.6 Hz	-31.6 Hz	-5.2 Hz	-51.9 Hz

Table E.4. Eigenfrequency simulations of the mechanical structure of the nanotweezers according to DNA molecule mechanical stiffness k_{DNA} and mass M_{DNA}.

E.4 Conclusion

These FEM studies allowed to:

1. understand the key parameters involving performance variation between the designed and the real device;
2. evaluate the other dynamics of the mechanical structure;
3. and to measure the sensitivities of the device for characterization of mechanical parameters at the end of the tip.

It appears that in the designed configuration, the nanotweezers is suitable for the characterizations of small mechanical stiffness using the dynamic of the motion in the plane (especially in the x-direction, cf. **Figure** E.1).

F

Tweezers characterizations with force sensor

Summary. This appendix is here to explain the methodology of tweezers characterizations with force sensor FT-S540 of Femto-Tools.

F.1 FT-S540 force sensor description

The FT-S540 force sensor is a load cell for measuring forces with micronewton resolution (**Figure** F.2). Both compression and tension forces can be measured. The sensor element, which is based on single crystalline silicon, measures the load by a change of capacitance. A readout electronics is integrated in the sensor package converting the load into an output voltage proportional to the force.

The characteristics of the sensor are summarized into the **Table** F.1. The principle of the sensor have been explained and published in [Beyeler 2008, Beyeler 2009].

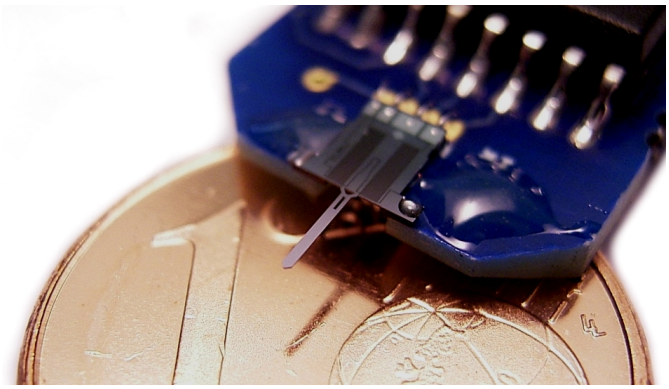

Fig. F.1. FT-S540 force sensor from Femto-Tools (www.femtotools.com).

Characteristics	Typical	S-2501	S-2502
Force range (µN)	180		
Sensitivity (µN/V)	90	85.03	88.38
Output signal (V)	0-5		
Ouput at zero load (V)	2.25		

Table F.1. Performance characteristics of the FT-S540 force sensor.

F.2 Tweezers stiffness characterizations

Sensor stiffness characterization

The experimental set-up is composed of the force sensor and a 3-axis nanometric manipulator, which provides a precise and accurate measurement of the displacement. Indeed, the manipulator is built from 3 SLC-1720 positioners of SmarAct GmbH (www.smaract.de) for displacements along 3 orthogonal axis. The positioners integrated sensor with nanometer resolution and are characterized by their high rigidity and straightness (block force informed > 3 N).

Since the objective is to characterize device rigidity and only the force sensing characteristic is informed, a first experiment should allow the characterization of the sensor rigidity. Knowing the spring topology of the sensor and the dimensions of the springs, a theoretical value is calculated. The sensor rigidity is given by 4 clamped-guided beams with $540 \times 10 \times 50$ µm dimensions. The equivalent stiffness considering the silicon Young's modulus equal to 165 GPa is approximatively 210 N/m (**Equation** F.1). *slope* is the slope of linear fit, and S is the sensitivity of the sensor.

$$k_{\text{sensor}} = 4 \times \frac{12EI}{L^3} = 4 \times \frac{12E\frac{w^3 t}{12}}{L^3} \sim 210 \text{ N/m} \tag{F.1}$$

The sensor is sticked on the manipulator and position orthogonal to a surface, which is part of a heavy object (> 1 kg). With the manipulator, 10 nm step displacements are applied from 0 to 1.4 µm and from 1.4 to 0 µm. **Figure** F.2 shows the force linear increase, $k_{\text{sensor}} \times x$, from no-contact to sensor saturation back-and-forth. No hysteresis is observed during this experiment. From the slope of the curve, the stiffness of the sensor is figured out as 195.6 N/m $\pm$ 1.9 N/m (**Equation** F.2).

$$k_{\text{sensor}} = slope \times S = 2.30 \times 10^{-3} \times 85.03 \times 10^{-6} = 195.6 \text{ N/m} \tag{F.2}$$

Tweezers stiffness characterization

Knowing the sensitivity and the spring constant of the sensor, the same experiment is performed on the compliant structures of the MEMS tweezers. **Figure** F.3 shows the approach and the contact of the sensor probe toward the movable tip of the tweezers.

It assumes that the displacement is accurately provided by the robotized manipulator on which the force sensor is mounted, and that the bulks of the tweezers' chip and the sensor's chip are at the ground reference, such as the springs of the force sensor and the tweezers are in series. The spatial distribution of the stiffness is therefore neglected.

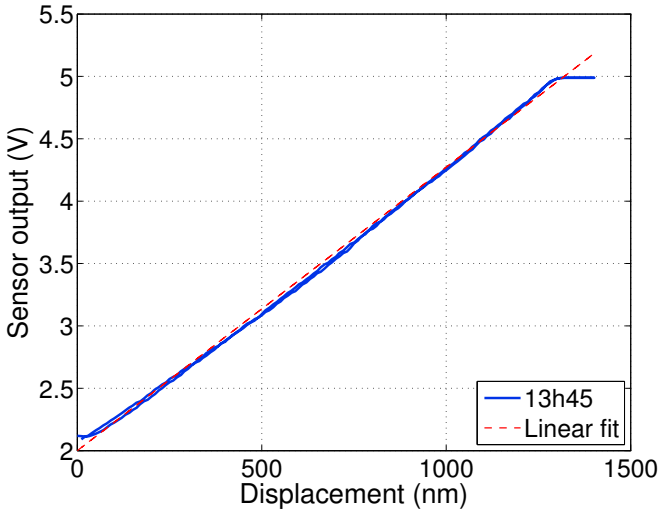

Fig. F.2. FT-S540 (S-2501) force sensor characterization.

Consequently we expect the output sensing to be linearly depending to the following force:

$$F = \frac{k_{\text{sensor}} k_{\text{tweezers}}}{k_{\text{sensor}} + k_{\text{tweezers}}} \times x \tag{F.3}$$

Figure F.4 shows several tries from no-contact to output saturation. A little hysteresis is seen between the forward and the backward paths. Moreover, characteristic forces of pull-off are observed before the contact and during the release (> 40 µN if we considered the minimum recorded output).

Considering the mean slope of the curves (0.41 V/µm), we deduced a system stiffness of 34.9 N/m, and therefore a tweezers stiffness of 42.4 N/m (**Equation** F.4).

$$k_{\text{tweezers}} = \frac{k_{\text{sensor}} k_{\text{system}}}{k_{\text{sensor}} - k_{\text{system}}} \tag{F.4}$$

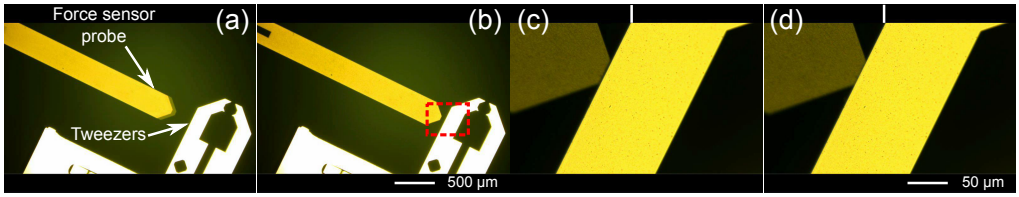

Fig. F.3. Video sequences of force sensing on MEMS tweezers. (a-b) Approach of the force sensor probe toward the movable tip of the tweezers. (c-d) Contact and force application between the force sensor and the tweezers tip. White line are supposed to help the reader to see the relative displacement of the tip despite the sub-micrometric displacement.

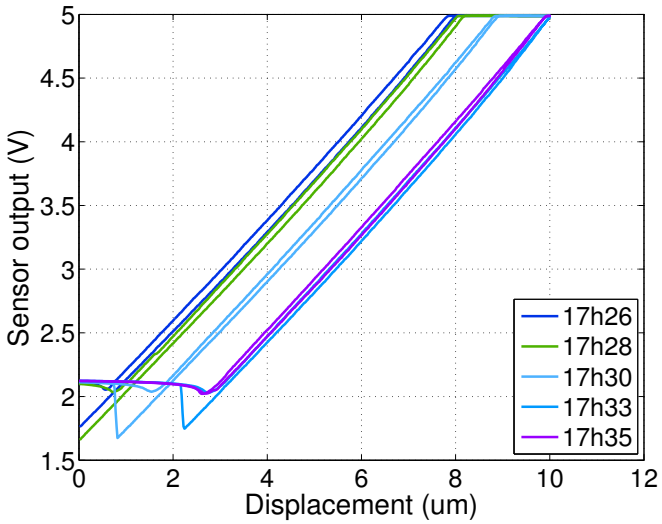

Fig. F.4. Tweezers stiffness characterizations with FT-S540 force sensor.

Tweezers out-of-plane stiffness characterization

The rigidity of the tweezers in the "working" direction have been characterized previously. The rigidity of the movable structure out-of-plane can also be studied. Those characterizations try to spread the understanding of the device behavior. The experimental set-up is the similar to the previously described despite the fact that the force sensor is positioned orthogonal to the tweezers chip in order to apply a normal force to the tweezers structure.

Once again the spatial distribution of the stiffness is neglected. Considering it, the equivalent stiffness analyzed with the force sensor must be different according to the force application point. For this experiment, the sensor is applied at the middle of the tweezers' tip where the center of mass is supposed to be (according to layout design).

Figure F.5 shows 3 tries similar to previous ones from no-contact to output saturation. Repeatedly, the characteristic forces of pull-off are observed before the contact and during the release. The minimum recorded output is limited by the lower saturation limit (0 V), i.e. forces superior to 180 µN.

From the mean slope of the curves (0.24 V/µm), we deduced a system stiffness of 20.4 N/m, and therefore an out-of-plane stiffness of 22.8 N/m (**Equation** F.4).

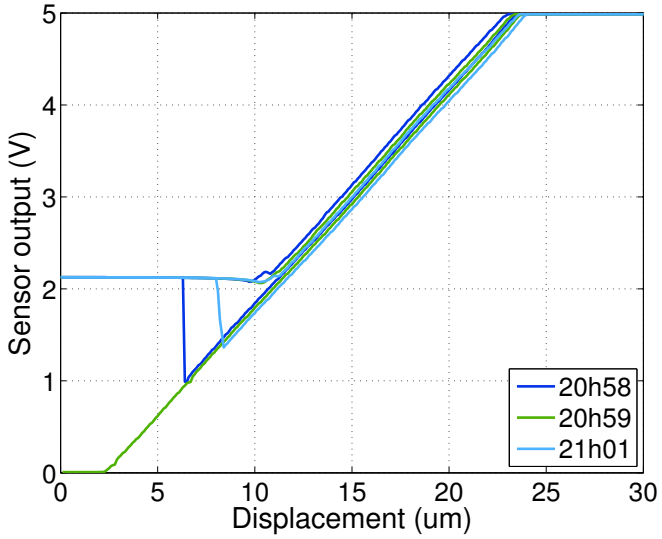

Fig. F.5. Tweezers out-of-plane stiffness characterizations with FT-S540 force sensor.

G

Microfluidic fabrication process

Process name	Active microfluidic fabrication
Date	January 2010
Author	Dr. Moeto Nagai (Former Fujita lab. PhD student) & Nicolas Lafitte (LIMMS PhD student)
Short description	Integration of pneumatic valves into PDMS microfluidic device
Process type	PDMS
Substrate	SOI wafer: 30 µm/2 µm/400 µm, standard resistivity
Masks	2.5″ masks with 2 mm minimum feature
Keywords	SU-8 photoresist, AZ-(4903) photoresist, PDMS, replicate molds, HDMS

Summary. This appendix outlines the process necessary for fabricating the molds and chips for two layer active microfluidic devices. Spin curves for AZ-4903 and SU-8 are included. More details can be asked to the author (lafitte@iis.u-tokyo.ac.jp).

G.1 Flow wafer fabrication

The flow wafer will be fabricated using positive photoresist, compatible with multilayer soft-lithography valves. Compatible photoresists are AZ 4620 for channels $\sim 10-20$ µm tall, AZ 4903 for channels $\sim 20-30$ µm tall, or AZ 50XT for channels $\sim 25-50$ µm tall.

Resist Properties: AZ-4903 is a thick positive photoresist, sensitive to g, h, and i line wavelengths.
Procedure:

1. Clean wafers. Piranha is not necessary for positive resist. A simple cleaning process is to rinse with acetone, methanol and ISO (isopropanol), then dry with nitrogen. Place the wafer on a hotplate at 200°C for about 5 minutes to dry the wafer.

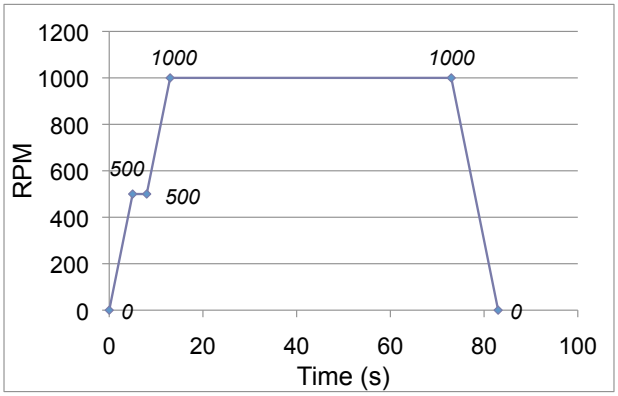

Fig. G.1. Spin coating profile (AZ photoresist).

2. Apply adhesion promoter containing HMDS to the wafer with a pipette while spinning your wafer at above 1000 r/min. Higher speed is better.
3. Coat the wafer with AZ-P4903 positive resist. Coat only about 30% of the wafer. This reduces the edge beading effect. The spin speed determines the thickness. Refer to **Figure** G.1. Based on the amount of thickness required multiple coatings can be performed.
4. Place the wafer for 10 minutes at room temperature. Put them on a hotplate and ramp at 100°C/h from room temperature (20°C) to $\sim$ 110°C. Keep the wafers at 110°C for 1 hour.
5. Allow the wafer to rest for at least 1 hour after baking before exposure.
6. Expose the wafer for 60 seconds with the flow layer mask (30 mW/cm^2). Exposure time should be divided into several times for reducing the effect of Joule heating. It is also possible to slightly longer exposures to improve development.
7. Develop photoresist with diluted AZ-400K developer or NMD-3. Use $\sim$ 1 : 3 AZ-400K developer:water in a glass dish, and agitate for a couple minutes until fully developed. Rinse with water and dry with nitrogen.
8. The development takes approximately 3 minutes in the developer solution to develop. This time may slightly vary based on the amount of resist and non-resist area desired on the wafer.
9. Rinse the wafer well under DI water.
10. Inspect the wafer under the microscope for proper resist development. If residual resist is found repeat steps 7 and 8 untill a good pattern transfer is obtained.
11. To reflow the resist –i.e. to give the channel is a round cross section (**Figure** 4.5)– place them on a hotplate and ramp at 100°C/h from room temperature (20°C) to $\sim$ 150°C. Since AZ is sensitive to rapid thermal heat, take care a thermal heating. After that, let the wafer bake for a couple of hours.
12. *Optional: if you're patterning SU-8 later, remove the wafer from the hotplate after several hours and place in the hard bake oven at* 150°C *for at least 1 hour. Test hardness of the resist with acetone away from your channels before going on new patterning.*s

G.2 Control wafer fabrication

This wafer will be fabricated using multiple layers (3 in this example) of SU-8 resist for thick channel patterning. This layer features control valves, chambers, and via ports between flow and control layers.

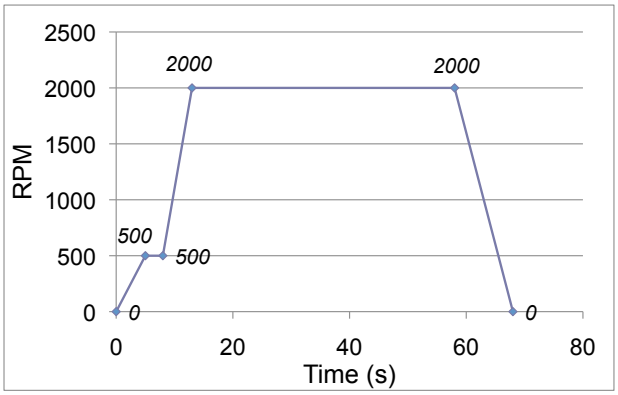

Fig. G.2. Spin coating profile (SU-8 photoresist).

Procedure:

1. Clean wafers using piranha for at least 15 minutes (1:3 hydrogen peroxide:sulfuric acid). Piranha cleaning is mandatory.
2. Rinse with water and dry with nitrogen. Place on a hotplate at 200°C for 5 minutes to dry.
3. Layer of SU-8 resist (50 µm):
   - Spin coat SU-8 50 at 1500 r/min for 45 seconds. **Figure** *G.2 shows nominal spin coating profile for* 50 µm*-thick SU-8 50 photoresist.*
   - Bake at 65°C for 6 minutes, and then 95°C for 20 minutes. Cool slowly back to room temperature.
   - Spin coat again to obtain thicker photoresist layer
   - Bake at 65°C for 6 minutes, and then 95°C for 20 minutes. Cool slowly back to room temperature.
   - Repeat last 2 steps in order to obtain the desired layer thickness.
   - ...
   - Expose using mask for 10 seconds continuously.
   - Post expose bake at 65°C for 1 minute, and then 95°C for 5 minutes. Cool slowly back to room temperature.
4. Develop the resist using "SU-8 developer" and rinse with Isopropanol/Aceton. Dry with nitrogen gas. 200 µm of SU-8 takes 8 minutes to develop.

G.3 PDMS device fabrication

Once the molds for flow and control layers have been fabricated, it will be possible to create the microfluidic device for experiments. The process of multilayer soft-lithography

will be used to create a chip with integrated valves.

1. Treat the wafers with fluorosilane for ~ 20 minutes in the chemical hood.
2. Prepare PDMS (SYLGARD 184). Prepare one cup with ~ 30 g 5:1 PDMS (25 g base +5 g curing agent) or 18 g 5:1 PDMS (15 g base +3 g curing agent) for one petri dish, and ~ 21 g 20:1 PDMS (20 g base +1 g curing agent).
3. Clean the mold. Pour the 5:1 PDMS over the flow mold and degas in the vacuum bell for about 5 minutes.
4. Spin coat the 20:1 PDMS over the control mold. Refer to the PDMS spin curves for the appropriate thickness. In general, $15 - 25$ μm PDMS layer is wished over the control layer to make a valve. For example, if your control layer is 50 μm thick, spin coat ~ 70 μm PDMS. For the control wafer described above, the control valves are nominally 150 μm tall, much larger than usual, so it may take a few different trials to find the ideal spin speed (475 r/min which provides a nominal thickness of ~ 175 μm).
5. Partially cure the PDMS of both wafers using the curing oven at 80°C. Approximate times for the flow and control layer are $\sim 15 - 16$ minutes, and $\sim 12 - 13$ minutes respectively. These times can vary significantly depending on oven temperature. Try to time it, such that both wafers are removed from the oven around the same time.
6. Cut the thick layer chip. The PDMS of the control layer should feel tight, but slightly sticky. Align these chip to the features of the flow layer under the microscope. After alignment, place the wafer with both layers back in the oven for at least a few hours.
7. Cut the chips from the control wafer, and carefully peel them off.
8. Use puncher (i.e 0.5 mm diameter) to punch the holes for via connection between layers.
9. Clean chips using tape and ethanol.
10. Bond to clean glass slides using the plasma bonder (~ 30 seconds on medium power).

G.4 Remarks

For different device/layer settings, different photoresists of AZ or SU-8 may be more suitable. Fit on their datasheets in order to obtain the desired features.

H

Characterizations of the pre-amplifiers used for sensing

Summary. This appendix is related to the specifications and the performances of the pre-amplifiers used for the sensing of the tweezers' motion. Indeed A/V pre-amplifiers are required to amplify pico-ampere currents from the integrated capacitive sensor to milli-volt range. However in dynamic measurements of the displacement, high sensitivity gain are limited by the bandwidth, which are lower than 2 kHz.

H.1 General description

For the amplifications of the sensor currents, we use A/V pre-amplifiers from Signal Recovery (http://www.signalrecovery.com/). The model 5182 is a current-to-voltage preamplifier of low noise and low input impedance designed to amplify the extremely low currents encountered in such areas as photometry and semiconductor research. It has five standard sensitivity settings including a special low-noise mode on the highest gain position for even better low current measurement capability.

Table H.1 summarized the characteristics of the different gain modes in term of amplification and noise. Further specifications are available in the datasheet of the model. However we will focus on the frequency characteristics of the amplification which are the main restriction of the sensing.

Gain (A/V)	Max DC input current	Noise current at 1 kHz
10^{-5}	9 mA	10 pA/$\sqrt{\text{Hz}}$
10^{-6}	900 µA	5 pA/$\sqrt{\text{Hz}}$
10^{-7}	9 µA	135 fA/$\sqrt{\text{Hz}}$
10^{-8}	900 nA	45 fA/$\sqrt{\text{Hz}}$
10^{-8} Low Noise	90 nA	15 fA/$\sqrt{\text{Hz}}$

Table H.1. Amplification characteristics of the A/V pre-amplifiers (Signal Recovery model 5182).

H.2 Frequency characteristics

Figure H.1 shows the frequency characteristics of the pre-amplifiers provided by the company. **Figure** H.2 are the results from an experimental study of the frequency characteristics of the pre-amplifiers of the set-up.

The interesting feature of **Figure** H.2 is the phase shifting of the output from the input signal. At 2 kHz and with 10^{-8} LN gain, the phase shift is $-16°$, when with 10^{-7} gain, there is not a significant shift. This explains the delay in the loop when the feedback is implemented, and the consequences in the closed-loop system characteristics.

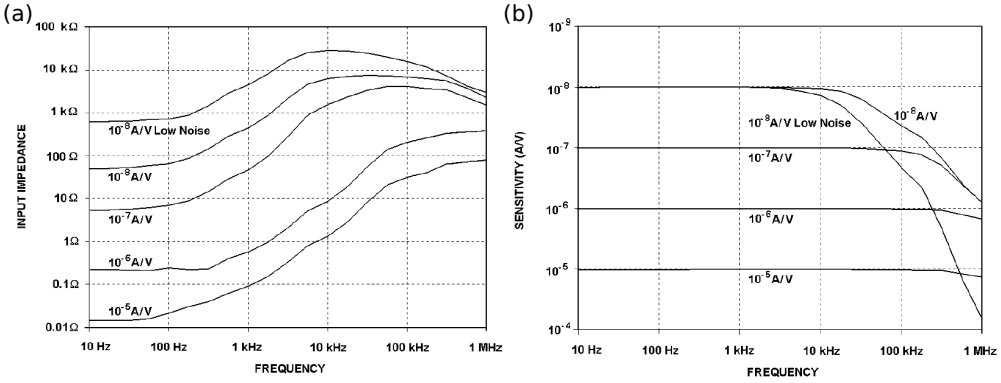

Fig. H.1. Frequency characteristics according to the sensitivity modes of the A/V pre-amplifiers (Signal Recovery model 5182).

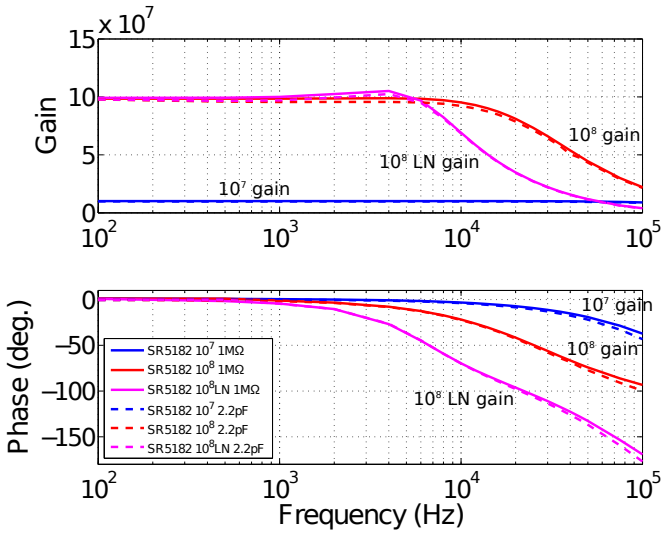

Fig. H.2. Frequency characterizations of the A/V pre-amplifiers (Signal Recovery model 5182) for 10^{-7}, 10^{-8} and 10^{-8} LN sensitivity modes.

Glossary

μTAS Micro Total Analysis System
AC Alternative Current
AFM Atomic Force Microscopy
Al Aluminum
APCVD Atmospheric Pressure Chemical Vapor Deposition
BHF Buffered Hydro-Fluorhydric
BioMEMS Biomedical Micro ElectroMechanical Systems
BOX Buried Oxyde
CNRS Centre National de la Recherche Scientifique (France)
CVD Chemical Vapor Deposition
DC Direct Current
DEP Dielectrophoresis
DLP Digital Light Processing (DLP technology from Texas Instruments)
DMD Digital Mirror Device
DNA DeoxyRibonucleic Acid
DRIE Deep Reactive-Ion Etching
dsDNA Double-stranded DeoxyRibonucleic Acid
EDM Electro-Discharge Micromachining
ENSMM Ecole Nationale de Supérieure de Mécanique et des Microtechniques de Besanǫn (France)
FCCS Fluorescence Cross-Correlation Spectroscopy
FCS Fluorescence Correlation Spectroscopy
FEM Finite Element Method
FIB Focused Ion Beam
GaAs Gallium Arsenide
Ge Germanium
HDMS Hexamethyldisilazane
HF Hydrofluoric acid
HILO Highly Inclined and Laminated Optical (microscopy)
IIS Institute of Industrial Science (the University of Tokyo, Japan)
KOH Hydroxide of potassium
LIGA LIthographie Galvanoformung Adformung

LOCOS LOCal Oxidation of Silicon
LPCVD Low Pressure Chemical Vapor Deposition
LSCM Laser Scanning Confocal Microscopy
MEMS Micro ElectroMechanical Systems
MNEMS Micro and Nano ElectroMechanical Systems (or NMEMS)
MOEMS Micro Opto-ElectroMechanical Systems
MPC 2-methacryloyloxyethyl phosphorylcholine
MST MicroSystem Technology
MT Magnetic Tweezers
NEMS Nano ElectroMechanical Systems
NSOM Near-field Scanning Optical Microscopy
OT Optical Tweezers
PCB Printed Circuit Board
PDMS Polydimethylsiloxane
PLL Phase-Locked Loop (in electronics) or Poly-L-Lysine (in bio-chemistry)
PZT Lead Zirconate Titanate ($Pb[Zr_xTi_{1-x}]O_3$ $0 \leq x \leq 1$)
RIE Reactive-Ion Etching
RMS Root Mean Square
SEM Scanning Electron Microscopy
Si Silicon
SiC Silicon Carbide
SiO_2 Silicon Oxyde
SMA Shape Memory Alloys
SNR Signal-To-Noise
SOI Silicon-On-Insulator
SPM Sulphuric acid/hydrogen Peroxide/water Mixture
ssDNA Single-stranded DeoxyRibonucleic Acid
STM Scanning Tunneling Microscope
TEM Transmission Electron Microscopy
TIRF Total Internal Reflection Fluorescence (microscopy)
TMAH TetraMethylAmmonium Hydroxide
XeF_2 Xenon Difluoride

References

[Abbondanzieri 2005] Elio A Abbondanzieri, William J Greenleaf, Joshua W Shaevitz, Robert Landick and Steven M Block. *Direct observation of base-pair stepping by RNA polymerase.* Nature, vol. 438, no. 7067, pages 460–465, November 2005. **This is an experimental "tour de force" in which individual 0.34 nm base-pair steps of transcribing RNA polymerases were directly measured with optical tweezers.** 4, 12

[Ahmad 2012] Irfan Ahmad, Alina Voda, Gildas Besançon and Gabriel Buche. *Robust digital control approach for high performance tunneling current measurement system.* Control Engineering Practice, pages 1–11, March 2012. 78

[Alberts 2002] Bruce Alberts, Alexander Johnson, Julian Lewis, Martin Raff, Keith Roberts and Peter Walter. Molecular Biology of the Cell, Fourth Edition. Garland Science, 4 édition, March 2002. 4

[Ali 2001] B M Ali, R Amit, I Braslavsky, A B Oppenheim, O Gileadi and J Stavans. *Compaction of single DNA molecules induced by binding of integration host factor (IHF).* Proceedings of the National Academy of Sciences of the United States of America, vol. 98, no. 19, pages 10658–10663, September 2001. 4

[Allemand 1998] JF Allemand, D Bensimon, R Lavery and V Croquette. *Stretched and overwound DNA forms a Pauling-like structure with exposed bases.* Proceedings of the National Academy of Sciences, vol. 95, no. 24, page 14152, 1998. 156

[Amblard 1996] F Amblard, B Yurke, A Pargellis and S Leibler. *A magnetic manipulator for studying local rheology and micromechanical properties of biological systems.* Review of Scientific Instruments, vol. 67, no. 3, pages 818–827, 1996. 4

[Arai 1998] F Arai, D Andou, Y Nonoda, T Fukuda, H Iwata and K Itoigawa. *Integrated microendeffector for micromanipulation.* Mechatronics, IEEE/ASME Transactions on, vol. 3, no. 1, pages 17–23, 1998. 20

[Arai 1999] Y Arai, R Yasuda, K Akashi, Y Harada, H Miyata, K Kinosita and H Itoh. *Tying a molecular knot with optical tweezers.* Nature, vol. 399, no. 6735, pages 446–448, June 1999. 8, 11

[Ashkin 1986] A Ashkin, J M Dziedzic, J E Bjorkholm and S Chu. *Observation of a single-beam gradient force optical trap for dielectric particles.* Optics letters, vol. 11, no. 5, page 288, May 1986. **First demonstration of optical trapping of dielectric particle: Trapping principle used by optical tweezers.** 11

[Bancaud 2006] Aurélien Bancaud, Natalia Conde E Silva, Maria Barbi, Gaudeline Wagner, Jean-François Allemand, Julien Mozziconacci, Christophe Lavelle, Vincent Croquette, Jean-Marc Victor, Ariel Prunell and Jean-Louis Viovy. *Structural plasticity of single chromatin fibers revealed by torsional manipulation.* Nature Structural & Molecular Biology, vol. 13, no. 5, pages 444–450, May 2006. 4

[Bensimon 1994] A Bensimon, A Simon, A Chiffaudel, V Croquette, F Heslot and D Bensimon. *Alignment and sensitive detection of DNA by a moving interface.* Science (New York, NY), vol. 265, no. 5181, pages 2096–2098, September 1994. 4, 5

[Bensimon 1995] D Bensimon, AJ Simon, V Croquette and A Bensimon. *Stretching DNA with a receding meniscus: experiments and models.* Physical review letters, vol. 74, no. 23, pages 4754–4757, 1995. 156

[Beyeler 2007] F Beyeler, A Neild, S Oberti, DJ Bell, Y Sun, J Dual and BJ Nelson. *Monolithically fabricated microgripper with integrated force sensor for manipulating microobjects and biological cells aligned in an ultrasonic field.* Microelectromechanical Systems, Journal of, vol. 16, no. 1, pages 7–15, 2007. 20, 157

[Beyeler 2008] F Beyeler, S Muntwyler, Z Nagy, C Graetzel, M Moser and BJ Nelson. *Design and calibration of a MEMS sensor for measuring the force and torque acting on a magnetic microrobot.* Journal of Micromechanics and Microengineering, vol. 18, page 025004, 2008. 129

[Beyeler 2009] F Beyeler, S Muntwyler and BJ Nelson. *A Six-Axis MEMS Force–Torque Sensor With Micro-Newton and Nano-Newtonmeter Resolution.* Microelectromechanical Systems, Journal of, vol. 18, no. 2, pages 433–441, 2009. 129

[Binnig 1986] G Binnig, C Quate and C Gerber. *Atomic force microscope.* Physical review letters, vol. 56, no. 9, pages 930–933, March 1986. **The demonstration of the concept of AFM by the combination of a scanning tunneling microscope and a stylus profilometer that is able to investigate surfaces of insultators on an atomic scale.** 13

[Block 1989] S M Block, D F Blair and H C Berg. *Compliance of bacterial flagella measured with optical tweezers.* Nature, vol. 338, no. 6215, pages 514–518, April 1989. 11

[Block 1990] S M Block, L S Goldstein and B J Schnapp. *Bead movement by single kinesin molecules studied with optical tweezers.* Nature, vol. 348, no. 6299, pages 348–352, November 1990. 11, 12

[Bouchiat 1999] C Bouchiat, MD Wang, JF Allemand, T Strick, SM Block and V Croquette. *Estimating the persistence length of a worm-like chain molecule from force-extension measurements.* Biophysical Journal, vol. 76, no. 1, pages 409–413, 1999. 21, 75

[Bruchez Jr 1998] M Bruchez Jr, Mario Moronne, Peter Gin, Simon Weiss and A. Paul Alivisatos. *Semiconductor Nanocrystals as Fluorescent Biological Labels.* Science (New York, NY), vol. 281, no. 5385, pages 2013–2016, September 1998. 10

[Bryant 2003] Zev Bryant, Michael D Stone, Jeff Gore, Steven B Smith, Nicholas R Cozzarelli and Carlos Bustamante. *Structural transitions and elasticity from torque measurements on DNA.* Nature, vol. 424, no. 6946, pages 338–341, July 2003. 4

[Bunimovich 2006] Yuri L Bunimovich, Young Shik Shin, Woon-Seok Yeo, Michael Amori, Gabriel Kwong and James R Heath. *Quantitative real-time measurements of DNA hybridization with alkylated nonoxidized silicon nanowires in electrolyte*

solution. Journal of the American Chemical Society, vol. 128, no. 50, pages 16323–16331, December 2006. 72

[Bustamante 1994] C Bustamante, JF Marko, ED Siggia and S Smith. *Entropic elasticity of lambda-phage DNA*. Science (New York, NY), vol. 265, no. 5178, page 1599, 1994. 4

[Bustamante 1995] JO Bustamante, A. Liepins, RA Prendergast, JA Hanover and H. Oberleithner. *Patch clamp and atomic force microscopy demonstrate TATA-binding protein (TBP) interactions with the nuclear pore complex*. Journal of Membrane Biology, vol. 146, no. 3, pages 263–272, 1995. 15

[Bustamante 2003] Carlos Bustamante, Zev Bryant and Steven B Smith. *Ten years of tension: single-molecule DNA mechanics*. Nature, vol. 421, no. 6921, pages 423–427, January 2003. **Reference review about single-molecule experiments.** 4, 16, 25, 64, 162

[Cai 2003] H Cai, C Chan, CS Thian, XM Zhang, C Lu and AQ Liu. *A study of electronic interface for MEMS Variable Optical Attenuator (VOA)*. Design, Test, Integration & Packaging of MEMS/MOEMS, Symposium on, pages 75–78, 2003. 20

[Celedon 2010] Alfredo Celedon, Denis Wirtz and Sean Sun. *Torsional mechanics of DNA are regulated by small-molecule intercalation*. The journal of physical chemistry B, vol. 114, no. 50, pages 16929–16935, December 2010. **Study of the effect of Ethidium Bromide intercalation on DNA torque stiffness.** 4

[Chiou 2005] Pei Yu Chiou, Aaron T Ohta and Ming C Wu. *Massively parallel manipulation of single cells and microparticles using optical images*. Nature, vol. 436, no. 7049, pages 370–372, July 2005. 17

[Chronis 2005] N Chronis and LP Lee. *Electrothermally activated SU-8 microgripper for single cell manipulation in solution*. Microelectromechanical Systems, Journal of, vol. 14, no. 4, pages 857–863, 2005. 20

[Clark 1999] TCN Clark and RT Howe. *An integrated CMOS micromechanical resonator high-Q oscillator*. IEEE Journal of Solid-State Circuits, vol. 34, no. 4, pages 440–455, 1999. 21

[Cluzel 1996] P Cluzel, A Lebrun, C Heller, R Lavery, J L Viovy, D Chatenay and F Caron. *DNA: an extensible molecule*. Science (New York, NY), vol. 271, no. 5250, pages 792–794, February 1996. **DNA extension with micro-needle.** 4, 11

[Cornish 2007] Peter V Cornish and Taekjip Ha. *A survey of single-molecule techniques in chemical biology*. ACS chemical biology, vol. 2, no. 1, pages 53–61, January 2007. 10, 156

[Croft 1999] D Croft and Santos Devasia. *Vibration compensation for high speed scanning tunneling microscopy*. Review of Scientific Instruments, vol. 70, no. 12, pages 4600–4605, 1999. 78

[Dai 2007] W Dai, K Lian and W Wang. *Design and fabrication of a SU-8 based electrostatic microactuator*. Microsystem Technologies, vol. 13, no. 3, pages 271–277, 2007. 21

[de Vries 2005] Anthony H B de Vries, Bea E Krenn, Roel van Driel and Johannes S Kanger. *Micro magnetic tweezers for nanomanipulation inside live cells*. Biophysical Journal, vol. 88, no. 3, pages 2137–2144, March 2005. **First example**

of in vivo manipulation. Small magnetic probes are manipulated as magnetic tweezers inside living cells. 17

[Devasia 2007] S Devasia, E Eleftheriou and SOR Moheimani. *A survey of control issues in nanopositioning.* Control Systems Technology, IEEE Transactions on, vol. 15, no. 5, pages 802–823, 2007. 78

[Dohn 2005] S Dohn, R Sandberg, W Svendsen and A Boisen. *Enhanced functionality of cantilever based mass sensors using higher modes.* Applied Physics Letters, vol. 86, page 233501, 2005. 81, 163

[Dolbow 1996] J Dolbow and M Gosz. *Effect of out-of-plane properties of a polyimide film on the stress fields in microelectronic structures.* Mechanics of materials, vol. 23, no. 4, pages 311–321, 1996. 25, 122

[Dubourg 2003] F Dubourg, JP Aimé, G Couturier and J Salardenne. *Apparent hardening of soft samples through Q factor change in AFM.* EPL (Europhysics Letters), vol. 62, page 671, 2003. 78

[Dumont 2006] Sophie Dumont, Wei Cheng, Victor Serebrov, Rudolf K Beran, Ignacio Tinoco, Anna Marie Pyle and Carlos Bustamante. *RNA translocation and unwinding mechanism of HCV NS3 helicase and its coordination by ATP.* Nature, vol. 439, no. 7072, pages 105–108, January 2006. **In this work optical tweezers are used to unwind RNA attached between two beads and study RNA mechanisms.** 4

[Edidin 2001] M Edidin. *Near-field scanning optical microscopy, a siren call to biology.* Traffic (Copenhagen, Denmark), vol. 2, no. 11, pages 797–803, November 2001. 9

[Engel 1991] A Engel. *Biological Applications of Scanning Probe Microscopes.* Annual Review of Biophysics and Biophysical Chemistry, vol. 20, no. 1, pages 79–108, June 1991. 15

[Evans 1995] E Evans, K Ritchie and R Merkel. *Sensitive force technique to probe molecular adhesion and structural linkages at biological interfaces.* Biophysical Journal, vol. 68, no. 6, pages 2580–2587, June 1995. **Force sensing technique with biomembrane force probe.** 11

[Fan 1989] LS Fan, YC Tai and RS Muller. *IC-processed electrostatic micromotors.* Sensors and Actuators, vol. 20, no. 1-2, pages 41–47, 1989. 20

[Fleming 2003] A Fleming and S Moheimani. *Precision current and charge amplifiers for driving highly capacitive piezoelectric loads.* Electronics Letters, vol. 39, no. 3, pages 282–284, 2003. 78

[Galletto 2006] Roberto Galletto, Ichiro Amitani, Ronald J Baskin and Stephen C Kowalczykowski. *Direct observation of individual RecA filaments assembling on single DNA molecules.* Nature, vol. 443, no. 7113, pages 875–878, October 2006. 7, 8

[Ghatkesar 2007] MK Ghatkesar, V Barwich, T Braun, JP Ramseyer, C Gerber, M Hegner, HP Lang, U Drechsler and M Despont. *Higher modes of vibration increase mass sensitivity in nanomechanical microcantilevers.* Nanotechnology, vol. 18, page 445502, 2007. 81

[Giepmans 2006] Ben N G Giepmans, Stephen R Adams, Mark H Ellisman and Roger Y Tsien. *The Fluorescent Toolbox for Assessing Protein Location and Function.* Science (New York, NY), vol. 312, no. 5771, pages 217–224, April 2006. 10

[Gittes 1998] F Gittes and CF Schmidt. *Thermal noise limitations on micromechanical experiments*. European biophysics journal, vol. 27, no. 1, pages 75–81, 1998. 16

[Granéli 2006] Annette Granéli, Caitlyn C Yeykal, Ragan B Robertson and Eric C Greene. *Long-distance lateral diffusion of human Rad51 on double-stranded DNA*. Proceedings of the National Academy of Sciences of the United States of America, vol. 103, no. 5, pages 1221–1226, January 2006. 7, 156

[Greenleaf 2007] William J Greenleaf, Michael T Woodside and Steven M Block. *High-resolution, single-molecule measurements of biomolecular motion*. Annual review of biophysics and biomolecular structure, vol. 36, pages 171–190, 2007. 14

[Gueroui 2002] Z Gueroui, C Place, E Freyssingeas and B Berge. *Observation by fluorescence microscopy of transcription on single combed DNA*. Proceedings of the National Academy of Sciences of the United States of America, vol. 99, no. 9, pages 6005–6010, April 2002. 4, 6

[Hamdan 2007] Samir M Hamdan, Donald E Johnson, Nathan A Tanner, Jong-Bong Lee, Udi Qimron, Stanley Tabor, Antoine M van Oijen and Charles C Richardson. *Dynamic DNA helicase-DNA polymerase interactions assure processive replication fork movement*. Molecular cell, vol. 27, no. 4, pages 539–549, August 2007. **In this work, DNA helicase and DNA polymerase activities are studied on a single DNA molecule attached between a glass surface and a paramagnetic bead. The molecule is stretched by a flow.** 4

[Hashiguchi 2003] G Hashiguchi, T Goda, M Hosogi, K Hirano, N Kaji, Y Baba, K Kakushima and H Fujita. *DNA manipulation and retrieval from an aqueous solution with micromachined nanotweezers*. Anal. Chem, vol. 75, no. 17, pages 4347–4350, 2003. 1, 27

[Haustein 2004] Elke Haustein and Petra Schwille. *Single-molecule spectroscopic methods*. Current opinion in structural biology, vol. 14, no. 5, pages 531–540, October 2004. **Detailled review on fluorescence spectroscopy with technical explanation of microscopy techniques for achieving high temporal and spatial resolution.** 4, 5, 16

[Hosaka 2001] S Hosaka. *SPM based recording toward ultrahigh density recording with trillion bits/inch2*. Magnetics, 2001. 78

[Humphris 2000] ADL Humphris, J Tamayo and MJ Miles. *Active quality factor control in liquids for force spectroscopy*. Langmuir, vol. 16, no. 21, pages 7891–7894, 2000. **This paper shows the improvement of sensitivity sensing with AFM by applying positive feedback and enhancing the Q factor of the system.** 78

[Hurley 2002] Laurence H Hurley. *DNA and its associated processes as targets for cancer therapy*. Nature Reviews Cancer, vol. 2, no. 3, pages 188–200, March 2002. **Overview of new anticancer drug development targetting more specifically and efficiently DNA and DNA-associated processes** 72, 106

[Ishijima 1991] A Ishijima, T Doi, K Sakurada and T Yanagida. *Sub-piconewton force fluctuations of actomyosin in vitro*. Nature, 1991. 4

[Ishijima 1998] A Ishijima, H Kojima, T Funatsu, M Tokunaga, H Higuchi, H Tanaka and T Yanagida. *Simultaneous observation of individual ATPase and mechanical events by a single myosin molecule during interaction with actin*. Cell, vol. 92,

no. 2, pages 161–171, January 1998. **Combination of single-molecule fluorescence microscopy with optical tweezers.** 17

[Itoh 2004] Hiroyasu Itoh, Akira Takahashi, Kengo Adachi, Hiroyuki Noji, Ryohei Yasuda, Masasuke Yoshida and Kazuhiko Kinosita. *Mechanically driven ATP synthesis by F1-ATPase.* Nature, vol. 427, no. 6973, pages 465–468, January 2004. 4, 12

[Johnson 1995] WA Johnson and LK Warne. *Electrophysics of micromechanical comb actuators.* Microelectromechanical Systems, Journal of, vol. 4, no. 1, pages 49–59, 1995. 22

[Kim 2005] DH Kim, MG Lee, B Kim and Y Sun. *A superelastic alloy microgripper with embedded electromagnetic actuators and piezoelectric force sensors: a numerical and experimental study.* Smart materials and structures, vol. 14, page 1265, 2005. 20

[Kim 2007] Ji Hoon Kim and Ronald G Larson. *Single-molecule analysis of 1D diffusion and transcription elongation of T7 RNA polymerase along individual stretched DNA molecules.* Nucleic Acids Research, vol. 35, no. 11, pages 3848–3858, 2007. **Enzymatic activity of polymerase enzymes have been monitored in real-time by fluorescence on DNA molecule previously combed onto a surface.** 4, 6

[Kohl 2000] M Kohl, E Just, W Pfleging and S Miyazaki. *SMA microgripper with integrated antagonism.* Sensors and Actuators A: Physical, vol. 83, no. 1-3, pages 208–213, 2000. 20

[Krasnoslobodtsev 2007] Alexey V Krasnoslobodtsev, Luda S Shlyakhtenko and Yuri L Lyubchenko. *Probing Interactions within the synaptic DNA-SfiI complex by AFM force spectroscopy.* Journal of molecular biology, vol. 365, no. 5, pages 1407–1416, February 2007. 15

[Kumemura 2007] M Kumemura, D Collard, C Yamahata, N Sakaki, G Hashiguchi and H Fujita. *Single DNA molecule isolation and trapping in a microfluidic device.* ChemPhysChem, vol. 8, no. 12, pages 1875–1880, 2007. 58

[Kumemura 2010] M Kumemura, D Collard, S Yoshizawa, D Fourmy, N Lafitte, L Jalabert, S Takeuchi, T Fujii and H Fujita. *Direct bio-mechanical sensing of enzymatic reaction On DNA by silicon nanotweezers.* In Micro Electro Mechanical Systems (MEMS), 2010 IEEE 23rd International Conference on, pages 915–918, 2010. **This work was presented as a poster at the 2010 MEMS conference in Hong Kong.** 51, 103, 161, 164

[Kumemura 2011] M Kumemura, D Collard, N Sakaki, C Yamahata, M Hosogi, G Hashiguchi and H Fujita. *Single-DNA-molecule trapping with silicon nanotweezers using pulsed dielectrophoresis.* Journal of Micromechanics and Microengineering, vol. 21, page 054020, 2011. 60

[Lafitte 2010] N Lafitte, M Kumemura, M Nagai, L Jalabert, D Collard and H Fujita. *An open microfluidic device with active valves for accurate trapping of DNA by silicon nanotweezers.* In 14th Int Conf. on Miniaturized Systems for Chemistry and Life Sciences, MicroTAS2010, pages 1865–1867. LIMMS-CNRS/IIS, UMI2820, The University of Tokyo, JAPAN and IIS, The University of Tokyo, JAPAN, 2010. **This work was presented at the 2010 MicroTAS conference in Groningen, The Netherlands.** 103, 161

[Lafitte 2011] N Lafitte, M Kumemura, L Jalabert, D Collard and H Fujita. *Real-Time sensing of molecule binding on DNA with silicon nanotweezers*. In 15th Int Conf. on Miniaturized Systems for Chemistry and Life Sciences, MicroTAS2011, pages 389–372, 2011. **This work was presented at the 2011 MicroTAS conference in Seattle, The USA.** 103, 161, 164

[Leang 2007] K Leang and Santos Devasia. *Feedback-Linearized Inverse Feedforward for Creep, Hysteresis, and Vibration Compensation in AFM Piezoactuators*. Control Systems Technology, IEEE Transactions on, vol. 15, no. 5, pages 927–935, 2007. 78

[Lebofsky 2003] Ronald Lebofsky and Aaron Bensimon. *Single DNA molecule analysis: applications of molecular combing*. Briefings in functional genomics & proteomics, vol. 1, no. 4, pages 385–396, 2003. 6

[Leger 1998] J F Leger, J Robert, L Bourdieu, D Chatenay and J F Marko. *RecA binding to a single double-stranded DNA molecule: a possible role of DNA conformational fluctuations*. Proceedings of the National Academy of Sciences of the United States of America, vol. 95, no. 21, pages 12295–12299, October 1998. 4

[Leger 1999] JF Leger, G Romano, A Sarkar, J Robert, L Bourdieu, D Chatenay and JF Marko. *Structural transitions of a twisted and stretched DNA molecule*. Physical review letters, vol. 83, no. 5, pages 1066–1069, 1999. 4

[Legtenberg 1996] R Legtenberg, AW Groeneveld and M Elwenspoek. *Comb-drive actuators for large displacements*. Journal of Micromechanics and Microengineering, vol. 6, no. 3, pages 320–329, 1996. 21

[Lipfert 2010] Jan Lipfert, Jacob W J Kerssemakers, Tessa Jager and Nynke H Dekker. *Magnetic torque tweezers: measuring torsional stiffness in DNA and RecA-DNA filaments*. Nature methods, October 2010. 13

[Lu 2003] Y Lu and Chang-Jin Kim. *Micro-finger articulation by pneumatic parylene balloons*. TRANSDUCERS, Solid-State Sensors, Actuators and Microsystems, 12th International Conference on, 2003, pages 276–279 vol.1, 2003. 20

[Mammen 1996] M Mammen, K Helmerson, R Kishore, S K Choi, W D Phillips and G M Whitesides. *Optically controlled collisions of biological objects to evaluate potent polyvalent inhibitors of virus-cell adhesion*. Chemistry & biology, vol. 3, no. 9, pages 757–763, September 1996. 11

[Mehregany 1988] M Mehregany, KJ Gabriel and WSN Trimmer. *Integrated fabrication of polysilicon mechanisms*. Electron Devices, IEEE Transactions on, vol. 35, no. 6, pages 719–723, 1988. 20

[Melin 2007] Jessica Melin and Stephen R Quake. *Microfluidic large-scale integration: the evolution of design rules for biological automation*. Annual review of biophysics and biomolecular structure, vol. 36, pages 213–231, 2007. 61, 62

[Millet 2004] O Millet, P Bernardoni, S Régnier, P Bidaud, E Tsitsiris, D Collard and L Buchaillot. *Electrostatic actuated micro gripper using an amplification mechanism*. Sensors and Actuators A: Physical, vol. 114, no. 2-3, pages 371–378, 2004. 20

[Moffitt 2008] Jeffrey R Moffitt, Yann R Chemla, Steven B Smith and Carlos Bustamante. *Recent advances in optical tweezers*. Annual review of biochemistry, vol. 77, pages 205–228, 2008. 4, 16, 17

[Molhave 2004] K Molhave, TM Hansen, DN Madsen and P Boggild. *Towards pick-and-place assembly of nanostructures.* Journal of Nanoscience and Nanotechnology, vol. 4, no. 3, pages 279–282, 2004. 20

[Molhave 2005] K Molhave and O Hansen. *Electro-thermally actuated microgrippers with integrated force-feedback.* Journal of Micromechanics and Microengineering, vol. 15, page 1265, 2005. 20

[Neuman 2003] Keir C Neuman, Elio A Abbondanzieri, Robert Landick, Jeff Gelles and Steven M Block. *Ubiquitous transcriptional pausing is independent of RNA polymerase backtracking.* Cell, vol. 115, no. 4, pages 437–447, November 2003. 12

[Neuman 2004] Keir C Neuman and Steven M Block. *Optical trapping.* Review of Scientific Instruments, vol. 75, no. 9, pages 2787–2809, September 2004. **a detailed and thorough technical review of optical trapping** 7, 8, 11, 12

[Neuman 2008] Keir C Neuman and Attila Nagy. *Single-molecule force spectroscopy: optical tweezers, magnetic tweezers and atomic force microscopy.* Nature methods, vol. 5, no. 6, pages 491–505, June 2008. **Review paper on optical and magnetic tweezers and AFM.** 4, 12, 15, 16, 157

[Neuman 2010] Keir C Neuman. *Single-molecule measurements of DNA topology and topoisomerases.* The Journal of biological chemistry, vol. 285, no. 25, pages 18967–18971, June 2010. 4

[Pingoud 2001] Alferd Pingoud and Albert Jeltsch. *Structure and function of type II restriction endonucleases.* Nucleic Acids Research, vol. 29, no. 18, page 3705, 2001. 69

[Rifai 2007] O M El Rifai and Kamal Youcef-Toumi. *On automating atomic force microscopes: An adaptive control approach.* Control Engineering Practice, 2007. 78

[Roberts 2005] Richard J Roberts. *How restriction enzymes became the workhorses of molecular biology.* Proceedings of the National Academy of Sciences of the United States of America, vol. 102, no. 17, page 5905, 2005. 69

[Roch 2003] I Roch, P Bidaud, D Collard and L Buchaillot. *Fabrication and characterization of an SU-8 gripper actuated by a shape memory alloy thin film.* Journal of Micromechanics and Microengineering, vol. 13, page 330, 2003. 20

[Rocha 2007] M S Rocha, M C Ferreira and O N Mesquita. *Transition on the entropic elasticity of DNA induced by intercalating molecules.* The Journal of chemical physics, vol. 127, no. 10, page 105108, September 2007. 74

[Rohrbach 2002] Alexander Rohrbach and Ernst H K Stelzer. *Trapping forces, force constants, and potential depths for dielectric spheres in the presence of spherical aberrations.* Applied optics, vol. 41, no. 13, pages 2494–2507, May 2002. 11

[Sacconi 2005] Leonardo Sacconi, Iva M Tolić-Nørrelykke, Chiara Stringari, Renzo Antolini and Francesco S Pavone. *Optical micromanipulations inside yeast cells.* Applied optics, vol. 44, no. 11, pages 2001–2007, April 2005. **First example of in vivo manipulation. Lipid granules are optically trapped and manipulated inside yeast cells.** 17

[Salapaka 2002] S Salapaka, A Sebastian, JP Cleveland and MV Salapaka. *High bandwidth nano-positioner: A robust control approach.* Review of Scientific Instruments, vol. 73, page 3232, 2002. 78

[Salapaka 2005] S Salapaka and Abu Sebastian. *Design methodologies for robust nano-positioning*. Control Systems Technology, 2005. **This paper presents a systematic control design and analysis for a two-dimensional nanopositioner.** 78

[Salerno 2010] Domenico Salerno, Doriano Brogioli, Valeria Cassina, Diana Turchi, Giovanni Luca Beretta, Davide Seruggia, Roberto Ziano, Franco Zunino and Francesco Mantegazza. *Magnetic tweezers measurements of the nanomechanical properties of DNA in the presence of drugs*. Nucleic Acids Res, vol. 38, no. 20, pages 7089–7099, November 2010. **Mechanical characterization of DNA binders (as intercalting agents and minor groove binder) with magnetic tweezers.** 13

[Sarajlic 2010] E Sarajlic, C Yamahata, M Cordero and H Fujita. *Three-Phase Electrostatic Rotary Stepper Micromotor With a Flexural Pivot Bearing*. Microelectromechanical Systems, Journal of, vol. 19, no. 2, pages 338–349, 2010. 20

[Schitter 2001] G Schitter, P Menold, H Knapp, F Allgower and A Stemmer. *High performance feedback for fast scanning atomic force microscopes*. Review of Scientific Instruments, vol. 72, no. 8, pages 3320–3327, 2001. 78

[Seidel 2004] Ralf Seidel, John Van Noort, Carsten Van Der Scheer, Joost G P Bloom, Nynke H Dekker, Christina F Dutta, Alex Blundell, Terence Robinson, Keith Firman and Cees Dekker. *Real-time observation of DNA translocation by the type I restriction modification enzyme EcoR124I*. Nature Structural & Molecular Biology, vol. 11, no. 9, pages 838–843, September 2004. 4

[Shao 1995] Z Shao, J Yang and A P Somlyo. *Biological atomic force microscopy: from microns to nanometers and beyond*. Annual review of cell and developmental biology, vol. 11, pages 241–265, 1995. 15

[Skoko 2004] Dunja Skoko, Ben Wong, Reid C Johnson and John F Marko. *Micromechanical analysis of the binding of DNA-bending proteins HMGB1, NHP6A, and HU reveals their ability to form highly stable DNA-protein complexes*. Biochemistry, vol. 43, no. 43, pages 13867–13874, November 2004. 4

[Smith 1992] S B Smith, L Finzi and C Bustamante. *Direct mechanical measurements of the elasticity of single DNA molecules by using magnetic beads*. Science (New York, NY), vol. 258, no. 5085, pages 1122–1126, November 1992. **DNA flow-induced stretching.** 7

[Soen 2007] Jonathan Soen, Alina Voda and Cyril Condemine. *Controller design for a closed-loop micromachined accelerometer*. Control Engineering Practice, vol. 15, no. 1, pages 57–68, January 2007. 78

[Spanoudakis 2003] P Spanoudakis, P Schwab and P Johnson. *Design and production of the METOP satellite IASI corner cube mechanisms*. 10th European Space Mechanisms and Tribology Symposium, vol. 524, pages 97–103, 2003. 25

[Stemmer 2005] A Stemmer, G Schitter, JM Rieber and F Allgower. *Control strategies towards faster quantitative imaging in atomic force microscopy*. European journal of Control, vol. 11, no. 4-5, pages 384–395, 2005. 78

[Strick 2000a] T Strick, J Allemand, V Croquette and D Bensimon. *Twisting and stretching single DNA molecules*. Progress in biophysics and molecular biology, vol. 74, no. 1-2, pages 115–140, 2000. 4

[Strick 2000b] T R Strick, V Croquette and D Bensimon. *Single-molecule analysis of DNA uncoiling by a type II topoisomerase.* Nature, vol. 404, no. 6780, pages 901–904, April 2000. **This was the first single-molecule measurement of topoisomeraseactivity using magnetic tweezers.** 12

[Sun 2005] Yu Sun, Steven N Fry, D P Potasek, Dominik J Bell and Bradley J Nelson. *Characterizing fruit fly flight behavior using a microforce sensor with a new comb-drive configuration.* Journal of Micromechanical Systems, vol. 14, pages 4–11, 2005. 23

[Svoboda 1993] K Svoboda, C F Schmidt, B J Schnapp and S M Block. *Direct observation of kinesin stepping by optical trapping interferometry.* Nature, vol. 365, no. 6448, pages 721–727, October 1993. 11, 12

[Tang 1989] WC Tang, T-C H Nguyen and RT Howe. *Laterally driven resonant microstructures.* Sensors and Actuators, vol. 20, pages 25–32, 1989. 20, 21

[Tokunaga 2008] Makio Tokunaga, Naoko Imamoto and Kumiko Sakata-Sogawa. *Highly inclined thin illumination enables clear single-molecule imaging in cells.* Nature methods, vol. 5, no. 2, pages 159–161, January 2008. 9

[Ueda 1999] M Ueda, Y Baba, H Iwasaki, O Kurosawa and M Washizu. *Direct measurement of DNA by means of AFM.* Nucleic acids symposium series, no. 42, pages 245–246, 1999. 15

[Unger 2000] MA Unger, HP Chou, T Thorsen, A Scherer and SR Quake. *Monolithic microfabricated valves and pumps by multilayer soft lithography.* Science (New York, NY), vol. 288, no. 5463, page 113, 2000. 61, 162

[van Mameren 2006] Joost van Mameren, Mauro Modesti, Roland Kanaar, Claire Wyman, Gijs J L Wuite and Erwin J G Peterman. *Dissecting elastic heterogeneity along DNA molecules coated partly with Rad51 using concurrent fluorescence microscopy and optical tweezers.* Biophysical Journal, vol. 91, no. 8, pages L78–80, October 2006. 9, 11

[van Mameren 2008] Joost van Mameren, Erwin J G Peterman and Gijs J L Wuite. *See me, feel me: methods to concurrently visualize and manipulate single DNA molecules and associated proteins.* Nucleic Acids Research, vol. 36, no. 13, pages 4381–4389, August 2008. **Review on macromolecules visualization by fluorescence microscopy.** 4, 5, 6, 7, 8, 9, 16, 156

[Vladescu 2007] Ioana D Vladescu, Micah J Mccauley, Megan E Nuñez, Ioulia Rouzina and Mark C Williams. *Quantifying force-dependent and zero-force DNA intercalation by single-molecule stretching.* Nature methods, vol. 4, no. 6, pages 517–522, June 2007. **Study and quantification of Ethidium Bromide intercalation in between DNA base pairs on molecule stretching** 4, 72, 74, 106

[Volland 2002] BE Volland, H Heerlein and IW Rangelow. *Electrostatically driven microgripper.* Microelectronic engineering, vol. 61, pages 1015–1023, 2002. 20

[Vosch 2007] Tom Vosch, Yasuko Antoku, Jung-Cheng Hsiang, Chris I Richards, Jose I Gonzalez and Robert M Dickson. *Strongly emissive individual DNA-encapsulated Ag nanoclusters as single-molecule fluorophores.* Proceedings of the National Academy of Sciences of the United States of America, vol. 104, no. 31, pages 12616–12621, July 2007. 10

[Walter 2008] Nils G Walter, Cheng-Yen Huang, Anthony J Manzo and Mohamed A Sobhy. *Do-it-yourself guide: how to use the modern single-molecule toolkit.* Nature methods, vol. 5, no. 6, pages 475–489, June 2008. 16, 17, 18, 157

[Waring 1981] M J Waring. *DNA modification and cancer.* Annual review of biochemistry, vol. 50, pages 159–192, 1981. 106

[Washizu 1990] M Washizu and O Kurosawa. *Electrostatic manipulation of DNA in microfabricated structures.* Industry Applications, IEEE Transactions on, vol. 26, no. 6, pages 1165–1172, 1990. 1, 58, 160

[Washizu 1995] M Washizu, S Suzuki, O Kurosawa, T Nishizaka and T Shinohara. *Molecular dielectrophoresis of biopolymers.* Industry Applications, IEEE Transactions on, vol. 31, no. 3, pages 447–456, 1995. 58

[Watson 1953] JD Watson and FH Crick. *Molecular structure of nucleic acids; a structure for deoxyribose nucleic acid.* Nature, vol. 171, no. 4356, pages 737–738, April 1953. **1953 was an annus mirabilis for science. This is one of the classic papers describing discoveries on DNA structure.** 1

[Weber 1989] P C Weber, D H Ohlendorf, J J Wendoloski and F R Salemme. *Structural origins of high-affinity biotin binding to streptavidin.* Science (New York, NY), vol. 243, no. 4887, pages 85–88, January 1989. 15

[Yamahata 2008a] C Yamahata, D Collard, B Legrand, T Takekawa, M Kumemura, G Hashiguchi and H Fujita. *Silicon Nanotweezers With Subnanometer Resolution for the Micromanipulation of Biomolecules.* Microelectromechanical Systems, Journal of, vol. 17, no. 3, pages 623–631, 2008. 1, 20, 21, 23, 28, 54, 65, 157, 160, 164

[Yamahata 2008b] C Yamahata, D Collard, T Takekawa, M Kumemura, G Hashiguchi and H Fujita. *Humidity dependence of charge transport through DNA revealed by silicon-based nanotweezers manipulation.* Biophysical Journal, vol. 94, no. 1, pages 63–70, 2008. 21

[Zhou 2003] G Zhou and P Dowd. *Tilted folded-beam suspension for extending the stable travel range of comb-drive actuators.* Journal of Micromechanics and Microengineering, vol. 13, no. 2, pages 178–183, 2003. 21

Résumé en français

Caractérisation et commande de micropince en silicium pour l'amélioration de la sensibilité paramétrique d'expériences biologiques sur des molécules d'ADN

Mots-clefs

Micropince MEMS, détection biologique, molécules d'ADN, enzymes, commande par retour d'état, observateur

Introduction

L'objectif de ce travail de thèse est de démontrer pour la première fois la capture, la manipulation et la caractérisation de molécules biologiques grâce à une micropince réalisée en technologie microsystème. La molécule d'ADN étant, dans un premier temps, la molécule cible, des fibres d'ADN sont capturées grâce à l'immersion de la micropince dans un petit volume inférieur à 1 µL de solution contenant les molécules. Elles sont ensuite caractérisées mécaniquement et électriquement grâce aux fonctionnalités intégrées sur la même puce en silicium.

Le second volet de ce travail consiste à améliorer les performances du système pour atteindre la résolution d'une seule molécule. En effet dans le but d'étudier les phénomènes d'interactions au niveau moléculaire, il s'avère essentiel d'améliorer le système. Dans ce but précis, une commande par retour d'état de la micropince est étudiée. Elle permet alors de spécifiquement sensibiliser le système aux variations de raideur mécanique du système {micropince + molécules d'ADN}.

Etat de l'art

Les expériences sur la molécule unique d'ADN, par opposition aux expériences dans des tubes à essai, ont apporté de nouveaux résultats longtemps recherchés par les biologistes.

A partir de la fin des années 90 et grâce par exemple aux travaux de Croquette et al. [Bensimon 1995, Allemand 1998], il a été possible d'éprouver protéine par protéine, enzyme par enzyme, l'interaction de chacune d'entre elles avec la molécule unique d'ADN. Le rôle de chaque molécule a pu être étudié afin de comprendre des mécanismes complexes tels que la transcription ou la réplication de l'ADN. Ces expériences reposent néanmoins sur la mise en application d'outils très sophistiqués tels que des micropinces optiques ou magnétiques. Ces outils requièrent des connaissances et des moyens importants pour leur mise en pratique, rendant des analyses systématiques impossibles.

Les techniques communément utilisées pour des expériences sur molécule unique se distinguent en deux catégories : expériences par spectroscopie de fluorescence ou par spectroscopie de force. D'une part, les molécules d'ADN sont individuellement visualisées par fluorescence ; d'autre part elles sont directement attrapées et "testées".

La **Figure** H.3 démontre un principe de spectroscopie de fluorescence. Les molécules d'ADN sont préparées avec des fluorophores et, à l'aide d'un système microfluidique, sont étirées afin de les visualiser sur leur longueur. La majeure difficulté de ce type de méthode consiste à observer et différencier les molécules. Différentes méthodes de microscopie à fluorescence existent [Cornish 2007]. Une autre restriction de la méthode provient du fait qu'il est indispensable de marquer les molécules avec des fluorophores qui interagissent avec les molécules cibles et modifient par conséquence leur structure. Enfin, la fluorescence est limitée dans le temps.

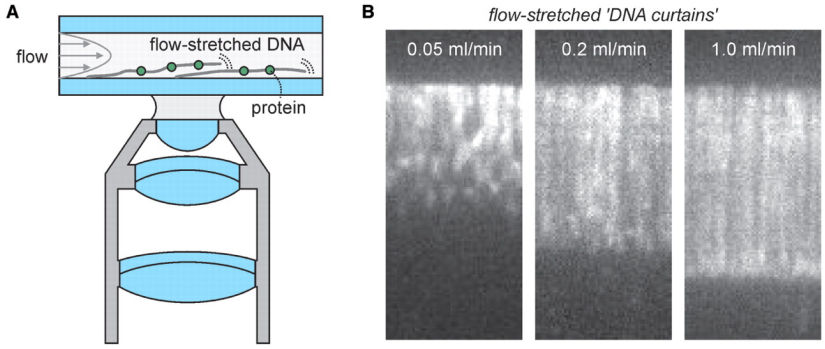

Fig. H.3. Etirement de molécules d'ADN par attachement de celles-ci à une surface et en appliquant une force par le biais d'un écoulement. (A) Schéma de principe. Les molécules sont attachées par un bout à une surface tandis que l'écoulement d'un liquide dans le micro-canal permet d'étirer l'ADN. La visualisation est réalisée par microscopie à fluorescence [van Mameren 2008]. (B) Application de la technique avec des molécules d'ADN-λ labellisé avec des fluophores YOYO-1. L'expérience démontre l'étirement de l'ADN en fonction de la vitesse de l'écoulement [Granéli 2006]. Images extraites de [van Mameren 2008].

La **Figure** H.4 illustre les quatre principales techniques de spectroscopie de force : TPM[1], micropince optique, micropince magnétique ou AFM[2]. Dans les quatre cas de

[1] TPM pour *Tethered Particle Motion* en anglais.
[2] AFM pour *Atomic Force Microscopy* en anglais.

figures, la molécule est nécessairement attachée entre deux supports. Pour cela les supports et la molécule cible doivent être préparés pour permettre l'attachement. Enfin, des techniques de mesures par voie optique doivent être mises en œuvre pour suivre les déplacements de la cible (qu'elle soit bille ou poutre).

Ces différentes techniques permettent toutes une petite diversité de manipulations comme la traction ou la torsion mécanique des molécules, des gammes d'intensité de forces très faibles (quelques piconewtons) mais aussi des échelles de temps de manipulation différentes mais communément importantes. [Neuman 2008] apporte une vue d'ensemble des avantages et des inconvénients de ces techniques.

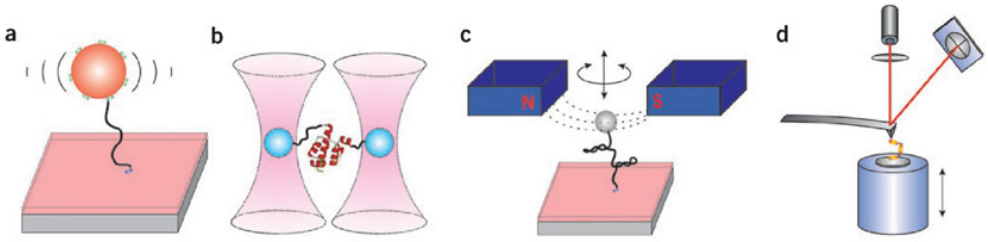

Fig. H.4. Schémas de principe des méthodes de microscopie en force sur une molécule unique (connue comme *single-molecule force microscopy*). (a) *Tethered-particle motion (TPM).* Une micro-particule est attachée à une surface par une molécule. Le mouvement brownien de la particule restreint par la molécule est suivi optiquement. (b) *Optical tweezers (OT).* Une micro-sphère transparente est suspendue grâce à un faisceau laser. Une molécule peut être attachée entre deux sphères ou entre une sphère et une surface motorisée. (c) *Magnetic tweezers (MT).* Les pinces magnétiques attrapent une molécule entre une micro-sphère superparamagnétique et une surface. La sphère est contrôlable en déplacement et en rotation par le biais d'un champ magnétique. (d) *Atomic force microscopy (AFM).* La molécule est attrapée entre une micro-poutre et une surface. La surface est déplacée tandis que le fléchissement de la poutre est mesuré grâce à la déflexion d'un laser sur un capteur photodiode. Images extraites de [Walter 2008].

Les microsystèmes électromécaniques (dits MEMS[3]) peuvent devenir des dispositifs plus appropriés, capables d'intégrer les différentes fonctionnalités indispensables à la manipulation d'objets comme des molécules biologiques [Beyeler 2007]. Une grande variété d'actionnement (électrostatique, électromagnétique, piézoélectrique, thermique et magnétostrictif) ainsi que l'intégration de capteur (e.g. électrostatique ou piézorésistif) permettent de concevoir des systèmes sophistiqués.

Des micropinces MEMS ont été développées et fabriquées dans le but précis de la manipulation de molécules biologiques [Yamahata 2008a]. Cependant, les premières caractérisations du système {micropince + ADN} montre certaines limites qui ne permettent pas de mesurer les caractéristiques mécaniques d'une seule molécule d'ADN.

[3] MEMS pour *Micro ElectroMechanical Systems* en anglais.

Micropince en technologie silicium pour expériences sur molécules d'ADN

Les micropinces mécaniques ont été développées avant le début de ce travail de thèse dans le laboratoire du Pr. Hiroyuki Fujita (IIS, Université de Tokyo). Elles sont fabriquées suivant des procédés courants de la microfabrication sur substrat silicium, intégrant sur une puce de 4 mm sur 5 mm toutes les fonctions indispensables à l'analyse de molécules. Elles permettent ainsi de procéder à des expériences biologiques de manière rapide et systématique.

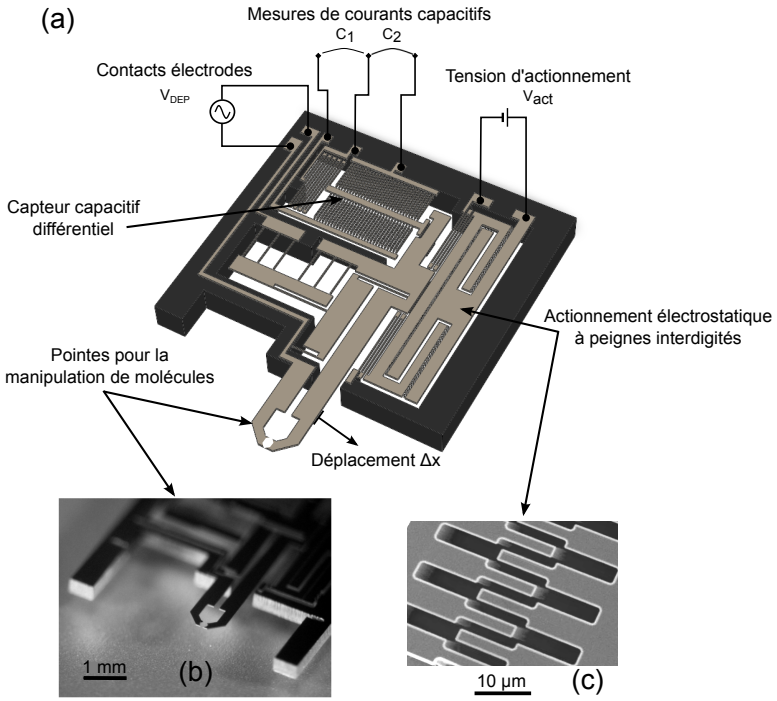

Fig. H.5. (a) Schéma 3D de la micropince en silicium. L'électrode mobile est actionnée par force électrostatique (via la tension d'actionnement V_{act}) et le déplacement, Δx, engendre une variation des capacités C_1 et C_2. La force de diélectrophorèse est produite en appliquant une tension sinusoïdale entre les électrodes V_{DEP}. Dimensions de la puce : 4.5 mm × 5.5 mm. (b) Photo des pinces de la puce. (c) Image de microscopie électronique à balayage (MEB) des peignes interdigités de l'actionneur.

La **Figure** H.5 illustre les différentes parties de la micropince. Elle consiste en deux fines pointes acérées agissant comme électrodes, pour l'application d'une tension de diélectrophorèse d'une part, ou pour la mesure de la conductivité des molécules d'autre part. Une des électrodes est fixe, alors que l'autre électrode peut être déplacée grâce à un actionnement électrostatique. Le déplacement peut être mesuré grâce à un capteur capacitif différentiel. Le dispositif est donc principalement composé de trois parties :

1. Deux électrodes pointues formant la pince ;
2. Un actionneur électrostatique à peignes interdigités ;
3. Un capteur capacitif différentiel.

Les différentes parties du dispositif sont électriquement isolées les unes des autres mais mécaniquement bien reliées grâce à la technologie SOI[4]. De fait, le substrat silicium inférieur est utilisé pour la liaison mécanique des parties, alors que l'oxyde de silicium entre les deux couches de silicium assure l'isolation électrique.

La **Figure** H.11 montre la réponse en fréquence de la micropince. Elle démontre une résonance avec un pic d'amplitude et la rotation de la phase, par laquelle le composant est aisément caractérisé. Les paramètres mécaniques de la pince sont identifiés à travers les réponses statiques et dynamiques. Puis les expériences de détection sont réalisées en suivant la résonance du système et ses variations.

Une détection à boucle de verrouillage de phase (PLL[5]) permet de suivre en temps réel les variations des paramètres du système et, par conséquent, de caractériser en temps réel les interactions entre molécules d'ADN et protéines.

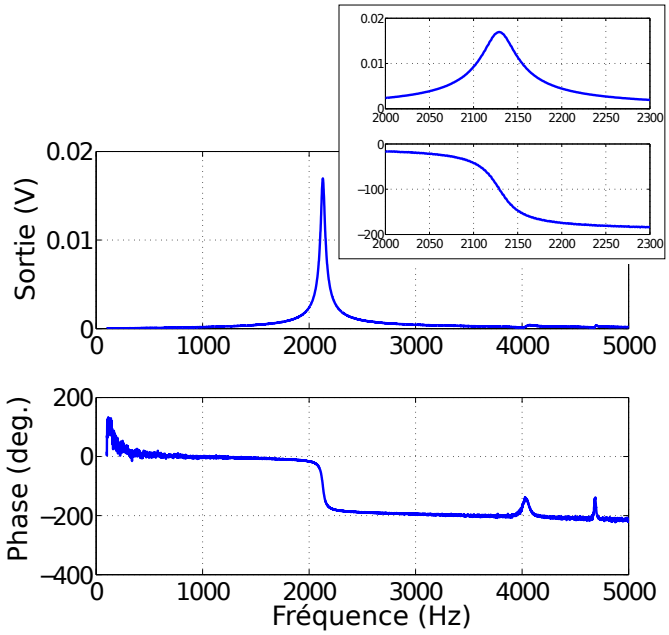

Fig. H.6. Réponse en fréquences de la micropince. Le mouvement est actionné avec un signal de 1 V_{eff} à différentes fréquences de 100 à 5000 Hz avec des pas de 1 Hz. La mesure est effectuée à travers le capteur intégré. V_{sortie} est proportionnelle à la vitesse du mouvement de la pince.

[4] SOI pour *Silicon-On-Insulator* en anglais.
[5] PLL pour *Phase-Locked Loop* en anglais.

Caractérisations biophysiques de molécules d'ADN

La caractérisation des propriétés mécaniques de l'ADN se fait à travers les changements dans la réponse en fréquences de la pince. La **Figure** H.7 démontre les variations de la résonance du système avec le nombre de molécules d'ADN attrapées. La fréquence de résonance du système augmente avec la rigidité des molécules, alors que les pertes visqueuses dues à l'étirement des molécules tendent à diminuer le facteur de qualité de la résonance.

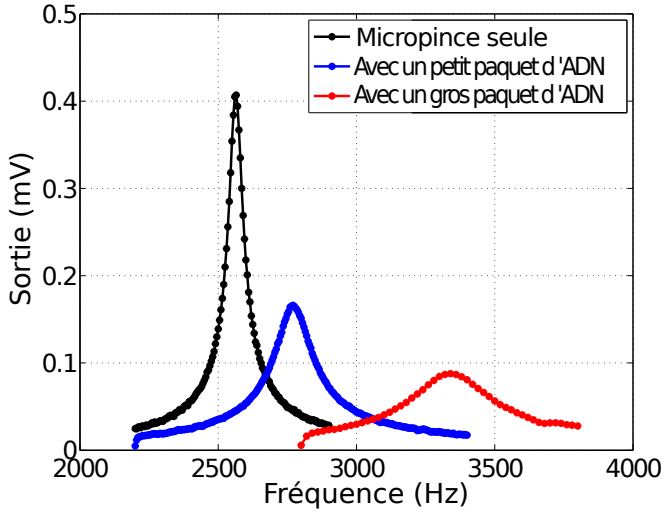

Fig. H.7. Caractérisations de molécules d'ADN par le biais de la mesure de la résonance mécanique de la micropince (dans l'air à pression atmosphérique). La réponse en fréquences du système est mesurée grâce à un amplificateur à détection synchrone. La fréquence de résonance augmente alors que le coefficient de qualité diminue avec le nombre de molécules d'ADN attrapées [Yamahata 2008a].

Le protocole des expériences biologiques est le suivant. La capture de brins d'ADN se fait (1) par simple immersion des pinces dans une solution d'ADN et (2) par l'application d'une tension alternative entre les pinces. Les molécules sont alors attirées et étirées par diélectrophorèse [Washizu 1990]. L'actionneur électrostatique permet ensuite de stimuler les molécules d'ADN et le capteur capacitif de percevoir la réponse de celles-ci. Ayant connaissance du modèle de la micropince, il est alors possible de suivre l'évolution dans le temps de l'état du paquet de molécules d'ADN.

La caractérisation d'interactions entre molécules et protéines se fait par immersion des molécules attrapées dans une solution de protéines (**Figure** H.8). L'interaction entre molécules et protéines modifiant les propriétés mécaniques des molécules d'ADN, la réponse du système change. Dans le cas d'expériences avec des enzymes de restriction, les molécules sont coupées tel que la rigidité du paquet de molécules d'ADN diminue petit à petit dans le temps (**Figure** H.9).

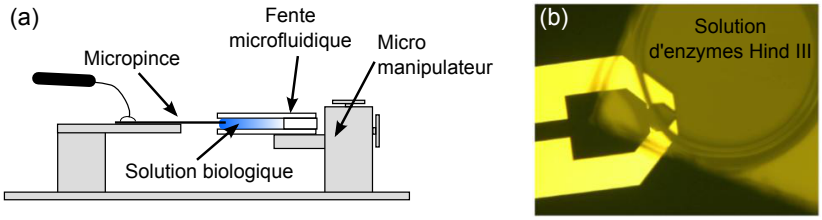

Fig. H.8. Montage expérimental de la micropince pour des réactions biologiques avec des molécules d'ADN et des enzymes *Hin*dIII. (a) Schéma du montage (vue de côté). La micropince est immergée par la fente du composant microfluidique contenant une solution d'enzymes. (b) Photo de microscopie optique des bras de la micropince immergés dans la solution d'enzymes.

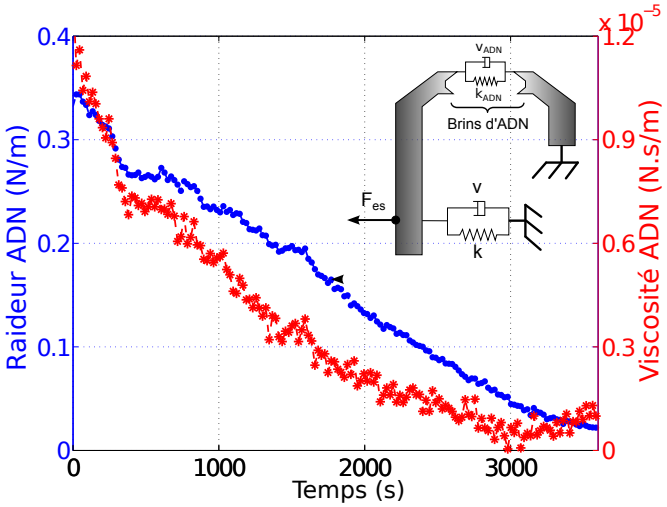

Fig. H.9. Evolution de la raideur mécanique et des pertes visqueuses des molécules d'ADN durant leur digestion par des enzymes *Hin*dIII.

Des expériences ont été réalisées pour contrôler la capture des molécules par diélectrophorèse [Lafitte 2010], et pour caractériser les interactions entre molécules d'ADN et protéines avec des enzymes *Hin*dIII donc [Kumemura 2010], et des protéines de Bromure d'Ethidium qui s'attache à l'ADN double-brin [Lafitte 2011].

Cependant, afin de réaliser des expériences biologiques pertinentes et les plus précises possibles, un contrôle rigoureux des opérations est recherché. Du fait de la volonté de travailler avec un minimum d'espèces biologiques, nos expériences sont sujettes à de nombreux inconvénients comme l'évaporation et l'évolution de la concentration des solutions par exemple. Un composant microfluidique a été conçu et développé pour contrôler les temps de réactions et le volume des solutions [Lafitte 2010]. Le composant est fabriqué par superposition de deux couches de PDMS[6] moulées sur un substrat de silicium, lui-même modelé avec une résine photosensible. Une couche du composant permet d'ouvrir ou de sceller les canaux de l'autre couche grâce à des valves actionnées par pression

[6] PDMS pour Polydimethylsiloxane

pneumatique qui écrase les fins canaux de la couche contrôlable (comme décrit dans [Unger 2000]). La maîtrise de l'écoulement des solutions permet alors de commander les moments de réactions biologiques et de compenser l'évolution des volumes par évaporation.

Commande de la micropince

Il a été démontré que les micropinces mécaniques réalisées en technologie silicium sont des outils appropriés pour la caractérisation de molécules biologiques. Toutefois, par rapport aux outils décrits dans l'état de l'art, les micropinces ne présentent pas une sensibilité suffisante pour caractériser une molécule unique d'ADN.

L'objectif est ici d'utiliser les techniques de l'automatique pour améliorer sensiblement les performances du système. L'enjeu porte sur la mise en œuvre d'une commande en boucle fermée permettant d'augmenter la sensibilité du système à des variations paramétriques. Les principales difficultés résident dans la prise en compte des bruits importants, des erreurs de modélisation et du faible nombre de mesures accessibles. En outre la connaissance des phénomènes dynamiques prépondérants à ces échelles (forces de capillarité et viscosités des milieux par exemple) et leurs modélisations restent aussi un aspect important pour améliorer la compréhension des résultats.

Typiquement, la caractérisation des molécules d'ADN se fait par l'identification des caractéristiques mécaniques des molécules, à savoir raideurs et pertes visqueuses. La raideur équivalente du microsystème est, cependant, d'un ordre de grandeur 6 fois plus important que celle d'une seule molécule d'ADN-λ (i.e. 30 µN/m [Bustamante 2003]). Enfin, fabriquer un microsystème complet (i.e. intégrant actionnement, préhenseur et capteur) avec une partie mobile soutenue par des suspensions dont la raideur est inférieure à 1 N/m est un réel défi technologique.

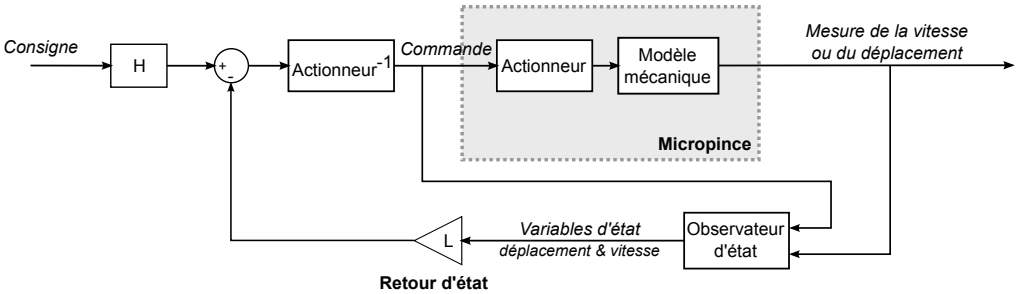

Fig. H.10. Schéma de la commande par retour d'état. Pour l'implémentation du retour d'état L, un observateur d'état est requis dans le but d'estimer les variables d'état du système. Le capteur assure la mesure du déplacement ou de la vitesse. De plus, parce que l'actionneur obéit à une loi non-linéaire, la fonction inverse de l'actionneur (Actionneur^{-1}) est intégrée pour linéariser la commande.

On propose ici de concevoir un système en boucle fermée par retour d'état avec placement des pôles dont les caractéristiques sont plus proches des grandeurs mesurées (cf.

Figure H.10). Dans la détection d'espèces chimiques par des micro-poutres, il est souvent utilisé les modes de résonance les plus hauts en fréquence car la fonction de sensibilité de la fréquence de résonance est inversement proportionnelle à l'inertie [Dohn 2005]. Dans notre cas, la présence et l'évolution des molécules sont détectées grâce à la variation de la fréquence de résonance due à la rigidité ajoutée par les molécules. La fonction de sensibilité de la fréquence de résonance est alors directement proportionnelle à la raideur du système.

Les premières simulations démontrent qu'il est possible de multiplier par 10 cette sensibilité en divisant par 10 la fréquence de résonance du système boucle ouverte (**Figure** H.11). Toutefois, les techniques employées par retour d'état demandent la connaissance de l'état du système, de telle manière qu'une stratégie particulière doit être mise en œuvre pour concevoir un observateur. La dynamique de l'observateur doit permettre de suivre les évolutions du modèle. D'autre part, il doit pouvoir filtrer des mesures dont le ratio signal sur bruit est très faible.

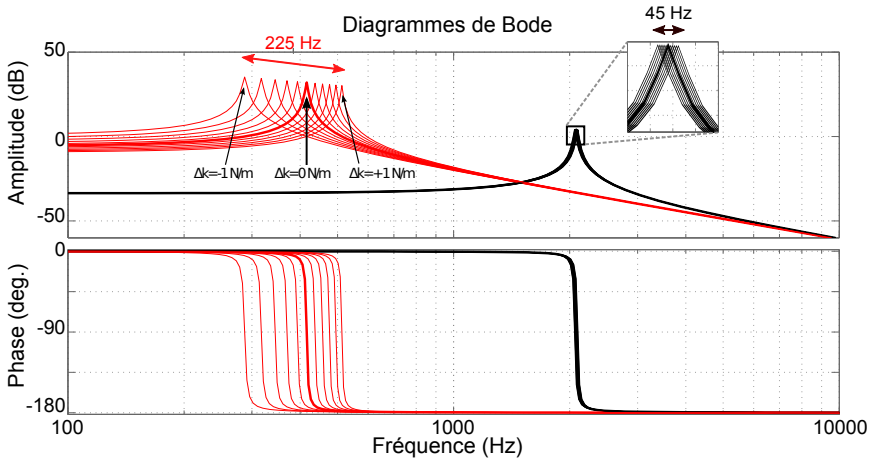

Fig. H.11. Résultats de simulation. En noir est tracée la fonction de transfert de la micropince. En rouge est tracée la fonction de transfert du système en boucle fermée. Les deux systèmes sont soumis à une variation du paramètre raideur k qui induit un changement notable du pic de la résonance. Δk varie de -1 à 1 N/m par pas de 0.2 N/m.

La **Figure** H.12 démontre les performances expérimentales de la méthode. L'immersion des pinces dans un liquide provoque une modification de la résonance due aux pertes dans le liquide et la masse du liquide entraînée par le mouvement. Dans des conditions données, la fréquence de résonance diminue de 0.6 Hz par une commande classique en boucle ouverte. Suite à notre méthode, la fréquence du système boucle fermée diminue de 1.45 Hz rendant la détection de variations plus aisée.

La méthode reste à être appliquée à un processus biologique. Toutefois, les restrictions du système provenait du manque de résolution des mesures. Avec cette méthode on espère augmenter la sensibilité du système afin de rendre les changements détectables avec la résolution actuelle des appareils de mesures.

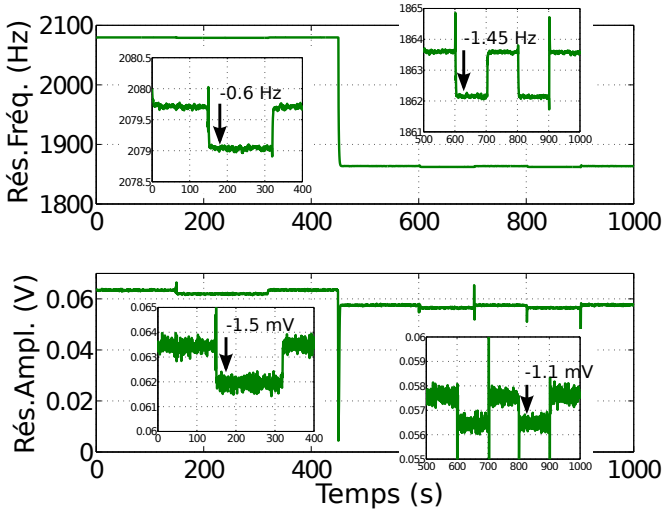

Fig. H.12. Performances des systèmes commandés en boucle ouverte et en boucle fermée ($\beta = 1.1$). Au début de l'expérience la micropince est commandée en boucle ouverte. L'immersion des pinces dans l'eau provoque un décalage de la fréquence de résonance de -0.6 Hz. Ensuite, à $t = 450$ s, la micropince est commandée en boucle fermée. Lors de l'immersion des pinces dans l'eau, le décalage en fréquence est cette fois de -1.45 Hz. L'actionnement des pinces est réalisé avec un signal sinusoïdal de 0.2 V_{cc} autour d'une tension continue de 20 V.

Conclusion

Il a été démontré que les micropinces mécaniques réalisées en technologie silicium sont des outils appropriés pour la manipulation et la caractérisation systématiques de molécules biologiques [Yamahata 2008a, Kumemura 2010, Lafitte 2011].

La résolution des mesures a été notablement diminuée en améliorant différents aspects du système. La boucle à verrouillage de phase permet d'une part de profiter de la rotation abrupte de la phase pour se concentrer sur la fréquence de résonance, et d'autre part de caractériser des interactions très rapides (inférieures à la seconde). Le conditionnement de la puce silicium a aussi été développé pour protéger la mesure des différents bruits ambiants et, compte tenue des dimensions, des couplages entre l'actionnement et le capteur. Toutefois malgré ces efforts, la meilleure résolution obtenue est de l'ordre d'une trentaine de molécules d'ADN-λ (i.e. de la détection de la rigidité mécanique d'une trentaine de molécules d'ADN-λ).

Dans le but d'être aussi compétitif que les outils actuels utilisés en spectroscopie de force, il est nécessaire d'atteindre la détection d'une seule molécule d'ADN et d'améliorer la résolution des mesures. L'implémentation d'une commande par boucle fermée montre qu'il est possible d'améliorer sensiblement la sensibilité du système. Expérimentalement la sensibilité a été améliorée d'un facteur supérieur à 2.

Cependant la méthode est limitée par certaines contraintes comme la difficulté de modéliser précisément un microsystème. Concrètement, la méthode a été limitée par la présence d'autres dynamiques dans la bande de fréquences dans laquelle la micropince est utilisée. Par conséquent un retour sur la conception de la micropince devrait permettre une meilleure implémentation de la méthode.

Slides of the Ph.D. defence on April 4th 2012

Modeling and control of silicon nanotweezers for the characterization of bio-reactions on DNA molecules

Caractérisation et commande de micropinces en silicium pour l'amélioration de la sensibilité paramétrique d'expériences biologiques sur des molécules d'ADN

Nicolas Lafitte

LIMMS Ph.D. student

April 4, 2012

Experiment on a single molecule of DNA
What can we learn experimenting on DNA molecules?

The cell machinery

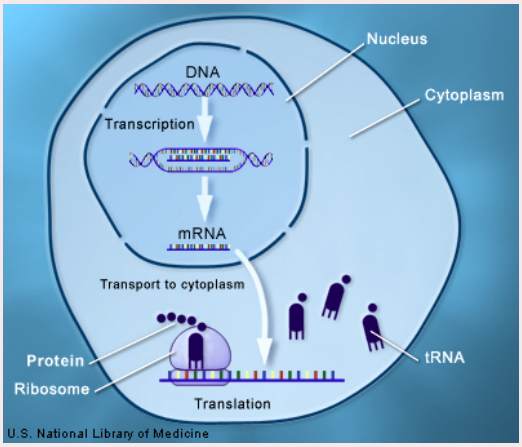

[http://medicineworld.org]

A DNA molecule

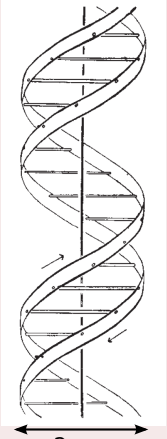

2 nm
[Watson1953]

Experiment on a single molecule of DNA
Force spectroscopy on a single molecule with magnetic tweezers

Single-molecule analysis of DNA uncoiling by a type II topoisomerase

Terence R. Strick, Vincent Croquette & David Bensimon

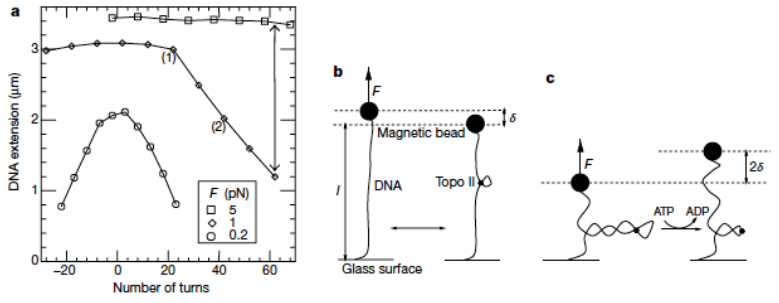

[Strick2000]

Outline

Optical tweezers
Force spectroscopy

Principle

- Trapped micro-size bead (in an optical well)
- Measurement of the bead position/displacement
- With a sub-piconewton force resolution

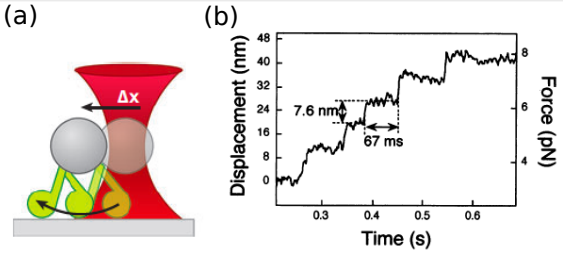

[Kojima1997]

Magnetic tweezers
Force spectroscopy

Principle

- Trapped micro-size bead (in a magnetic field)
- Measurement of the bead position or displacement and rotation
- With a sub-piconewton force resolution

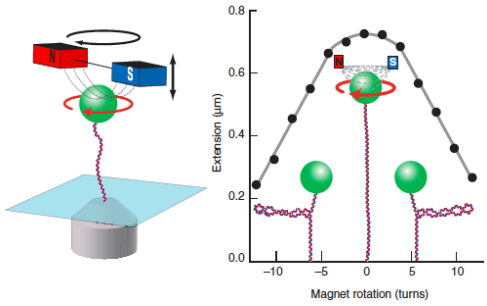

[Strick1996]

Scanning Force Microscopy
Force spectroscopy

Principle

- Anchoring of the molecule to micron-size beam
- Static measurement of the probe deflection
- With a force resolution of 10^{th} of pN

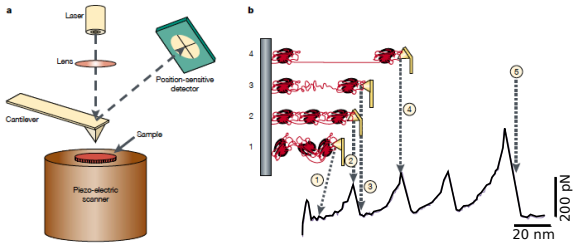

[Carion-Vasquez1999]

Manipulation of single molecule of DNA
Why single molecule methods?

The advent of methods of single molecule manipulation has made it possible, for the first time to:

- Measure the forces and stress that maintain the structure of macromolecules
- Measure the forces generated in chemical & biochemical reactions
- Investigate time-averaged and time-dependent fluctuations
- Characterize the dynamics of molecular motors
- Exert external forces and torques to alter the extent and fate of chemical reactions

Single molecule techniques
Summary table of force spectroscopy techniques

Good / Average / Bad

	Displ. range (nm)	Force meas. (pN)	High forces	Torsion meas.	Elec. meas.	Cost	Exp. protocol	ufluidic compatibility
Optical tweezers	0.1 - 2	0.1 - 10^2	●	●	●	●	●	●
Magnetic tweezers	2 - 10	10^{-3} - 10^2	●	●	●	●	●	●
AFM	0.5 - 1	10 - 10^3	●	●	◐	◐	◐	◐
Silicon tweezers	?	?	●	●	●	●	●	●

Design of the silicon nanotweezers

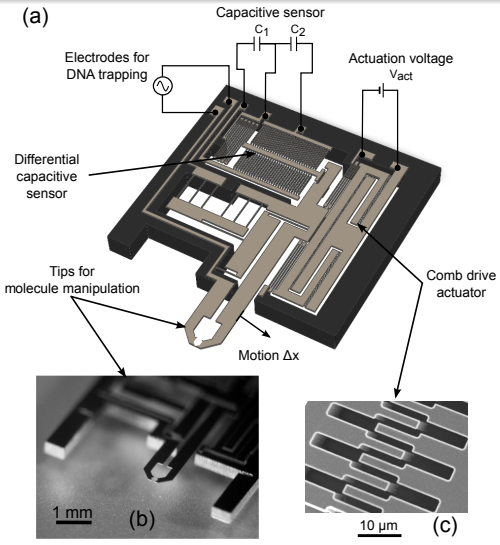

[Yamahata2008]

Experimental setup

Instrumentation

- Direct actuation by a voltage
- Sensing of capacitive currents
  - Measurement of very small currents ($\sim$ pA)
  - I/V Preamplication
  - Lock-in detection for noise rejection

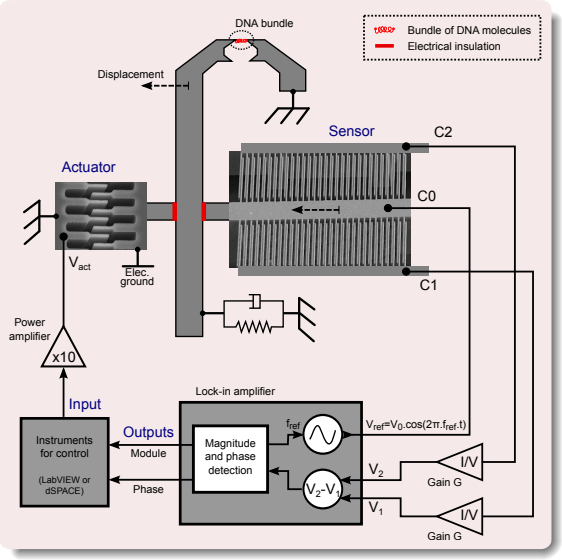

Characterization of the nanotweezers
Static characterization

Direct measurement

- Direct measurement by the sensor output
- Characterization of the square law of the electrostatic actuator

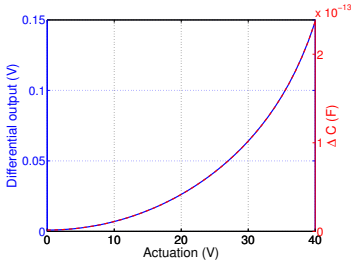

Identification

- Characterization of the non-linearity of the sensor
- Identification of the model parameters

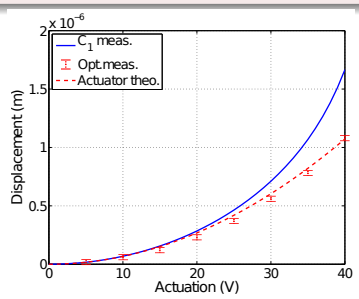

Characterization of the nanotweezers
Frequency characterization

Characterization of the main resonance

- Direct measurement by the sensor output
- Characterization of the main mechanical resonance
- Presence of other dynamics

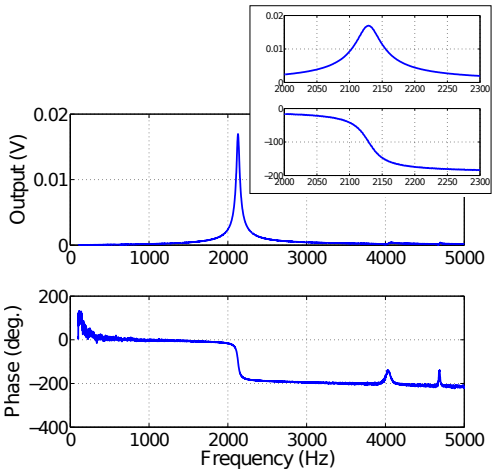

Modeling of the nanotweezers

Mechanical model of the nanotweezers

The mechanical behavior of the tweezers is considered as:

- A 2^{nd} order model
  - identified on the main resonance
- With identified parameters
  - Mass M
  - Stiffness k
  - Viscous losses ν

Actuator and sensor are considered as perfect transducers and simple gains

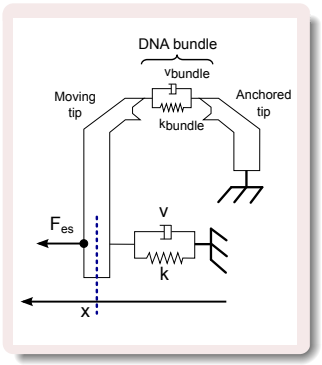

Bioexperiments on DNA molecules with silicon nanotweezers

Video

(Loading video : Biocharacterization on DNA with silicon nanotweezers)

Characterizations of restriction enzymes on DNA
with *Hind*III enzymes

(1) Bioexperiments with *Hind*III

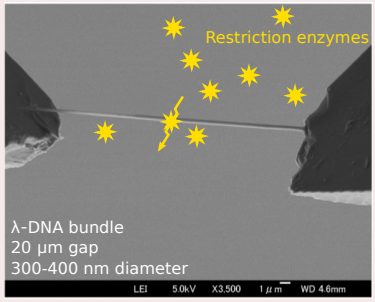

→The mechanical stiffness k of the bundle decreases with interactions with restriction enzymes

(2) Monitoring of the bioreactions

From the Equation of the resonant frequency of a 2^{nd} order system:

$$f_R = \frac{1}{2\pi}\sqrt{\frac{k}{m}}$$

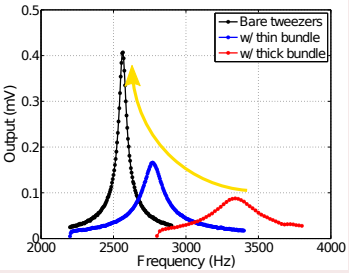

Characterizations of restriction enzymes on DNA (2)

with *Hind*III enzymes

Method

- After trapping of bundle of DNA
- Immersion of the tweezers' tip in the enzyme solution
- Monitoring of the mechanical resonance

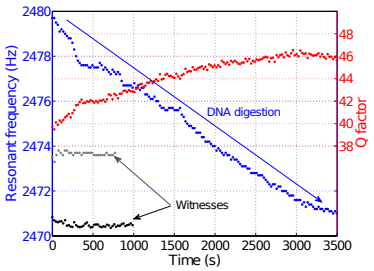

Results

During 1 hour,

- The resonance is monitored
- The resonance frequency and the losses decrease
- The time constant depend on the enzyme concentration

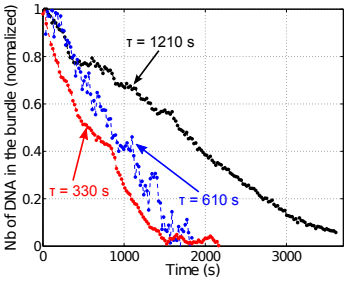

Resolution of the measurement

- If, during the monitoring of the resonance frequency, the frequency is measured with a precision of ± 0.01 Hz ...

$$\frac{\partial f}{\partial k} = \frac{1}{2\pi} \frac{1}{2M\left(\frac{k}{M}\right)^{\frac{1}{2}}} = \frac{1}{8\pi^2 M f_R}$$

- ... and from the $\partial f / \partial k$ sensitivity function, we deduced a precision on the stiffness measurement of 0.9 mN/m
- ... that is to say the equivalent stiffness of ~ 30 λ-DNA molecules

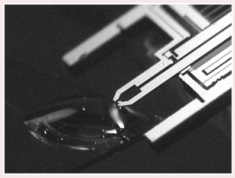

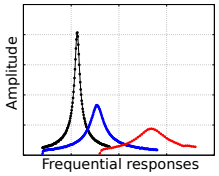

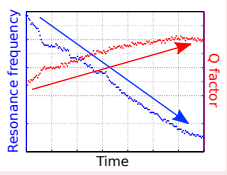

Resolution of the measurement

- From Equation of the resonance frequency, if the stiffness k of the system decreases, **the sensitivity of resonant frequency to stiffness variations increases**:

$$\Rightarrow k \searrow \quad \Rightarrow \frac{\partial f_R}{\partial k} \nearrow$$
$$\Rightarrow f_R \searrow \quad \Rightarrow \frac{\partial f_R}{\partial k} \nearrow$$

- Then it is problematic to design a new MEMS with this degree of complexity with very low mechanical stiffness (< 1 N/m)
  - Need to deal with the mass of the system and sticky surface forces between small-gap separated surfaces

Nanotweezers (50 N/m)

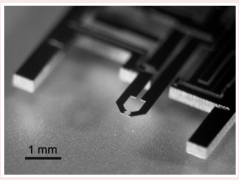

λ-DNA (30 µN/m)

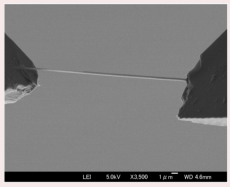

Improvement of the parametric sensitivity
... by a feedback approach

Idea
Implement closed-loop method to **improve the sensitivity of the system to parameter detection or evolution**

Goal
Design a new system, as we can design new tweezers, with new characteristics convenient to specific parameter detection

Nanotweezers (50 N/m)
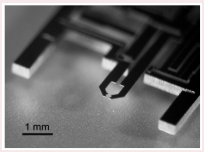

λ-DNA (30 µN/m)
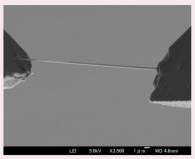

Implementation of a state feedback (1)
... for improvement of the parametric sensitivity

Control scheme
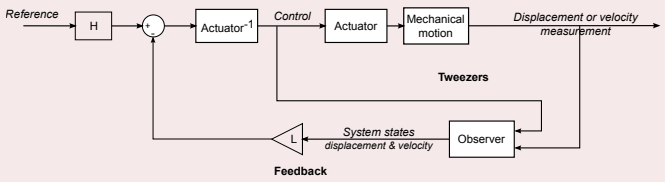

Implementation of a state feedback
The tweezers equation is recasted in the state space representation

$$\dot{X} = \begin{bmatrix} 0 & 1 \\ -\frac{k}{M} & -\frac{\nu}{M} \end{bmatrix} X + \begin{bmatrix} 0 \\ \frac{1}{M} \end{bmatrix} U$$

The state feedback modifies the command as: $U = \text{Ref} - LX$

Implementation of a state feedback (2)

... for improvement of the parametric sensitivity

Control scheme

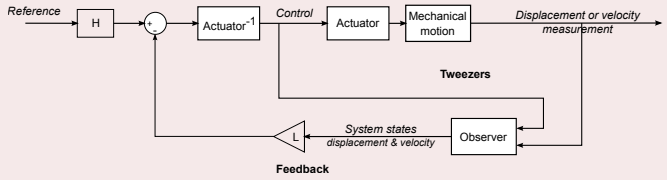

State representation of the closed-loop

$$\dot{X} = \begin{bmatrix} 0 & 1 \\ -\dfrac{k+l_1}{M} & -\dfrac{\nu+l_2}{M} \end{bmatrix} X + \begin{bmatrix} 0 \\ \dfrac{1}{M} \end{bmatrix} \text{Ref}$$

Design of the state feedback by pole placement

The state feedback L is designed by pole placement of the closed-loop system.

Poles are placed such as the resonance frequency is *lowered*, which lies with the *lowering* of the stiffness of the system (by l_1 in particular).

Root locus

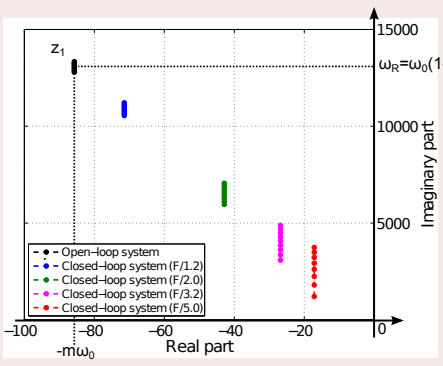

Improvement of the parametric sensitivity
Simulations

Simulated bode plot

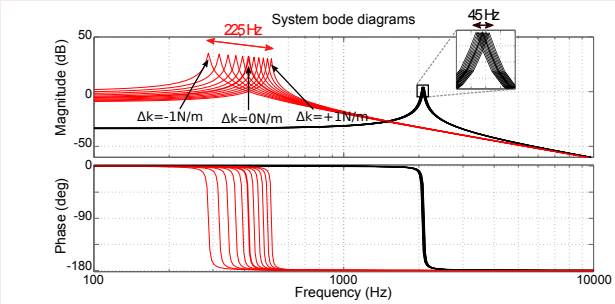

Open loop sensitivity

$$\frac{\partial f_R}{\partial k} = \frac{1}{2\pi} \frac{1}{2M\sqrt{\frac{k}{M} - \frac{1}{2}\frac{\nu^2}{M^2}}}$$

Closed-loop sensitivity

$$\frac{\partial f_R}{\partial k} = \frac{1}{2\pi} \frac{1}{2M\sqrt{\frac{k+l_1}{M} - \frac{1}{2}\frac{(\nu+l_2)^2}{M^2}}}$$

Design of an observer for the state reconstruction

The implementation of a state feedback requires the availability of the state of the system. An observer is needed to reconstruct the state of the system from the measurement.

The dynamic of the observer needs to be designed with respect to preserve the sensitivity enhancement.

Root locus

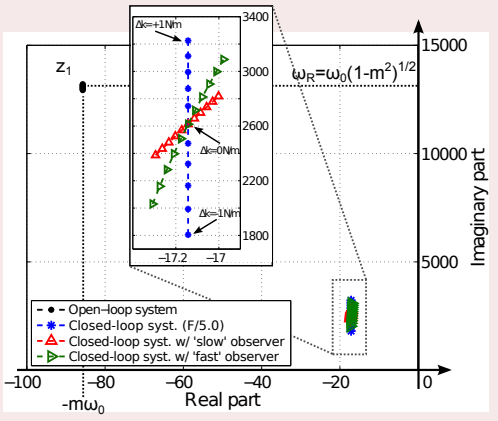

Experimental setup in Besançon
Measurement of the position with an interferometer

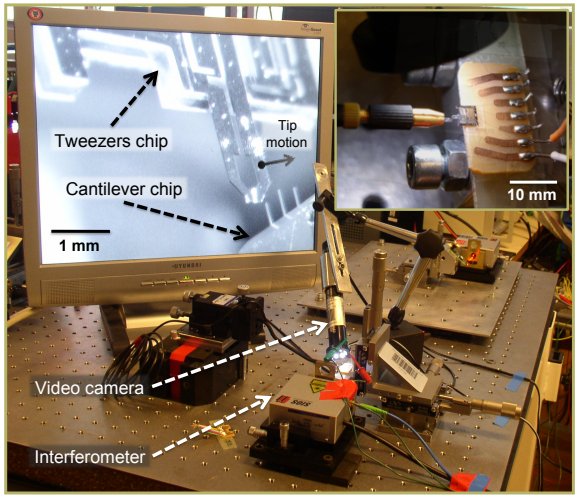

Results with velocity observation (1)
Open loop step response

- Model parameters around an operating point ($250\ \mu m$)
- Step responses in open loop as reference
- Added stiffness using the contact with a cantilever
  - Oscillation frequency shift of $+9.3\ Hz$

Open loop system

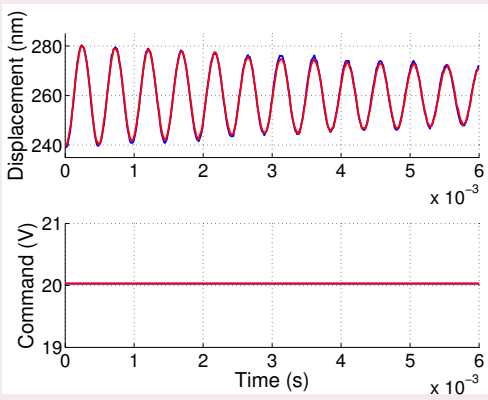

Results with velocity observation (2)

Closed-loop system step response $F/1.1$

- Step responses around $250\ \mu\text{m}$ point
- Oscillation frequency shift of $+12.1$ Hz

Closed-loop system $F/1.1$

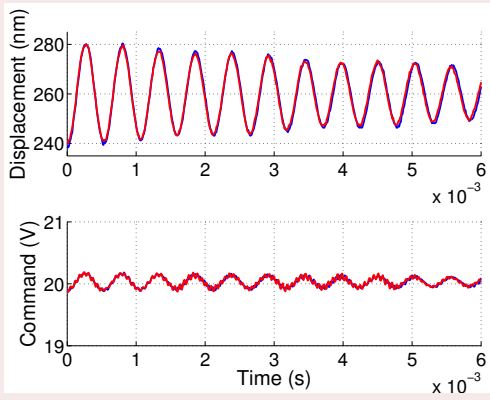

Results with velocity observation (3)

Closed-loop system step response $F/1.3$

- Step responses around $250\ \mu\text{m}$ point
- Oscillation frequency shift of $+16.7$ Hz
- **Presence of frequency modulation**

Closed-loop system $F/1.3$

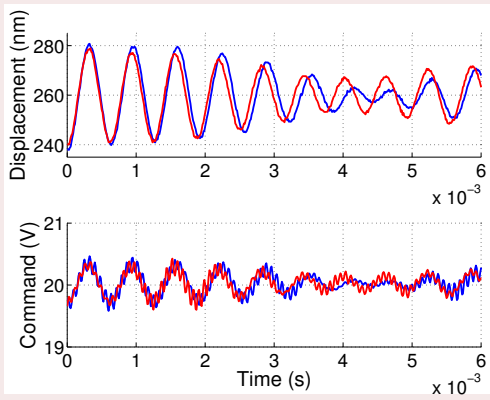

Results with velocity observation (4)

Closed-loop system step response $F/2.0$

- Step responses around $250\ \mu\text{m}$ point
- Oscillation frequency shift of $+38.8$ Hz
- Presence of frequency modulation

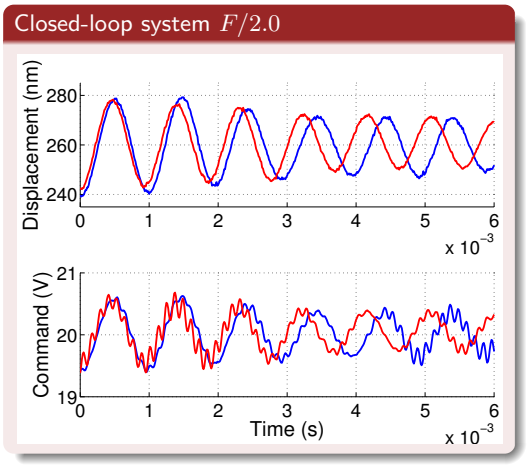

Performance summary

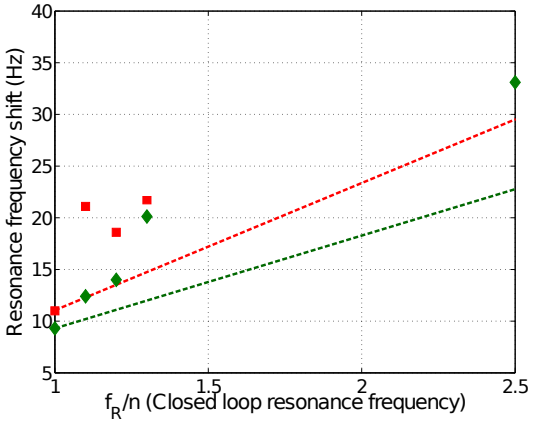

Limits of the method

The method is limited by the presence of the other dynamics and the subsequent inaccuracy of the model.

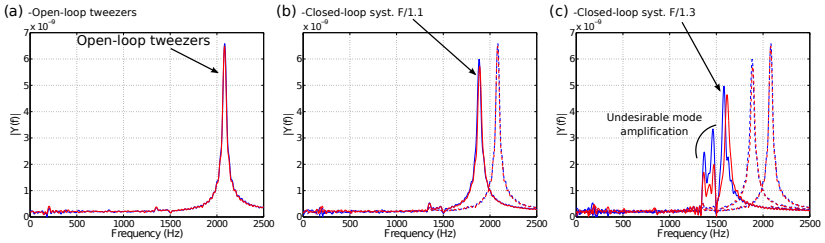

Further characterizations of the nanotweezers
Optical measurements

By optical characterization and stroboscopic video, other dynamics of the tweezers are characterized.

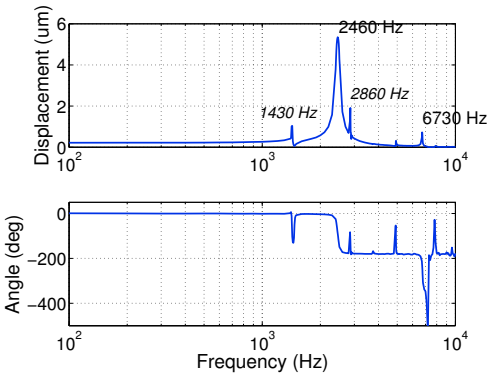

Further characterizations of the nanotweezers (2)
Finite-Element simulations

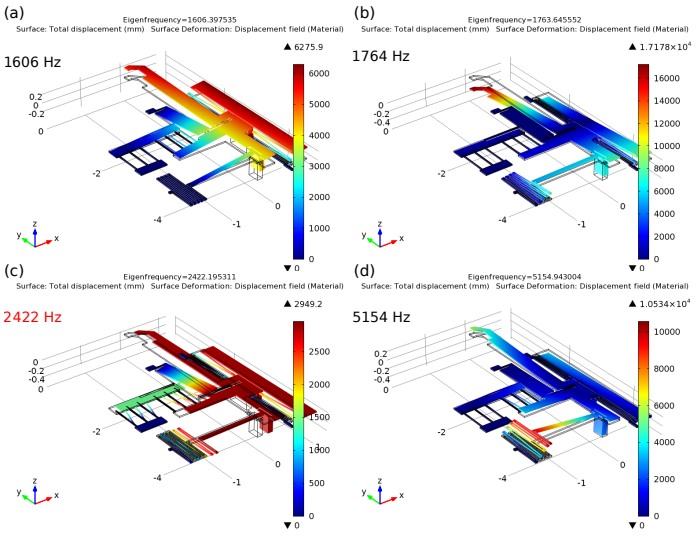

Characterization of DNA molecules
Results with displacement observation

Open loop driven and closed-loop system $F/1.1$

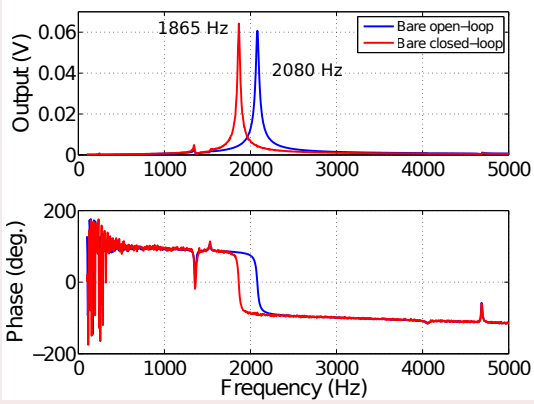

Characterization of DNA molecules
Results with displacement observation

Open loop driven tweezers

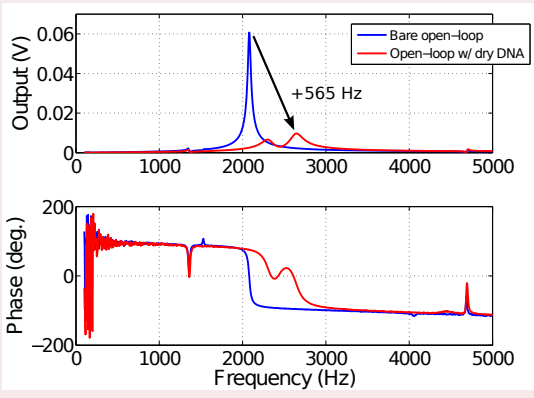

Characterization of DNA molecules
Results with displacement observation

Closed-loop system $F/1.1$

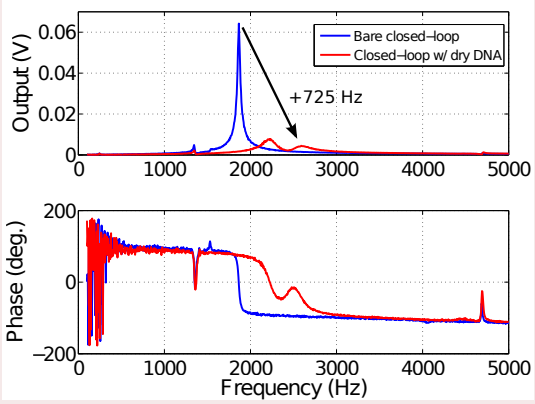

New design of the tweezers
.... with requirements for feedback implementation

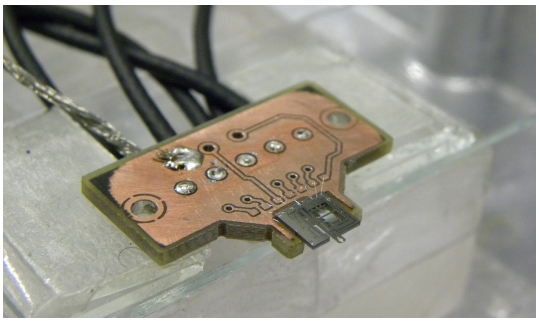

Design of new silicon nanotweezers
Finite-Element simulations

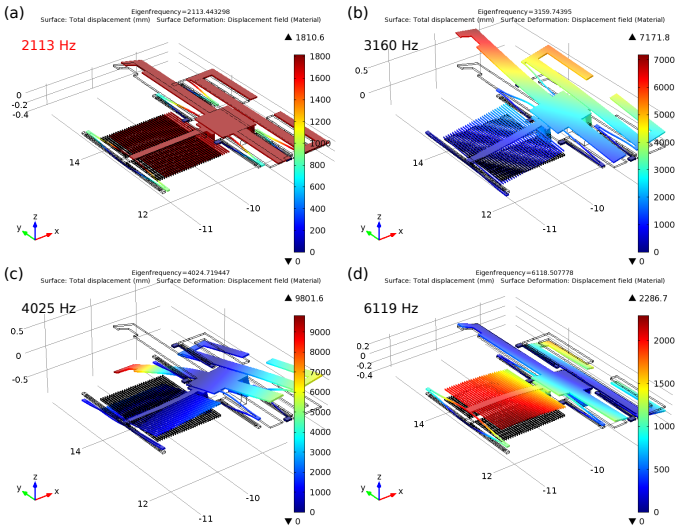

Frequency characterization of the new tweezers
Bode plot

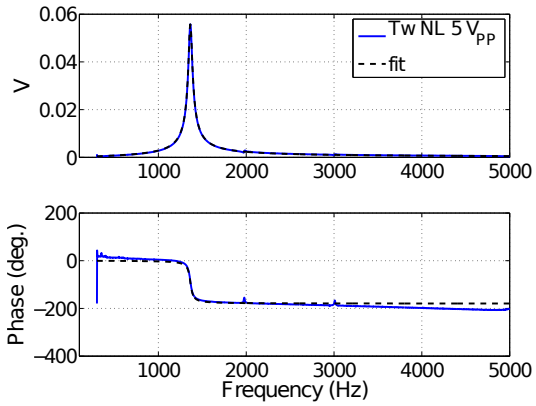

Feedback implementation with the new tweezers
Results with displacement observation

Open loop driven and closed-loop systems

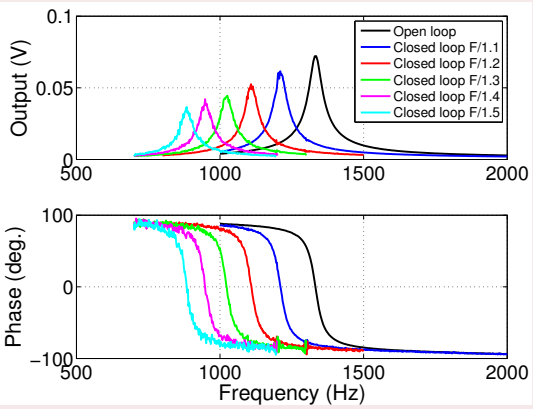

Characterization of Fibronectin molecules with new tweezers
Results with displacement observation

Open loop driven tweezers

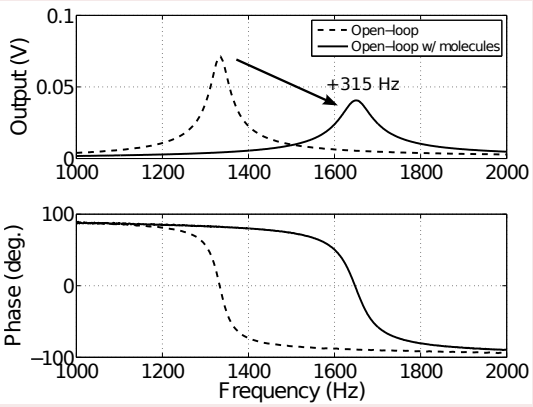

Characterization of Fibronectin molecules with new tweezers
Results with displacement observation

Closed-loop system $F/1.2$

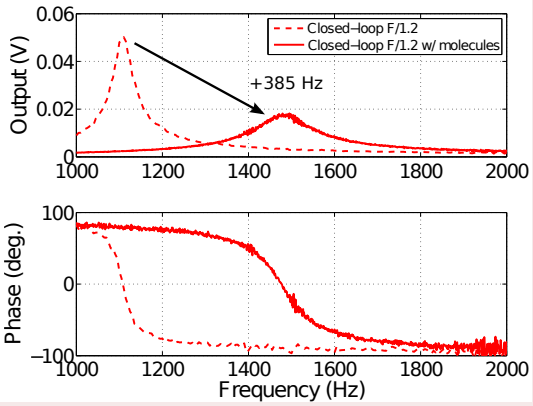

Characterization of Fibronectin molecules with new tweezers
Results with displacement observation

Closed-loop system $F/1.5$

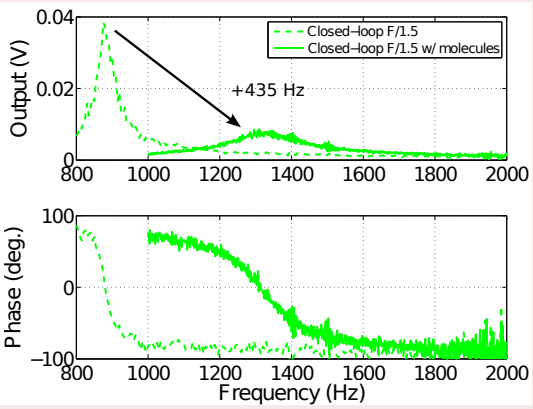

Characterization of Fibronectin molecules with new tweezers
Results with displacement observation

Closed-loop system $F/2.0$

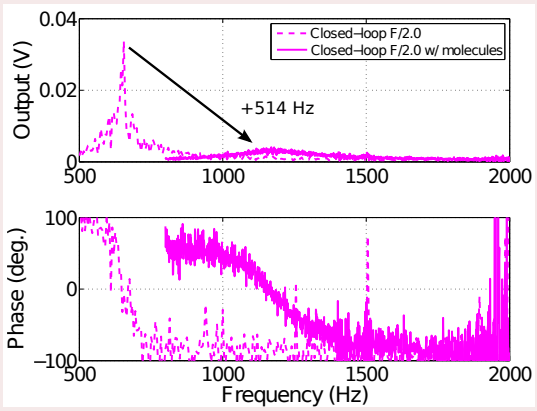

Characterization of Fibronectin molecules with new tweezers
Performance summary

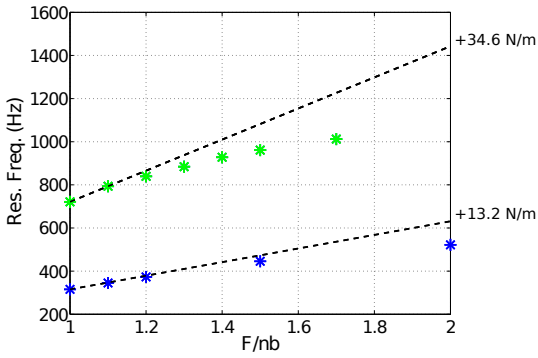

Characterization of Fibronectin molecules with new tweezers
Performance summary in liquid

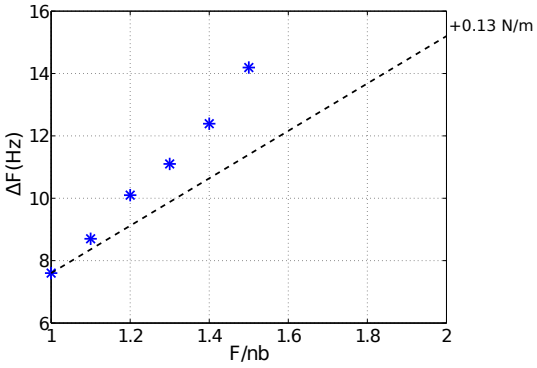

Conclusions (1/2)

- The monitoring of biological reaction with silicon nanotweezers has been shown
  - with restriction enzymes and binding proteins
- The development and the implementation of a feedback controller have been demonstrated
  - The improvement was higher than theory expected
  - The implementation was hindered by the presence of other dynamics
- Return on the design of the tweezers - Design and fabrication of new tweezers
- The modeling and the implementation of a feedback controller have been demonstrated
  - with better accuracy with the theory

Conclusions (2/2)
Summary table of performances

Good / Average / Bad

	Displ. range (nm)	Force meas. (pN)	High forces	Torsion meas.	Elec. meas.	Cost	Exp. protocol	ufluidic compatibility
Optical tweezers	0.1 - 2	0.1 - 10^2	●	◐	●	●	●	●
Magnetic tweezers	2 - 10	10^{-3} - 10^2	●	●	●	●	●	◐
AFM	0.5 - 1	10 - 10^3	●	●	◐	◐	◐	◐
Silicon tweezers	*Static* 0.2 - 10^4 / *Dynamic* 0.2	10^4 - 10^8 / ~~30~~ 15	●	●	●	●	●	●

Perspectives

- Further improvement of the design of the tweezers
  - with respect to feedback requirements (dynamics)
  - with respect to experiment resolution (Q factor)
- Improvement of the feedback design and implementation
  - More accurate characterization and modeling of the tweezers
  - Consideration and modeling of the liquid meniscus
- Upgrading of the microfluidic device with piezo-actuated valves
- Development of new biological experiments
  - First step: re-do the experiments with restriction enzymes and binding molecules to validate the approach
  - Second step: develop new experiments with a systematic protocol with microfluidic

Thank you for your attention

Acknowledgement

Supervisors:
Pr. Dominique COLLARD
Pr. Hiroyuki FUJITA
Pr. Yassine HADDAB
Pr. Yann LE GORREC

Colleagues:
Pr. Hervé GUILLOU
Dr. Laurent JALABERT
Dr. Momoko KUMEMURA
Pr. Pierre LAMBERT

All the members of
- the Fujita lab.
- the LIMMS lab.
- the AS2M lab.
- the Jury

And I would like to express all my gratitude to my parents and close friends for their unconditional love and encouragement.

Abstract

Modeling and control of silicon nanotweezers for the characterization of bio-reactions on DNA molecules

Keywords: silicon nanotweezers, DNA, biosensing, control, parameter sensitivity, state feedback, state observer

Abstract: The main objective of this Ph.D. work is to achieve biological experiments on DNA molecules with versatile silicon nanotweezers. Experiments on single molecule rely mostly on Optical Tweezers, Magnetic Tweezers or Atomic Force Spectroscopy, but have a low throughput since preparations are done one at a time. To move towards systematic biological or medical analysis, micro- and nano-systems (MNEMS) are the appropriate tools as they can integrate accurate molecular level engineering tools and can be cheaply produced with highly parallel process.

Design and fabrication of the silicon tweezers are made by ourselves in the lab of Pr. Hiroyuki Fujita (U. of Tokyo, Japan). DNA molecules are firstly trapped in solution by dielectrophoresis. Then biological reactions are characterized in real-time by monitoring the mechanical resonance of the system {tweezers + DNA bundle}. The resolution of the measurements allowed the sensing of about 30 of λ-DNA molecule stiffness (i.e. about 20 mN/m). To achieve the single molecule resolution, we propose to implement a feedback strategy to alter the system.

State feedback was developed to emulate a new system more sensitive to mechanical stiffness parameter detection. As it remains problematic to design and fabricate new micro mechanical device with extremely low stiffness (< 1 N/m), we propose to emulate a compliant system. By simulations it was demonstrated an enhancement of the sensitivity of about 10 when the resonant frequency of the closed-loop system is designed to be 10 times lower than the tweezers resonant frequency (i.e. reducing the stiffness parameter of the system). Experimentally we demonstrated an improvement of the the sensitivity of superior to 2. However the issue is here to obtain stability, robustness with respect to disturbances and unmodeled dynamics. Before to attain the sensitivity of the single molecule, problematics about the model of the device or about the several dynamics of the device needs to be dealt in order to control and fit the improvement with the theory.